REMOTE GEOTECHNICAL CLASSIFICATION OF SEABED SEDIMENTS USING ACOUSTIC TECHNIQUES

Scott Duncan Hadden

A Thesis Submitted for the Degree of PhD
at the
University of St Andrews

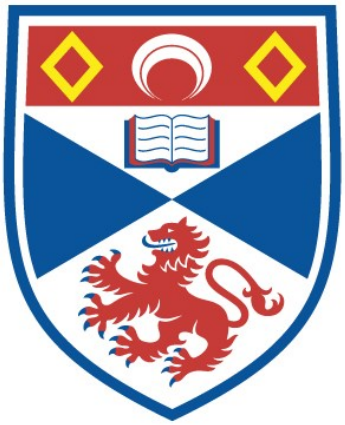

2002

REMOTE GEOTECHNICAL CLASSIFICATION OF SEABED SEDIMENTS USING ACOUSTIC TECHNIQUES

By

Scott Duncan Hadden

A thesis submitted in accordance with the requirements of the University of St Andrews for the award of Doctor of Philosophy.

University of St Andrews
School of Geography and Geosciences
Irvine Building
North Street
St Andrews
Scotland

CONTENTS

LIST OF FIGURES

LIST OF TABLES

LIST OF PLATES

LIST OF TRIGONOMETRIC PARAMETER SYMBOLS

v_1	Speed of Sound in water
t	total 2-way travel time
X_1	Northing location of transducer
Y_1	Easting location of transducer
Z_1	Height of transducer
X_2	Northing location of element
Y_2	Easting location of element
Z_2	Height of element
H_d	Distance from transducer to element in X,Y plane
D_t	Distance from transducer to element in Z plane
r	Distance from transducer to element in X, Y & Z planes
E_w	Element width
E_L	Element length
E_{area} **or** dA	Area of Element
Sl_e	Slope length between elements E_{n-1} and E_{n+1}
α_H	Angle of incidence assuming a flat, horizontal seabed
α_S	Elevation angle of seabed slope between elements E_{n-1} and E_{n+1}
α	Total angle of incidence of acoustic wave at the water-sediment interface

LIST OF ACOUSTIC PARAMETER SYMBOLS

$\mathbf{R_{sens}}$	Receive Sensitivity of the transducers
SL	Source Level
Ab	Absorption Loss
$\mathbf{K_{ab}}$	Absorption Factor
SS	Spherical Spreading
TTL	Total two-way Transmission Loss
BD	Beam Directivity
ϕ	Beam Elevation
β	Beam Azimuth
EA	Elevation Angle
K	Kseg
DI	Directivity Index of Ping
$\mathbf{RX_e}$	Receive Response of transducer
$\mathbf{TX_e}$	Transmit Response of transducer
RV	Receive Voltage
Amp	16-bit Amplitude value output by ISIS
RL	Received Level
TS	Target Strength
EL	Echo Level
$\mathbf{Bsk_0}$	Backscatter value normalised to 0^0
$\mathbf{AL_{ws}}$	Acoustic Loss at the water-sediment interface
Ri	Roughness indicator
RI	Roughness Index

ACKNOWLEDGEMENTS

I would like to take this opportunity to thank my supervisory team of Professor C. D. Green and Professor John McManus for their guidance throughout the duration of this research, especially when the former could be tracked down. I would also like to thank Dr Richard Bates for his help during fieldwork and for his valued input during the preliminary stages of the project. Thanks also to Colin Cameron, Stuart Allison, and the rest of the staff at the Department of Geography and Geosciences.

Many thanks also to Dr Matt Geen, Mr Paul Byham, and the rest of the team at Submetrix Ltd, Bath, England, for their time, effort and continued technical support throughout the fieldwork programme. Thankyou also to Mr Mike Baker, formerly of Sage Survey Ltd, Bath, England, for getting the ball rolling with the Teaching Company Scheme project.

I am eternally grateful for the support and encouragement received from my mother and father, who have stood by me throughout, and who, during the final year of my research, placed a roof over my head and served up lots of top notch cuisine and copious quantities of good wines. Without you, this would never have been possible.

Many, many thanks also to Amanda – thankyou very much for your patience and understanding. Finally, I wish to thank my close friends, especially Dan, Duncan, Gary, Gavin, John, and Pepa, for providing ample distractions and keeping my sense of humour from fading.

I wish to dedicate this thesis to those who have made me the person I am today;

My parents, Ronald & Irene Hadden,

and my grandparents, John & Janet Duncan, and Alfred & Elizabeth Hadden.

I, Scott Duncan Hadden, hereby certify that this thesis, which is approximately 54,810 words in length, has been written by me, that it is the record of work carried out by me and that it has not been submitted in any previous application for a higher degree.

date 28/09/01 signature of candidate .....

I was admitted as a research student in September 1997 and as a candidate for the degree of PhD. in September 1999; the higher study for which this is a record was carried out in the University of St Andrews between 1997 and 2001.

date 28/09/01 signature of candidate .....

I hereby certify that the candidate has fulfilled the conditions of the Resolution and Regulations appropriate for the degree of PhD. in the University of St Andrews and that the candidate is qualified to submit this thesis in application for that degree.

date 28/09/01 signature of supervisor .....

In submitting this thesis to the University of St Andrews I wish access to it to be subject to the following conditions:

for a period of 5 years from the date of submission, the thesis shall be withheld from use.

I understand, however, that the title and abstract of the thesis will be published during this period of restricted access; and that after the expiry of this period the thesis will be made available for use in accordance with the regulations of the University Library for the time being in force, subject to any copyright in the work not being affected thereby, and a copy of the work may be made and supplied to any *bona fide* library or research worker.

date 28/09/01 signature of candidate .....

ABSTRACT

Although the sonar amplitude of return is undoubtedly determined by the acoustic-sediment interaction at the seabed, the raw amplitude of return is of little practical use to geotechnical engineers. By focusing upon the relationships between the strength of the acoustic scattering and the roughness of the surficial seabed sediments, this research aims to derive a remote acoustic methodology that can be used to predict the geotechnical characteristics of the seabed sediment.

The main field survey areas selected were Loch Earn, Scotland, and the Portsmouth coastal waters in the Solent, England, with the precise location of the field sites being determined by the distribution of differing sediment types. The sonar data was acquired by a 234kHz Interferometric Seabed Inspection Sonar system, which provided not only high precision and high resolution, but also extensive and very dense data coverage. These sonar datasets were then complemented by a sediment ground-truthing programme within the same area.

Using trigonometry and the 'sonar equation' parameters, the complex post-processing of the bathymetric and acoustic data resulted in the generation of an acoustic roughness measurement. The sediment grain size analysis then followed standard techniques to derive values for the statistical roughness parameters of the sediment.

The correlation between the acoustic and sediment roughness uncovered a good correlation between the mean grain size and also the finest modal value, with an increase in acoustic scattering strength reflecting an increase in the mean and finest modal grain sizes. The reversal of this correlation therefore enables a prediction of mean or finest modal grain size, thereby demonstrating an approach towards an 'unsupervised' acoustic sediment classification scheme.

This study was carried out over a very narrow grain size range, from muds to fine sands, and therefore the addition of sonar datasets recorded over coarser sediments are required to complete the classification scheme.

CHAPTER 1:

INTRODUCTION AND OBJECTIVES

1.1. Introduction

Underwater sonar systems were initially developed to monitor the depth to seabed (bathymetry) in order to aid the safe navigation of shipping vessels through the oceans. As marine technology has advanced over the past sixty years however, so mans utilisation of the oceans has extended from the sea surface, through the water column, to the seabed and beyond.

This extension in use also brought about a change in the perceived application of sonar systems from relatively low precision, low resolution bathymetric monitoring, to very high precision, high resolution mapping studies of submerged surface topographies. In addition to deriving bathymetric data, the variations in the amplitude of the acoustic returns recorded by the sonar have also been used to identify acoustic anomalies on the seabed. In many cases these acoustic anomalies can be directly related to the locations of topographic irregularities such as rocky outcrops, shipwrecks, mines, and ocean-bottom cables and pipelines.

The combination of high-resolution bathymetric and acoustic amplitude data has resulted in bathymetric side-scan sonar systems being used as the primary reconnaissance surveying tool for a variety of commercial and military applications including dredging surveys, pipeline/cable route planning surveys and post-installation monitoring, mine detection, and marine aggregate resource recovery projects. This versatility of application has also helped to drive the research and development of the sonar systems towards maximising the potential of the sonar reconnaissance by enhancing the precision and resolution of both the bathymetric and acoustic data.

In-spite of this extensive development and universal application, the role of the high precision, high resolution bathymetric side-scan sonar survey system remains restricted to that of a relatively basic reconnaissance tool, constrained by the present inability to derive any further forms of geotechnical surface data required by marine engineers.

However, recent advancements on the work of Rayleigh (1945) and Urick (1963) have suggested that through a combination of underwater acoustical studies and theoretical studies of the physical processes acting upon an acoustic signal as it strikes the seabed, it may be possible to extract additional acoustic information from the sonar which can be directly related to the physical properties of the seabed sediment.

If these processes and techniques could ultimately be proven to derive geotechnical information relating to the seabed properties using existing technology, then this would evidently represent a very significant scientific development with regard to the quality and quantity of information generated from sonar reconnaissance surveys.

1.2. Objectives

The main objective of this research is to enhance the potential of data collected by existing bathymetric side-scan sonar systems towards the derivation of geotechnical information relating to the material properties of the seabed surface sediments.

This investigation will therefore comprise of a comprehensive, two-fold analyses of sonar and sediment data acquired over the same area, in order to facilitate the examination of direct correlations between the amplitude of the acoustic response and the statistical and compositional characteristics of the sediments.

In order to advance science towards the generation of a remote geotechnical classification scheme, the acoustic-sediment analysis will not only aim to derive a technique for the remote discrimination between basic sediment classes, but will also aim to establish a correlation between the acoustic response of the seabed and the

primary statistical characteristics that reflect the roughness of the seabed surface sediments.

The successful identification and derivation of any correlations between the bathymetric and acoustic datasets, and the roughness characteristics of the sediments, will thereby promote the application of the associated empirical relationships towards the generation of a comprehensive technique for the remote geotechnical evaluation of seabed sediments. If this technique is based solely upon the bathymetric and amplitude data recorded by existing sonar systems, then this research will have identified a primary mechanism towards the future creation of an unsupervised remote seabed classification technique.

CHAPTER 2:

AN INTRODUCTION TO ASPECTS OF UNDERWATER ACOUSTICS

2.1. Evolution of underwater acoustics – A chronological account

"Acoustic systems have been used as nondestructive sensors of the water column, ocean bottom, and marine and continental geological structures for several decades."

Clay and Medwin, 1977

The first commercial application of underwater acoustics came in the form of an echo-sounder. This echo-sounding system, developed in the early 20th Century, was designed to provide depth data from directly beneath a vessel in order to monitor the 'clearance' distance between the vessel bottom and the seabed (Matthews, 1939; Eckart, 1946). The echo-sounder utilises a single sonar pulse emitted from a hull-mounted transducer* (* the electromechanical component of a sonar system, mounted underwater, used to convert electrical energy to sound energy and vice versa) directed vertically downwards, and measures the time taken for the pulse to travel between the source and seabed, and back again (known as 'two-way travel'). In general wave propagation and reflection laws, the time recorded represents the shortest path between the source and seabed, which in this case is assumed to be directly beneath the source (Hersey, 1960). The distance between the vessel bottom and the seabed is derived by halving the two-way travel time and then multiplying by the speed of sound in water. Kunze (1957) offers further information on the application of echo-sounding within shipping. Figure 2.1 illustrates a typical bathymetric profile derived by echo-sounders.

This method of determining the range from a source to a reflecting surface, known as echo-location, was further developed as the primary guidance/navigation system for early submarines (Ewing *et al,* 1946). The deployment of echo-sounding transducers in

a horizontal sense provided a forward-looking sonar image, enabling the measurement of range to objects/surfaces in the vessels' line of travel (Roe, 1943; Kunze, 1957). The work of Roe (1943), Ewing (1946), etc in the field of submarine navigation induced a military quest for techniques to monitor the movements of these submarine craft, as illustrated by Urick and Pieper (1952).

Figure 2.1 Example of a traditional echo-sounder trace (from Hooper, 1979)

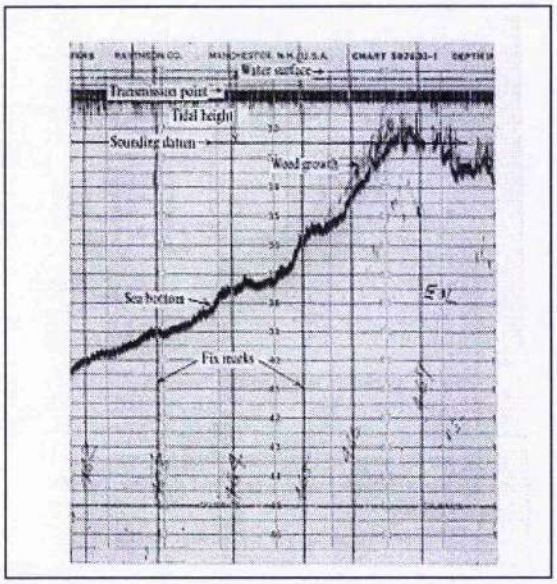

The anti-submarine warfare of World War II instigated the development of a 'sideways-looking' sonar system (Hersey, 1960; Donovan and Stride, 1961; Somers and Stubbs, 1984). These 'side-scan' sonars use the echo-sounding transducer in a lateral sense relative to the vessels' movement (Figure 2.2), to echo-locate any submerged reflective surface to the side of the vessel. The degree of sonar coverage was effectively doubled by mounting transducers on both port and starboard sides of the vessel, creating a sonar swath centred along the vessels track line (Figure 2.2). The transducers were slanted slightly below the horizontal and towards the seabed, sacrificing horizontal range to obtain a more comprehensive sonar coverage beneath the vessel.

The side-scan technique enabled the sonar pulse to cover a larger lateral area as it travels diagonally through the water column and 'across' the seabed - as opposed to

straight to it in the case of the echo-sounder (Donovan and Stride, 1961). Instead of the pulse reaching the seabed at one point in time (as in the echo-sounder), the slanted angle of incidence resulted in a graduated incidence of the pulse with the seabed, thereby increasing the time-frame during which the pulse is in 'contact' with the seabed. The receive method of the side-scan was modified by extending the 'listening' period beyond the first detection of echo return (as in echo-sounders), in order to record the full echo return of the 'contact'. The recording of the full echo enabled the generation of a backscatter strength (amplitude of return) profile across the seabed (Figure 2.3), where the positioning of reflection points in the profile is determined solely by the travel time (range) between the source and reflector.

Despite the application of side-scan sonar during World War II, it was not until the late 1950's that scientists realised the commercial potential of the side-scan for mapping the seafloor (Kunze, 1957; Aherns, 1957; Chesterman *et al.*, 1958; Stride, 1959).

Figure 2.2 Diagram of side-scan set-up

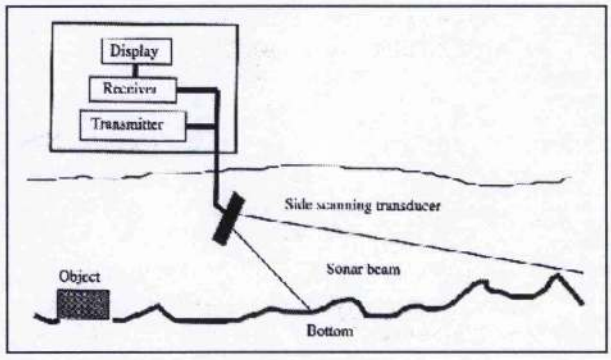

Figure 2.3 Typical side-scan imagery

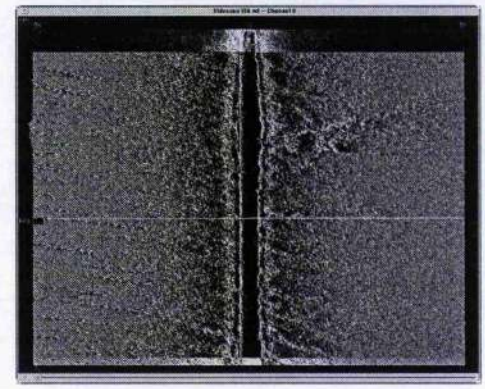

This led to the initial development and use of side-scan sonar systems in marine surveying (Donovan and Stride, 1961; Tucker and Stubbs, 1961; Haines, 1963). In recording the backscatter amplitude variations across each ping profile, the side-scan sonar effectively produces a backscatter variability map of the seabed. Analysis of the variability of acoustic backscatter amplitudes detected by the side-scan sonar found that geological features, and objects (Figure 2.4) or targets with anomalous or sharply

contrasting backscatter levels, could be identified and mapped upon the seafloor (Clay *et al.*, 1964; Greischar and Clay, 1972; Somers and Stubbs, 1984; Hughes-Clarke, 1993). This finding resulted in the immediate military application of side-scan in the field of underwater mine detection, carrying on from Roe (1943).

Figure 2.4 Side-scan imagery showing anomalous backscatter from a sunken barge (Courtesy of Submetrix)

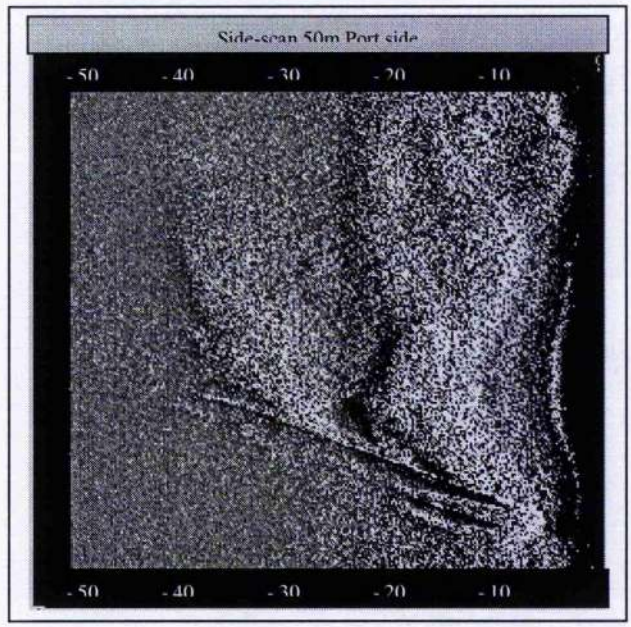

To-date, the commercial application of side-scan sonar remains predominantly focused upon reconnaissance, for the identification/detection of sonar 'targets' such as mines, cables, pipelines, wrecks, and other man-made objects, on the seafloor (Somers & Stubbs, 1984). This restricted field of application is essentially limited by two factors:-

1. In the absence of a depth profile, the spatial positioning of the side-scan data remains confined to a crude 'slant range' from the sonar system, which is clearly insufficient information for the pin-pointing of objects, especially mines, on the seafloor.
2. The commercial application of mapping acoustic backscatter from the seafloor is restricted because backscatter strength variations may also be induced by

changes to the angle of incidence between the wave and the reflection plane (See sections 2.3 - 2.5). This may cause topographic changes to appear as areas of differing backscatter strengths in side-scan imagery.

The absence of bathymetric data illustrating topographic changes on the seafloor prevents the simple 3-dimensional locations of sonar targets. In order to compensate for this shortfall, standard underwater survey practices necessitated the deployment of both side-scan and echo-sounder systems, with the vessel sailing over the approximate location of a sonar target as identified by the side-scan, to provide depth data via the echo-sounder.

In parallel to the interest in qualitative information provided by the side-scan sonar, there was also a growing commercial demand for high-density bathymetric measuring during the 1960's and 1970's. A solution was found by applying the 'side-looking' characteristic of side-scan sonar to the bathymetric technology of the traditional echo-sounder.

The first idea was to arrange a number of echo-sounding transducers in a line parallel to the ships track, to produce a bathymetric profile similar in form to that of a side-scan image (Haines, 1970; Richie, 1970). Although this technique provided more bathymetric information 'per vessel run' than a single echo-sounder, the data density was limited by the spacings between each transducer and the total number of transducers used.

Tucker (1960), and Howson and Dunn (1961), described a refined approach using a transducer arrangement that provided a number of beams directed at incremental angles from the vertical (Figure 2.5). The practical application of this multiple beam system proved difficult in terms of identifying each respective beam, until Tucker (1961) proposed that each beam should be given a different sensitivity.

Figure 2.5 Diagram illustrating the transducer arrangement for multi-beams (From Medwin and Clay, 1998)

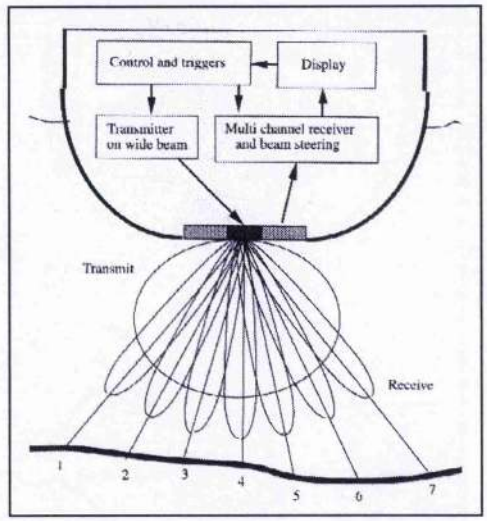

The successful development of multi-beam technology allowed the depth to seabed to be calculated in the same manner as for an echo-sounder, but had the additional ability to derive the angle of reflection on the seabed by assuming the return angle is equal to the source angle for each beam. Knowledge of the angle of return (α) and the range to the reflection plane (r) enables the 3-dimensional spatial positioning of each reflection point relative to the source (Figure 2.6). From this 'slanted' approach, the bathymetric data density and resolution on the seabed is now determined by the depth of water and the angular spacing between the beams (Figure 2.6), rather than the horizontal spacing between each echo-sounder profile.

Figure 2.6 Diagram illustrating the 'multi-beam' depth and angle derivation.

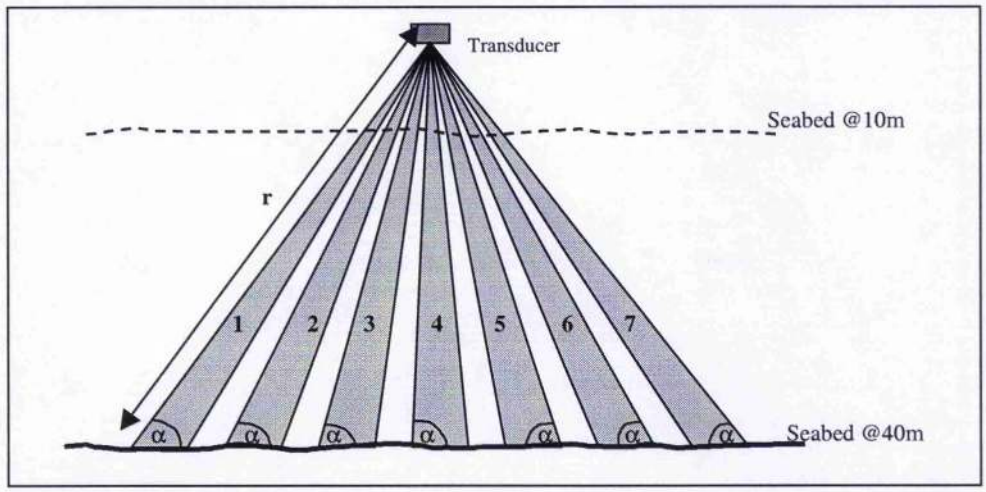

The work of Hickley (1966), Glenn (1970) and Beldenson (1972), guided the implementation of improvements and refinements to the multi-beam sonar, which ultimately resulted in its arrival on the commercial market in the 1970's. This multi-beam sonar technique essentially works on the same principles as the single beam echo-sounder, and may indeed be regarded as an array of single beam echosounders set up in a convex-downwards arc beneath the vessel. Each beam has a fixed angle of direction (directivity), thus enabling it to work as a side-ways facing or slanted echo-sounder, measuring the distance to the seabed in its directional plane. As a result of using multiple beams, this sonar technique is able to provide a lateral depth profile of the seabed as opposed to a solitary bathymetric point beneath the vessel.

At the same time as multi-beam sonars were becoming commercially available, a chance discovery in the late 1960's had already led scientists to instigate an alternative method of research into the development of a side-scan system which would also be capable of collecting bathymetric data.

Early users of side-scan systems had noticed that interference patterns were sometimes observed whilst surveying in calm seas. This 'interference' caused the side-scan display to be modulated with alternate light and dark bands running parallel to the vessels track where the seafloor was flat, but deviating in sympathy with undulations on the seafloor. These interference fringes were correctly ascribed to be a Lloyd Mirror effect created by the detection of a coherent reflection of the returning echo from the sea surface (Chesterman et al, 1967; Heaton & Haslett, 1971).

Denbigh (1977) soon realised that a second or third array of receivers could be used to produce an interferometric system, capable of deriving the angle of return of the acoustic reflections. Interferometric theory is based upon the derivation of an angular approach of a wavefront by using two or more receivers to record the phase of the wave as it passes over. The phase difference between two points is translated into the distance

travelled by the wavefront between its first and second detection, and thus the angular approach of the wavefront can be calculated by comparing this distance to the actual distance from one receiver to the other. An in-depth explanation of this interferometric theory is provided in Chapter 4.

The application of interferometry to remote surface topography mapping was already well-practised in airborne and satellite surveying, having originated in the field of astronomy as a method for calculating the distance of the stars from the earth.

The development of interferometry within marine acoustics followed a similar pattern to that of early acoustic survey systems. Howson and Dunn (1961) initiated the integration of interferometry within marine acoustics through the development of a downwards facing interferometer which they called a 'directional echo-sounder.' In 1974, Stubbs modified this technique to unveil the 'Telesounder', a side-ways looking directional echo-sounder. This system was capable of deriving a wide swathe of seabed depth measurements akin to that of multi-beam technology, but derived through interferometry.

The application of interferometry to marine acoustics then advanced from echo-sounders to side-scan sonar, resulting in the development of a phase-only side-scan sonar (Denbigh, 1977) prior to the conception of a 'BAthymetric Side-scan Sonar' (BASS) by Denbigh in 1983.

The BASS system enables the rapid measurement of acoustic backscattered amplitudes from large areas of the seabed, whilst simultaneously measuring the depth of the seabed. The depth is derived from the two–way travel time of the sonar pulse giving the range to the seabed, and the interferometric angle of return determining the location on the range arc from the transducer (Figure 2.7). The system is also capable of assigning both a depth and an acoustic amplitude value to a specific spatial location, determined relative to the location of the transducer. This system has been supported and endorsed

in papers such as Denbigh (1977 & 1979), Shishido (1979), Denbigh (1980, 1981 and 1983), and Gapper and Hollis (1985).

Figure 2.7 Diagram illustrating the methodology behind the bathymetric side-scan sonar. For clarity, only the port side is shown.

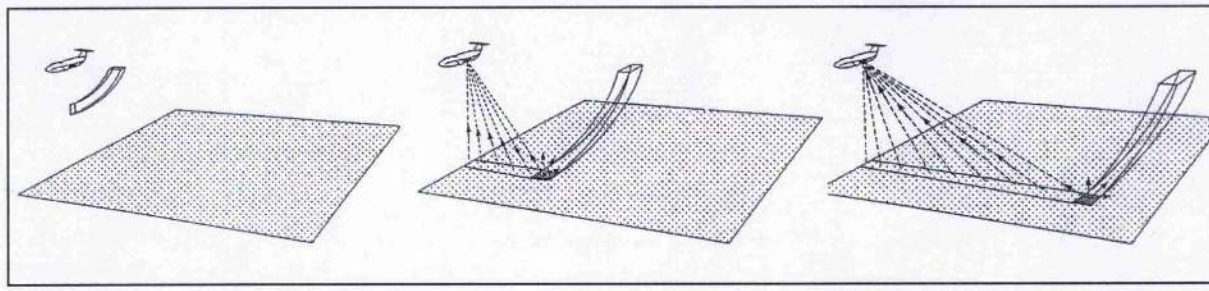

Since the mid-1980's interferometric sonars have been refined for commercial applications, enabling them to compete directly with multi-beam technology. This refinement has culminated in the development of a variety of high precision interferometric sonar systems.

In summary, the evolution of swathe bathymetric sonar systems to date has furnished the commercial market with several variants of both the multi-beam and interferometric systems. The merits of each regarding different survey types are determined by a combination of system specifications and the environment within which it is to be applied. All sonar survey systems have been developed to optimise their marketability for survey specific deployment, by using high frequencies and narrow beams for precision surveys to using lower frequencies and wide beams for reconnaissance surveys.

However, whichever system is used in whichever environment, it's success will always be subject to the physical constraints of the transmitting medium, water. Thus a comprehensive understanding of acoustic propagation in water is critical in the evaluation of each sonar survey systems' capability.

2.2. The 'Sonar Equation'

Throughout the evolution of sonar survey systems, the design and specification of the acoustic instrumentation has been determined by certain aspects of the transmission of an acoustic pulse through the water column. Although there have been many different sonar survey techniques, the dependency upon the acoustic propagation factor has remained the same.

As a result of the relentless industrial demand for enhanced data acquisition from marine geophysical surveys, underwater acoustics and the general principles of sound propagation within the water column have been the subject of much discussion during the past four or five decades. Most of this discussion can be found condensed in Urick's "Principles of Underwater Sound (1983)," which outlines the acoustic and environmental parameters of primary interest in underwater acoustics, and details the majority of accepted equations and relationships with respect to each parameter.
However, the complexity of underwater acoustics is such that each parameter requires a degree of knowledge of another, and so a thorough analysis necessitates a full understanding of the inter-relationships between all the parameters.

In seabed surveying, an acoustic pulse must travel through the water column twice as well as being reflected by the ocean-bottom as it moves between source and receiver. During this journey, the pulse is subjected to a variety of processes that alter the strength of the pulse. As side-scan and bathymetric systems use a "transducer" as a combined source and receiver, the path of the acoustic wave lies only between two points, the transducer and the ocean-bottom.
After some years of discussion, an equation designed to account for the complete sonar cycle, from source to seafloor to receiver, was established – the Sonar Equation.

$$\mathbf{RL} = \mathbf{SL} - \mathbf{2.TL} + \mathbf{DI} + \mathbf{TS} - \mathbf{NL} \qquad \textbf{Equation 2.}\mathit{1}$$

Where;

RL = Received Level

SL = Source Level

TL = Transmission Loss (Multiplied by 2 to indicate 2-way travel path)

DI = Directivity Index

TS = Target Strength

NL = Background Noise Level (Urick, 1983)

All of which are measured in decibels (dB).

The signal emitted is of a known source level (SL). On travelling through the water column, this source level is reduced by the transmission loss (TL). Transmission loss comprises of the effects of absorption within the water column and spreading of the wave as it radiates from the transducer. The overall effects of both absorption and spreading are determined by the distance travelled from source to ocean-bottom, through the water column. At the ocean-bottom, the level of the acoustic signal is reduced by transmission loss to give SL – TL. The directivity index (DI) is added at this stage to represent the acoustic intensity at the seabed with respect to the main direction of the pulse, giving SL-TL+DI which represents the actual acoustic intensity at the seabed. At this point the pulse interacts with the seabed material and is scattered back up into the water column in the direction of the receiver with a certain degree of effectiveness, which is described by the target strength (TS) parameter. The SL-TL+DI+TS then loses a further TL as it travels back through the water column to the receiver, to give an intensity of SL-2TL+DI+TS at the receiver. The true amplitude is enhanced by the presence of background water column noise (NL) which adds itself to the received level (RL) actually recorded by the receiver.

The processes encapsulated within the sonar equation are illustrated in Figure 2.8 to further clarify the sequence in which they occur.

Figure 2.8 Diagram of the Sonar Equation in terms of SL, DI, TL, TS, NL, and RL.

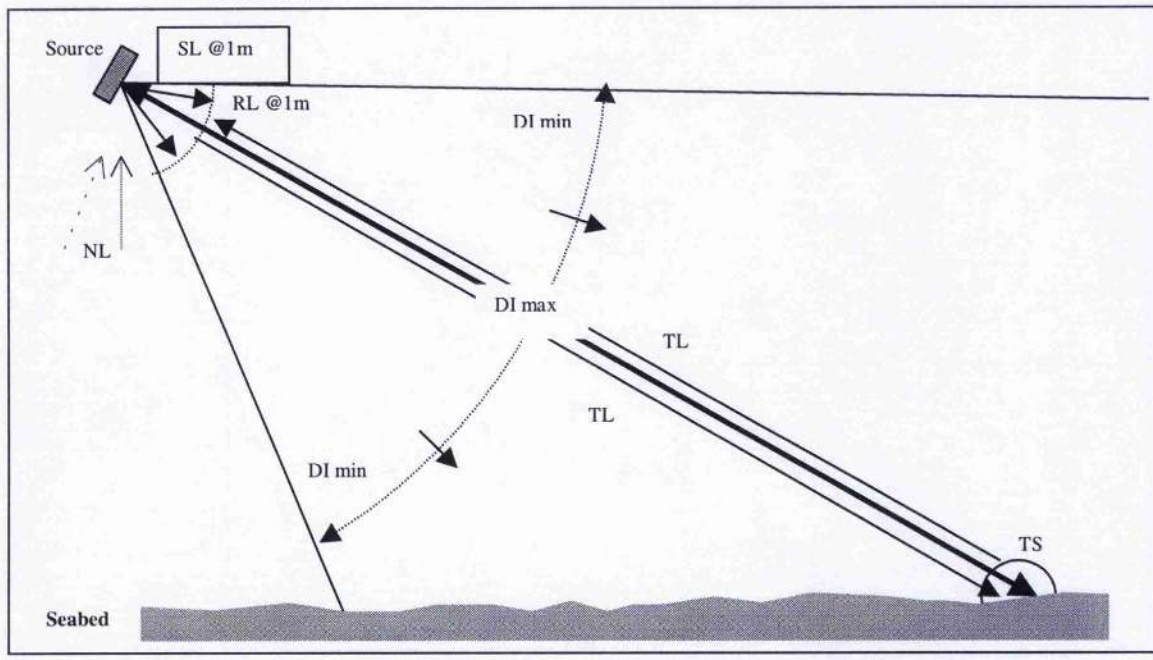

The inter-relationships between these parameters can be examined by splitting the sonar equation into its individual components and using a standard decibel scale to measure the overall effects of each parameter.

2.2.1. Source Level (SL)

Source levels are traditionally calculated as a ratio between the source level and a reference level, measured at a standard distance of 1 metre from the source.

$$\text{Source Level Ratio} = I / I_{ref} = (P / P_{ref})^2 \qquad \text{(Nishimura, 1997)}$$

Where;

I = Intensity, and P = Pressure

In marine acoustics however, the standard unit of measurement for sound intensity or pressure level is the 'decibel,' which is actually a means of describing sound pressure levels. As the decibel was initially used to indicate power levels during electrical transmissions, its adoption to measure sound pressure levels requires the conversion of

pressure to power. In the same way as a reference distance is required, the U.S. Navy selected one micropascal (μPa) to be the reference sound pressure (Nishimura, 1997).

The resultant conversion of the source level ratio, into a measured sound pressure level, measured in decibels with respect to the reference values, gives;

$$\text{Source Level} = 20 \log_{10} (P / P_{ref}) \text{ dB re } [(\mu\text{Pa}) @ 1\text{m}] \qquad \textbf{Equation 2.}\textit{II}$$

(Nishimura, 1997)

In the field, it is necessary to derive an optimum or desired source level for the outgoing signal that will enhance the objectives of the survey given the localised field conditions.

2.2.2. Transmission Loss (TL)

"The sea, together with its boundaries, forms a remarkably complex medium for the propagation of sound." (Urick, 1983).

As it travels through the sea, an underwater sound signal becomes delayed, distorted, and weakened. The degree to which it is 'altered' is dependent upon many factors such as bathymetry, sound-speed profiles, multipath arrivals, range, source frequency, character of the divergence from the source to receiver, possibility of caustics, and absorption and scattering along the way (Medwin & Clay, 1998).

However to simplify the analysis, these complexities of underwater acoustic propagation have been encapsulated within the general concepts of the transmission factor, and its logarithmic form *TL* (dB) (Medwin & Clay, 1998).

The transmission factor, or transmission loss, accounts for the loss of signal energy by assessing the geometric nature of the sound signal as it spreads outwards from the source, *spreading*, and the inter-relationship between the source signal characteristics and those of the transmitting medium, *attenuation*.

2.2.2.1. *Spreading*

This parameter can be visualised by recalling the effects of a stone being dropped into the middle of a still pond, causing large ripples/waves to emanate in a spherical manner from the point of impact, and decrease in amplitude as they travel further out from the centre. This simple analogy perfectly illustrates the phenomenon of spherical spreading as a factor determining the transmission loss of acoustic waves.

As a 3-dimensional wave-form disseminates from a point source in a homogeneous, unbounded medium, it will spread equally in all directions so as to be equally distributed over the surface of a sphere surrounding the source. In assuming no other losses within the medium, the power crossing all such spheres must be the same, and given that power equals intensity times area, it follows that;

$$P = 4\pi r_1^2 I_1 = 4\pi r_2^2 I_2 = \ldots\ldots \qquad \text{(Urick, 1983)}$$

If r_1 is set as the reference distance of 1m, the power level at r_2 can be defined by;

$$4\pi r_1^2 I_1 = 4\pi r_2^2 I_2$$

$$\Rightarrow \quad I_1 = r_2^2 I_2$$

$$\Rightarrow \quad I_1 / I_2 = r_2^2$$

The intensity may now be said to decrease as the square of the range.

However, the spherical spreading *loss* (SS), measured in decibels, is defined by the following equation;

$$SS = 10 \log (I_1 / I_2) = 10 \log r_2^2 = 20 \log r_2 \qquad \textbf{Equation 2.}\textit{III}$$

(Urick, 1983)

which through substitution suggests that the transmission loss due to spherical spreading is determined by the logarithm of the range.

In summary, at any given point the intensity or amplitude of the disseminating wave will be related to the surface area of the spreading sphere, where the radius of the sphere is equal to the range from the source.

2.2.2.2. *Attenuation*

Absorption (Ab) is a form of loss that involves a process of conversion of acoustic energy into heat, causing a certain fraction of the intensity to be lost per unit distance travelled. It therefore obeys a different law of variation with range than the loss due to spreading.

The first measurements of the absorption coefficient (K_{ab}) of seawater were made by Stephenson (1935) using sinusoidal pulses transmitted through the sea between a surface ship and a submerged submarine (Urick, 1983).

Further studies drew attention to unexpectedly high absorption losses in sea water, compared to those in pure water, leading to Liebermann (1949) proposing the existence of a form of chemical reaction involving one of the minor dissolved salts in the sea, with the sound wave acting as a catalyst. In 1977, this work was reviewed and refined by Fisher and Simmons using existing data and theory, resulting in the following expression:-

$$K_{ab} = A_1 P_1 \left(\frac{f^2}{f_1^2 + f^2} \right) f_1 + A_2 P_2 \left(\frac{f^2}{f_2^2 + f^2} \right) f_2 + A_3 P_3 f^2$$

<----Term 1------> <------Term 2-----> <--Term 3->

Where the terms A_1, A_2, A_3, f_1, f_2 are complicated functions of temperature; P_1, P_2 and P_3 are functions of pressure; and K_{ab} represents the absorption coefficient/factor measured in dB per kilo-yard. The three terms represent the effects of boric acid, magnesium sulphate, and viscosity, respectively. The above expression proposed by Fisher and Simmons generates the graphical displays shown in Figure 2.9 for the absorption coefficient in seawater under a variety of conditions. Figure 2.9 enables absorption coefficients to be obtained for known sonar frequencies and water temperatures. This absorption coefficient represents the degree of loss relative to a given travel distance, and in the absence of further data, must be assumed to be constant

throughout the water column transmission. Indeed, the shallower the water, the easier it becomes to justify this assumption.

Figure 2.9 Absorption Coefficients in sea-water according to the expressions of Fisher and Simmons (1977) for zero depth, salinity 35 ppt, pH=8, and three temperatures.

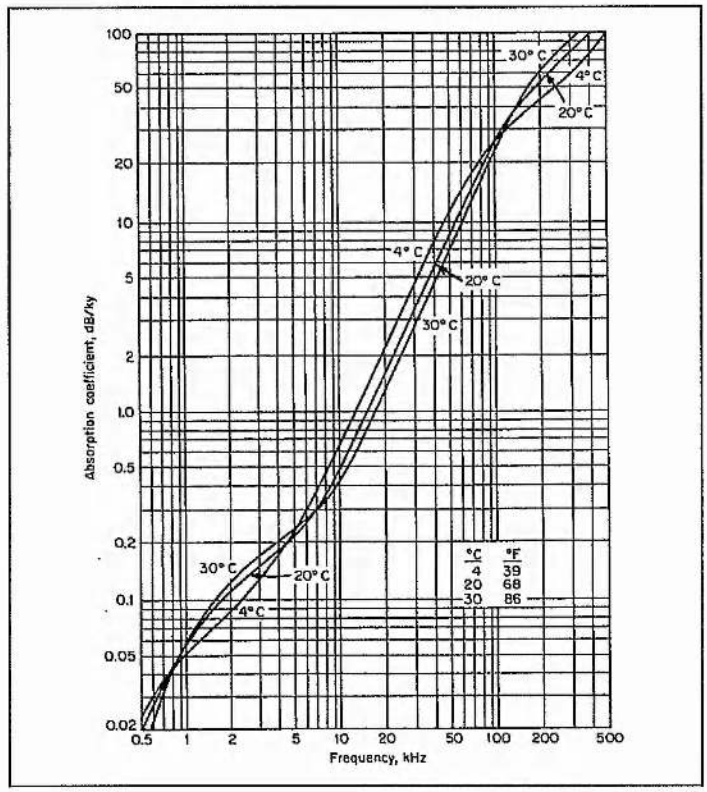

In order to calculate the overall absorption loss (**Ab**) the absorption coefficient (K_{ab}) must be multiplied by the distance (**r**) travelled through the medium relative to the unit distance of the coefficient;

$$\mathbf{Ab} = K_{ab} \cdot \mathbf{r} \qquad \textbf{Equation 2.}\textit{IV}$$

2.2.2.3. *Summary*

When propagation measurements are made at sea, it is found that spherical spreading and absorption provide a reasonable fit to the measured data under a wide variety of conditions (Urick, 1983). Therefore, the full assessment of transmission loss requires the addition of spherical spreading losses to that of absorption losses, which can be expressed by the following equation:-

$$TL = SS + Ab = (20 \log r) + (K_{ab} \cdot r) \times 10^{-3} \quad \textbf{Equation 2.}V$$

where 10^{-3} is required to convert from kilo-yards to yards.

NB. This absorption factor must be multiplied again by 1.094 to convert from dB/y to dB/m.

The total transmission loss between emission and reception must be multiplied by 2, to compensate for the outward and return journey of the wave, giving;

$$TTL = 2 \cdot TL = 2 [(20 \log r) + ((K_{ab} \cdot r) \times 10^{-3}).(1.094)] \quad \textbf{Equation 2.}VI$$

2.2.3. Directivity Index (DI)

Although acoustic waves are 'assumed' to propagate in a spherical manner, they may also be constrained by the nature of the emission from the source. In the same way as a spotlight can 'concentrate' a beam of light, so an acoustic source can concentrate its sound beam.

The analysis of beam directivity can essentially be broken down into beam shape, transducer transmit response and transducer receive response (Urick, 1983). For this purpose, the beam shape is determined by the method of emission, whilst both the transducer transmit and receive responses are determined by the response of the transducer relative to the outgoing and reflected beam fields.

With so much sound energy being lost to the transmitting medium, the ability to focus the beam energy within the desired direction will obviously benefit the performance and increase the energy efficiency of underwater sonars. In underwater acoustics, the main focal point of the acoustic beam will have the highest level of sensitivity and this will drop off with increased distance from the centre. However, as acoustic detection is

dependent upon a reflected signal, we must also apply this sensitivity to the relationship between the receiver and the reflected wave.

The transducer transmit and receive responses are a function of the nature of the stave array within the transducer. For example, by increasing the number of staves in the array the sensitivity of the array will increase, and also, by using more than one stave in the array it gains directional properties which allow it to discriminate between sounds arriving from different directions (Urick, 1983).

The generic evaluation of this directivity parameter is very difficult due to the system-specific nature of the directivity index of each sonar system. Therefore the background analysis of the three main components of directivity will be reviewed only in principle.

2.2.3.1. *Beam Directivity*

Firstly, the actual directivity/shape of the beam is determined by a combination of the elevation and azimuth of the acoustic beam (Figure 2.10). Using the equation stated by Geen (1997) the beam directivity can be represented by;

$$BD = 10 \log [(4\pi) / (\phi . \beta)] \qquad \textbf{Equation 2.}\textit{VII}$$

Where;

BD = Beam Directivity/Shape
ϕ = Beam elevation
β = Beam azimuth

Figure 2.10 Schematic of acoustic beam shape

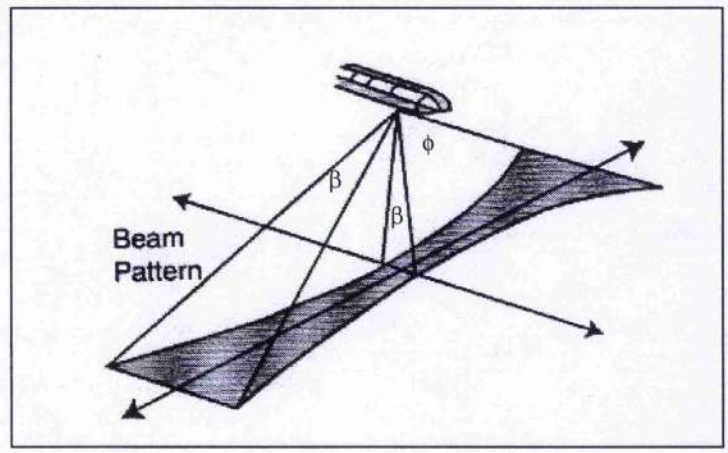

In this context, the elevation of the beam is defined as the width of the beam arc in a vertical sense, and the azimuth of the beam represents the horizontal component of the beam shape (Figure 2.10).

2.2.3.2. *Transducer Transmit Response*

As already explained, the transducer transmit response (TR) is a system specific value which numerically accounts for the focal point of the emitted beam and allows regions off-centre to be compensated for a reduction in transmitted source level.

2.2.3.3. *Transducer Receive Response*

In a similar manner, the transducer receive response (RR) is designed to compensate for the systems angular sensitivity towards the apparent wavelength of the reflected beam. Again this value is system specific, relating to the stave set-up within the transducer and the attitude of the transducer.

2.2.3.4. *Summary*

To derive the total directivity index of a system's acoustic beam it is necessary to sum the values of beam shape, transducer transmit, and transducer receive responses – all of which are measured in decibels. Therefore, the full directivity index of a sonar system is defined by the following equation;

$$\mathbf{DI = BD + TR + RR} \qquad \textbf{Equation 2.}\textit{VIII}$$

Where;

DI = Directivity Index
BD = Beam Directivity
TR = Transmit Response (of transducer)
RR = Receive Response (of transducer)

2.2.4. Target Strength (TS)

The target strength parameter is designed to assign a numerical value of acoustic 'strength' or 'scattering strength,' measured in decibels, to the 'target' object causing the acoustic reflection or scatter. In underwater acoustics the 'strength' of a target may be determined by its' degree of efficiency in reflecting an acoustic wave.

In order to accurately measure the *strength* or *efficiency* of the acoustic response, it is necessary to relate the intensity of the returned wave to that of the incident wave. This fundamental ratio upon which reverberation depends, is the ratio of the intensity of sound scattered by a unit area or volume, referred to a standard distance (1yard or 1 metre), to the incident plane-wave intensity (Urick, 1983). This ratio results in the target strength parameter being defined as:-

$$TS = 10 \log \frac{I_r}{I_i} \qquad \textbf{Equation 2.}\textit{IX}$$

Where; I_r = Intensity of reflection at reference distance (1 yard or 1m)

I_i = Incident intensity

This target strength value can be expressed in decibels by taking the logarithm of the ratio of return and incident intensities.

Target strength is essentially an echo returned by an underwater 'target.' Traditionally excluded from this category are inhomogeneities in the sea of indefinite extent, such as scattering layers and the ocean surface and bottom, which, because of their indefinite size, return sound in the form of reverberation instead of as echoes (Urick, 1983). In cases where sonar systems permit the area of seabed to be delimited however, the seabed scattering strength can be assigned an 'echo level' thereby satisfying the definition of a sonar target.

However, it is important to note that this target strength measurement provides no insight into the factors determining the magnitude by which the acoustic wave is returned.

The resultant theories and relationships which have been proposed with regard to evaluating the scattering properties are discussed in detail in sections 2.3, 2.4 and 2.5.

2.2.5. Noise Level (NL)

The noise level parameter is included within the sonar equation in order to account for the *background noise* factor. In acoustic terms, *background noise* is referred to as the level of 'unwanted' sound, whether systematic or random, upon which the desired signal/reflection is superimposed. The systematic component of the background noise refers to the electrical and acoustical interference generated by the sonar system itself, and is therefore a system specific variable. The random component essentially comprises of the noise generated by ambient sources extraneous to the sonar, which are regarded as being isotropic, i.e. the noise level detected by simply lowering the receiver into the water and listening. The measuring of ambient noise is dependent upon the sensitivity of the receivers to the background noise, and so it too may be regarded as a system specific variable.

In generic terms the noise level can be defined as:-

$$NL = (SN - R_{sens}) + (AN - R_{sens}) \qquad \textbf{Equation 2.}X$$

Where;

NL = Noise Level
SN = Systematic Noise
R_{sens} = Receive sensitivity
AN = Ambient Noise

The randomness of ambient noise and the system specific nature of the electrical and acoustical interference mean that this noise level parameter will vary with the field conditions and the sonar system specifications.

2.2.6. Received Level (RL)

The received level is defined as the amplitude of the backscattered acoustic wave detected back at the receiver. Although normally measured in terms of volts across the staves, this can be converted back into decibels to complete the sonar equation. It is important to acknowledge that the received level comprises of two different sonar responses, namely the returned or backscattered acoustic wave and the noise level. Therefore, a true assessment of the backscattered sound relating to a specific reflection point requires the noise level to be subtracted from the received level.

2.2.7. Summary

The application of this sonar equation to underwater acoustics links every known parameter active upon the acoustic wave from source to seabed to receiver, and enables each factor to be evaluated in terms of decibels for comparative and mathematical purposes. It therefore offers the sediment acoustician a very valuable technique towards analysing the target strength parameter, because by reducing this parameter to its component level, it becomes possible to evaluate the actual processes and relationships active upon the acoustic wave at the water-sediment interface.

Although the Target Strength parameter within the sonar equation offers a numerical assessment of the targets scattering strength, it does not provide an insight into the causes and effects determining the degree of scattering recorded. By numerically accounting for all the variables within the sonar equation, other than that of TS, it is possible to determine the exact decibel loss incurred by the acoustic wave at the water-sediment interface.

It is worthy of note that the target strength equation relates only the incident and response intensities, and in no manner does it evaluate or account for the actual processes acting upon the incident wave at the water-sediment interface.

2.3. Acoustic interaction at the water-sediment interface

The aim of this section is to relate the magnitude of the target strength parameter described by the sonar equation to the processes active upon an incident wave at the water-sediment interface, and to evaluate the potential of each process in terms of providing a correlation between the acoustic response and the seabed sediment characteristics.

This analysis is restricted to the evaluation of these processes with regard to conventional side-scan, multi-beam and interferometric sonar set-ups, whereby the source and receiver are housed within the same unit. This sonar configuration is known as monostatic imaging geometry, and confines the receiver measurement of the returned signal to the portion which has a return angle that is the reverse of the grazing angle.

The processes that act upon an incident acoustic wave at the water-sediment interface are governed by the interrelationship between the sediment-acoustic properties of the interface and the sonar characteristics. The sediment-acoustic properties of the interface are defined as the resistance to acoustic transmission from the water body to the sediment body (**Reflection Coefficient**) and the roughness of the water-sediment interface (**Seabed Roughness**).

The **Reflection Coefficient** is a measure of the interface resistance to acoustic transmission from one medium to another, and is essentially determined by the contrast between the acoustic impedance values of the two media. The analogy to Ohm's law for electrical impedance defines the *acoustic impedance* (Z) of a medium as the product of the density (p) and acoustic velocity (ν) of the medium (Equation 2.*XI*).

$$Z = p \cdot \nu \qquad \textbf{Equation 2.}\textit{XI}$$

Buchan *et al.* (1972) state that for an acoustic wave travelling at normal incidence to an acoustic impedance boundary, the reflected energy is defined as the square of the difference divided by the sum of the acoustic impedances of the two materials. The square root of this equation is known as the reflection coefficient (Equation 2.*XII*), which similarly uses material density and sound velocity contrasts at the interface between two media (Figure 2.14) to determine the ratio between the amplitudes of the reflected (A_{refl}) and incident waves (A_{inc}).

$$\text{Reflection Coefficient} = \frac{A_{refl}}{A_{inc}} = \frac{z_2 - z_1}{z_2 + z_1} = \frac{\rho_2 v_2 - \rho_1 v_1}{\rho_2 v_2 + \rho_1 v_1} \qquad \textbf{Equation 2.}\textit{XII}$$

Where;

A = amplitude of the reflected (refl) and incident (inc) waves

z = acoustic impedance of media 1 and 2

ρ = density of media 1 and 2

v = sound speed in media 1 and 2

Where the reflection coefficient is low, there is little resistance to acoustic transmission across the interface, and so a large proportion of the sound energy will be 'absorbed' by the lower medium. On the other hand, interfaces with high reflection coefficients strongly resist this 'absorption' of sound energy, and causing the sound energy to be deflected or returned by the interface. The nature of the sound energy deflected by the interface must therefore be determined by the roughness of the interface (surface).

The measurement of **surface roughness** is entirely dependent upon the scale of the analysis because although *in-situ* testing and sediment sampling may determine the true roughness on a metre/centimetre/millimetre scale, the critical 'roughness' measurement is that detected by the incident acoustic wave. The effects of this scale factor can be illustrated in Figure 2.11 which shows that the degree of *roughness* of any surface is intrinsically linked to the resolvable scale of the analysis.

Figure 2.11 Illustration of variable seabed 'roughness' scales

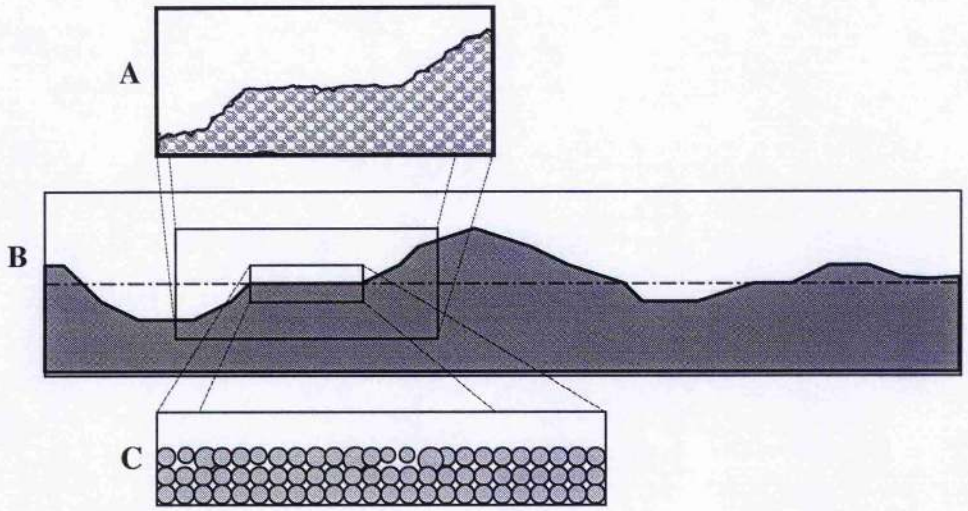

The resolvable scales A, B and C in Figure 2.11 show that the roughness element in B (large scale) will be dominated by the bathymetric undulations, whilst at A (medium scale) the roughness will comprise of both bathymetry and bed roughness. The small-scale resolution achieved at C shows that the bathymetric 'roughness' factor can be eliminated by reducing the scale of the analysis, resulting in the roughness measurement being entirely dependent upon the bed or grain roughness.

In sonar techniques, the resolvable scale of roughness detected by the incident wave is directly related to the sonar frequency, which determines the wavelength 'measuring stick,' and the planar angle of analysis. This means that in theory, by reducing the wavelength of the sonar signal to a millimetre scale the roughness of the water-sediment interface may be measured on a granular scale, with each individual sedimentary particle becoming a scatterer of sound. In acoustics, the roughness of the surface is determined by the 'Rayleigh Roughness Parameter,' following Lord Rayleigh's studies of wave-scattering by rough surfaces in the late 1800's. The Rayleigh Roughness Parameter provides a measure of surface roughness by evaluating the spatial phase shift experienced by the wave relative to the path difference (AA to BB), induced by the phase of reflection from the mean surface (Figure 2.13). The spatial difference caused

by the phase shift is calculated by Equation 2.*XIII* which relates the wavelength of the acoustic wave (λ) to the vertical range of the surface (ζ) and the angle of incidence (θ), as illustrated in Figure 2.13.

$$Ra = 2k\zeta \cos\theta \qquad \textbf{Equation 2.}\textit{XIII}$$

Where;

Ra = Rayleigh Roughness Parameter

k = acoustic wavenumber (i.e. reciprocal of the wavelength, $k = 1/\lambda$)

ζ = the surface displacement

θ = the incident angle

NB. *The incidence angle (θ) can be replaced with the grazing angle (α) by replacing 'cos θ' with 'sin α.'*

From equation 2.*XIII*, it is clear that both the frequency and the angle of incidence factors can alter the true roughness (ζ) of the surface to give an 'effective roughness' as perceived by the incident wave. Where the roughness of the surface is small relative to the acoustic wavelength (Ra <<1), the smooth nature of the surface promotes the reflection of the sound energy. Where the Ra value is >>1 this corresponds to a rough surface which causes considerable sound scattering.

Figure 2.12 shows the general effects of surface roughness upon the nature of the returned sound energy, in which the coherent field represents the reflected energy and the diffuse field represents the scattered energy.

Figure 2.12 Illustration of the effects of seabed roughness upon the returned sound energy using three cases; (a) smooth, (b) semi-rough, and (c) rough. (From Ogilvy, 1991)

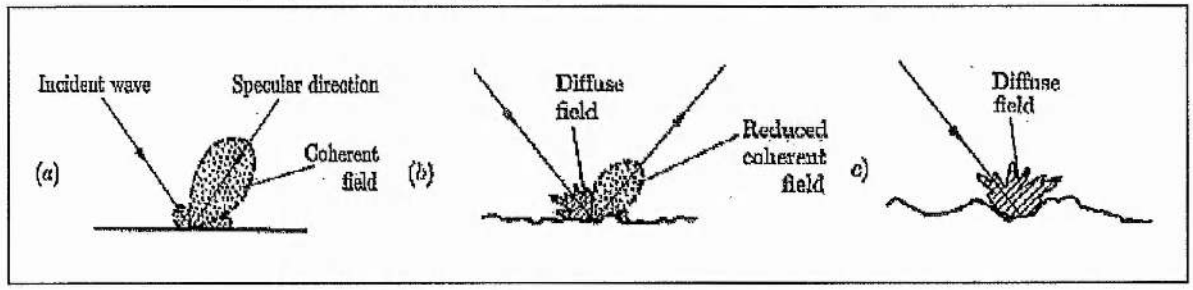

In summary, the reflection coefficient determines the trade-off between the absorbed and returned sound energy, and the surface roughness determines the reflection and scattering compositions of the returned sound energy.

The sediment-acoustic properties of the interface can therefore cause an incident acoustic wave striking the seabed to be reflected, absorbed (attenuated), and scattered by the water-sediment interface, with the relative magnitudes being dependent upon the frequency and grazing angle of the incident acoustic wave.

The potential correlation of the acoustic response measured by a monostatic imaging sonar with the associated seabed characteristics therefore requires the evaluation of each of the acoustic processes of reflection, absorption (attenuation) and scattering.

2.3.1. Acoustic Reflection

The reflective component of the incident acoustic wave is called the specular reflection, and is defined by Sheriff (1973) as the portion of sound scattered in the direction of the mirror reflection, where the angle of scatter equals the angle of incidence (represented by θ in Figure 2.13).

Figure 2.13 Schematic of specular reflection at a rough surface (Medwin and Clay, 1998).

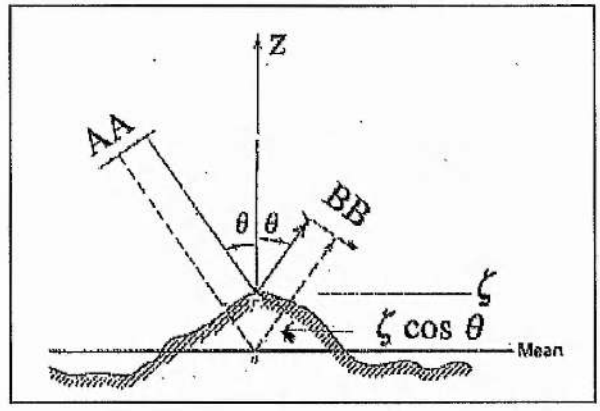

As a result of the mirrored reflection, specular reflection is often referred to as 'normal incidence (nadir) reflection' and 'forward reflection/scattering.' This specular reflection

is induced by regular inhomogeneities at the interface, and results in the reflection being characterised by a coherent component, which has a fixed-phase relation with respect to the incident sound. The magnitude of the coherent specular reflection is dependent upon the surface roughness and the reflection coefficient of the interface, and is calculated using the following equation (Medwin and Clay, 1998):-

$$R_{coh}^2 = R_{12}^2 e^{-g_R} \qquad \textbf{Equation 2.}\textit{XIV}$$

Where;

R_{coh} = Coherent reflection intensity

R_{12} = Reflection coefficient at the interface between media 1 and 2

g_R = Acoustical roughness = $Ra^2 = \left(4k^2\zeta^2\cos^2\theta\right)$

Although the specular reflection process is generally regarded as being the dominant process at near normal incidence angles, its magnitude can be enhanced at lower ensonification angles where the seabed is very flat (Figure 2.12). The reflection process is characterised by a relatively strong echo return, with the amplitude of the reflection being controlled by the reflection coefficient (Equation 2.*XIV*) of the water-sediment interface.

2.3.2. Absorption

At the water-sediment interface, absorption represents the portion of the incident wave that is transmitted across the interface and into the sediment layer, giving the effect that is has been 'absorbed' by the sediment layer. Mitchell (1992) states that the ability of an acoustic wave to penetrate into the seabed is determined by a combination of the following parameters:-

- Angular approach of the acoustic wave
- Reflection coefficient at the water-sediment interface
- Sonar frequency

The angular approach of the acoustic wave relates to Snell's law (Equation 2.*XV* and Figure 2.14), which governs refraction and reflection through media of differing seismic velocities.

Snells Law $$\frac{\sin\theta_1}{v_1} = \frac{\sin\theta_2}{v_2}$$ **Equation 2.*XV***

Figure 2.14 Geometry of Snell's law

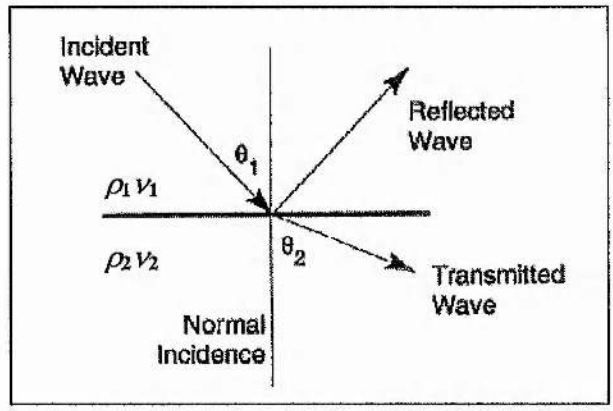

Snell's Law implies that when v_2 is greater than v_1, the transmitted ray is inclined to a shallower grazing angle creating an 'upward refracting environment,' with the converse conditions creating a 'downward refracting environment.' Under the conditions like that found at the seafloor when $v_2 > v_1$, Rayleigh (1945) found that as the incident angle θ_1 increases, this upwardly refracting trend continues until a critical angle is reached. The critical angle is described as the incident angle that induces a refraction angle of 90^0 ($\sin\theta_2 = 1$), thereby refracting the wave along the boundary between the media and so inhibiting penetration of the acoustic wave. This critical angle is illustrated in Figure 2.15 and represented by Equation 2.XVI.

For angles beyond θ_c the acoustic wave will be unable to penetrate into the sediment, thereby eliminating acoustic attenuation within the seabed from the target strength equation. In addition to refraction, the ability of a sound wave to pass across an interface between two media is also determined by the acoustic impedance between each medium.

Figure 2.15 Critical Angle

$$\theta_c = \sin^{-1}\left(\frac{v_1}{v_2}\right) \qquad \textbf{Equation 2.}\textit{XVI}$$

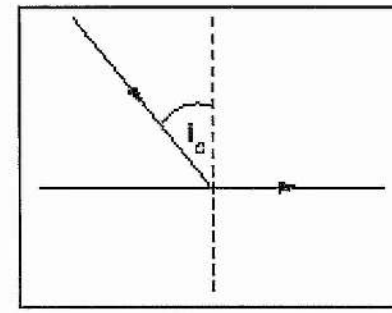

Where;

θ_c = *Critical angle*
v_1 = Seismic velocity in layer 1
v_2 = Seismic velocity in layer 2

The properties of the transmitting medium also interact with the sonar frequency to determine the attenuation of the acoustic wave within each medium. The degree of attenuation describes the portion of the decrease in sonar signal strength with distance travelled due to the processes of reflection, scattering and absorption (attenuation), all of which are attributed to the physical characteristics of the transmitting media. The sonar frequency parameter is regarded as having a linear relationship with attenuation, whereby the degree of attenuation in a constant medium will increase as the acoustic frequency increases (Figure 2.9; Fisher & Simmons, 1977; Mitchell, 1992). This relationship translates into an inverse trend between frequency and penetration, with an increase in the sonar frequency causing a decrease in penetration, for constant material properties.

The importance of this acoustic absorption process at the water-sediment interface, which generally has a high impedance contrast, becomes significantly reduced when high sonar frequencies are used.

2.3.3. Acoustic Scattering

The scattering component of the incident acoustic wave striking an interface occurs at all angles of incidence and is generally caused by the presence of random inhomogeneities within the media at the interface. The nature of the random scattering inhomogeneities is dependent upon the acoustic resolution of the sonar (defined by frequency and grazing angle), as scattering will occur only when the acoustic signal can

detect the acoustic properties at the interface of the scatterer. These scattering inhomogeneities may range from irregular bodies within a medium at low acoustic resolution, to particulate scatterers at very high acoustic resolution.

The random scattering of the coherent incident wave results in a wide-angle dissipation of diffuse and incoherent waves, as illustrated in Figure 2.12, so-called because they lack any form of phase relationship with the incident wave (Goodfellow, 1996). Although the wide-angled dissipation results in acoustic scattering at all angles of incidence and return, the monostatic imaging geometry of conventional sonars means that the portion of primary importance is that which is scattered 'backwards' towards the sonar unit. As mentioned previously within section 2.2.4, this returned portion of the incident acoustic wave is termed the *backscattered wave* and the backscattering analysis is ultimately defined by the ratio of *incident* to *backscattered* energy (Figure 2.17).

In general, this acoustic scattering process can occur both within a medium and at the interface between two media, and so the nature of the scattering can be classified by the location of the scattering inhomogeneities. At the water-sediment interface the scattering inhomogeneities can occur either at the interface or within the sediment, depending upon the degree of penetration (transmission) into the sediment, and are therefore referred to as *interface* and *volume* scattering, respectively (Figure 2.16).

Figure 2.16 Diagram illustrating the difference between Volume scattering and Interface scattering from the seafloor (from Nishimura, 1997).
The volume scattering shown is from discrete point scatterers in the sub-bottom

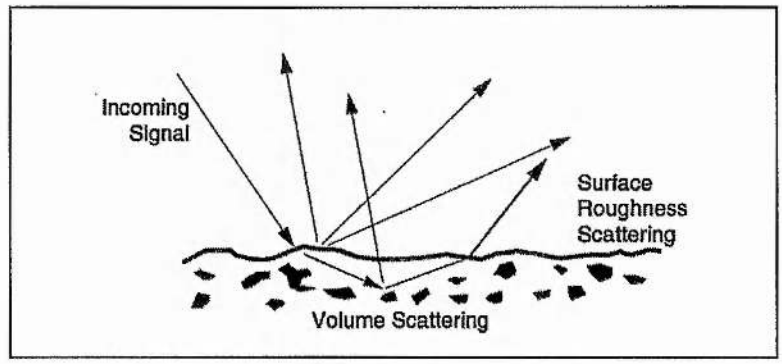

Figure 2.17 shows how these mechanisms of scattering can be related to the overall target strength of the area, as defined by the sonar equation.

From figures 2.16 and 2.17 it is evident that this process will also scatter a portion of energy in the specular direction, which is often referred to as the incoherent component of the specular reflection.

Figure 2.17 Conceptual definitions of scattering strength for volume scattering (a), and interface (surface) scattering (b) (Urick, 1983).

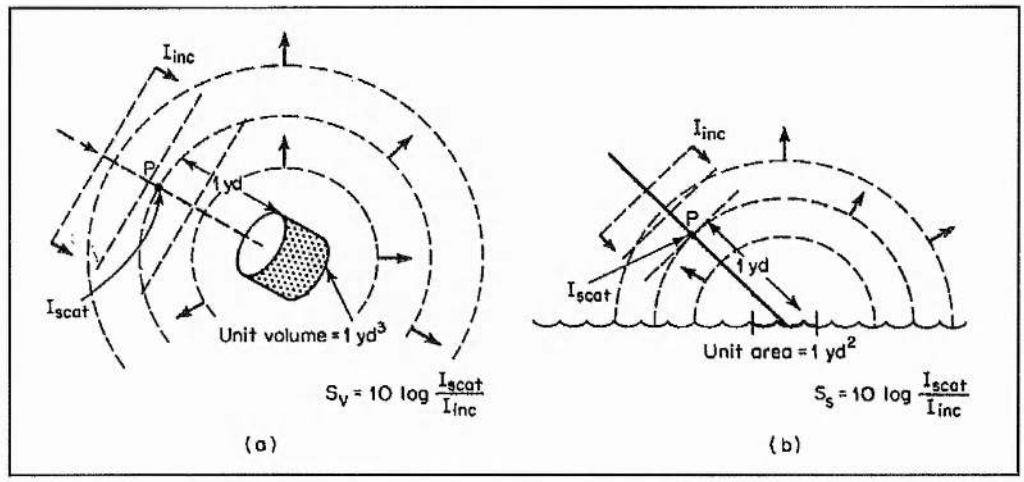

The prediction of the actual intensity or amplitude of the scattered sound energy using mathematical techniques is very complex due to the random nature of the scattering inhomogeneities at the interface. The understanding of this scattering process is critical to the monostatic imaging sonar because it is the only mechanism for the return of sound energy from the seabed at off-nadir locations, and so an in-depth analysis is provided in sections 2.4 and 2.5.

However, at this stage of the evaluation the following general rules can be considered and applied to the acoustic scattering process at the water-sediment interface. The relative magnitude of the interface and volume scattering processes will be governed by the impedance contrast and surface roughness of the interface, relative to the sonar frequency and grazing angle of the incident wave. Where penetration or transmission is minimised by the presence of a high impedance contrast at the interface, then the

acoustic scattering process will be dominated by interface scattering, but when acoustic penetration/transmission occurs, the scattering process will comprise of both interface and volume scattering.

2.3.4. Summary

If the scattering component is of primary importance to the monostatic imaging setup in wide-swath sounding sonars, then the analysis can be simplified by reducing the effects of reflection and transmission, and enhancing the relative magnitude of the backscattering process. As stated earlier, specular reflection is dominant at near normal incidence angles, and more importantly, is only detectable by side-scans, multi-beams and interferometers at normal angles of incidence. This means that by eliminating the data with 90^0 incidence, the specular reflection can be removed from the analysis.

The removal of the absorption factor presents more of a problem, as simply focusing upon the data with incidence angles beyond the critical angle would severely restrict the application of the analysis. Thus, the removal of the absorption factor hinges upon the frequency of the sonar, because an increase in sonar frequency causes a reduction in acoustic penetration into the sediment. Experiments by Boehme and Chotiros (1988) suggest that for frequencies below 10kHz the backscattering strength may be dominated by the material (volume) properties of the seabed, whilst at 300kHz and above, the backscattering strength is dominated by seabed (surface) roughness. Between 10kHz and 300kHz, they hypothesise that the backscattering strength is dependent upon a mixture of both processes. This suggests that the methodology for evaluating backscattering strength is primarily determined by the acoustic frequency, with low frequency acoustics being scattered by volume inhomogeneities, and high frequency acoustics being scattered by surface inhomogeneities.

The empirical relationships of Boehme and Chotiros (1988) suggest that if the sonar frequency is upwards of 150kHz then the interface dispersion of the incident wave will

be more due to surface scattering than volume scattering, because of decreased penetration. Although Boehme and Chotiros (1988) state that surface scattering becomes the dominant process for sonar frequencies of 300kHz and above, the field application of such frequencies is restricted due to very high attenuation rates within the water column significantly reducing the sonar range.

In conclusion, through the use of sonar frequencies in excess of 150kHz and the elimination of near-normal incidence angles, the acoustic processes active at the water-sediment interface and relevant to monostatic imaging sonars, can be limited to interface scattering. If scattering is the only active factor, then the acoustic analysis of side-scan, multi-beam and interferometric sonar data can be directly related to the small-scale inhomogeneities that determine the degree of interface scattering at such high acoustic frequencies.

2.4. Theoretical Scattering Models

Many seafloor backscattering models have been developed in order to understand the underlying physics of the scattering mechanism and to investigate the relative importance of the individual parameters affecting the backscatter strength (Stockhausen, 1963; Brekhovskikh *et al.*, 1982; Crowther, 1983; Jackson *et al.*, 1986; Ogilvy, 1987; Lyons *et al.*, 1994). Whilst various theoretical models have been formulated by physicists to describe and predict the backscattering process, no independent model can claim to accurately assess backscatter under a variety of conditions.

The main theoretical approaches to backscatter prediction from rough surfaces fall into three general classifications:-

1) ***Perturbation Model***
2) ***Kirchhoff Approximation method***
3) ***Composite Roughness Model***

This section will provide a summary of these theoretical roughness prediction models, whilst evaluating their potential field applications.

2.4.1. Perturbation Model

The perturbation approximation model for rough surface scattering incorporates restrictions on the height and gradient of the surface, by assuming that the root mean square surface height measurement of roughness is small compared to the acoustic wavelength. This assumption essentially means that the surface must be only slightly rough, with gradual variations and no discontinuities.

This model gives an approximation of the total intensity field by summing the incident field and a low-order derivative term for the scattered field (Equation 2.*XVII*).

$$\psi(r) = \psi^{inc}(r) + \sum_{j=0}^{\infty} \psi_j^{sc}(r) \qquad \textbf{Equation 2.}\textit{XVII}$$

Where;

$\psi(r)$ = total intensity field

$\psi^{inc}(r)$ = incident field

$\psi^{sc}_j(r)$ = j^{th}-order term of the scattered field

The simple nature of this theory does not lend itself to accounting for the random nature of the scattering from multiple inhomogeneities, because it assumes a smooth, continuous, and planar scattering surface.

2.4.2. Kirchhoff Approximation

The Kirchhoff, or tangent plane, theory is probably the most widely used method for the study of wave scattering from rough surfaces. It provides an approximation to the wave field on the surface of the scatterer by applying Huygen's principle, which states that every point on the wavefront can be considered as a source of secondary waves that

collectively constitute a new wave front (Figure 2.18). Further information on Huygens principle can be found in Baker and Copson (1950) and Born and Wolf (1965).

The Kirchhoff approximation assumes that any point on the rough surface can be approximated to be locally flat (planar), thereby permitting the use of reflection and tranmission coefficients which are calculated for an infinite plane interface.

Figure 2.18 Illustration of Huygen's Principle

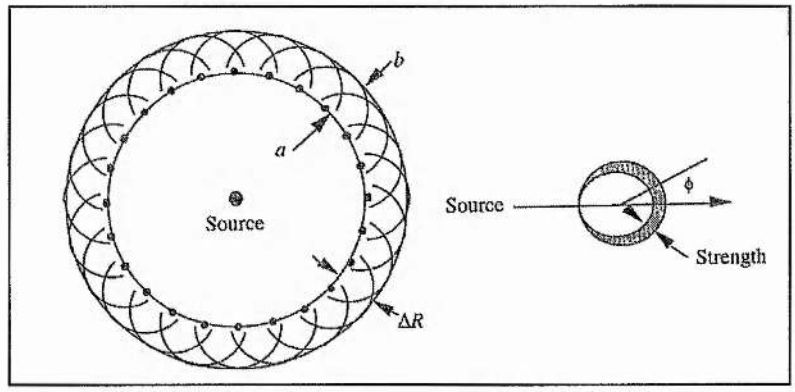

This means that each point on the scatterer is considered part of an infinite plane, parallel to the local surface tangent, and results in the Kirchhoff theory being very accurate for surfaces that are infinite, smooth and planar. In order for the Kirchhoff approximation to be valid the perceived roughness of the surface must satisfy the following condition;

$$k\,a\cos^3\theta \gg 1 \qquad \textbf{Equation 2.}\textit{XVIII}$$

Where;

k = the modulus of the wave vector

θ = angle of the incident wave relative to the mean plane normal direction

a = the radius of curvature of the surface

This condition restricts the radius of curvature of the surface relative to the wavelength of the incident wave, with the magnitude of the restriction being dependent upon the angle of incidence.

Where the above condition is satisfied, the scattered field can be calculated from the integral over all the elementary sources, such as Huygen's principle and the Helmholtz integral (which describes the scattered acoustic pressure field at a reference point). The resultant integral is referred to as the Helmholtz-Kirchhoff integral, which relates the field on the scattering surface to the field at any point.

The wider application of this Kirchhoff theory to scattering surfaces which are not infinite, planar and smooth, is that they are found to suffer from inconsistency and a lack of energy conservation (Ogilvy, 1991). The inconsistency problem arises because the Kirchhoff theory attempts to specify all the boundary conditions on the surface of the scatterer, which becomes an unrealistic goal for finite, rough, and/or discontinuous surfaces. The lack of energy conservation is attributed to the fact that the Kirchhoff theory ignores all forms of wave propagation at a smooth sediment interface, and neglects multiple scattering events at rough interfaces.

The conditions and limitations of the Kirchhoff theory for rough surfaces leads to it being referred to as the 'High-frequency approximation,' because the smaller the wavelength, the smaller the distance over which the surface is restricted to being virtually planar, and therefore the higher the reliability of the measurement.

2.4.3. Composite Roughness Model

The two previous methods of theoretical wave scattering from rough surfaces assume that the surface roughness is considered on only one scale, whereas in reality the scale of roughness can range from atomic to the overall length of the surface. The Composite Roughness Model attempts to overcome this limitation by using two independent components to model the surface with a small amplitude, high frequency roughness, superimposed on a low-frequency variation of larger amplitude. This is achieved by encompassing both the Perturbation Theory and the Kirchhoff Approximation, and as a

result this method has become the most widely accepted theoretical scattering model. In this model the Perturbation theory, which focuses upon acoustic scattering by surfaces with a roughness scale smaller than the acoustic wavelength, is found to be most effective in modelling the shorter wavelength component at low grazing angles, where the radii of the surface curvature are small. The Kirchhoff Approximation on the other hand, is used to assess surfaces with a roughness scale greater than the acoustic wavelength, which dominates at steep grazing angles (Barrick and Peake, 1968; McDaniel and Gorman, 1983). This division of technique reflects the basics of the Rayleigh criterion for surface roughness.

One of the first composite roughness models was developed by Kuryanov in 1963, although this was soon revised by techniques which relied upon a low to high frequency separation of the surface roughness spectrum. However, such techniques proved very susceptible to incorrect selections of the low and high frequencies which resulted in scattering models being applied beyond their domain (McDaniel and Gorman, 1983).

The early model was then improved by the subsequent work of Bachmann (1973), McDaniel and Gorman (1982 & 1983), and Jackson et al. (1986), and has significantly increased the confidence and robustness of the model.

For further reference, the most comprehensive composite roughness model to date for theoretical backscatter, is that derived by Jackson (1994), which includes additional values such as volume scattering, backscatter at a two-fluid boundary and spectral roughness (Figure 2.19).

It should be noted from figure 2.19 that this model treats scattering as a function of both seabed and volume inhomogeneities, irrespective of the relationship between the sonar frequency and acoustic penetration. This factor combined with the assumptions of both the Perturbation and Kirchhoff approximations, means that the Composite Roughness

Model is heavily dependent upon the ability to accurately account for every variable on every scatterer.

Figure 2.19 Graph of backscatter strength versus grazing angle illustrating the Composite Roughness Model and Kirchhoff Approximation trends (from Jackson et al., 1986)

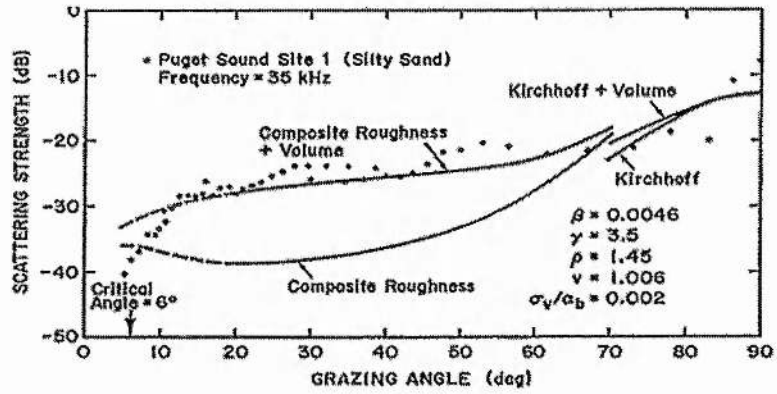

2.5. Real World Scattering Models

In reality, it is far from feasible to even attempt to describe the exact distribution of scatterers on the seafloor. Consequently additional studies have been carried out in order to derive scattering theories for application in the field.

2.5.1. Random Phase Scattering Model

Instead of attempting to precisely model the seabed roughness, this model applies statistical techniques to account for both the microroughness and the random distribution of scatterers within the seabed. Imaging results using this technique suggest that the backscattered signal is characterised by random interference terms, if the scattering body is greater in size than the wavelength of the incident signal (Nishimura, 1997).

Whilst being a more practical method than those developed by complex physics theory, this model maintains an air of complexity as it is inherently dependent upon the ability

to relate accurately recorded phase and amplitude components of the backscattered signal, to the 3-dimensional volume of the scatterer.

2.5.2. Lambertian Scattering

One of the simplest descriptions of surface roughness scattering strength is that defined by Lamberts Rule or Law (Figure 2.20). Lambert's law relates the surface backscatter strength to the square of the horizontal component of the incident angle (grazing angle). This rule is based upon the assumption that the sound is scattered proportionally to the sine of the grazing angle – a parameter which is relatively easy to measure.

Figure 2.20 Diagram illustrating Lambert's Law for a scattering surface (from Urick, 1983)

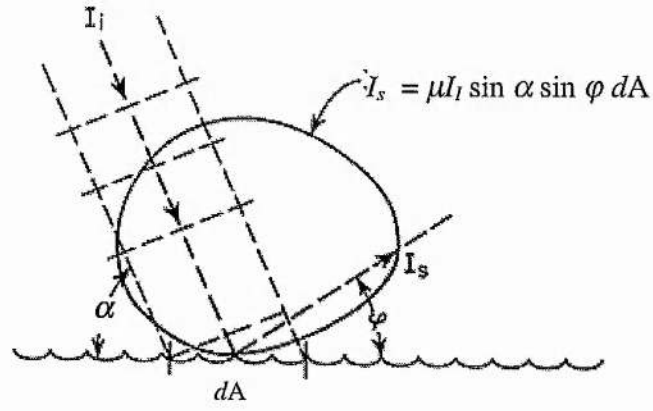

$$I_s = \mu I_i \sin\alpha \sin\varphi\, dA \qquad \textbf{Equation 2.}\textit{XIX}$$

Where;

I_s = scattered sound intensity

I_I = incident sound intensity

μ = the proportionality constant

α = the grazing angle

φ = the scattering angle

dA = the ensonified area of the surface.

Under backscattering conditions the direction of the scattering back towards the source will be $\varphi = \pi - \theta$, and therefore the Lambertian rule for backscattering states that the

strength of backscatter must vary as the square of the sine of the grazing angle. On taking 10 times the logarithm of each side of equation 2.*XIX*, the backscattering strength can be defined as;

$$S_B = 10\log\frac{I_s}{I_i} = 10\log\mu + 10\log dA\sin^2\alpha \qquad \textbf{Equation 2.}\textit{XX}$$

The term 10 log μ is defined as the mean normalised backscatter strength, determined by the frequency and source level of the sonar system. This equation also shows that the backscattering strength (S_B) is equal to the target strength parameter of the sonar equation as defined in section 2.2.4.

Due to the presence of the sine component, Lambert's rule states that the backscattering strength should be greatest at near-90^0 grazing angles and lowest at low grazing angles. In practice however, Lambert's rule is only regarded as being an adequate approximation of backscatter strength for grazing angles between 15^0 and 75^0 (Nishimura, 1997), as below 15^0 scattering becomes negligible, and above 75^0 the acoustic return will be dominated by the coherent reflected energy.

It should be noted however, that the application of Lambert's Rule is constrained by the frequency and wavelength of the acoustic wave, as it does not facilitate a mechanism to compensate for losses due to acoustic absorption *within* the sediment.

2.5.3. Volume Scattering

Volume scattering is essentially dependent upon sediment inhomogeneities and acoustic absorption (Figure 2.16), in the same way as the incident wave is affected by absorption and scattering. In this case, the degree of absorption within the sediment body is determined by the same equation as for transmission loss, with density and speed of sound again dominating the absorption process at given frequencies.

The practical application of acoustic impedance to volume scattering is dependent upon the measurements of density and speed of longitudinal sound, both in the seabed and at

the base of the water column, which limits its use to studies where sediment samples have been assessed in situ.

2.6. Summary

Having discussed all the processes active upon an acoustic wave at the water-sediment interface, it is clear that the methodology employed for calculating acoustic backscattering hinges upon the acoustic frequency of the sonar system,

Whilst low frequency systems offer the ability of assessing the volume properties of materials on the seafloor, high frequency systems are dominated by interface scattering thereby limiting the acoustic analysis to roughness measurements of the seafloor.

The generation of a precise theoretical methodology for the quantitative analysis of sediment-acoustic relationships requires the assumption that all variables can be accurately measured. In reality, the measurement of these variables is virtually impossible as it is entirely dependent upon the technology available to the sediment acoustician.

The aim must therefore be to identify the material characteristics required to broadly classify a sediment, and to match this requirement with a sonar technique that can measure this criterion, and minimise the number of additional sediment-acoustic properties which must be accounted for. The scattering model that best fits this criterion is the Lambertian scattering law or rule, as all the variables within this model can be accounted for without requiring assumptions or conditions for which it holds true.

The analysis must therefore focus upon a sonar technique that minimises the number of scattering variables or processes, but which provides sufficient information in order to classify seabed sediments.

CHAPTER 3:

A BRIEF REVIEW OF ACOUSTIC-SEDIMENT FIELD STUDIES

3.1. Introduction

Chapter 2 has demonstrated that the interrelationships between the characteristics of the water-sediment interface and the strength of the acoustic backscatter will be the primary mechanisms for the remote classification of seabed sediments using acoustics. The actual relationships discussed in Chapter 2 are very intricate, theoretical models of 'ideal' acoustical scattering however, and thus it is necessary to evaluate the empirical relationships between backscatter strength and sediment properties derived from scientific field experimentation.

The results of this research will then be used to evaluate the potential of the various forms of sonar survey techniques towards accurately assessing the relationships between acoustic scattering and the properties of the seabed sediments.

3.2. Empirical acoustic-sediment scattering relationships

The research of Nolle (1963), and McKinney and Anderson (1964) investigated the scattering mechanism by focusing on the dependency of backscattered reverberation upon grazing angles, frequency and most importantly, bottom type. In characterising the bottom type based upon grain/particle size (micro-topography) and surface roughness (relief or macro-topography), they deduced that whilst bottom relief was a major factor in the backscattering of sound, the role played by the particulate nature of the sediment was also very significant. Indeed, the results of McKinney and Anderson (1964) showed a 25dB difference in backscatter values for sediment types ranging from muds to gravels (Figure 3.1).

This relationship between backscatter strength over sediments from muds to gravels closely matched that found by Urick (1956), Mackenzie (1961), Urick and Saling

(1962), and Wong and Chesterman (1968). The empirical results relating to these papers have been summarised by Wong and Chesterman (1968) and are presented in Figures 3.2, 3.3, 3.4, and 3.5, in which different survey areas are denoted by different symbols.

Figure 3.1 Plot of average backscatter strength as a function of grazing angle for different sediment types (McKinney and Anderson, 1964)

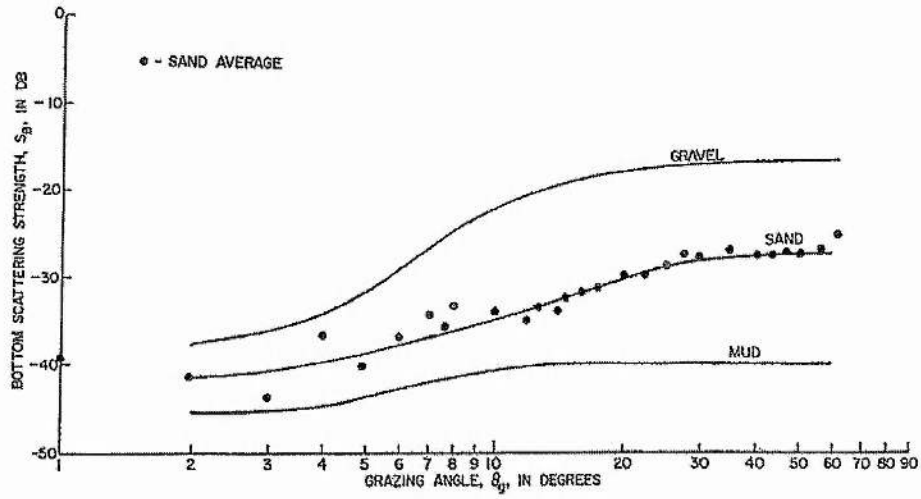

It is worthy of note that in order to focus their results upon interface scattering, McKinney and Anderson (1964), and all others listed, relied heavily upon the assumption that at fairly high frequencies there will be relatively little penetration of sound into an ocean bottom composed of sand and gravel, and more penetration into mud bottoms.

Figure 3.2 Plot of backscatter strength versus grazing angle for a clay seabed, as summarised by Wong and Chesterman (1968).

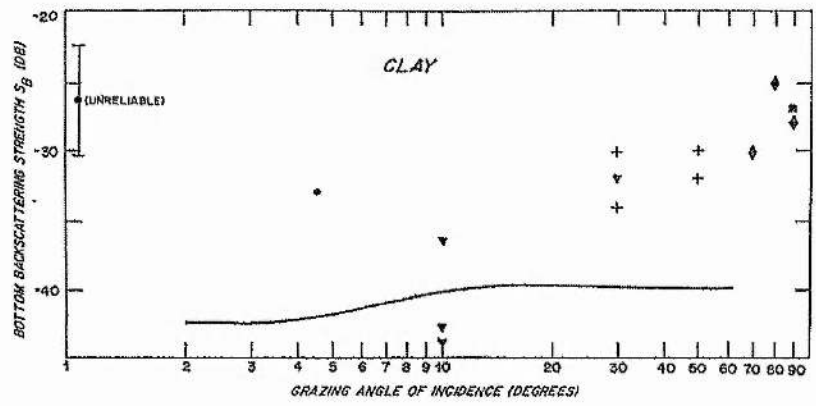

Figure 3.3 **Plot of backscatter strength versus grazing angle for a silt seabed, as summarised by Wong and Chesterman (1968).**

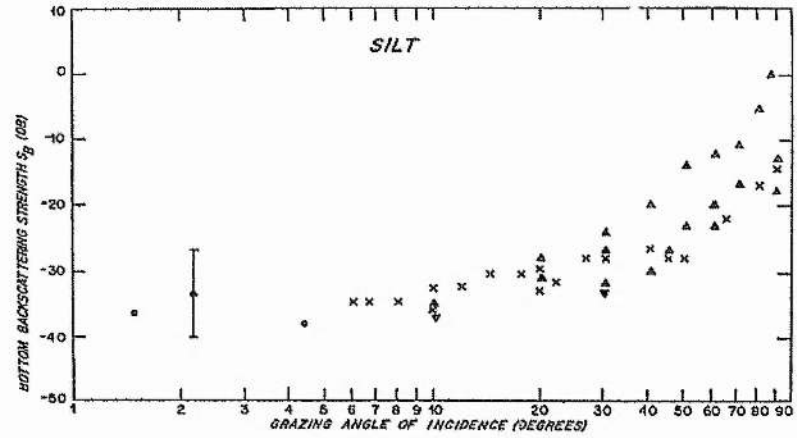

Figure 3.4 **Plot of backscatter strength versus grazing angle for a sand seabed, as summarised by Wong and Chesterman (1968).**

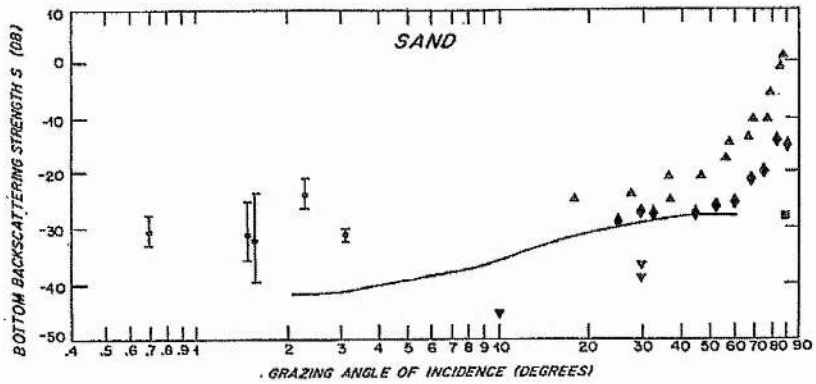

Figure 3.5 **Plot of backscatter strength versus grazing angle for a rocky seabed, as summarised by Wong and Chesterman (1968).**

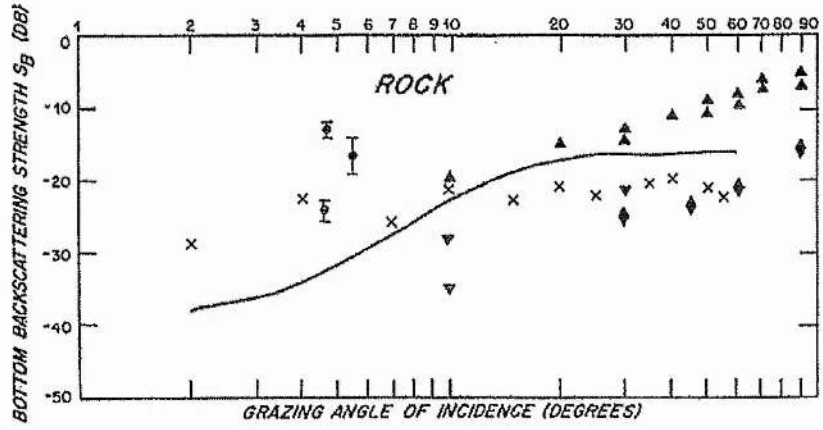

These early experiments during the 1960's and 1970's succeeded in demonstrating a dependence of backscatter strength upon sediment type by analysing the relationship between recorded backscatter coefficients and grazing angles, for different sediment types. It should be noted however, that these studies were primarily focused upon the analysis of low resolution echo-soundings from deep waters, which thereby inhibited an assessment of the precise physical mechanisms controlling the acoustic return, as detailed in Chapter 2 section 2.3. In addition, it is evident that whilst these relationships were proposed to be between backscattering strength and seabed roughness, no-one could profess to having evaluated the true scale of roughness accountable for the variations in backscatter strength.

These early limitations resulted in the acoustic-sediment research of the 1980's and 1990's being dominated by more refined field approaches to the assessment of the interaction between an acoustic signal and the seabed surface. In his study of the relationship between the seabed and acoustic scattering, Crowther (1983) concluded that the interrelationship was governed by the sonar frequency. He stated that for frequencies in excess of 200kHz, there will be certain beds where scattering is dominated by grain scatter effects, and that this is especially true of coarser sediments which are found to be dominated by interface scattering. This conclusion thus supported the interface scattering assumptions made by McKinney and Anderson (1964).

Boehme (1985) and Chotiros (1985) expanded the analysis to incorporate the acoustic beam dimensions (resolution) in order to derive a scale for the roughness of the seabed. They analysed the acoustic data to determine the behaviour of backscatter strength as a function of grazing angle, horizontal beam width, transmit signal type, frequency and bottom type. This comprehensive analysis led to the conclusion that the backscatter results were attributable to bottom roughness, and also that the backscatter curves approximately reflected Lambert's Law.

In contrast, Stanic and Briggs (1988) found little correlation between scattering strength and particle or grain size, or between scattering strength and root mean squared bottom roughness. Even using a surficial layer of coarse shell fragments, and observing an increase in backscatter of between 8 and 10dB, Stanic and Briggs (1989) still failed to prove a significant dependence upon root mean squared roughness.

Stanic *et al.* (1991) thus advanced the analysis to incorporate both frequency change and measured grain roughness. Working in frequencies from 20 kHz to 180 kHz, they observed that by increasing the acoustic frequency over an area of constant roughness, the backscatter strength was found to increase.

This finding implied that given the same angle of incidence and constant scale of roughness, the increase in backscatter strength must have been induced by the enhanced sensitivity of the wave's increased frequency to the scale of 'measurable' bottom roughness (Stanic *et al.*, 1991). Therefore, Stanic *et al.* (1991) stated that as resolution (frequency) increases so the scale of detectable roughness increases, causing an increase in the acoustic scattering strength at the water-sediment interface.

The benefits of increasing the acoustic frequency are not without limit however, as Thorne *et al.* (1994) discovered that frequencies in excess of 1 MHz are usually scattered, often by suspended sediment, before they reach the bottom.

The relationship between acoustic scattering and seabed roughness was also investigated by Lyons *et al.* (1994) who concluded that the scattering results obtained using a 6.5kHz sonar in 4450m water depth closely correlated with those of Jackson *et al.* (1986).

Thus the acoustic-sediment field studies of the 1980's and 1990's appear to unanimously conclude that the seabed roughness was the main determinant of acoustic scattering at high frequencies. However, the most important implication was that the actual correlation between the actual scattering levels and those predicted by theory

were entirely dependent upon the frequency, resolution and data density relating to the sonar system used.

In summary, it is surprising how little work has been done over the years to correlate the environmental, geotechnical, and acoustical parameters, particularly in shallow water areas (Lambert *et al.*, 1993). This means that the majority of the acoustic-sediment field research to date is subject to a significant level of uncertainty due to the low resolution and low precision factors associated with deep-water acoustics.

In-spite of this, some of the findings detailed are still invaluable in terms of identifying the requirements of a successful acoustic-sediment analysis. In summarising all of the experimental hypotheses to date, Stewart (1994) concluded that in order to achieve a complete characterisation of the seabed, the following three parameters are required;

(1) Geometry of the acoustic sensor

(2) Seafloor topography

(3) Physical properties of the seafloor

In addition to the geometry of the acoustic sensor, the seafloor topography should also be regarded as a system-dependent parameter because the bathymetric resolution and acoustic sensitivity of the sonar will determine the scale of the topographical analysis. Therefore, the acoustic-sediment analysis can be focused upon the effects attributed to the seabed surface roughness by using a very high-frequency sonar (>200kHz).

This means that the most suitable sonar systems for interrogating the roughness factor are those that can precisely measure the macro and micro-topographic undulations of the seabed, with a high sample density and a high sample resolution. The next step is therefore to discuss the potential of each sonar survey technique in terms of analysing the acoustic sensitivity towards seabed surface roughness.

3.3. Applications of varying sonar techniques to seabed sediment classification

In order to remotely classify the seabed using acoustic techniques, it is of paramount importance to understand the characteristics of the reflecting plane which control the strength of the reflected wave. *Urick,1983*

The potential of each sonar technique towards remote sediment classification, based on seabed surface roughness, hinges upon the nature and accuracy of information extracted from the acoustic return. As discussed in Chapter 2, sonar systems can be divided into four distinct categories;

(1) Echo-sounders

(2) Side-scan sonars

(3) Multi-beam bathymetric side-scan sonars

(4) Interferometric bathymetric side-scan sonars

each of which must be evaluated in terms of the quality and quantity of the acoustic data recorded, that relates to the roughness of the reflecting plane, the seabed.

3.3.1. Echo-sounder analysis

Echo-sounder technology is undoubtedly the simplest, cheapest, and most practical sonar technique currently available, and as a result the application of echo-sounder systems to the problem of seabed classification is the most documented methodology to date. Simple single-beam echo sounders are designed to measure the vessels vertical clearance over the seabed, and consequently they provide a very narrow depth profile. The depth measurement, determined by the first reflection of the acoustic wave detected back at the receiver, is always assumed to represent the seabed directly beneath the vessel. Also, by using only a single beam this technique is susceptible to very localised / erratic changes in seabed topography, caused by boulders, man-made debris, and ocean-bottom flora and fauna. Using such datasets to construct a three dimensional map of the

seafloor may therefore generate wholly inaccurate results, which would be enhanced by any large-scale interpolation required between the low density data or track lines.

Despite the presence of so many assumptions inherent within the recorded data, many scientists (such as Winn *et al.*, 1983; Bennell *et al.*, 1993; de Moustier and Matsumoto, 1993; Collins and Voulgaris, 1993; Lambert *et al.*, 1993; Thorne *et al.*, 1995; Collins *et al.*, 1996; Davis *et al.*, 1996; Haynes *et al.*, 1997) have persisted with attempts to derive a seabed classification system based upon the data recorded by an echo-sounder.

This is because the echo-sounder classifier is based not just upon the first return, as required for bathymetry, but also the full acoustic signature of all reflections. The theory is that the full acoustic signature incorporates both the first and second echo return, each of which is influenced by a different characteristic of the sediment, namely roughness and hardness respectively (Figure 3.6).

Echo-sounding bottom classifier tools are referred to as 'Normal Incidence Classifiers'; a name which reflects the systems' data acquisition limitation. The knock-on effect of this limitation was that early versions of normal incidence classifiers encountered difficulties in obtaining identical acoustic reflection results from repeat surveys. This meant that each dataset had to be complemented by a ground-truthing programme that enabled spot values of known seabed characteristics to be linked to backscatter values, to form basic sediment-acoustic relationships. The process of relating all other acoustic responses to this relationship results in the derivation of a 'supervised' sediment classification scheme, so-called because of its dependency upon ground-truthing.

More recently however, the robustness of these normal incidence classifiers has been enhanced by using a combination of echo character, database, statistical, pattern recognition, and ground-truthed analysis to discriminate between different types of seabed sediments, and also to detect differing compositions of organic and carbonate matter.

The 'RoxAnn' and 'QTC View' systems are examples of normal incidence classifiers that are currently used extensively by academic and naval institutes for successful seabed classification.

Figure 3.6 Diagram of RoxAnn first and second echo return (from Collins and Voulgaris, 1993).

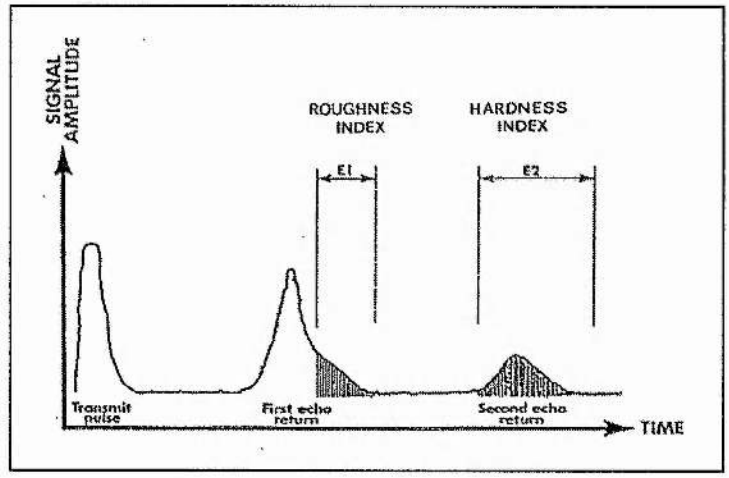

In terms of classifying sediments based solely upon seabed surface roughness alone, the application of normal incidence classifiers are tempered by a reliance upon the "hardness" factor (measured from the second echo), and the low data density and low data coverage inherent within the echo-sounding methodology.

The reliance upon the "hardness" factor is illustrated by Winn *et al.* (1983), who found that the use of an low frequency (18kHz) echo-sounder resulted in an acoustic penetration of 10-12cm into the sediment, and thereby partially confused the correlation between mean grain size (roughness) and acoustic reflectivity (hardness).

The problem of data density and data coverage is highlighted as recently as 1998 by Ligdas and Davies, whose sediment mapping programme was forced to run a 50kHz RoxAnn system along track lines 5 nautical miles apart in an attempt to cover the site whilst meeting time and cost restraints.

In essence therefore, the echo-sounding technique for sediment classification is limited in its practical application by two primary factors. Firstly, it is incompatible with wide

swath bathymetric systems because their focus upon the backscattering alone means that they are unable to facilitate the collection of both the first and second echo in order to measure roughness and hardness.

Secondly, the resultant inability to increase the lateral coverage and density of the spatial data means that the echo-sounding technique is reliant upon 'assuming' a normal angle of incidence. This has the potential of inducing problems within this classification technique, as a failure to accurately measure the angle of incidence can cause inaccuracies in variables such as the 3-dimensional location of reflection, the seabed slope angle, the area of insonification, and the slant range.

3.3.2. Side-scan seabed classification techniques

Side-scan systems have also been applied to the remote acoustic seabed classification investigation (Czarnecki, 1979; Reut *et al.*, 1985; Pace & Gao, 1988; Johnson and Helferty, 1990; Beck, 1991; Mitchell, 1993; Tamsett, 1993; Hughes-Clarke, 1994; Talukdar *et al.*, 1995; Linnett *et al.*, 1996; Volgin and Woodside, 1996). In the absence of accurate depth and angle of incidence information, the *texture analysis* methodology of seabed classification focuses upon the ability of side-scan systems to 'illuminate' topographical features or bedforms which are characteristic of specific sediment types (Figure 3.7).

As shown in Figure 3.7 features such as ripples and dunes can be pictured by the side-scan, although the clarity is heavily dependent upon the attitude of the ripples relative to the side-scan. If their respective attitudes are aligned in a parallel manner then the side-scan beam will travel across the ripples at right-angles to their attitude, thereby accentuating the characteristic peaks and troughs of the ripple feature. Therefore the side-scan image is one which essentially highlights the varying acoustic reflection amplitudes, as a function of angle of incidence, across the seabed surface.

Figure 3.7 Diagram illustrating the ability of side-scan to map seabottom textures

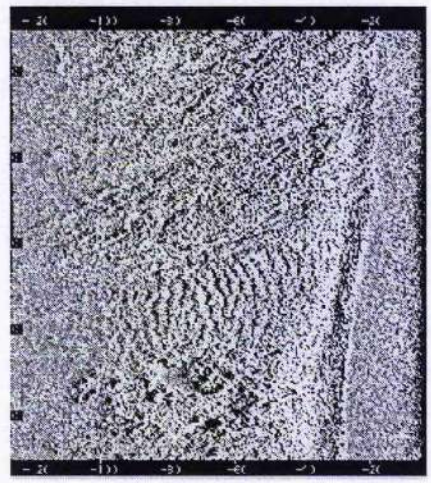

In addition to the textural classifications, side-scan sonar has also been applied to the remote sensing of acoustic scattering from the seafloor by using low-frequency, long-range systems (Fox & Hayes, 1985; Lyons *et al.*, 1994). Lyons *et al.* (1994) used a 6.5kHz GLORIA side-scan system to study the acoustic backscatter over 1000km^2 of seabed in 4450m of water, in order to model the scattering parameters. The backscatter modelling was done using a combination of the Rayleigh-Rice, composite roughness and Kirchhoff scattering models, depending upon the roughness scale and grazing angle. The results recorded further endorsed the scattering model described by Jackson *et al.* (1986).

The side-scan techniques for sediment classification have been further enhanced by Linnett *et al.* (1996) using frequencies of up to 500kHz. However, in the absence of accurate angle of incidence values this technique is unable to distinguish whether the acoustic return is attributed to the process of reflection or scattering. Therefore it remains best suited to large-scale "textural" sediment classification in deep-water.

3.3.3. Multibeam Seabed Classification Techniques

Multibeam bathymetric sonars offer the ability to combine both bathymetric and side-scan data for application within seabed classification. The bathymetric data facilitates

the calculation of the angle of incidence values that incorporate local seabed slope angles, and which can be directly related to the acoustic backscatter amplitude values. In addition to slope corrections, the data can also be compensated for specific acoustic beam-patterns and pulse widths (de Moustier & Alexandrou, 1991), thereby delimiting the area of insonification or fresnel zone.

Broadly speaking, the multi-beam bathymetric side-scan sonar satisfies the sensor geometry and seafloor topography criteria outlined by Stewart (1994) as the main sonar system requirements for the derivation of a seabed classification scheme.

Given the ability to derive the required criteria, the classification potential of the system is therefore dependent upon the precision and resolution of the sonar system (de Moustier & Matsumoto, 1993), and the density of data acquired.

As multi-beams work on a similar principle to echo-sounders, each beam or ping provides bathymetric and acoustic data for one specific fresnel zone. The resolution and precision of that zone is defined by the sonar frequency and the systems transmit and receive sensitivity, and can therefore be enhanced by optimising each within the system. However, the data density factor is predetermined by the fixed nature of the beam spacings in multi-beams.

Multi-beam systems are essentially 'multiple echo-sounders,' with each swath consisting of a number of echo beams. In obtaining maximum swath coverage, the number of beams required is determined by the resolution of the sonar, with low resolution (low frequency) systems requiring only a few beams, whilst high resolution (high frequency) systems require a large number of beams. In seeking the high resolution bathymetry and acoustic data demanded by de Moustier and Matsumoto (1993), multi-beam sonars are constrained by the physical limitation of the number of beams and hydrophones that the system can accommodate.

As the data density is determined by both the size of the fresnel zone relating to each beam and the spatial relationships between fresnel zones from adjacent beams, the optimisation of a multi-beam sonar for seabed classification requires a high frequency system designed to obtain high data densities.

Indeed, Matsumoto *et al.* (1993) conceded that the horizontal sampling of 16 beams was insufficient for the removal of seabed slope effects due to the low density of sampling. Also, the features they aimed to study were smaller than the fresnel zone of the multi-beam, causing the results to represent a composite measurement of the component geological properties. This finding was reiterated by de Moustier and Michalopoulou (1994) when they tried to analyse the relationship between acoustic backscatter and seafloor roughness using a 12.158kHz, 16-beam multi-beam in deep waters.

In modern multi-beam sonars, the maximum number of beams used has risen to around 120 (Matsumoto *et al.*, 1993), thereby increasing the potential for multi-beam technology to derive a stable seabed classification model. Indeed, this technological advance in multi-beams has led to the very basic (first order) classification systems proposed by Hughes-Clarke (1993) and Matsumoto *et al.* (1993). In 1994, Mitchell and Hughes-Clarke also used multibeam sonar data to classify seafloor geology on the Scotian Shelf. In 1998, Collins and Galloway refined this classification scheme further based upon survey data collected from the Vancouver harbour area.

The primary concern regarding the multibeam survey methodology is that the beams transmitted are centred around the nadir, which means that over areas of horizontal seabed the innermost beams will be incident at a near-normal angle to the seabed – a condition which promotes acoustic reflection rather than acoustic scattering. This means that the acoustic-sediment analysis carried out by multibeam technology is not focused solely upon the acoustic "scattering", but must instead incorporate a combination of reflection and scattering across the swath. Therefore, multibeam technology is not

necessarily the perfect technique in terms of classifying sediments based upon the measurement of acoustic scattering from the seabed.

3.3.4. Interferometric Seabed Classification Techniques

The development of interferometric techniques (see Chapter 4) has led to a significant increase in data density and a decrease in sample size. In comparison with the multi-beams 120 beam footprints, an interferometric sonar can record between 1000 and 3000 areas of insonification (derived from phase angle and range samples from the acoustic return) from only one pulse or ping (Geen *et al.*, 1993). In recording the depth and angle of each reflection co-registered with the backscatter amplitude, in such high densities, the interferometric sonar enables a very small-scale analysis of the seafloor topography (Geen *et al.*, 1993) in relation to the acoustic response.

Interferometric bathymetric side-scan sonars also use known source levels, beam patterns and frequencies which enable the derivation of numerical values for sonar equation parameters (Geen *et al.*, 1993), thereby clarifying the acoustic-sediment interaction at the water-sediment interface.

In addition, the localised slope effects of the seabed can be included within the derivation of the true angle of incidence to compensate fully for Lambert's Law, thus enabling the relationship between sediment type and acoustic backscatter strength to be analysed on the smallest possible scale permitted by technology to date.

Indeed, Caruthers and Novarini (1993) stated that Lambert's Law of small-scale scattering can be used to replace the Composite Roughness Model, by using the high-resolution backscatter data from a bathymetric side-scan sonar.

3.3.5. Summary

Generally speaking, the raw acoustic information collected by sonars is predominantly dependent upon the material properties of the substrate and the micro-relief within the

insonified area (de Moustier & Matsumoto, 1993). The analysis of the physical properties of the seafloor can thus be scrutinised in more detail by enhancing the sensor geometry and the resolution of seafloor topography. This means that high-resolution bathymetry is important not only in determining the topography of the area surveyed, but also in providing accurate bottom slope corrections required to convert the arrival angles of the seafloor echoes detected by sonar transducers into true angles of incidence (de Moustier & Matsumoto, 1993).

The application of echo-sounder techniques is constrained by the associated low spatial coverage and requires a combination of "roughness" and "hardness" measurements to classify the sediment. Side-scans offer a general sediment classification tool through texture analysis, with the effectiveness being controlled by the "detectability" of the textures, and the relative attitude of the sonar to the topographic features. Side-scans also provide limited information on the sonar equation parameters, and are unable to discriminate between areas dominated by either acoustic reflection or scattering.

Whilst modern multi-beam sonars, with enhanced data density and resolution, have much potential application in this field, the fact that the survey technique incorporates the nadir zone means that its ability to classify sediments using the "scatter versus roughness" relationship is confined to the outer reaches of the swath.

However, the recent development of interferometric bathymetric side-scan sonars offers an increase in sampling data quantity over that achievable by the multi-beam at off-nadir locations, whilst also providing all the necessary information for analysis of the sonar equation. The angular information recorded also enables the discrimination between areas dominated by acoustic reflection and scattering. Therefore, the information obtained by the interferometric sonars may be viewed as the most comprehensive and precise datasets available towards analysing the relationship between acoustic scattering and bed roughness (Geen *et al.*, 1993; Goodfellow, 1996).

3.4. Conclusion

The empirical relationships between sediments and acoustic scattering suggested to date reveal very general trends that may be used to distinguish between broad clast sizes. Technological limitations also appear to have restricted researchers to basic, non-universal, discriminations between sediment types, with very little having been documented in terms of other variables such as the effects of;

- element area variations upon the seabed roughness resolution,
- angle of incidence variations on the ability to accurately compensate for local seabed slope angles,
- data density variations on the ability to perform an accurate 3-dimensional micro-topographic evaluation,
- the true properties of the sediment body, such as classification methods, mean grain size class, median, mode, or some other evaluation, on the 'roughness' of the seabed.

The net methodology for advancing the studies of these effects is the maximisation of the precision and resolution of sonars with respect to the evaluation of the acoustic scattering and sediment roughness analysis.

It is also important to note that the precision and reliability of any empirical relationships between sediments and acoustic scattering are entirely dependent upon the precision and reliability of the tools used to map the seafloor. This factor dictates that in order for scientific research to progress the understanding of sediment-acoustic relationships, the research should be carried out using survey tools which offer higher resolution, higher precision, and higher data density than has previously been applied.

In summary, the findings of this chapter dictate that the analysis of the relationship between acoustic scattering and seabed sediment roughness will focus upon the use of a very high precision, high resolution, and high frequency interferometric sonar system.

CHAPTER 4:

DIGITAL SURVEY EQUIPMENT

4.1. Introduction

Chapters 2 and 3 have highlighted the need for high precision and high-resolution survey equipment in order to significantly advance the studies of sediment-acoustic relationships. In bathymetric surveys, this high precision must be maintained throughout all the systems used, as inaccuracies in raw field data are very difficult to rectify post-survey.

This chapter will address the types of survey equipment utilised within this research to maximise the resolution, precision and data density of the bathymetric and side-scan data. The digital survey equipment has been grouped and assessed in three separate categories:

- Bathymetric and side-scan sonar system
- Global positioning and attitude sensors
- Environmental sensors

4.2. Bathymetric and side-scan sonar system

The high precision and high data densities demanded by this project were provided by an interferometric bathymetric side-scan system known as an "Interferometric Seabed Inspection Sonar (ISIS)" manufactured by Submetrix Ltd, of Bath, England. This ISIS system was selected following the findings of Chapter 3 which state that high resolution and high frequency interferometers offer the most comprehensive dataset for the evaluation of acoustic sediment relationships. As discussed in Chapter 2, the ISIS was developed from the refinement of the BAthymetric Side-scan Sonar (BASS) system conceived by Denbigh in 1983. The ISIS is essentially a wide-swath bathymetry system,

which operates using the principles of interferometry to record both bathymetric and amplitude data for the generation of depth profiles and true side-scan imaging (Geen, 1997). The survey methodology and geometric parameters incorporated within this sonar technique are illustrated in the detailed schematic of Figure 4.1.

The ISIS transmits an acoustic signal, identical to a side-scan pulse, through the water column to measure the water depth in a line extending outwards from the sonar transducer and perpendicular to the track line of the vessel ('across track').

Figure 4.1 Diagram illustrating the survey geometry of the interferometric sonar.

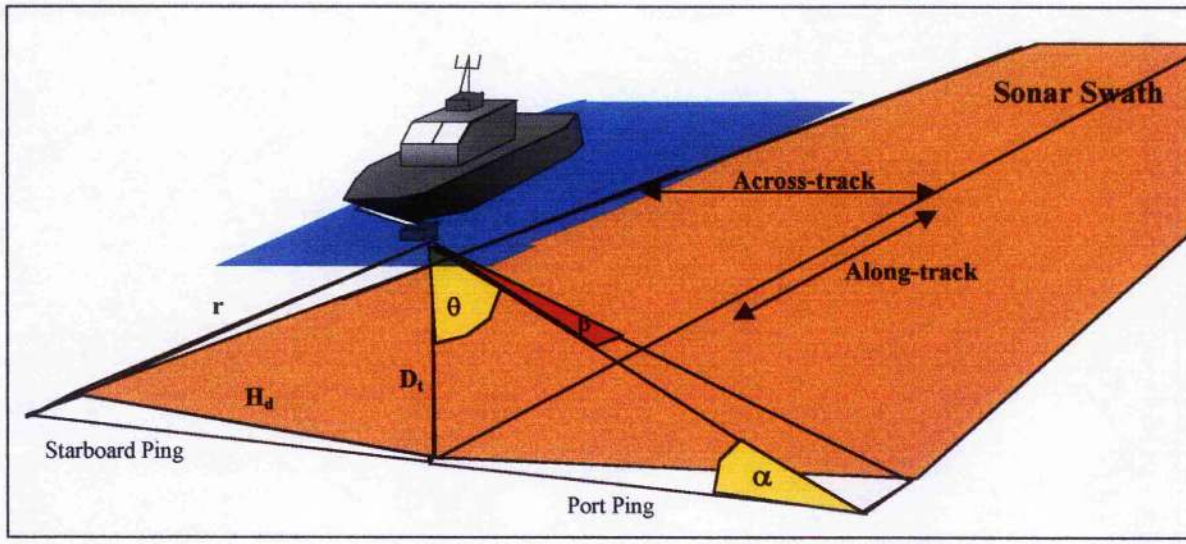

The signal or pulse, referred to as a 'ping', radiates as a beam-shape that is wide in the vertical plane (as determined by ϕ - Figure 4.5) and narrow in the horizontal plane (β). As the vessel moves forwards, the line of depth recordings from each ping, known as the "depth profile", collectively create a plane surface of depth measurements, known as a "swath", and centred around the track line of the vessel (referred to as 'along track').

The shallow water version, known as the ISIS 100, has been specifically designed to maximise data coverage and resolution whilst mapping underwater surfaces in shallow coastal waters, inland waterways, lochs and reservoirs. The deployment of the ISIS 100 has been specifically designed for shallow water surveys by replacing the traditional

tow-fish transducer mount with a vessel mounted transducer arrangement. This adaptation gives increased transducer stability whilst operating at variable survey speeds in confined spaces, and also offers increased lateral data coverage in very shallow water (<100m) as a result of the vessel-mounted transducers ride height being significantly higher than that of a tow-fish mount.

The ISIS sonar setup has also been modified for shallow water surveying by utilising very high sonar frequencies of 117kHz (for depths up to 200m) and 234kHz (for depths up to 100m), to give enhanced bathymetric resolution as demonstrated in section 2.3. The ISIS 100 234kHz was selected for use because it offers twice the resolution achieved using the 117kHz model in very shallow water depths, and is less susceptible to absorption/penetration within the sediment layer (Section 2.3.2).

4.2.1. Basic ISIS interferometry theory

The term 'interferometry' is generally used in marine acoustics to describe swath-sounding sonar techniques that measure the phase content of the reflected or scattered signal in order to derive the angle of the wave-front returning from the sonar target (Geen, 1997). In this context, the phase is defined as a stage in the periodically recurring sequence of changes (oscillation) of the wavelength of sound, and through the use of two or more receivers its measurement can be used to determine the direction of a signal (interferometry).

Figure 4.2 illustrates the basic geometry of a reflected signal as it travels back towards a transducer array, comprising of only two receivers to simplify the theory.

In interferometric sonars, the phase of the returned signal is measured across multiple receive staves which are aligned vertically and spaced out at varying multiples of the acoustic wavelength (Figure 4.2), within the transducer. Each receiver measures the

phase of this returning signal at a pre-determined rate (set at approx. 100,000 times per second for the ISIS).

Figure 4.2 Basic two-dimensional geometry between the receiver staves in the transducer, and the sonar target.

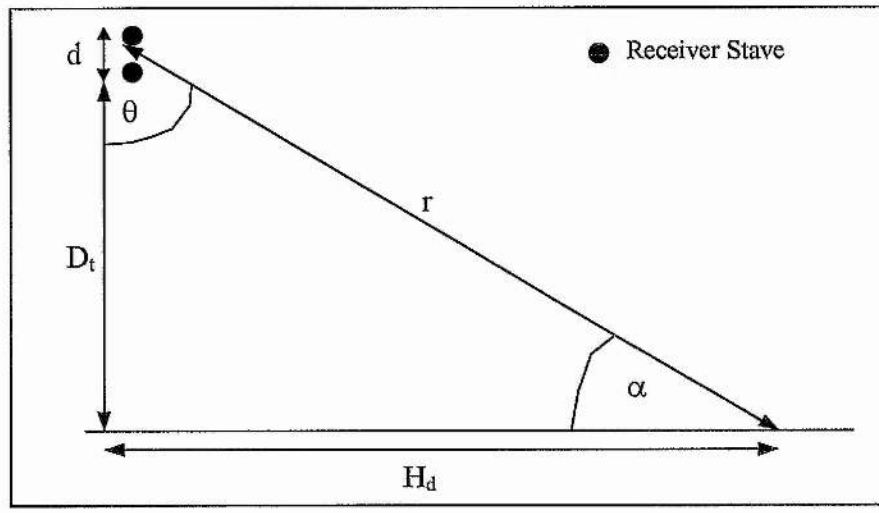

The crux of interferometric theory is the accurate measurement of this phase difference, and to achieve this the selection of the receiver spacing value 'd' (Figure 4.3) is critical. Where the receiver spacing (d) is much greater than the acoustic wavelength (λ), the system can measure precisely the phase difference between each receiver, but 'd' will be too large to confirm that the phase difference measured has occurred within only one cycle of the wavelength (0-2π). For example, using only this information the hardware cannot distinguish between a 1.5π phase shift and a 3.5π phase shift. On the other hand, spacings of less than 1λ ensure that the phase measurement must lie within the range of 0 to 2π, but because it is now trying to measure a very short range-difference the precision will be poor. The interferometer overcomes this problem by using the 'vernier' technique of subtracting the phases from two or more larger spacings from each other to synthesise the phase difference over the optimum receiver spacing of $d = \lambda/2$ (Geen, 1997).

In order to assess the phase angle, the precise phase difference between the receivers must first be converted into a distance measurement (x) based upon the known wavelength of sound (λ), as illustrated in Figure 4.3.

Figure 4.3 Wave-front arriving at the receivers (from Geen, 1997)

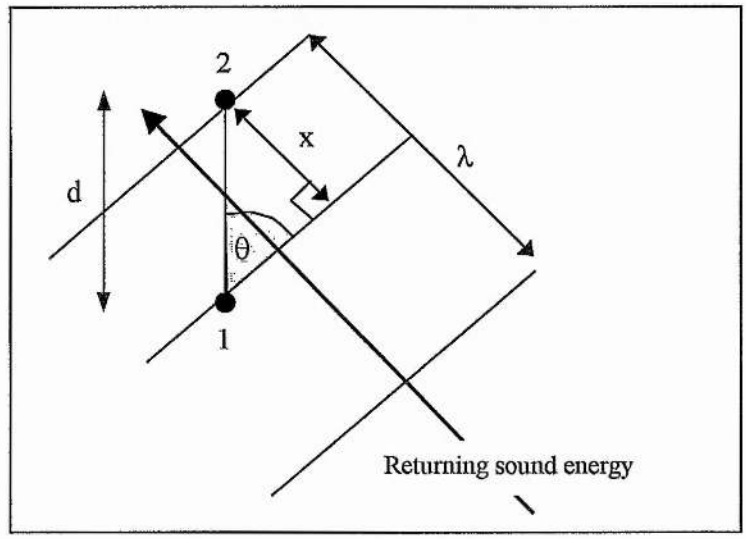

'*X*' effectively represents the 'perceived' distance between the transducers, along the approach angle of the wave-front. The right angled triangle incorporating 'x', 'θ' and with 'd' as the hypotenuse (Figure 4.3), enables the phase angle between the receivers (θ) to be calculated using the following trigonometric equation;

$$\sin(\theta) = \frac{x}{d}$$

Where;

x = perceived distance between receivers at angle of wave-front

d = true distance between receivers

θ = phase angle between the receivers

This method of phase difference measurement requires the assumption that each returned wave-front has been scattered by a single point on the seabed (Figure 4.2), otherwise the phase difference may be attributed to the spatial extent of the insonified

area (Geen, 1997). In sonars, the insonified area is often referred to as an 'element' of the depth profile.

With the three variables above known, simple trigonometry can also be used to derive the return angle (α) of the wavefront arriving at the transducer shown in Figure 4.2. The phase angle (θ) also represents the angle from the vertical (Figure 4.3), and so the associated angle from the horizontal can be defined as 90-θ.

The application of interferometry within sonar systems is relatively straightforward. In addition to recording the phase angle of return, the interferometric system simultaneously records both the two-way travel time (using a crystal clock) and the acoustic amplitude, of the backscattered wavefront. The two-way travel time is halved and then multiplied by the speed of sound in water to determine the slant range (r) of the insonified area from the transducer (Figure 4.2).

The combination of slant range (r) and return angle (α) determines the precise location of the reflecting point relative to the sonar transducer. This information also enables the derivation of the vertical distance (D_t) and horizontal distance (H_d) in Figure 4.2 through the use of Pythagoras' theorem. In reality, this reflecting point actually represents a rectangular area of the seabed insonified by the sonar pulse at one moment in time, and it is the dimensions of this area that determine the potential effectiveness of the ISIS as a bathymetric sonar system.

4.2.2. ISIS 100 System Specifications

The system specifications of the ISIS 100 are focused upon minimising this area of insonification in order to maximise data resolution and data quality. The size of the insonified area represented by each bathymetric point is dictated by the system specifications of sonar frequency and beam width, with the sonar frequency determining

the across-track resolution of the ping, and the beam width determining the along-track resolution in relation to the spread of the ping.

The set sonar frequency of 234kHz for the ISIS produces a smallest practical ping length of about ten wavelengths of the sonar frequency, which equates to approximately 0.064m (Geen, 1997). This gives a maximum across-track resolution of 0.064m as the ping moves outwards across the seabed, although the actual resolution obtained is dependent upon the angle of incidence of the ping with the seabed. In assuming a flat seabed, the across-track dimension of the insonified area will decrease with increasing horizontal distance from the transducer. The potential across track coverage is determined by a combination of the offset angle of the transducers and the beam elevation, as illustrated in Figure 4.5. The standard bracket mounting for the ISIS transducers is designed to incline the transducer face to 30^0 from the vertical in order to reduce the effects of sea surface scattering. For a similar reason the elevation angle of the beam (ϕ) emitted by the transducer is confined to 61^0 to minimise both sea surface reverberation, and acoustical interference ('cross-talk') between the port and starboard transducers. This 61^0 elevation gives 30.5^0 arc of coverage to either side of the line perpendicular to the transducer face, and offers a horizontal swath range versus depth ratio of up to 7.5:1 for each transducer, or 15:1 overall. The limits of the beam arc represent the angle from the axial plane at which the acoustic intensity of the axial beam is reduced by exactly half, -3dB (Medwin and Clay, 1998).

The along-track dimensions of the insonified area are directly related to the beam width (β), and by using a minimal width of 1^0 the 234kHz version of the ISIS 100 minimises the lateral spread of the beam, and also the along-track dimensions of the insonified area. The width of the insonified area is now simply dependent upon the slant range travelled by the ping, and will increase in size with increasing slant range from the

transducer. For example, increasing the slant range from 10m to 50m increases the beam width from 0.17m to 0.87m.

Figure 4.5 Diagram of ISIS angular set-up

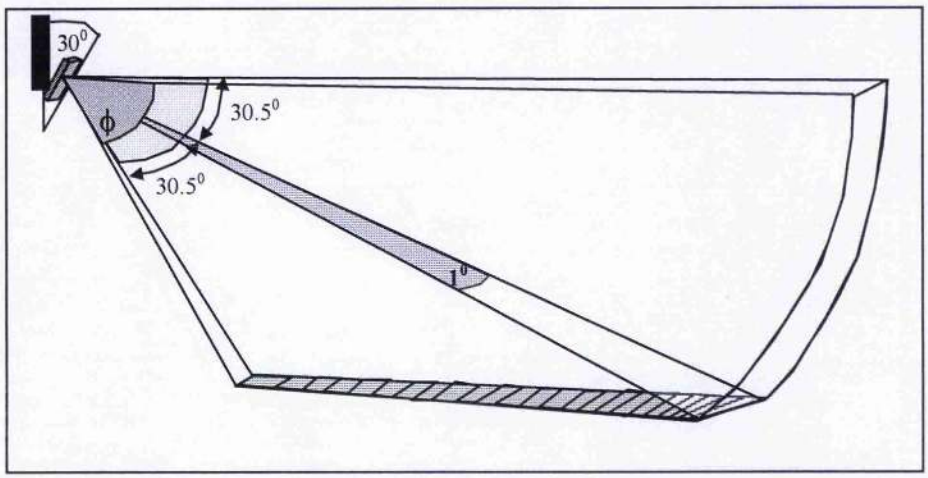

The across-track dimension (length) of each of these insonified areas is determined by the spatial resolution of the sonar signal. In this case, the spatial resolution is defined by the duration of the acoustic pulse, which can be measured by the number of wavelengths of the acoustic pulse. For the ISIS 100, the shortest practical pulse is found to be ten wavelengths of the sonar frequency, which equates to 4.274×10^{-5} seconds, for the 234kHz system. The duration of this pulse essentially represents the across-track dimension of the sonar signal, in the same way as the beam width determines the along-track dimension of the signal. This pulse duration can be converted into a spatial measurement by multiplying the pulse time by the speed of sound in water, to give the length of the pulse in metres. Figure 4.6 visualises the effect that the pulse length has on the spatial resolution of the seabed, by showing a transmitting pulse delimited by two arcs, travelling over two objects on the seabed.

In order for the sonar pulse to detect these objects, the length of the insonified area defined as the pulse length resolved onto the seabed at the incident angle, must be smaller than the length of the objects.

Figure 4.6 Geometry of pulse length intersection with the seafloor (Nishimura, 1997)

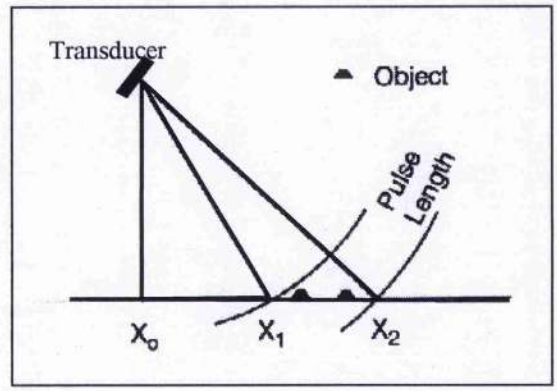

In figure 4.6, the objects fall within the insonified area making them indistinguishable in terms of bathymetry, and so they must therefore be included as roughness factors within the insonified area.

The combination of a high acoustic frequency and such an acute beam width creates a heavily sampled, yet very narrow depth profile of the seabed. In maximising both the along-track and across-track resolution of the ISIS, the system also requires additional compensatory specifications to complement this high precision by maximising the data density.

In a similar way to the resolution, the data density can be analysed both across-track, and along-track.

The across-track data density is governed by the rate at which the transducers sample the back-scattered return. The ISIS maximises this across-track data density by measuring the phase of the returned signal across the receivers at around one hundred thousand times per second, and simultaneously sampling the amplitude of the signal tens of thousands of times per second (Geen, 1993). This results in the profile of each pulse consisting of several thousand sets of range, angle and amplitude data, with 'samples' being taken approximately every 7.5cm along the profile (Geen, 1993). This high density sampling interval within each ping profile is illustrated in Figure 4.5, where the profile consists of a succession of small, two-dimensional, rectangular sample

areas, whose spatial interrelationship is dependent upon the sampling rate of the returned signal.

The along-track data density concerns the size of the spacings between each of the narrow ping profiles. This along-track spacing of the pings is determined by the relationship between the ping rate of the ISIS transducers and the velocity of the vessel. At 10m slant range each transducer must alternate between port and starboard pings every 0.085m to ensure 100% data coverage, and at an average vessel speed of 4 knots (approx. $2ms^{-1}$) this translates into an overall ping rate of 12Hz. As a result, the ISIS allows the operator to alter the ping repetition rate to compensate for variable vessel speeds and ensure complete along-track data coverage.

This process is complicated by the fact that the ping repetition rate also effectively governs the across-track range of the ISIS. For example, using the above figures a ping rate of 12Hz allows a backscatter recording time of only 0.083 seconds per ping, which equates to a maximum slant range of 62.5m (assuming speed of sound = $1500ms^{-1}$). If the across-track coverage is the critical parameter, then the vessel speed must reflect the ping rate. It is clear that there exists a trade-off between across-track coverage and along-track coverage, which is ultimately dependent upon the speed of the survey vessel.

The level of data sampling achievable with the ISIS is one of the most significant advantages over multibeam technology. The profile of each individual ping can consist of several thousand sets of range, angle and amplitude data, recorded every 7.5cm across-track, and any or all of this data can be made available to the user. Even assuming a moderate sampling rate of 10 per square metre this phenomenal quantity of data sampling can yield around one thousand million samples over a ten kilometre square survey area. Manufacturers figures also suggest that the ISIS can collect up to 36

million soundings per hour, which is approximately ten times the data density achieved by conventional multi-beam systems.

Geen (1997) illustrates the superior near-range coverage achieved by the ISIS relative to a typical multi-beam sonar. The values plotted in Figures 4.7 are based on the assumption of a time sampling interval of 36μs and a typical beam spacing of 1.5^0 for the multi-beam. These plots show that as the horizontal range from the transducer increases the horizontal sample spacing of the multi-beam increases, whereas with the ISIS it decreases. The crossover point between the ISIS and multi-beam trends illustrates the horizontal range at which the ISIS data density begins to exceed that of the multi-beam. The cumulative results for a variety of water depths state that the ISIS data density exceeds that of the multi-beam at horizontal ranges in excess of 4-7m.

Figure 4.7 Comparative near-range coverage of the ISIS and a 'typical' Multi-beam sonar (from Geen, 1997)

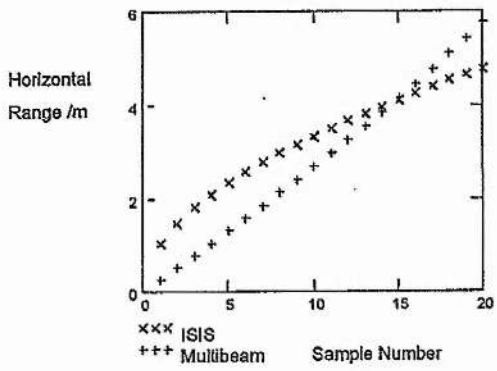

Location of the First Twenty Depth Samples, 10 m Water Depth

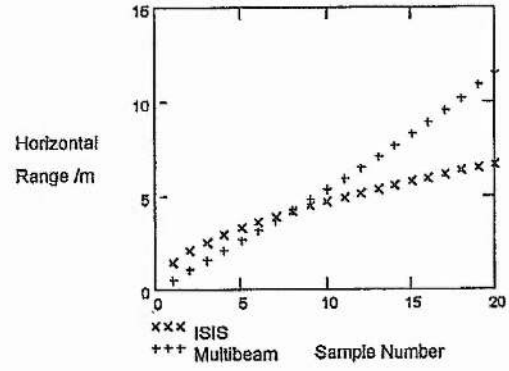

Location of the First Twenty Depth Samples, 20 m Water Depth

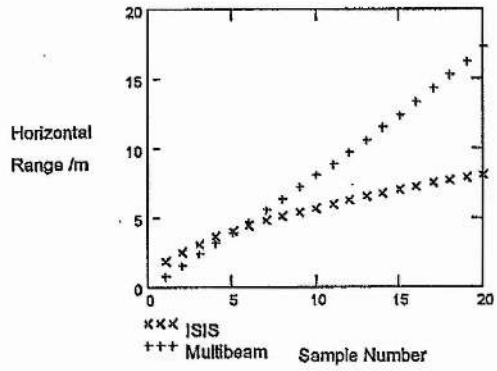

Location of the First Twenty Depth Samples, 30 m Water Depth

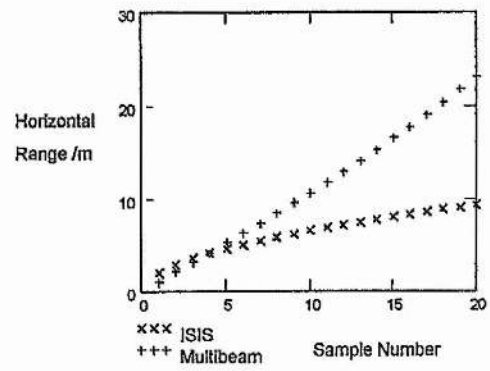

Location of the First Twenty Depth Samples, 40 m Water Depth

All of the aforementioned system specifications for the 234kHz version of the ISIS 100 have been summarised in Table 4.1 for future reference.

Table 4.1 System Specifications for the 234kHz model of the ISIS100 (as stated by the manufacturers)

System Parameter	ISIS 100 234kHz specification
Sonar frequency	234kHz
Operating depth	0 - 100m
Maximum swath width	300m
Horizontal range vs depth ratio	15:01
Width of acoustic beam	1 degree to -3dB points
Vertical arc of acoustic beam	61 degrees to -3dB points
Transducer angle from vertical	30 degrees
Transducer ping rate	up to 12Hz
Angular resolution	0.04 degrees
Size resolution across-track	0.075m
Transmit ping length	0.00008 secs
Phase sampling rate	100000 times a second
Time and amplitude sampling rate	10000 times a second

The ISIS has also been further adapted for shallow water surveying through the incorporation of four different power settings (Table 4.2), which allow the operator to find the threshold between optimising the data range and quality, and inducing acoustic saturation of the water column.

Table 4.2 Transmit Power Settings of the ISIS 100 234kHz system

ISIS Transmit Power Setting	Voltage Applied (in Volts)	Percentage of Maximum Power Output (%)	Resultant Source Level (dB re uPa/V @1m)
4	600	100	219.53
3	150	25	207.49
2	60	10	199.53
1	30	5	193.51

It is imperative to note that any real-time adjustments of the source level are not recorded digitally within the ISIS main rack or software, and must therefore be logged independently by the operator in real-time. This is of particular importance when applying the sonar equation (See Chapter 2) to the ISIS 100 acoustic analysis.

4.2.3. ISIS data precision and resolution

The slant range accuracy of the ISIS is determined by the accuracy of the ISIS crystal-controlled clock and the accuracy of the overall speed of sound in water calculation. The crystal clock runs at 256 times the sonar frequency, and is inherently highly stable, which means that any slant range inaccuracy will come from the speed of sound in water calculation.

The speed of sound can be calculated externally using a sound velocity probe (Section 4.4.1) or internally from Medwins' (1975) equation for the speed of sound in water, shown below. Either way, the manufacturers specifications state that the sound speed must be accurate to $\pm 0.2 ms^{-1}$.

$$v_1 = 1449.2 + 4.6T - 0.055T^2 + 0.00029T^3 + (1.34 - 0.01T)(S - 35) + 0.016D$$

Where;

v_1 = sound speed in water (ms^{-1})
T = temperature (^0C)
S = salinity (‰)
D = depth (m)

This equation claims an error of less than 0.2 ms^{-1} for temperatures between 0^0C and 32^0C, salinity values between 22ppt and 45ppt, and in water depths under 1000m. The resultant range error margin can be reduced by decreasing the slant range cover.

A conservative estimate by the manufacturers states that in considering this error margin, the ISIS 100 can measure the slant range to within 0.015m at the maximum range of 100m.

The resolvable accuracy of the ISIS sonar is maximised by a pulse length of only 0.064m (for the 234kHz system), which combined with a lateral beam spread of only 1^0, results in insonified areas of minimal dimensions. This small-scale resolution ensures

that the system is capable of eliminating variations in seabed topography from the 'roughness' evaluation, thereby leaving bed roughness as the only roughness variable present within each insonified area (refer back to Chapter 2 section 2.3).

4.3. Global positioning and attitude sensors

The ISIS 100 requires locational information in order to correctly position the depth and side-scan data in three dimensions with respect to the Earth's surface. It obtains this information through a combination of a Global Positioning System (GPS) and a Motion (Attitude) Reference Unit (MRU).

4.3.1. The Differential Global Positioning System (DGPS)

A sophisticated RACAL 'Landstar' DGPS was used to provide the high precision DGPS data for the ISIS 100, because of its exceptional centimetre precision.

Basic GPS may have been the most accurate radio-based navigation system ever developed for air and sea travel, but the development of 'differential' GPS (DGPS) has significantly reduced the inaccuracies of GPS, to give a universal measurement system capable of easily positioning targets to sub-metre accuracy (Fish and Carr, 1991).

Differential GPS involves the co-operation of two receivers, one *fixed*, and the other mobile and recording position measurements. The key to the enhanced accuracy comes from the fixed receiver that ties all the satellite measurements into a *fixed* local reference. The fixed receiver is designed to use its known location to calculate the timing signal errors from all visible satellites, and transmit this correctional information to the mobile GPS receivers within its zone (Fish and Carr, 1991). This technique allows the mobile GPS to adjust the timing signals received from at least four satellites, and virtually eliminate all errors from the system to derive pinpoint precision. The World Geodetic System 1984 (WGS 84) is the most common default datum used by GPS today.

The other important factor in maintaining precision is the method in which the DGPS data is recorded. The Universal Transverse Mercator (UTM) system, adopted by the US Army in 1947, was used for the designation of rectangular locational co-ordinates. The use of metric measurements replaces the degree measurements of latitude and longitude designed to account for earth surface curvature, thereby simplifying the gridding of maps.

The UTM system divides the earth into 60 zones, numbered 1 to 60 starting from longitude 180^0 (the international date line), each of 6^0 longitude wide. Each of these longitudinal zones is divided into horizontal bands spanning 8^0 of latitude, lettered from C at 80^0 South, to X at 84^0 North. A square grid is then placed over each zone, with the vertical grid lines aligned parallel to the centre of the zone.

These lat-long grid zones are converted into metric grids by expressing co-ordinates as a distance in metres to the east, referred to as 'easting', and a distance in metres to the north, referred to as 'northing'.

UTM easting co-ordinates are referenced to the centre longitudinal line of the zone, known as the central meridian, and it is assigned an eastings value of 500000m east. Since this 500,000m value is arbitrarily assigned, eastings are sometimes referred to as 'false eastings'. An easting of zero will never occur, since a 6^0 wide zone is never more than 674,000m wide. Due to the curvature of the zone boundaries, the minimum and maximum eastings values are;

Min 160,000 mE, and Max 834,000 mE at the Equator

Min 465,000 mE, and Max 515,000 mE at 84^0 N.

UTM northings coordinates are measured relative to the equator. For locations north of the equator, the equator is assigned the northings value of 0m north. To avoid negative

numbers, locations south of the equator are made with the equator assigned a value of 10,000,000m north.

The combination of UTM northings and eastings derived by DGPS allows any target to be precisely located on the Earth's surface, to within centimetre precision using current technology. The DGPS system was also used to provide the UTM co-ordinates for the grab sample locations of the ground-truthing programme to metre accuracy.

4.3.2. The Motion Reference Unit (MRU)

The TSS DMS-05 motion reference unit was selected for use in this project because it is one of the most accurate MRU's which is fully compatible with the ISIS system.

The ISIS 100 requires an MRU to measure accurately the motion of the transducers, in order to correct for changes in beam direction and phase angle measurements. The MRU contains both accelerometers and gyroscopes that are used to measure the linear and rotary motion of the transducers. The resultant motion measurements are output to the sonar system under the headings of roll, pitch, heave and yaw, all of which are summarised below and illustrated in Figure 4.8.

(1) Roll - the rhythmic movement of a vessel about its longitudinal axis

(2) Pitch - the pivotal motion causing the rise and fall of the bow and stern about a horizontal axis

(3) Heave - the vertical rise and fall of the entire vessel

(4) Yaw - the side to side movement (around the vertical axis) of the bow and stern of a vessel

(Fish & Carr, 1991)

These motion measurements are then used to correct the errors that are present in the raw sonar data. As the ISIS is basically an angle-measuring system, the most important

corrections are for the roll and pitch angles, which must be measured to within ±0.05° by the MRU.

Figure 4.8 Diagram illustrating the roll, pitch, heave and yaw motions of the vessel or unit

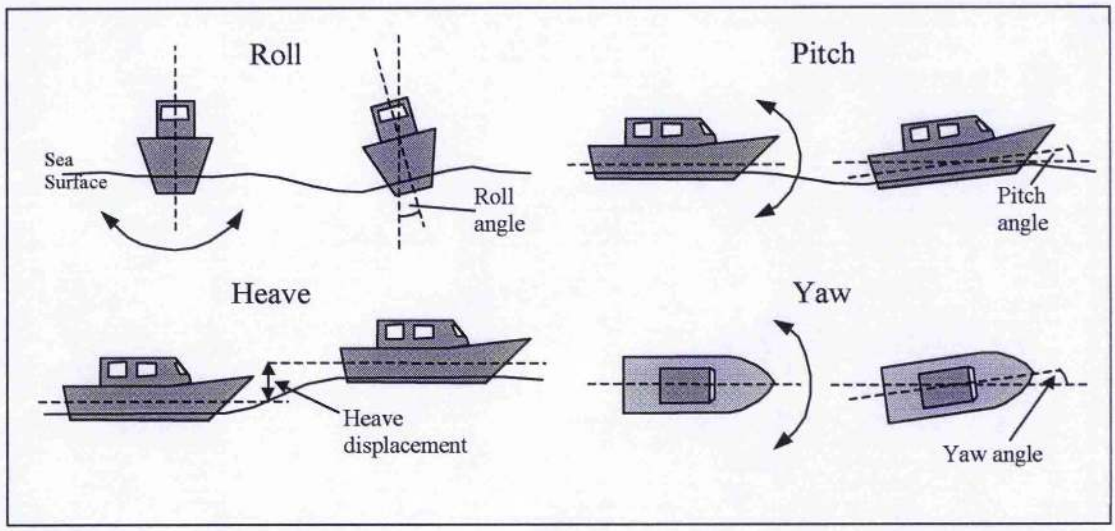

Although the MRU directly monitors the roll, pitch and heave, it is dependent upon the vessels navigation system to provide the vessel heading data to determine the yaw motion of the unit.

4.3.3. Summary of positioning and attitude sensors

One critical factor of sonar surveys in general, is that all the spatial relationships and locational data generated by the systems are calculated relative to the global 'position' of the transducers, using GPS. This means that although the highest precision is achieved using the RACAL 'Landstar' DGPS, any inaccuracies will affect the spatial relationship between the ping profiles, and the overall accuracy of any maps. The spatial relationships between elements within the same ping are unaffected as the ISIS only samples the DGPS data once per ping, and thus the DGPS inaccuracies are irrelevant within the sonar equation.

In contrast, although the ISIS only samples the MRU data once per ping, the accuracy of the MRU data is of great importance in determining the angular values of the trigonometric analysis.

Overall the RACAL 'Landstar' DGPS has a manufacturers accuracy to 0.1m, and the TSS DMS-05 MRU states an angular accuracy of 0.05^0 within a range of $\pm 50^0$.

4.4. Environmental Data

The calculation of depth values is dependent upon the two environmental factors of speed of sound in water, and tide height.

4.4.1. CTD Probe (sound velocity, temperature & salinity)

The speed of sound in water determines the distance between the source and the reflector, and so is a critical factor in the precision of the depth data. In measuring this environmental factor, it is recommended that a very high precision sensor is used to provide a sound velocity profile through the water column. Inaccuracies in this measurement will affect the depth values recorded by the system, and these errors will be exaggerated with distance, and more importantly with depth. This is a critical factor in the repeatability of surveys spanning climatic seasons. In terms of small-scale surveys in shallow waters, the sensitivity of the ISIS bathymetry to sound velocity inaccuracies is significantly reduced by the short-range measurements and the more constant temperature profiles through the water column.

A CTD probe, with sound velocity precision of within $\pm 0.2 ms^{-1}$, was used to provide a velocity profile of the water column at all survey sites. With this level of precision, the slant range error margin associated with the sound velocity error margin equates to ± 0.007m at a slant range of 50m, and is therefore negligible in shallow water environments. The profiles generated are then fed directly into the ISIS processing

software, which automatically corrects the speed of sound data and accounts for the any possible effects associated with ray bending (refraction) within the water column.

4.4.2. Tide Data

The measurement of tide height is also an important factor in the precise determination of water depth, as the altitude of the vessel itself obviously varies with tidal fluctuations. The localised tide data can be obtained using a 'tide plot' software program and cross-referenced with actual measurements recorded by coastguard stations and Harbour Authorities. In addition, some DGPS can generate accurate height measurements as part of the positioning data, which the ISIS can process in the same way as tide data. Such positioning systems make accurate tide measurements unnecessary.

The ISIS requires the tide data to convert the seabed depths it records into seabed depths relative to the lowest astronomical tide, which represents the reference plane used as a basis for navigational charts. Figure 4.9 shows how the tide height data is incorporated spatially within the vertical offset equation shown below.

Figure 4.9 Illustration of the vertical (Z plane) parameters required for the calculation of the depth values relative to the reference plane.

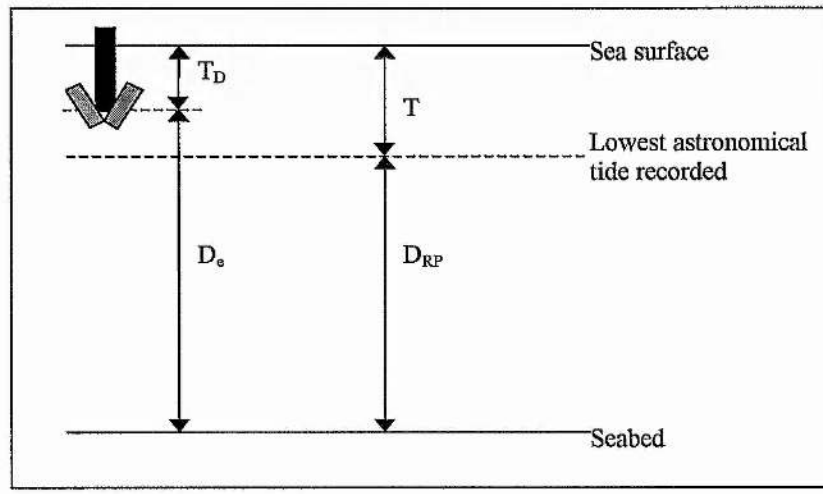

$$D_{RP} = (D_T + T_D) - T$$

Where;

D_{RP} = Depth below reference plane

D_e = Depth of element below the transducers

T_D = Transducer depth below the sea surface (manual measurement)

T = Tide level

This conversion within the ISIS software requires the tidal height to be accurate to within 0.01m, in order to preserve the precision of the bathymetric data for charting. The tide data is fed directly into the ISIS processing software to create a time-tagged tide file which is used to adjust the depth values relative to the tidal corrections, to give a bathymetric chart.

It is important to note that although inaccuracies in tide heights alter the final depth values generated relative to the lowest astronomical tide, the tidal values will not affect the measurement of the vertical distance between the transducers and the seabed, unlike the sound velocity data.

This means that the tidal correction factor focuses more upon maintaining the repeatability of surveys, by accounting for the seasonal and daily variation in tide levels.

4.4.3. Summary of environmental sensors

In summary, the sound velocity data will alter the calculation of the range between the elements and the transducer, and the tide data will affect the final depth values generated by the ISIS. It is important to note that although both of these factors affect the bathymetric data, any associated errors will not alter the spatial relationships between elements within the same swath, provided the swath is surveyed over a relatively short time period to minimise the effects of tidal fluctuations. Both of these environmental factors must be addressed within the pre-survey methodology to minimise the bathymetric error margins.

In practical terms, the bathymetric accuracy can be enhanced by minimising the water depth and the horizontal range to the target area, and by minimising the duration of survey lines in locations affected by tidal fluctuations.

4.5. Summary of overall depth accuracy and system precision

The angular accuracy of both the ISIS 100 sonar and the MRU is better than 0.05^0, giving a combined system accuracy of 0.1^0. The error in depth can be calculated using the following equation;

$$H_{\max} = \frac{D_{err}}{\sin \theta_{acc}}$$

Where;

H_{max} = maximum horizontal range where depth error criteria is still met

D_{err} = depth error

θ_{acc} = angular accuracy

This fixed angular accuracy means that the depth error is directly related to the horizontal range, as is illustrated in Figure 4.10, with sound velocity errors within $0.2ms^{-1}$ being negligible.

Figure 4.10 Depth error versus horizontal range for the ISIS 100

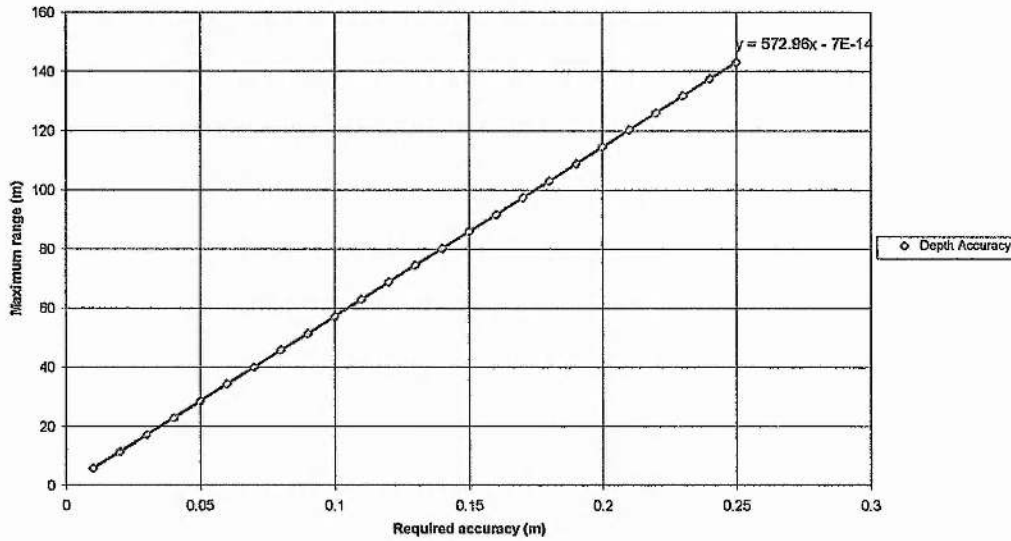

The errors incorporated within the DGPS and tide data are confined to the correlation between successive swaths and the repeatability of surveys (including ground-truthing surveys), as they do not affect the systems precision with regard to the sonar equation.

4.6. ISIS deployment and survey methodology

The main components of the ISIS 100 system are a pair of sonar transducers, a motion reference unit (MRU), the ISIS100 main rack (housing the sonar electronics), as shown in Figure 4.11, and also a computer workstation.

Figure 4.11 Photograph showing the main components of the ISIS100, except the workstation (*Courtesy of Submetrix*)

Figure 4.12 Examples of pole mountings for the transducers

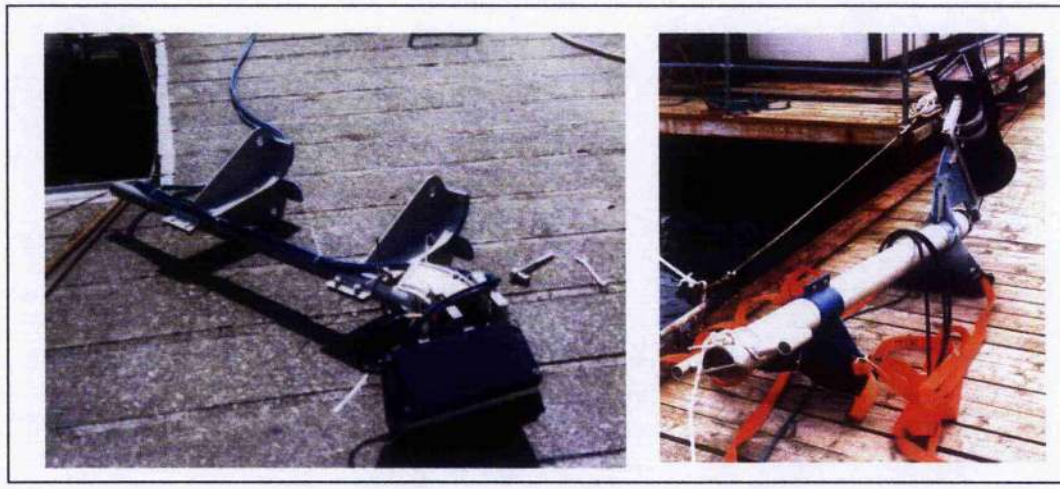

The two transducers required to survey on both port and starboard sides of the vessel can be mounted together with the motion reference unit, on either the hull of the vessel, or on a pole designed for bow or side mounting (Figure 4.12 and 4.13).

Figure 4.13 Photographs illustrating the installation of the pole on the vessel (All images courtesy of Submetrix)

Bow-mounted ISIS transducers (above)

Bow-mount on a Catamaran (above)

Estuary survey using a side-mount (above)

A cable is then used to connect the submerged transducers and MRU to the main ISIS rack onboard the vessel. In addition, the navigational data is also fed straight into the main rack to enable real-time processing. The entire system is then controlled and operated via a computer workstation, linked by ethernet, to the main rack. The only exception to this rule is the '*transmit power setting*' control on the ISIS main rack.

This additional control is designed to permit the operator to alter the source output level to suit the survey conditions. In general terms, as the source level increases so will the effective range of the system. Increasing the source level is not solely beneficial however, as it may have the adverse affect of saturating the water column with indistinguishable acoustic noise, thereby masking the desired returns from the seabed.

Therefore, the transmit power level must be adjusted to provide a satisfactory balance between data quality and data quantity.

An essential part of surveying with the ISIS 100 is the procedure for calibrating all of the high precision equipment. The first step is to accurately measure the physical offsets (to within 0.01m) by recording the three dimensional relative positions of the transducers, GPS antenna and the MRU, once they have been fully installed upon the vessel. The depth of the transducers below the water surface is also a critical measurement with regard to the vertical offset. Once the fixed positional offsets have been determined, the calibration of the ISIS itself can begin.

The sonar calibration procedure is carried out in essentially test conditions (shallow water, flat seabed) in order to determine any offsets which may be present in the sonar set-up. The most basic step involves the calibration of the ISIS depth measurements with the depth recordings from the vessels' echo-sounder. This eliminates vertical depth shifts which can be difficult to trace by comparing ISIS survey lines, and gives direct measurements of depth differences.

The self-calibration procedures should then be run on each instrument. The ISIS system facilitates the internal calibration for all of the survey parameters outlined in Table 4.3.

The most important offset requiring calibration is that of roll angle, as this have the strongest effect upon depth error. Although the MRU measures the roll angle to within 0.1^0 the calibration procedure is used to determine the actual offset angles of the transducers themselves, once they have been installed. The offset measurement is automated within the ISIS, but it requires five survey lines of 500-1000m length to be run in sequence with each line overlapping its neighbour on the same side of the system (port-port and starboard-starboard) by 100%. In post-processing, the ISIS compares the depth profiles measured by the same transducer over the same area, but from the

opposite direction, and selects a 'best-fit' offset angle measured to 0.1^0 which causes the two depth profiles to appear parallel.

Another problem occurs with the mis-application of tide corrections which may cause time-dependent depth errors. These errors must be measured during the actual survey, and can be estimated by running cross-lines at right angles to the main survey lines.

Table 4.3 ISIS calibration parameters and causes of error (as stated by manufacturers)

Calibration Parameter	Cause of offset or error	Method of measurement	Adjustment in ISIS post-processing software
Physical offsets 3D relationship between transducer, MRU & GPS	Spatial offset upon installation	Manual measurements to within 0.01m	Offset values input into ISIS processing software
Roll	Offset between MRU vertical and nominal transducer angle	Five parallel overlapping lines over a flat seabed	Corrected using ISIS internal calibration program
Position	Time delay in DGPS acquisition, & position-ing offsets and errors	Two lines; same position, different speed over seabed with identifiable features	Location comparison of features on each chart. Time delay entered into ISIS
Pitch	Mis-alignment between transducers and MRU	Two lines on same track in opposite directions, surveying identifiable features	Offset value derived from comparative feature locations
Heading	Along-track mis-align-ment of transducers, MRU and compass	Use roll calibration, but with features present	Calibrated using comparative feature location
Depth	mis-application of tide corrections	Run cross-lines at 90 degrees to the main survey lines	Compare with the echo-sounder traces

The basic survey methodology for the ISIS consists of parallel lines being run, with the spacings determined by the water depth and allowing for a data overlap of at least 20%. The data collection should be terminated at the end of each line, and not resumed until the vessel has fully rotated 180^0 and stabilised itself, if roll errors are to be minimised.

4.7. Conclusion

The high frequency ISIS sonar ultimately enables centimetre depth resolution on the seabed, from which a high-precision, detailed three-dimensional topographic map of the seabed can be constructed. It is important to remember that these topographic maps are made not of point reflectors, but from the small-scale insonified areas (measured in

centimetres to tens of centimetres) discussed in Chapter 6, and therefore the bathymetric data must be treated as an average reading from within each insonified area. The localised seabed slope angle measurements derived from the bathymetric data must also be treated as an 'average' measurement of the planar orientation of the insonified area. Although this averaging is inherent in all bathymetric systems, the ISIS suffers minimal loss of precision because it can accurately account for all the large and medium scale topographic variations, thereby eliminating the need for averaging the bathymetric values. The combination of the 234kHz sonar frequency, the focused beam shape, and the very high data sampling rate, minimise the dimensions of the insonified area itself, and reduce the roughness analysis to a grain or particulate scale (bed roughness).

The high resolution of bathymetry sets apart the sediment type classification methodology of the ISIS from the 'pattern recognition' methodologies employed by traditional side-scan sonars. This is because the ISIS can bathymetrically measure sedimentary features such as dunes and macro-ripples, which can only be classed as textures or patterns in other systems (discussed in detail in Chapter 3). In other words, the ISIS 100s' digital bathymetric resolution of bedforms (dunes, ripples, etc) enables the surface 'roughness' analysis to increase in resolution beyond the textural features to bed roughness.

As a result, the application of the ISIS 100 offers many benefits to sediment-acoustic research. Operating frequencies in excess of 100kHz provide high resolution bathymetric images of the seafloor, allowing the detection of micro-topographic undulations of only a few centimetres in height. The co-registering of acoustic amplitude with bathymetry enables the production of "side-scan" images that can be directly related to the bathymetric measurements in a spatial context.

The interferometric technique used by this system provides precise locations of each insonified patch (element point) as well as the ability to derive the angle of incidence of the acoustic wave with the water-sediment interface. This technique clearly allows the precise accountability of all the variables both within the sonar equation, and active upon the incident acoustic wave at the water-sediment interface.

In conclusion, the ISIS 100 234kHz sonar has been selected as the most suitable system to date for use in the advancement of remote seabed classification using acoustic techniques.

The next stage is to collect and analyse data both manually and digitally for cross-correlation, via digital data and sediment sample analysis.

CHAPTER 5:

DATA ACQUISITION

5.1. Introduction

One of the primary objectives of this research programme was to identify field sites that would optimise the quality of the datasets for analysis. Each potential survey location would have to satisfy the following criteria to achieve this status:

- **Shallow water (<20m)** – to maximise the insonified resolution at the water-sediment interface, and to minimise the risk thermal layering in the water column which can degrade the quality of the sonar data by refracting the acoustic signal.
- **Relatively flat (horizontal) bottom** – to minimise the impact of sediment surface undulations upon the angle of incidence (grazing angle) calculation, thus simplifying the relationship between the horizontal distance from the transducer and the angle of incidence with the seabed.
- **Readily identifiable areas of varying sediment type** – to enable survey lines to cross 'known' sediment boundaries, for direct comparisons of acoustic reflection variability.
- **Stable sediment type systems** – avoiding areas which may be susceptible to seasonal changes in sediment cover, e.g. estuaries, active coastal regions, rivers, etc.
- **Easily accessible / local site** – to enable repeat surveys at minimal cost.

The initial planning centred around the need for a 'test site' which would satisfy all of the above criteria. It was then anticipated that as the project progressed, so other sites

would be incorporated to permit a more universal application and assessment of the research findings. For this purpose, a collaboration with the University of St Andrews Archaeological Diving Unit (ADU) was initiated, offering the ADU access to high-tech geophysical survey tools in return for the use of a vessel in and around the British coastal waters. As a result of the dual-purpose surveys, all of the additional survey locations were to focus around historical wreck sites.

5.2. Loch Earn Survey

5.2.1. Introduction

Loch Earn was deemed to be the ideal 'local' location to host a 'laboratory test site' as much is already known of its sub-surface geology and geomorphology, through over 40 years of extensive research within the universities of St Andrews and Dundee.

Loch Earn itself is located in the heart of Scotland (Figure 5.1), very close to the Highland Boundary Fault, and is one of many lochs found within the Tay basin.

Figure 5.1 Map of Scotland showing location of Loch Earn.

It is situated within a steep-sided U-shaped valley of west-east orientation, carved out by Pleistocene glaciation (Al-Ansari, 1976), with the loch itself thought to have been a rock basin excavated by ice (Walker, 1963). The loch is essentially a basin of 10.5km in length and an average width of 1.2km, providing a surface area of roughly 8km^2 (Al-

Ansari, 1976). Although depths of up to 87m (Al-Ansari, 1976; Murray & Pullar, 1910) have been recorded in Loch Earn, the head of the loch is known to be relatively shallow (~20m) and flat – ideal for the purposes of this research.

5.2.2. Data Acquisition

The bathymetric-sidescan survey took place from the 9th-11th September 1997, and was managed by a two-man crew from Sage Survey Ltd, Bath, England, who utilised a specially designed survey-specific vessel, the Surveyor II, from Caledonian Geotech, Dundee. The survey methodology followed the code for industrial marine survey practice, as well as the system-specific survey criteria for the ISIS 100 (refer to Chapter 4 Section 4.6).

Initial plans to survey the entire loch using both the ISIS 100 and a traditional side-scan sonar had to be abandoned only hours after the survey commenced, with a skerry claiming the scalp of the side-scan tow-fish. This left the bow-mounted ISIS 100 as the only operational survey gear for the remainder of the survey – although that too suffered a heavy blow to the starboard transducer following a collision with another skerry on the first day.

The steep-sided valley also caused problems by rendering many areas *dead* in terms of DGPS coverage. In order to overcome this problem, a fixed GPS location was set up on the west shoreline of the loch, from which the relative movements of the boat could be monitored with precision.

In addition to the digital data acquisition, a day was spent surveying the shoreline of the loch. It was anticipated that a shoreline survey would reveal the active sedimentation and erosion patterns of tributaries and wave-action around the loch, thereby providing an insight into the 'expected' sediment types and topographic features that may be found at each submerged location.

The ground-truthing programme was delayed in order to incorporate the post-processed side-scan and bathymetric data within the design of the sediment sampling programme. The bathymetry was to be used to identify shallow, flat areas of loch bottom that may provide good test locations. The variations in reflection amplitude highlighted by the side-scan (Figure.5.5) were to be overlain upon the bathymetric chart, to highlight flat, horizontal areas on the bottom of the loch that had differing amplitudes of return. This procedure was included to help focus the ground-truthing analysis upon selected areas of the loch-bottom that reflected contrasting amplitudes of acoustic return.

Before the ground-truthing programme could take place, the post-processing of this dataset highlighted several factors that rendered the bathymetric and side-scan data useless.

5.2.3. Post-Processing

Upon post-processing the ISIS 100 data, it became apparent that the majority of the dataset was worthless in terms of scientific research.

One problem was that the poor GPS coverage had left large sections of vessel track-plot and swath coverage without positional co-ordinates.

Another was that the methodology employed for designing the survey route was fatally flawed. The track-lines of the vessel were set to run parallel to the shoreline of the steep-sided loch, resulting in the accentuation of the 'gap' in sonar coverage between the port and starboard swaths, as illustrated in Figure 5.2. This survey pattern created gaps of up to, and in excess of, 100m slope length between the port and starboard datasets. Also, because of the steep-sides of the loch, the coverage obtained by the shoreward facing transducer was minimal, while the other transducer was operating around the maximum survey range for the ISIS 100, as illustrated by Figure 5.2. This

problem was accentuated where the boat ran closer to the shoreline and in areas where the gradient of the loch-side increased.

Figure 5.2 Diagram illustrating the flawed survey technique employed in Loch Earn.

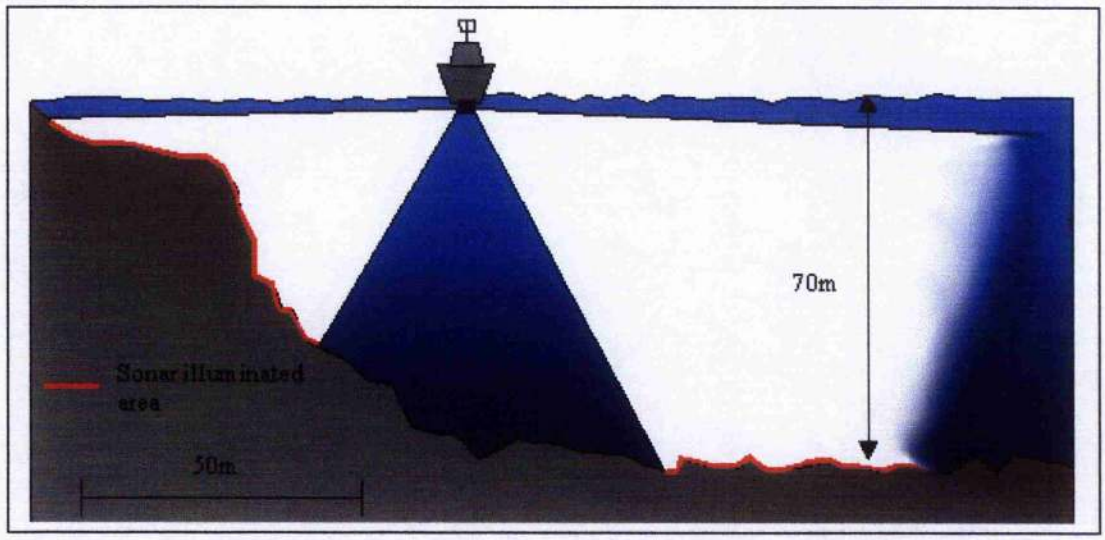

In addition to the above factor the MRU was also found to be faulty. This factor subsequently cast a cloud over the ability to precisely derive the three dimensional location of each reflection point, thereby causing major problems with data quality enhancement and data reduction. Despite this flaw in the survey methodology and the reduced data quality, it was still possible to produce 3-D charts of the submerged topography in Loch Earn (Figures 5.3 & 5.4) through the interpolation and smoothing of the 'good' bathymetric data. These images were generated by loading the XYZ file of Eastings, Northings, and depth, into a 3D graphics system called 'Fledermaus.'

The 3-D digital bathymetric map generated from eight swath survey lines was found to support the general bathymetric trends suggested by the 30 to 40 echo-sounder survey lines recorded by Al-Ansari in 1973 (Al-Ansari, 1976).

In contrast, there was no comparison in data density with the 500m spacing of Al-Ansari's echo-sounder depth profile recordings being surpassed by the depth profile (recorded by each ping from the transducer) spacings of less than 1m achieved by the ISIS 100.

Figure 5.3 **3-D image of the underwater terrain in Loch Earn looking eastwards down the loch from the mouth of the Beich Burn – constructed using Fledermaus.** The mouth of the Beich Burn is situated on the northern shoreline, approx. 2km east of the head of the loch.

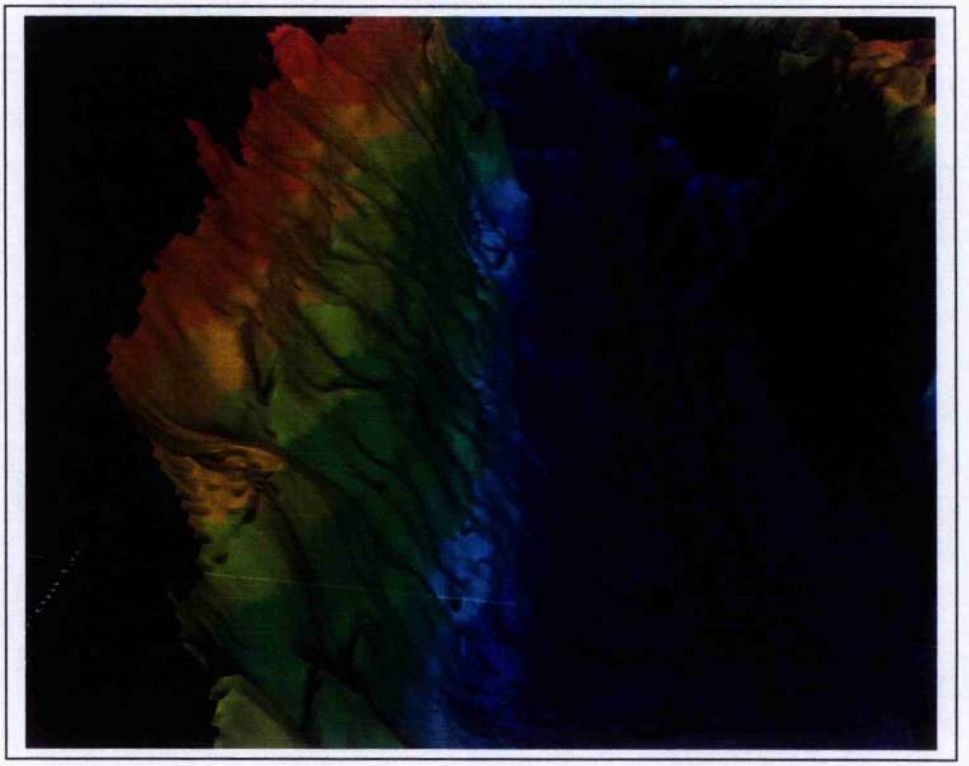

Figure 5.4 **3-D image of the steep loch sides on the northern shoreline of Loch Earn, slightly east of the mouth of the Beich Burn, constructed using Fledermaus.**

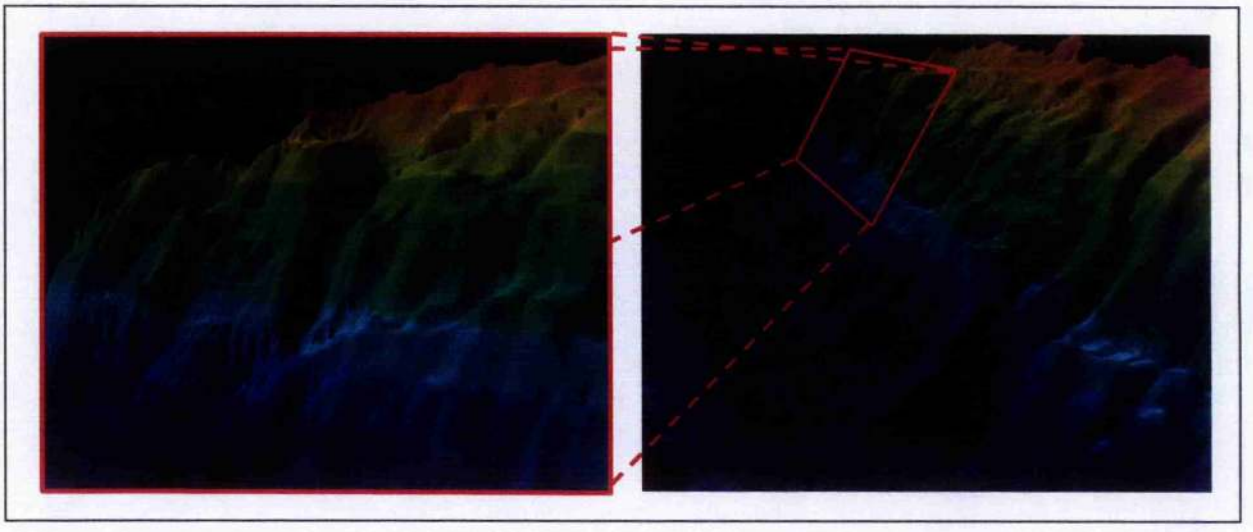

The ISIS 100 side-scan images also proved useful by locating several submerged ruins along the south bank of the loch (Figure 5.5), and highlighting areas of varying acoustic response which could have been revisited to collect sediment samples. The white

squares in Figure 5.5 mark the selected ground-truthing 'target' locations, which would have focused the sampling programme upon the variations in acoustic scattering amplitude.

Figure 5.5 Side-scan capture from the southern bank of Loch Earn

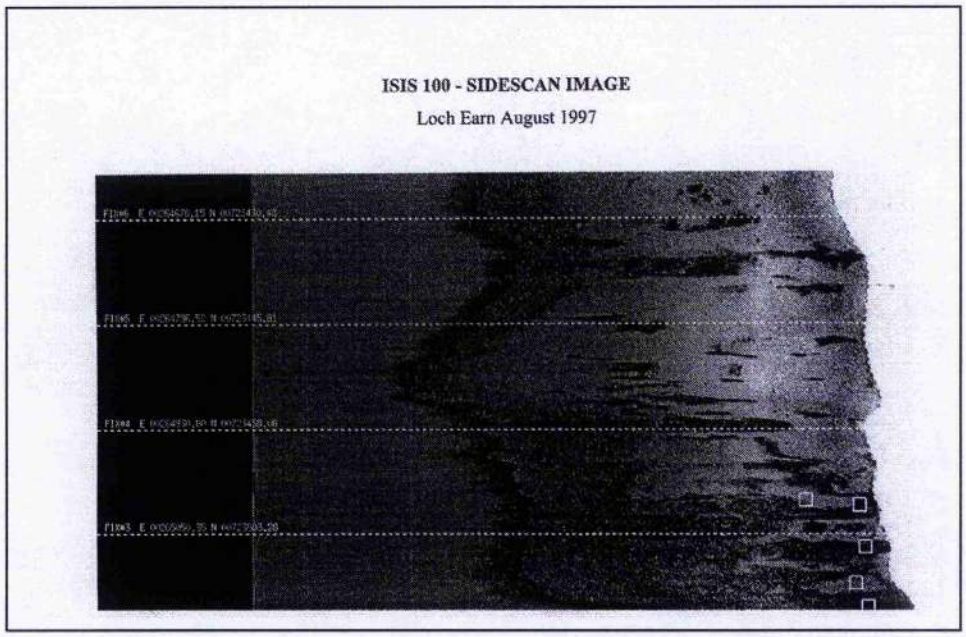

5.2.4. Summary

Although this survey did not provide the precision or accuracy sought in the sonar dataset for the analysis of the sediment-acoustic relationship, it did offer valuable field experience with regard to the installation and operation of all the survey equipment aboard the vessel, and a good induction into survey planning. The problems encountered also proved to be fruitful by generating an insight into;

(1) the critical factors which can affect the design of the sonar survey,

(2) the technique of setting up a local base station to cope with DGPS 'dead' zones, and

(3) the effects of roll, pitch, heave and yaw errors upon the quality of the ISIS data.

In addition, the post-processing of the datasets provided a valuable opportunity to evaluate the true effects of data processing upon the raw data quality.

Overall, the experience and additional understanding gained from this survey were used to refine the field techniques for future surveys.

5.3. Portsmouth coastal waters, Solent, South England

5.3.1. Introduction

In September 1998, the quest for a high quality dataset resumed, again in collaboration with the ADU. Operations at this late stage in the ADU's field season centred around the high density wreck zone of the Solent, South England (Figure 5.6).

Figure 5.6 Map showing general location of the Solent, Portsmouth (from the British Geological Survey map – Wight Sheet 50N 02W (SBS-Q)

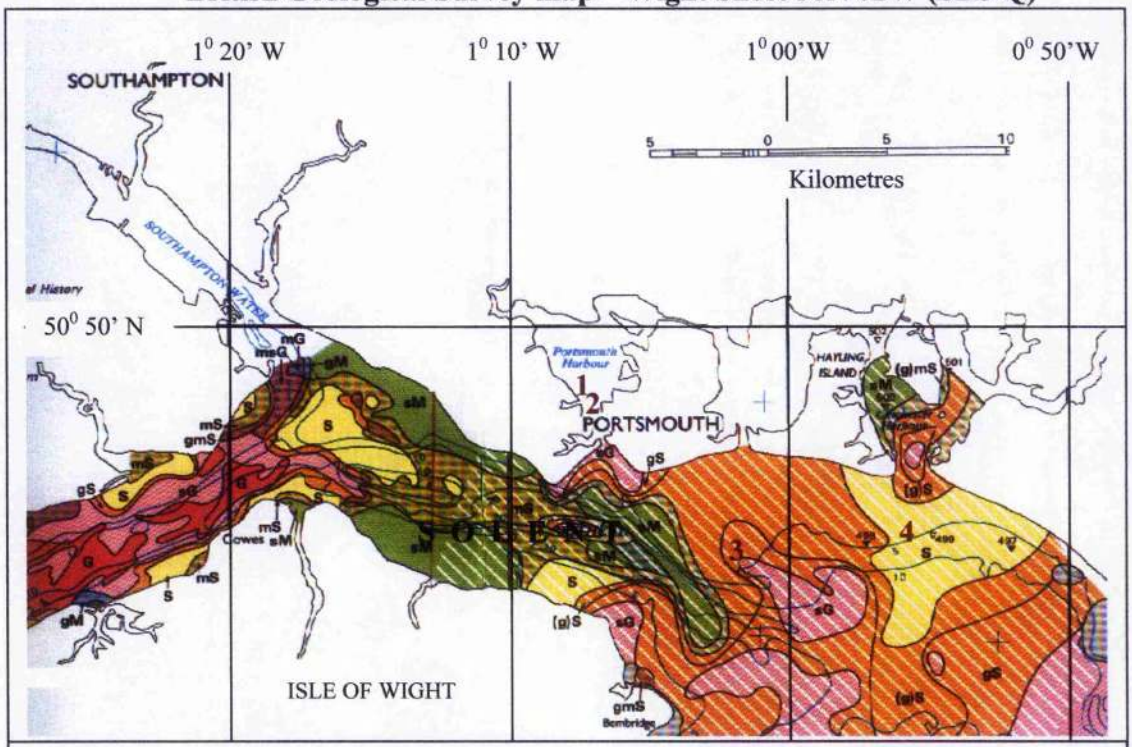

KEY 1 Calibration Site 2 Shingle Site 3 Invincible Site 4 A1 Submarine Site

M	- Mud	(g)mS	- slightly gravelly muddy Sand
sM	- sandy Mud	gmS	- gravelly muddy Sand
(g)M	- slightly gravelly Mud	gS	- gravelly Sand
(g)sM	- slightly gravelly sandy Mud	G	- Gravel
gM	- gravelly Mud	mG	- muddy Gravel
S	- Sand	msG	- muddy sandy Gravel
mS	- muddy Sand	sG	- sandy Gravel
(g)S	- slightly gravelly Sand		

The 2-day survey at Portsmouth focused upon a total of four separate survey areas, with two areas being covered each day. The four sites were accepted for inclusion in this research; (1) the 'Calibration' site, (2) the 'Shingle' site, (3) the 'Invincible' wreck site, (4) the 'A1 Submarine' site; due to their shallow, flat nature and the presence of

differing sediment types, all of which were discovered on previous archaeological surveys. The approximate locations of these survey areas are denoted by the relevant number in Figure 5.6. The shallowness of the sites reduced the margin of error in the depth calculations (and therefore in all other trigonometric calculations) and enhanced the insonified resolution, whilst the relative flatness of the sea bottom helped to simplify the angle of incidence analysis.

The vessel used for this survey was a twenty-five foot catamaran called the "Scimitar" (Figure 5.7), and hired by the ADU for the duration of the field season.

The basic survey methodology involved each area being extensively covered by ISIS 100 bathymetric swath data, and complemented by ground-truthed sediment samples, several CTD profiles, and tide level monitoring.

Figure 5.7 Photograph of the 'Scimitar' catamaran used during the Portsmouth site surveys

5.3.2. Sonar, Positional and Environmental survey methodology

The ISIS 100 was used in the acquisition of bathymetric and side-scan data over the Portsmouth survey sites. This was complemented by the careful collection of the positional and environmental datasets in order to optimise the resolution and precision of the ISIS 100. In accordance, this section will detail the ISIS 100 site survey methodology, and the methods used in collecting both tide and sound velocity data for inclusion in the digital data processing.

The side-mounting technique was used to install the pole-mounted ISIS transducers onboard the Scimitar because bringing the transducers closer to the processing hardware enabled the GPS receiver to be fitted directly to the top of the pole. This eliminated the error margins involved in the manual measurement of the northings and eastings offset between the GPS receiver and the transducers. The vertical offset still had to be carried out manually to measure the depth of the transducers below the water surface (T_D). This measurement returned values of 1.38m for the Calibration and Shingle sites, and 1.48m for the Invincible and A1 Submarine sites, with the difference being attributed to the redeployment of the transducers on the morning of the 24th September. It is recommended that this measurement should be carried out at the beginning and end of each survey, as the transducer depth below the water level is susceptible to buffeting of the hardware and the pole-mount itself, and also to changes in the ride height of the vessel.

The high precision DGPS data required by this survey was provided by a Racal 'Landstar' system (See Chapter 4 section 4.3.1). The World Geodetic System 1984 (WGS 84) was used as the default datum for the DGPS receivers. All of the DGPS data was recorded in metric using the Universal Transverse Mercator (UTM) system, and more specifically, the UTM zone 30U with a Central Meridian of 2^0W.

In order to coincide with the reference data on British Ordnance Survey maps, these UTM co-ordinates were converted into National Grid co-ordinates by applying the Ordnance Survey's National Grid Transformation OSTN97 which is incorporated within the ISIS software package. This conversion process reworks the UTM co-ordinates based upon the false origin of the National Grid which lies 400km West and 100km North of the true UTM origin of 2^0W 49^0N. This metric conversion of locational data enhanced the precision of the survey data for the reasons discussed in Chapter 4, and generated the National Grid lines displayed in Figure 5.8.

Figure 5.8 Portsmouth survey area overlain with National Grid gridlines

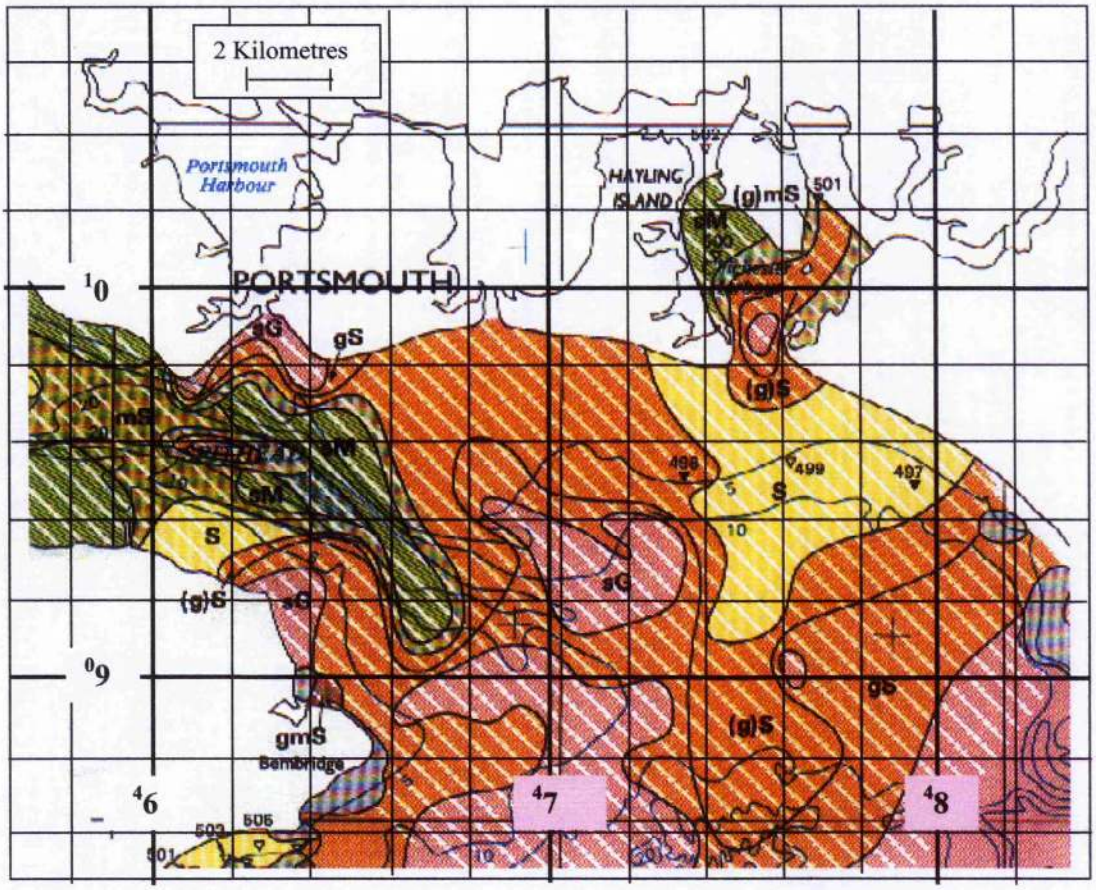

The tide levels were derived by obtaining real-time measurements received from the Portsmouth Harbour Authority at the beginning and end of each survey run, and using the prediction curve of the 'Tide-plot' software programme to interpolate the tide level for the duration of each survey. Figures 5.9 and 5.10 illustrate the tide height trends recorded and interpolated for each of the Portsmouth survey sites.

A CTD probe was used to record the environmental factors of temperature and salinity relative to water depth, and to generate an accurate sound velocity profile through the water column based upon the environmental conditions. One set of measurements was carried out within the Portsmouth harbour site, and applied to both the Calibration and the Shingle sites, because of their close proximity to each other.

Figure 5.9 Tide plot for the Calibration & Shingle survey sites (23-09-1998)

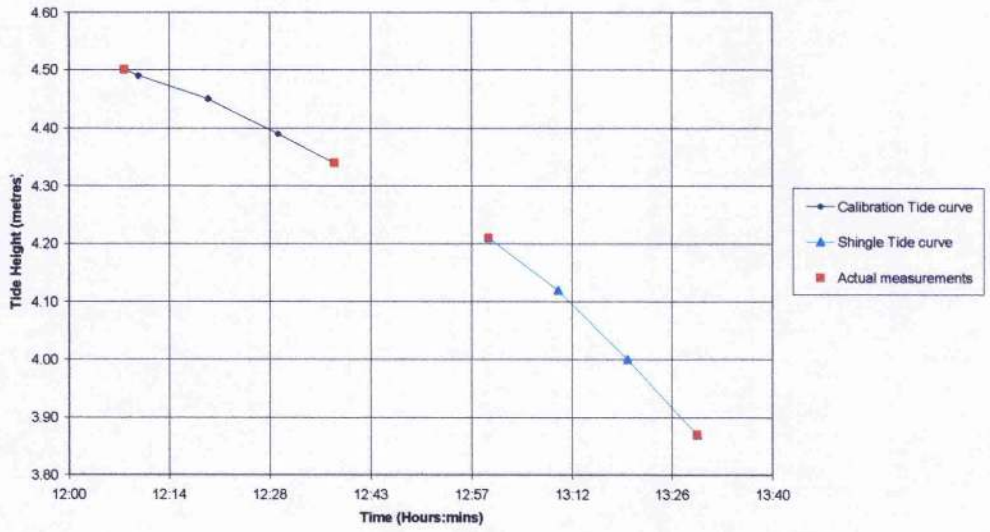

Figure 5.10 Tide plots for the Invincible and A1 Sub survey sites (24-09-1998)

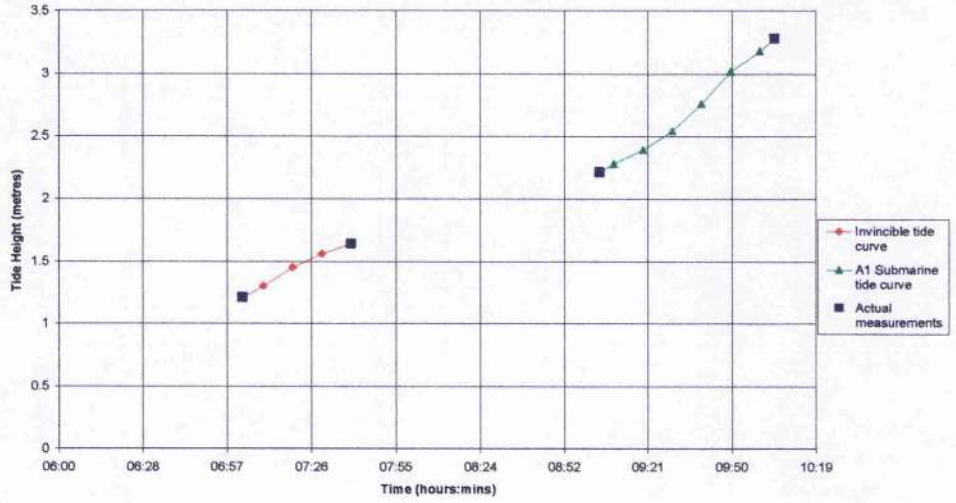

The other set of measurements was recorded mid-way between the Invincible and the A1 Submarine sites and these results were applied to both sites. The resultant temperature, salinity and sound velocity profiles can be seen in Figures 5.11, 5.12 and 5.13, respectively.

Figure 5.11 Temperature profiles recorded by the CTD probe for the Portsmouth survey sites

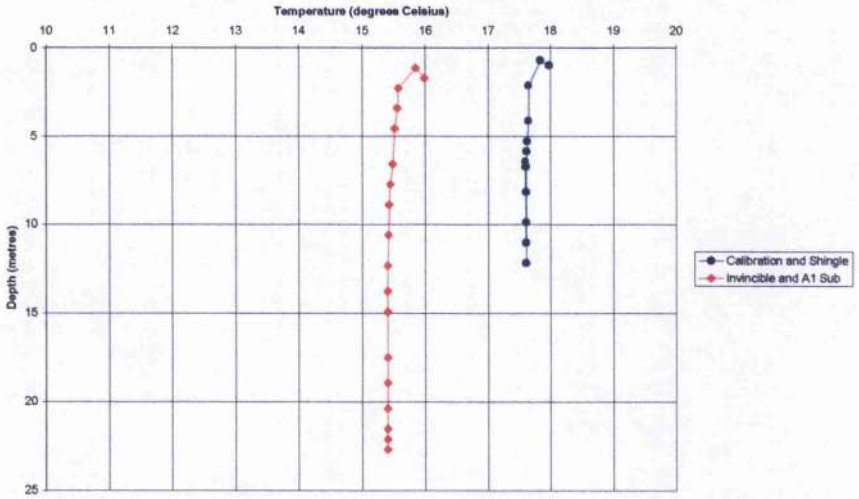

Figure 5.12 Salinity profiles recorded by the CTD probe for the Portsmouth survey sites

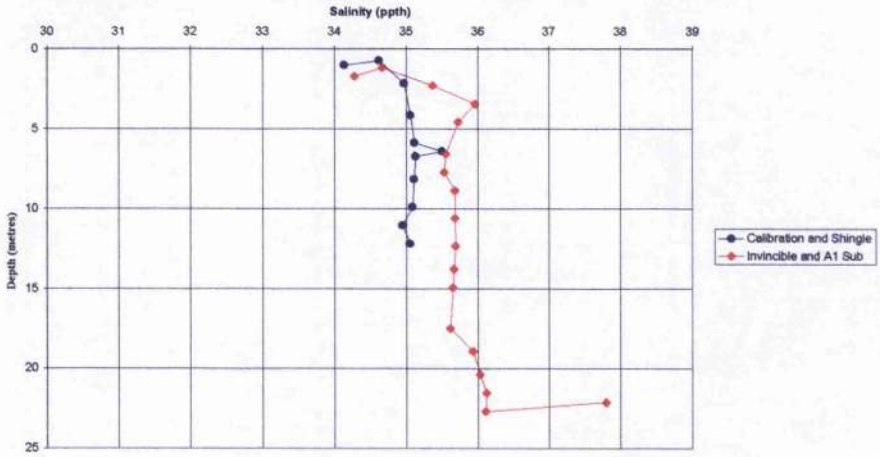

Although these sound velocities were calculated automatically by the CTD probe, they may also be regenerated by entering the temperature, salinity and depth values into Medwin's (1975) equation for the speed of sound in water (refer to Chapter 4).

Figure 5.11 shows that, as expected, the sheltered harbour area had a higher temperature profile than the open waters of the Invincible and A1 Submarine site. The lower salinity concentrations found in the harbour area (Figure 5.12) can be attributed to the fact that the harbour is built upon an estuarine system.

Figure 5.13 Sound velocity profiles recorded by the CTD probe for the Portsmouth Survey Sites

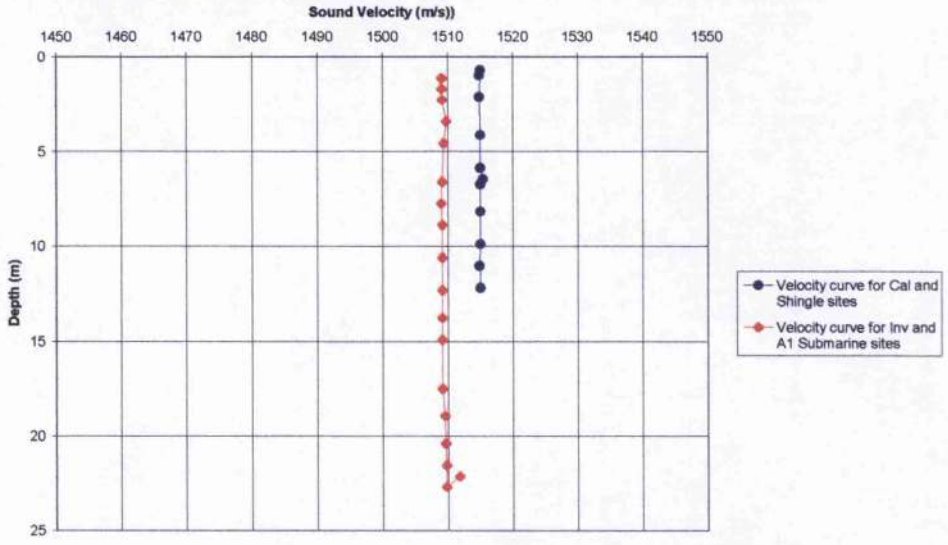

The resultant sound velocity profiles in Figure 5.13 suggest that the sound velocity is more sensitive to changes in temperature than salinity, thereby giving a sound velocity of 1514ms^{-1} for the harbour area compared to 1509ms^{-1} for the open waters of the Invincible and A1 Submarine sites. This finding is supported by Medwins' speed of sound in water equation (Chapter 4 section 2.3).

5.3.3. Sediment sample (ground-truthing) acquisition methodology

5.3.3.1. Introduction

In consideration of the nature of the acoustic analysis described in Chapter 2, and given the high frequency of the sonar system (Chapter 4), the analysis of the seabed sediments must focus upon only the surficial deposits. The sampling technique selected must therefore be one that facilitates the recovery of the surface layer of sediments with minimal disruption or mixing of the sample. Ideally, this sampling would be carried out at times when the sediments are exposed by low tides. As this was not an option in the off-shore areas surveyed, a methodology for sampling from a vessel had to be found.

5.3.3.2. Review of Grab Sampling techniques

Grab samplers in general operate by being attached to a rope and manually lowered to the seabed in an 'open' position. Upon impact with the seabed, the jaws sink into the sediment and the hinge releases, allowing the jaws of the grab to be pulled 'closed' within the sediment layer as retrieval begins.

In their review of grab samplers, Buller and McManus (1979) state that the van Veen (Figure. 5.14) grab is probably the best suited to shallow marine sampling because;

- It forms a tighter seal than that of the Petterson grab thereby enabling it to retain a larger portion of the fine particles; and,
- It is far less susceptible to premature or accidental release of the trip mechanism than the Shipek grab, making it safer and more reliable for operations upon a small vessel.

Although the Shipek grab is regarded as a more effective method for sampling coarser sediments such as gravel, the additional feature of teeth on the jaws of the van Veen grab greatly enhances its ability to sample gravels, and to penetrate and cut through closely packed sandy bottoms (Lees *et al* 1969).

An additional feature of the van Veen grab, which makes it ideal for this analysis, is the presence of inspection/observation ports. These inspection ports are located on the flat top of the sampler bucket, enabling the inspection of sediment surface structures and sampling of small cores before release of the sample (Buller and McManus, 1979). The ability to make visual observations of the surface sediment structures was further enhanced by the use of the underwater video equipment by divers during the archaeological dives. This enabled the sediments obtained from the grab sampler to be visually compared to those found *in-situ* on the sea floor (Figure 5.20).

Figure 5.14 Photograph of the 'van Veen' grab sampler (from Buller & McManus, in Dyer 1979)

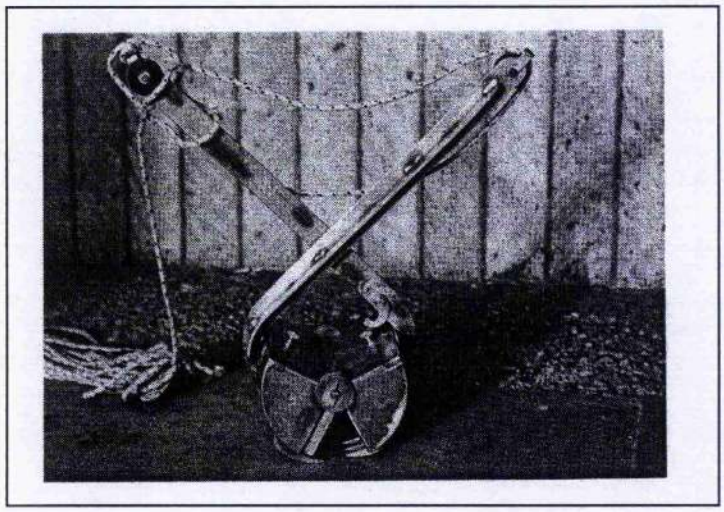

In summary, the 'van Veen' sampler was selected for use in this programme following the advice of Buller and McManus (1979) and Lees, Buller and Scott (1969).

5.3.3.3. Refined Sediment Sampling

As this project is focused upon the sediment-acoustic relationship within the sediment crust, it is crucial that the sediments analysed come only from the surface and 'very near-surface' (0-10mm). This depth limitation was placed upon the sediment collected because although the van Veen grab is regarded as a surface sampler, the analysis of the full body of sediment retrieved would provide an average assessment of the volume properties of the sediment to a depth of between 0 and 15cm.

The refined collection of surface sediment samples was achieved by utilising the inspection hatches on the van Veen grab, to extract only the upper 10mm of the sample including surficial materials with a pallet knife, prior to emptying the grab bucket. This technique enabled sampling of the very near-surface sediments in as close to an *in-situ* state as possible, and also permitted the inclusion of random surface inhomogeneities such as shell fragments and clay nodules.

The skimmed samples were then placed straight from the pallet knife into a plastic test tube, and sealed airtight. Notes were also taken of the general appearance of the sediment surface and the distribution of any features or anomalies. These test tube samples were placed in a cold storage unit upon returning to the University, to inhibit both anaerobic and aerobic activity within the sampled materials.

5.3.3.4. Portsmouth Grab Sampling Programme

Sediment sampling was carried out following the swath sonar survey, in order to permit any variations in backscattering amplitude of return (independent of changes in relief) to be 'tested' for changes in sediment properties. Where backscattering amplitudes appeared to be relatively uniform, the sampling program was carried out at random intervals within the surveyed site. The practice of creating a gridded sampling program proved arduous due to tidal influences and light-moderate winds moving the vessel.

The locational precision of the sampling program is critical to the correlation between the digital and ground-truthed data, and as a result the following steps were taken to maximise the ground-truthed precision;

(1) A heavy duty van Veen grab was used to give a near-vertical line of descent, in spite of the effects of the current and the drifting of the vessel

(2) the van Veen grab was rapidly lowered to the seabed directly beneath the GPS antenna to prevent any locational errors being induced by the offset calculations.

(3) The ground-truthing was confined to shallow water sites (>10m deep), again to minimise the time of descent, thereby reducing the effects of the current and drift.

Despite the positional error margins being minimised, an allowance must still be made for the positional inaccuracies induced by the remote sampling technique, as well as for the error margin of the DGPS data. Thus an ample error margin of ±1m has been applied to the Eastings and Northings co-ordinates of each sample location.

5.3.4 Data Acquisition

5.3.4.1. Calibration Site

On the 23rd September 1998, an attempt to survey the former resting place of the ***Mary Rose*** was cut short due to inclement weather and the vessel returned to the quieter waters of the harbour to carry out the calibration procedure for the ISIS 100, as described in Chapter 4 section 4.6. This area formed the first complete dataset for the project. Within the quiet, shallow lateral waters of the Portsmouth harbour system, the vessel carried out a full calibration run for the ISIS 100, as well as retrieving four samples of seabottom sediment from random locations (Figure 5.15)

From existing chart data this area was known to have a relatively flat, silt-mud seabed, with an average water depth of 12m, making it an ideal location for the analysis of the relationship between acoustic backscattering and very fine-grained sediments.

The Calibration dataset comprised of four survey lines (Cal1 – Cal4) of approximately 100m in length, running parallel to each-other, but alternating North-South and South-North (Figure 5.16). The line spacing was set to provide 100% overlap of Port-Port and Starboard-Starboard data, as is required for the systems calibration (See Chapter 4).

The ISIS 100 was run using power setting 3 (Table 4.2) to enhance the bathymetric data quality and to prevent acoustic saturation of the water column, as induced by the full power setting. The transducers were measured to be 1.38m below the water level when side-mounted. A surface water temperature reading of 18.8^{0}C was also taken as a form of cross-check with the CTD measurements.

Figure 5.15 Close-up of sample locations at the Calibration and Shingle sites

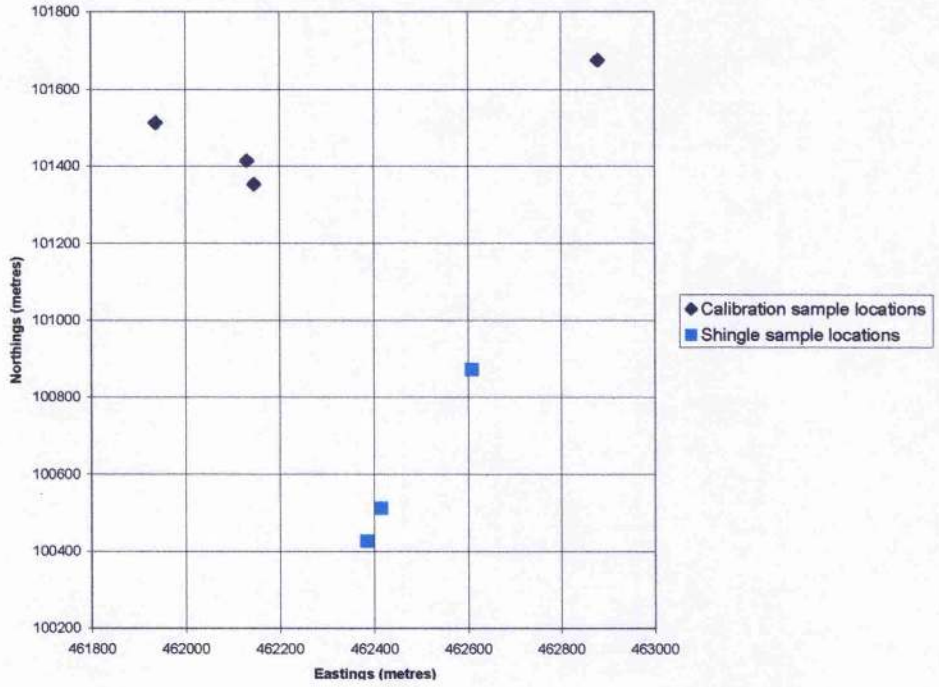

Figure 5.16 Basic schematic of track plots for the Calibration site

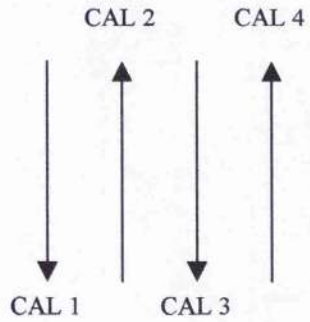

5.3.4.2. Shingle Site

This site was selected because according to local shipping charts, it contained patches of shingle. The vessel tracked laterally across the harbour, in water depths of up to 20m, in an attempt to survey areas of *shingle.* It was hoped that this area, close to that of the calibration site, would provide the necessary data for the upper limits of the analysis, between acoustic backscatter and coarse-grained sediments. However, several problems were encountered within this site. Firm track plots could not be used here due to difficulties encountered by the crossing of shipping channels. In addition, it proved very

difficult to carry out ground-truthing as the Harbour Authority was not keen to permit any vessel to stop within the shipping lanes. Although several attempts were made to collect sediment samples from areas where the side-scan imagery suggested a contrasting change in reflectivity, only three grab samples were successfully recovered. The limited success rate of sample returns suggests that the bottom material may have been too coarse for the grab to penetrate and encapsulate, and thereby infers the presence of shingles or gravels. The locations of these samples can be seen in Figure 5.15.

The shingle site was surveyed using continuous lines tracking across the shipping channel in search of areas of shingle. However, due to the stop-start nature of the survey (to accommodate grab sampling) the overload of data necessitated the splitting of swath lines. In error, no note was taken of changes in power settings during this run and therefore the processing of this data becomes difficult. However, some use may still be made as it is known that only Power settings 3 and 4 were used in this area, to compensate for the deeper waters.

Here also, the transducer remained in the same side-mount position set at 1.38m below the water surface, and the surface water temperature remained at 18.8^0C.

5.3.4.3. Invincible Site

The Invincible (originally L'Invincible), a 74 gun third rate, was captured from the French in 1747, and lost in 1758. In 1979, the wreck was located at the Horse Tail, East Solent; Grid Ref 50^0 44.34'N., 01^0 02.23'W. (Archaeological Diving Unit, 2000)

Previous dives by the ADU had identified this area as a shallow (approx. 6m below sea level), flat, sandy environment. This site was selected in order to provide data for the analysis of acoustic backscatter from medium-grained seabed sediments.

Four broadly spaced lines were run in an east-west orientation to delimit the wreck site, followed up by another three lines run in-between the first four to enhance the data quality and overlap data.

Four samples of ground-truthed data were taken from in and around the wreck site (Figure 5.17), taking special care to avoid debris from the wreck itself. This was further complemented by the additional collection of three sediment samples by divers on-site.

Figure 5.17 Sediment sample locations at the Invincible wreck site

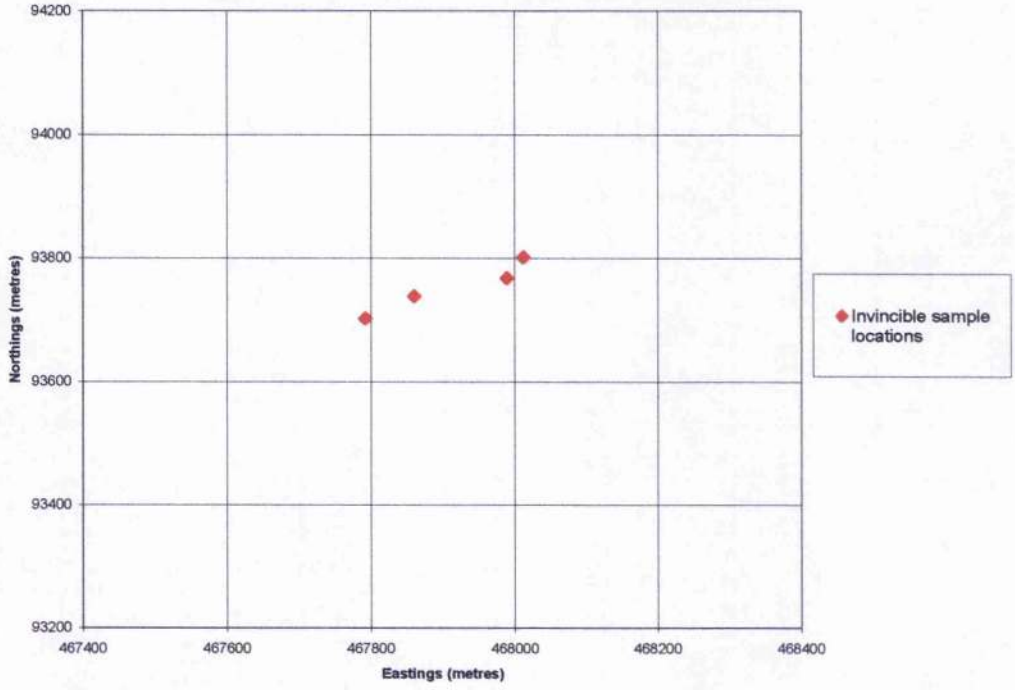

The swath coverage of the Invincible site consisted of a total of seven traverses in an east-west orientation (Figure 5.18). Initially four traverses were run in an effort to delimit the Invincible site. Once the site was defined, three more survey lines were added in between the first four to cover the gaps directly beneath the vessels first four runs.

A power setting of 2 was used throughout the majority of the survey, although at ping 1000 INV003 was reduced to power setting 1 due to acoustic saturation. It remained at one for the first part of INV001 before being increased to power setting 2 at ping 1100.

Figure 5.18 Basic schematic of track plots for the Invincible site

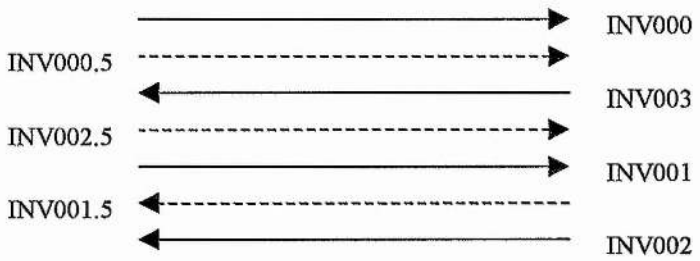

For the Invincible site the transducer set-up was unintentionally increased to 1.48m below water level, as a result of having to re-assemble the equipment at the start of the second day.

Surface water temperatures of 19.2^{0}C were recorded for cross-checking with the CTD data.

5.3.4.4. A1 Submarine Site

Designed by Captain Reginal Bacon DSO, and commisioned in 1903, the HM A1 Submarine was one of the first submarines to see active service for the British Navy. Following a less than impressive service: sunk with all hands during exercises on 18th March 1904; raised on 18th April 1904; damaged by explosion whilst moored at floating docks in 1910; vanished whilst running submerged automatically (no crew on board), as a target for torpedo practice in 1911 - but no trace of the submarine could be found. However, in 1989 a local fisherman stumbled across the wreck lying in 10m of water in Bracklesham Bay, Eastern Solent: Grid Ref; 50^0 44.52'N., 00^0 55.19'W.

(Archaeological Diving Unit, 2000)

The A1 submarine was known by the ADU to be situated in approximately 10m of water, and overlying compact sediments consisting of silty-sands and some areas of dead shell assemblages. Although the submarine had come to rest against a ridge, the surrounding area was known to be flat.

Again, four primary lines were run alternating east-west and west-east, with the addition of four cross-lines running south-south-west to north-north-east. These cross-lines were

run in order to gain data from enough aspects to permit a three dimensional image of the submarine to be created. Five ground-truthing sediment samples were collected in a grid-like pattern around the wreck (Figure 5.19). As in the Invincible site, the ground-truthing programme was enhanced by three sediment samples retrieved by divers from in and around the wreck (Figure 5.20).

Figure 5.19 Sediment sample locations at the A1 Submarine wreck site

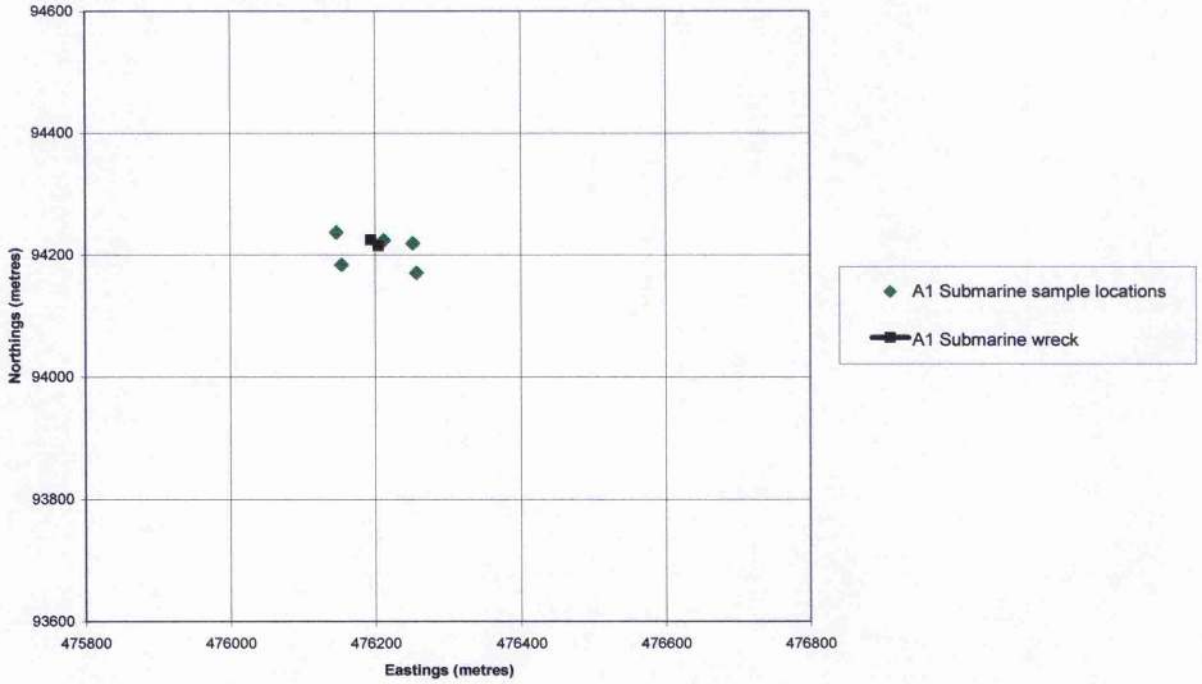

Figure 5.20 *In-situ* sediment sampling by divers on the A1 Submarine site (courtesy of ADU)

The swath coverage for the A1 Submarine site consisted of four main traverses complemented by three cross-lines designed to aid the creation of a 3-D image of the submarine using the depth soundings (Figure 5.21).

Figure 5.21 Basic schematic of track plots for the A1 Submarine site

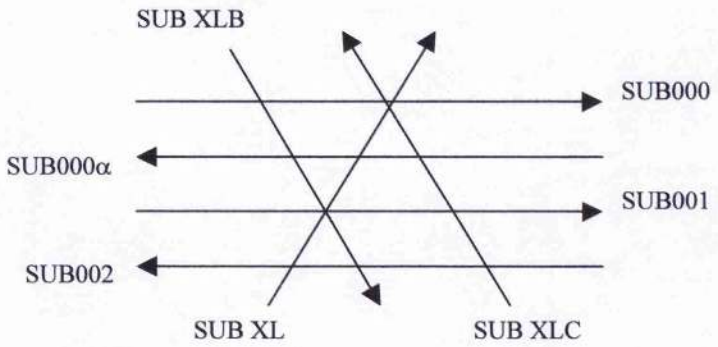

In two-dimensions the submarine was clearly visible (Figure.5.22) but in an attempt to create a comprehensive three-dimensional image of the vessel, the ISIS survey pattern traversed the target from several different aspects.

A power setting of 4 was used throughout this site survey to maximise swath coverage. Also, the transducer depth below the water level was unaltered from the Invincible site survey, remaining at 1.48m. The surface water temperature of 19.1^{0}C also showed very little variation from the Invincible site.

Figure 5.22 Real-time waterfall image and shaded bathymetric relief over the A1 submarine wreck.

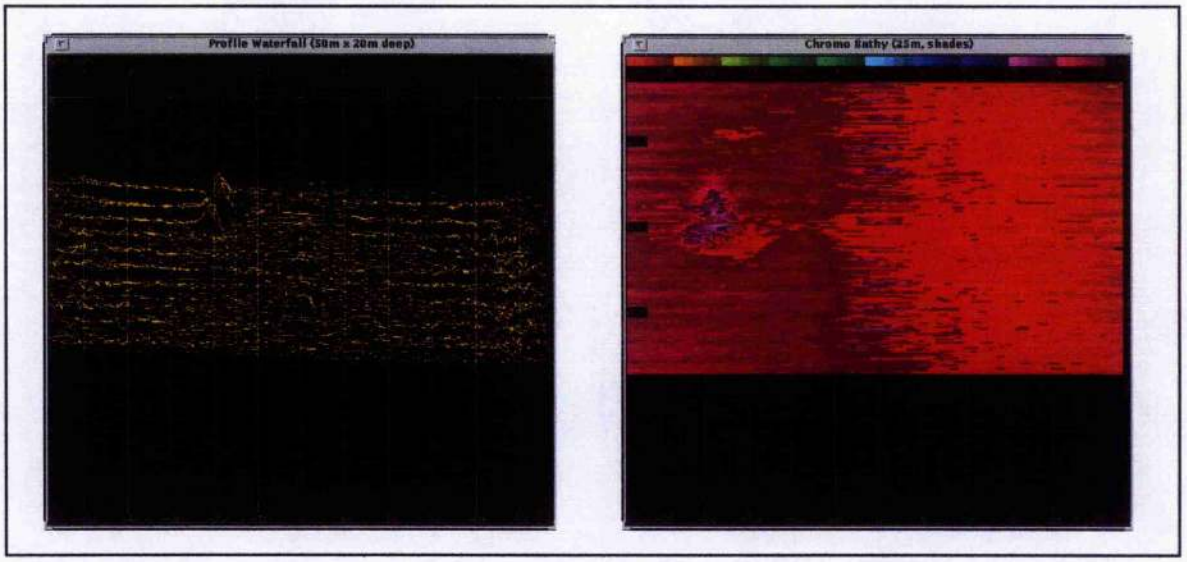

5.4. Post-survey evaluation of raw digital swath data coverage over actual ground-truthed locations

The most reliable data for the acoustic-sediment analysis is found in the immediate vicinity of the grab samples, the locations of which are summarised in Table 5.1.

Table 5.1 Summary of ground-truthed locations (accurate to ±1m) expressed in National Grid co-ordinates

Name of Sample Site	Sample No.	Sample Locations	
		Eastings (m)	Northings (m)
Calibration	1	461937	101513
	2	462146	101353
	3	462879	101676
	4	462131	101414
Shingle	5	462609	100871
	6	462415	100512
	7	462385	100426
Invincible	8	468012	93802
	9	467860	93738
	10	467792	93702
	11	467989	93768
	20	Sampled *in-situ* by divers.	
	21	Taken from the immediate	
	22	vicinity of the wreck site	
A1 Submarine	12	476154	94184
	13	476252	94219
	14	476257	94171
	15	476147	94237
	16	476212	94224
	17	Sampled *in-situ* by divers.	
	18	Taken from the immediate	
	19	vicinity of the wreck site	

The raw* swath files were reduced to manageable sizes by focusing upon a 30m square area around each grab sample location. This raw data reduction process was carried out using an 'element location filter' that extracted only those elements within $\bar{1}$5m of the sample locations northings and eastings. This filtering process is addressed more detail in Chapter 6 section 6.3.2.

(*It should be noted that the data files were 'raw' in terms of the post-processing, but that it had already been subject to a 'suppress zero weightings' filter applied by the Swath Converter Program to eliminate data points which exceed the pre-determined selection criteria for ISIS 100 bathymetric data (See Chapter 6, Section 6.2.2)).

This filtering successfully reduced the digital swath files to a manageable, but still very substantial, size as shown in Table 5.2.

Table 5.2 Digital Data Density within 30m x 30m square surrounding each sample location

Sample Number	Name of Survey Site	Limits of Digital Sample Zone				Data Coverage No. of Elements
		Max_E	Min_E	Max_N	Min_N	
1	Calibration	461952	461922	101528	101498	24161
2	Calibration	462161	462131	101368	101338	15584
3	Calibration	462894	462864	101691	101661	0
4	Calibration	462146	462116	101429	101399	38801
5	Shingle	462624	462594	100886	100856	126992
6	Shingle	462430	462400	100527	100497	103875
7	Shingle	462400	462370	100441	100411	23770
8	Invincible	468027	467997	93817	93787	3749
9	Invincible	467875	467845	93753	93723	15820
10	Invincible	467807	467777	93717	93687	11444
11	Invincible	468004	467974	93783	93753	46861
20,21,22	Invincible	467972	467872	93777	93677	268589
12	A1 Submarine	476169	476139	94199	94169	51874
13	A1 Submarine	476267	476237	94234	94204	91677
14	A1 Submarine	476272	476242	94186	94156	65939
15	A1 Submarine	476162	476132	94252	94222	59595
16	A1 Submarine	476227	476197	94239	94209	91478
17,18,19	A1 Submarine	476224	476184	94235	94195	152579

Table 5.3 Table showing the digital data coverage of sample locations in relation to individual swaths

Grab Sample Number	Name of Swath File	No. of Elements	Swath file Size (kB)
1	CAL 2	24161	2886
2	CAL 2	9252	1082
2	CAL 3	6332	762
4	CAL 2	23258	2712
4	CAL 3	15097	1806
4	CAL 4	446	53
5	Shingle 1	126992	14699
6	Shingle 4	103875	12200
7	Shingle 4	23770	2713
8	Inv 000	1272	145
8	Inv 001.5	21	2
8	Inv 005	2456	278
9	Inv 000	19	2
9	Inv 001.5	6810	774
9	Inv 002.5	8568	943
9	Inv 003	403	46
9	Inv 005	20	2
10	Inv 002.5	4365	488
10	Inv 003	7079	799
11	Inv 000	16200	1842
11	Inv 001.5	14558	1632
11	Inv 002.5	4	0.5
11	Inv 005	16099	1822

Grab Sample Number	Name of Swath File	No. of Elements	Swath file Size (kB)
12	Sub 000	984	113
12	Sub 001	12738	1451
12	Sub 002	22377	2531
12	Sub xlb	15775	1826
13	Sub 000	36993	4236
13	Sub 001	21405	2394
13	Sub 002	202	23
13	Sub xl	18961	2145
13	Sub xlb	836	95
13	Sub xlc	13280	1494
14	Sub 001	14743	1673
14	Sub 002	14894	1670
14	Sub xl	11405	1285
14	Sub xlb	15917	1807
14	Sub xlc	8980	1033
15	Sub 000	33272	3766
15	Sub 001	15570	1749
15	Sub xlb	10753	1224
16	Sub 000	30399	3463
16	Sub 001	23167	2579
16	Sub 002	33	4
16	Sub xl	4976	566
16	Sub xlb	21688	2461
16	Sub xlc	11215	1287

The exceptionally high level of coverage in samples 17, 18 and 19, and in samples 20, 21 and 22, is due to the fact that these samples have been taken from the immediate vicinity of the wrecks which were obviously the focal point of each survey site. The overall coverage of digital data has also been further quantified by reducing the above figures to the swath file component level, as tabulated in Table 5.3.

Examples of the density distribution of the raw swath data, relative to the sample locations and vessel track-lines, are illustrated in map form by Figures 5.23 to 5.30. These distribution maps clearly show the exceptionally high bathymetric data density achievable using the ISIS 100, with each line of elements representing the across-track profile of only one acoustic ping. As these figures show, this dense data coverage produced a 'blanket' effect over the majority of sample sites. The combination of the comprehensive sonar coverage and a very high degree of bathymetric resolution enables a full and precise accountability of the seabed surface topography variables present within the sediment-acoustic relationship.

The analysis of the spatial distribution, attitude, and relative lengths of the ping lines can also demonstrate the effects of vessel motion upon the acoustic ping. The elements plotted in Figure 5.23 show the spatial relationship between ping profiles that can be expected in laboratory conditions, or given a flat, clam sea surface, with the profiles running consistently parallel to each-other, and propagating perpendicularly to the vessels track-plot.

The variation in the spatial distribution of the ping profiles evident in Figure 5.28 and Figure 5.29 is the result of the vessel pitching, and causing the transducer to periodically send pings forwards and then backwards relative to the vessels position. The variation in the attitude or angle of propagation is caused by the yaw motion of the

vessel, and is characterised by the ping spacing either increasing ('fanning') or decreasing ('converging') with distance.

The element distribution for Inv001.5 plotted in Figure 5.25 illustrates the effect of the 'rolling' motion of the vessel, by showing variations in the range or length of successive pings. For example, when the port side of the vessel is rotated upwards, the port ping range shows an increase in the range of the data.

Figure 5.24 provides a very clear illustration of the impact upon data density, caused by a large reduction in vessel speed, and also a large swing in the vessels heading and direction of movement. The red line represents the track plot of the vessel as it slows down on approaching a sample location, resulting in the high density of the black elements. Whilst the sample is collected and documented, the current rotates the vessel and begins to carry it South West along the blue line. The continual collection of ISIS data results in high density repeat coverage represented by the grey elements.

Figure 5.23 **Illustration of raw data density within 30x30m^2 of sample location 2 in the Calibration survey area, and including vessel track plot and direction of movement**

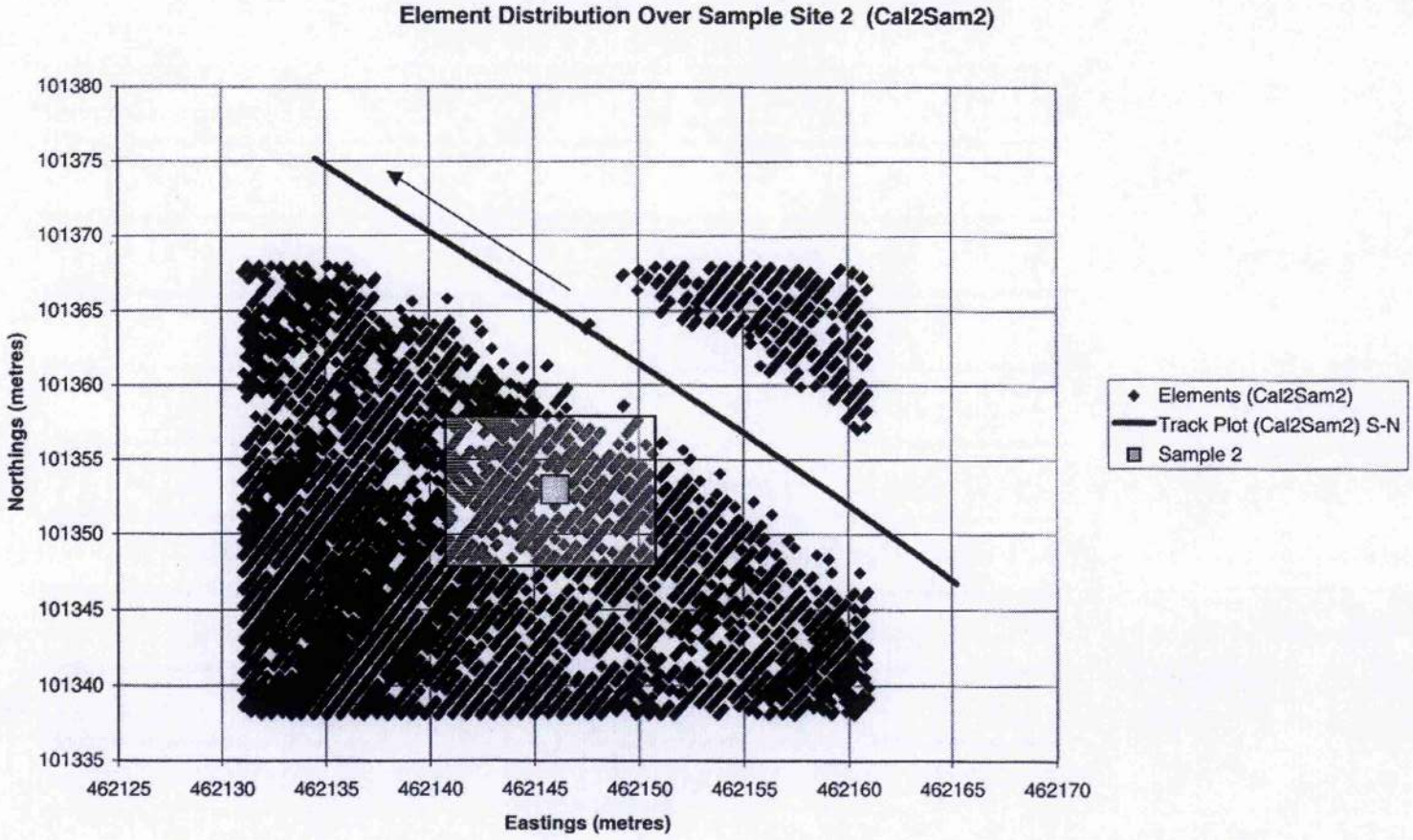

Figure 5.24 **Illustration of raw data density within 30x30m^2 of sample location 5 in the Shingle survey area, and including vessel track plot and direction of movement. Due to the data limitations of Microsoft Excel, this plot has been restricted to 64000 element locations (32000 from the vessels forward motion (in black) and 32000 from the vessels reverse motion (in grey) caused by drifting). The complex track plot results from the vessel halting to permit grab sampling. At the end of the red line, the vessel stops and begins rotate clockwise from a West heading to a North-East heading. The vessel then drifts backwards in a South West direction due to the current within the harbour channel.**

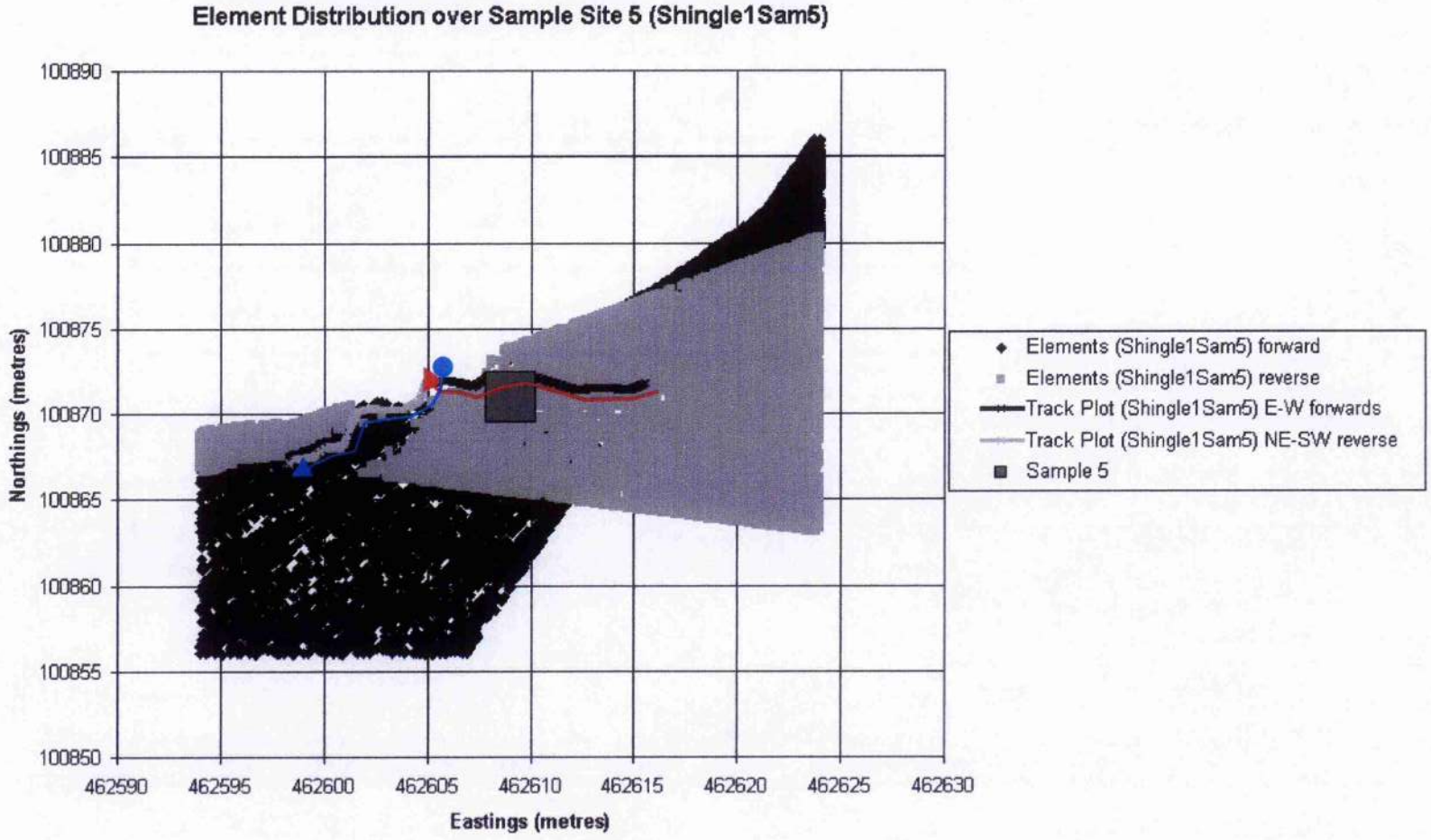

Figure 5.25 **Illustration of raw data density within 30x30m^2 of sample location 11 in the Invincible survey area, and including vessel track plot and direction of movement**

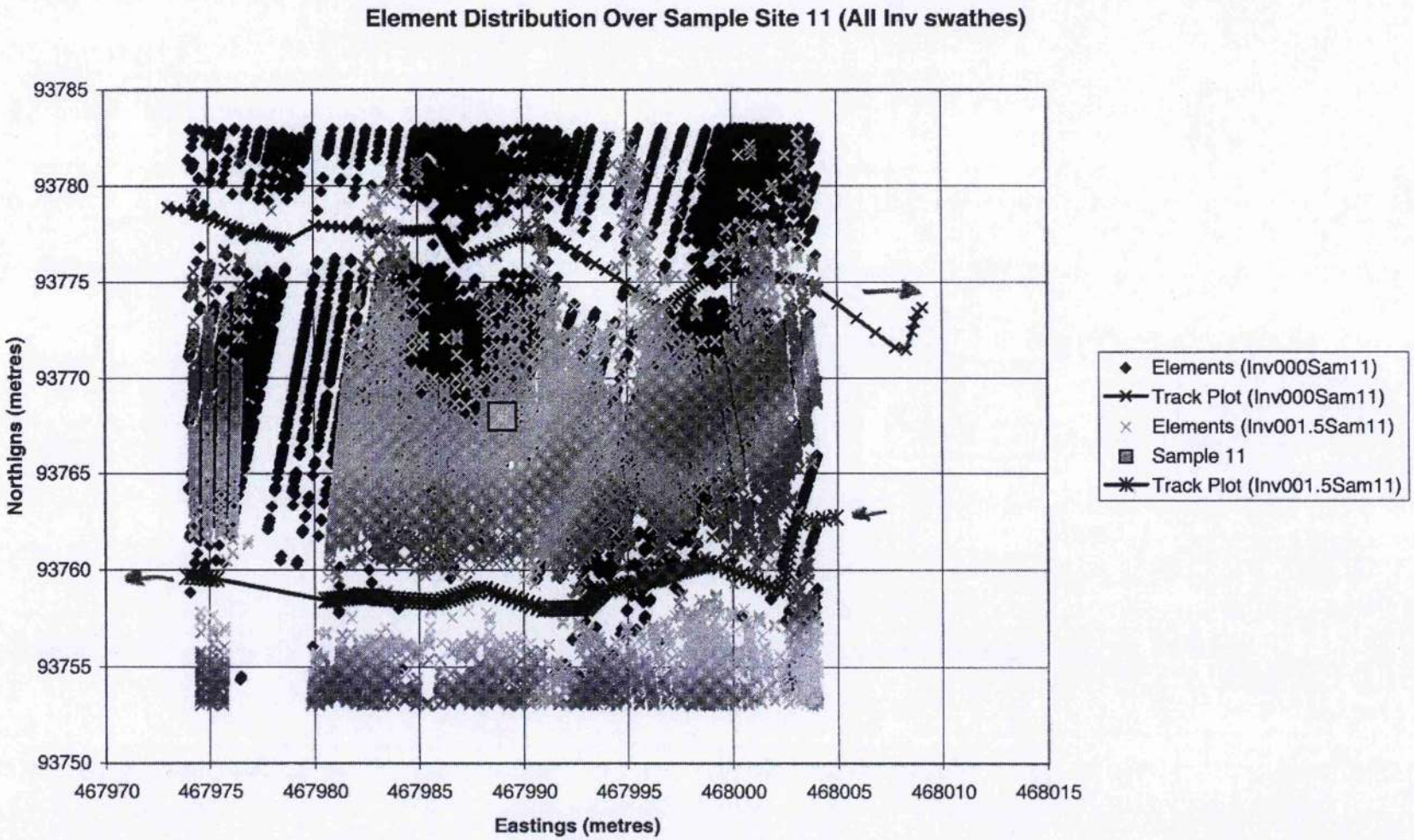

Figure 5.26 **Illustration of raw data density within 30x30m^2 of sample location 14 in the A1 Submarine survey area, and including vessel track plot and direction of movement**

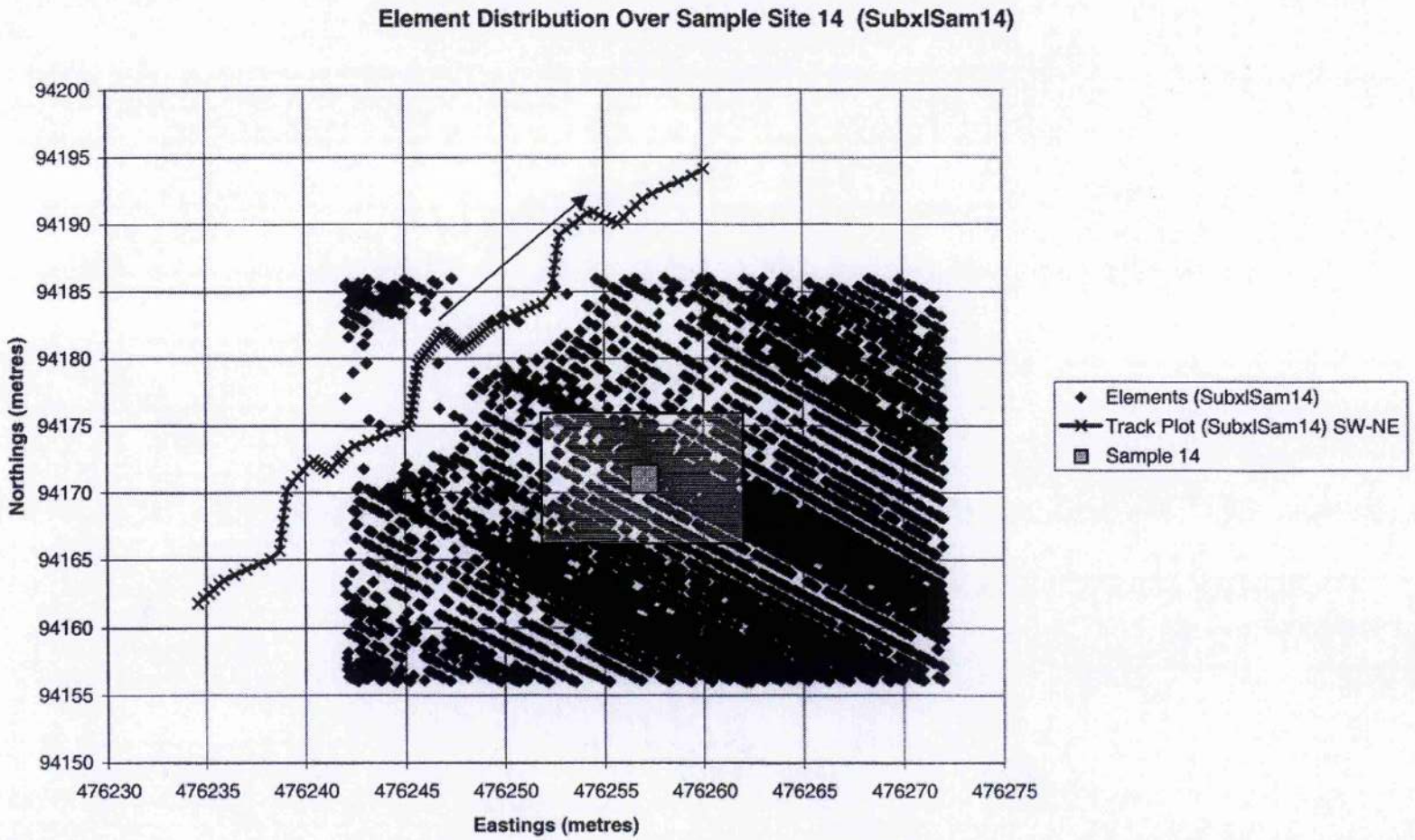

Figure 5.27 **Illustration of raw data density within 30x30m^2 of sample location 15 in the A1 Submarine survey area, and including vessel track plot and direction of movement**

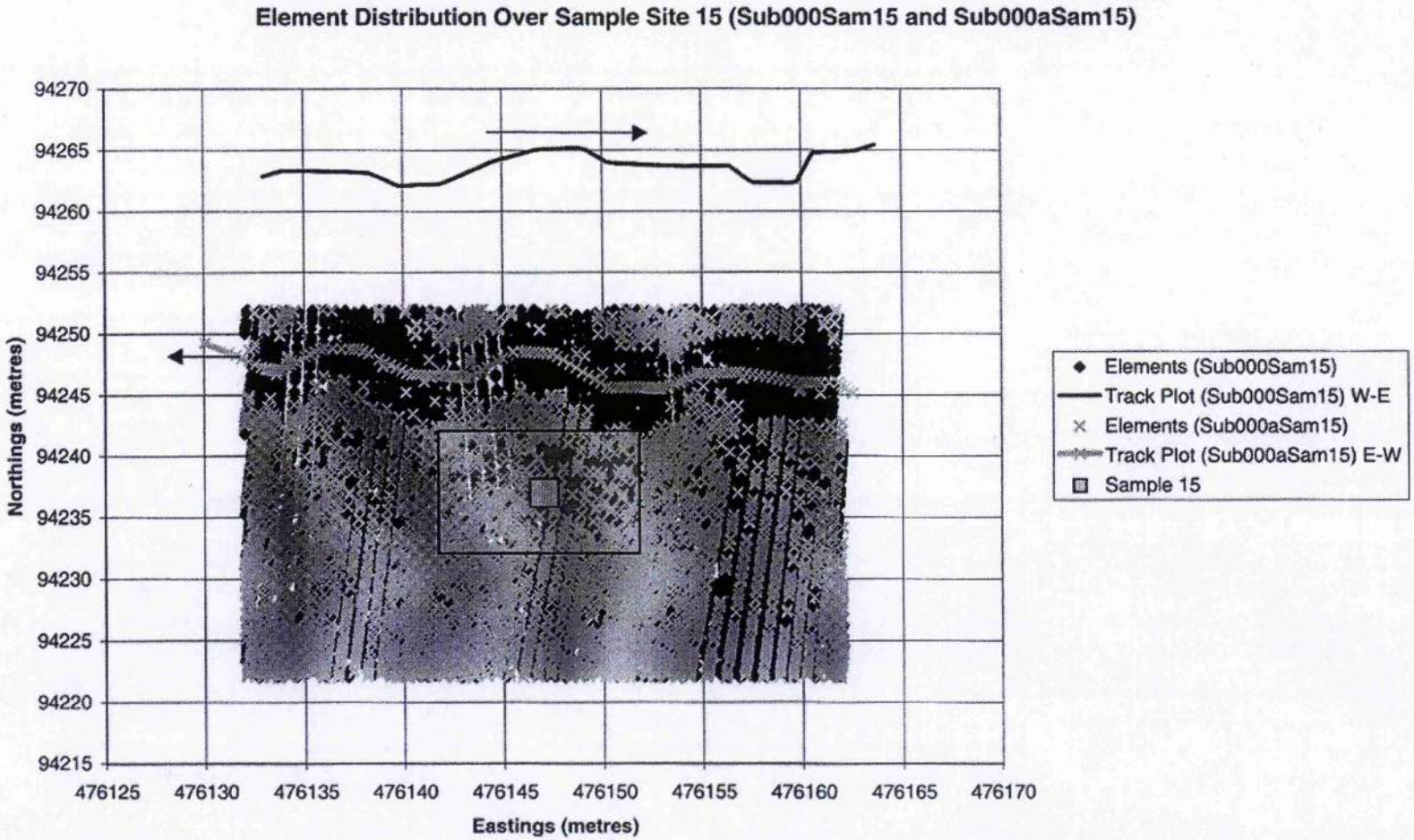

Figure 5.28 **Illustration of Sub000a raw data density within 30x30m^2 of sample location 16 in the A1 Submarine survey area, and including vessel track plot and direction of movement. This plot also shows the effects of pitch and yaw motion, causing the data to be inconsistently spaced, and resulting in the ping lines losing their parallel characteristic.**

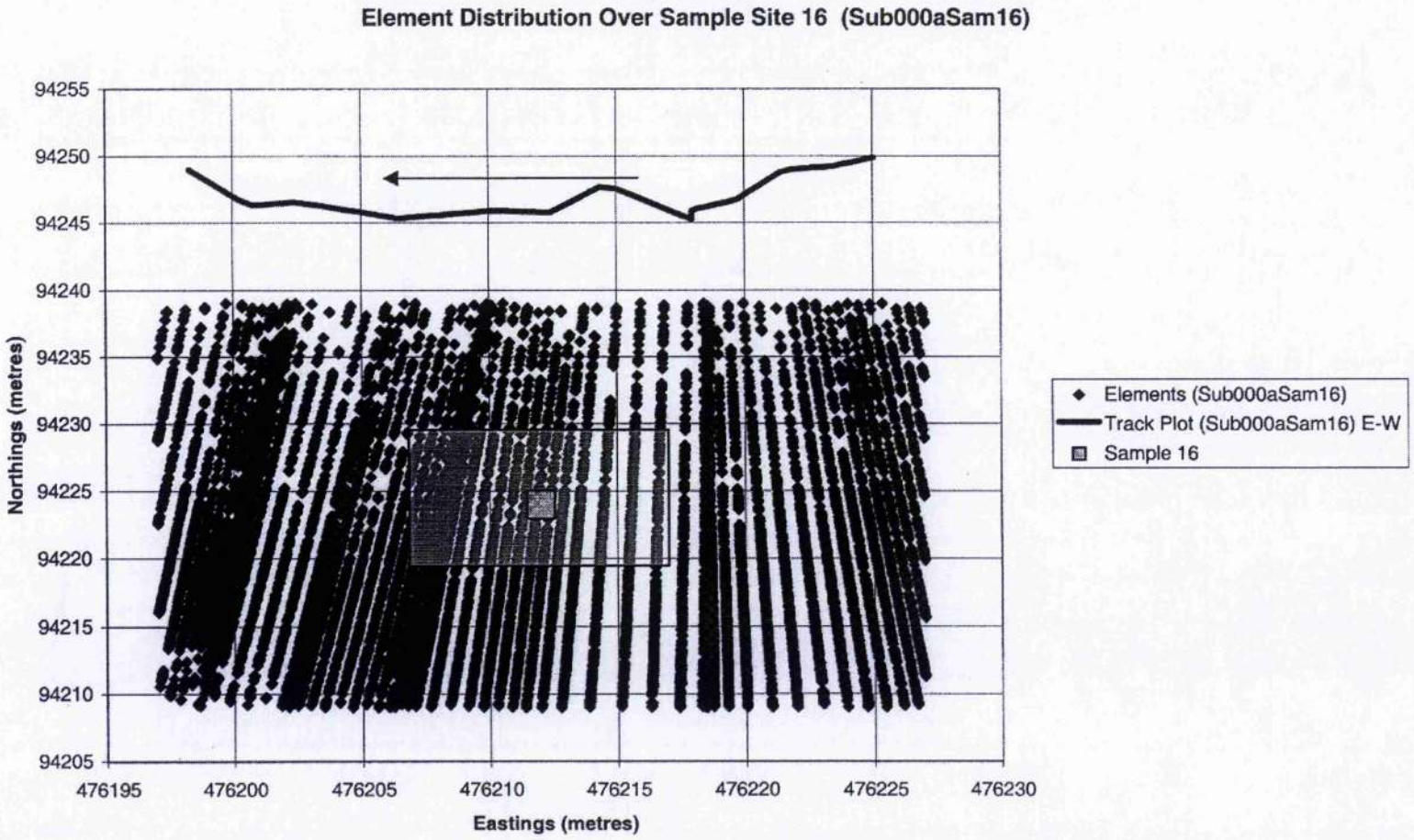

Figure 5.29 **Illustration of Sub001 raw data density within 30x30m^2 of sample location 16 in the A1 Submarine survey area, and including vessel track plot and direction of movement. This plot also shows the effects of wave motion upon the speed of the vessel, which results in the data being grouped with a periodicity that matches a gentle swell.**

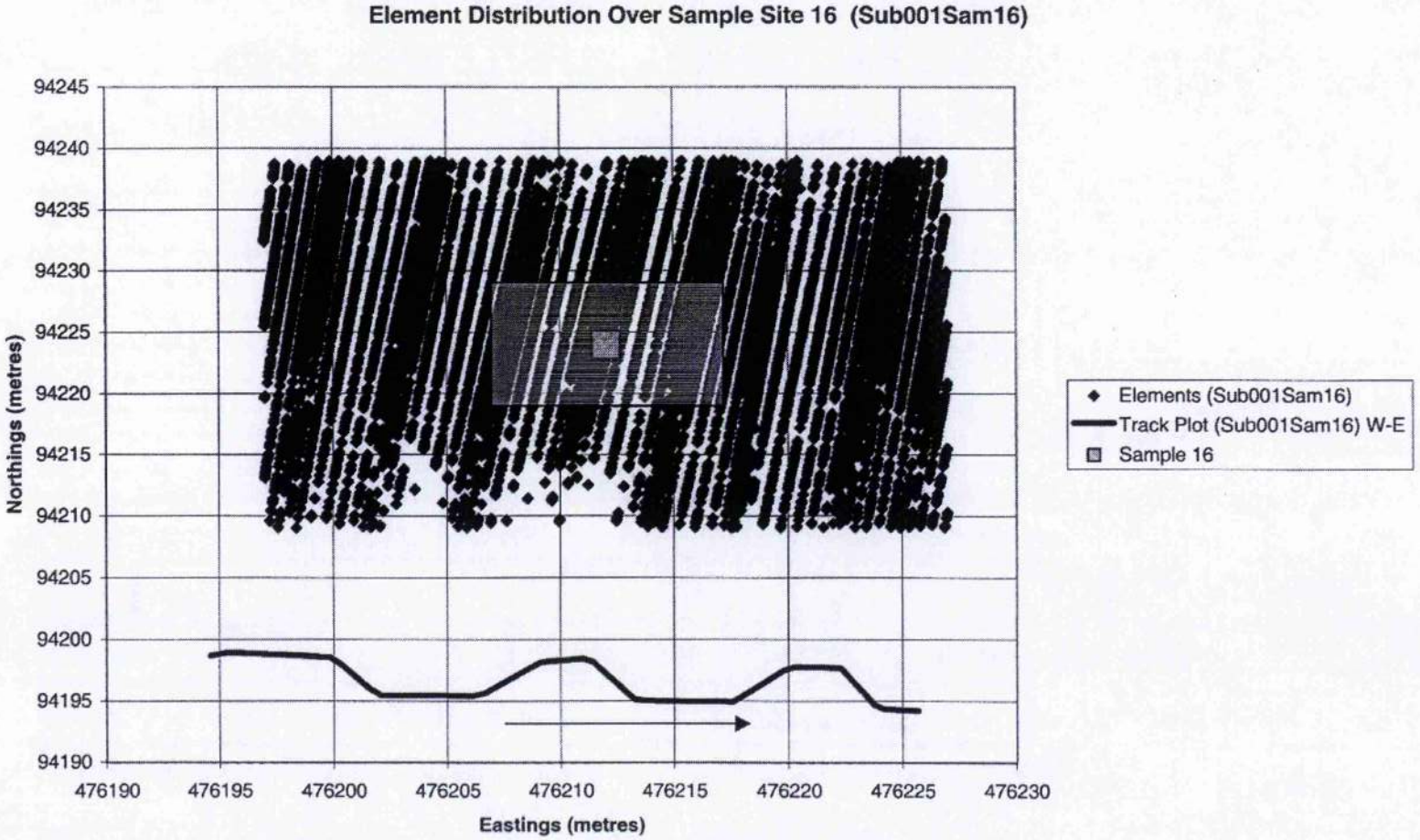

Figure 5.30 **Illustration of Subxlc raw data density within 30x30m^2 of sample location 16 in the A1 Submarine survey area, and including vessel track plot and direction of movement. This plot shows how the additional angles of traverse that were used to survey the A1 Submarine wreck, also provided aspect variations over the sample locations.**

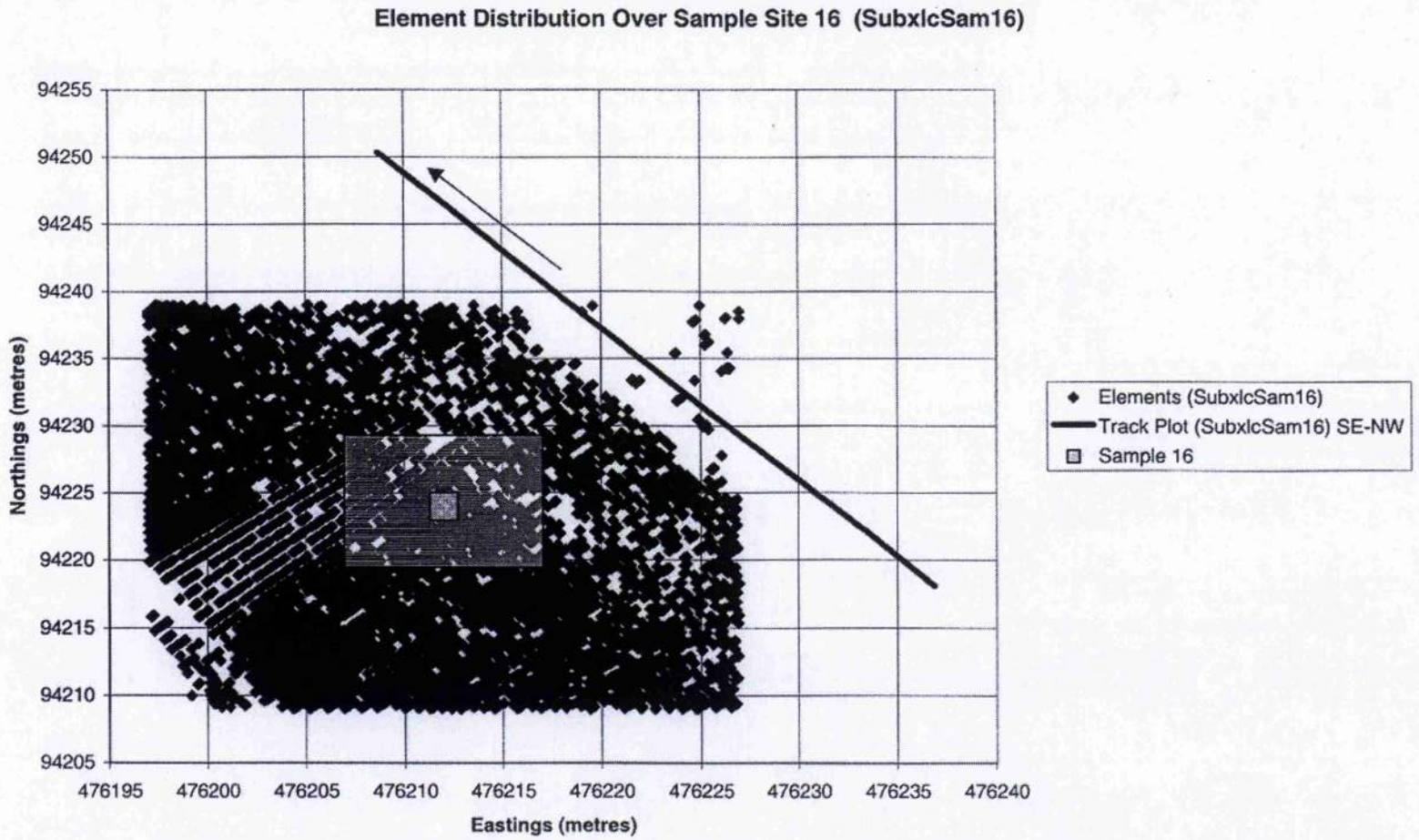

5.5. Summary

As a result of poor quality data from Loch Earn, the research project focused upon the data from the Portsmouth survey areas. The experiences of the Loch Earn survey were not wasted as they were critical in the refinement of the Portsmouth survey techniques. These experiences led to the focus of the sonar survey switching to a much smaller scale in order to obtain more comprehensive and intense sonar coverage, with a higher degree of variation in the angle and attitude of the sonar analysis. The four small-scale survey sites with relatively flat seabed also enabled shorter track lines to be run, and decreased the need to alter the power setting of the transducer during the survey. All of this helped to ensure the collection of high quality datasets, and to simplify the post-processing procedure.

The combination of the primary Solent sites, namely the ***Calibration***, ***Shingle***, ***Invincible*** and ***A1 Submarine***, offers a good quality ISIS 100 dataset collected in a shallow-marine environment and encapsulating sediment types ranging from very fine-grained to coarse-grained. These datasets acquired during the four-day survey window in Portsmouth form the backbone for the analysis of acoustic-sediment relationships in this study.

Where possible, the swath surveys were run prior to the ground-truthing programme in order to use the side-scan sonar imagery to highlight areas of contrasting backscatter amplitudes, and thereby determine the desired locations for the sediment sample locations.

Calibration Site

This site was surveyed by four parallel North-South trending swath lines of 100m in length, generating a rectangular survey area. Four separate ground-truthing samples

were collected from random locations within the survey site. The random nature of this sampling reflects the relatively homogeneous backscatter amplitude recorded over the calibration site.

The raw ISIS data coverage over each of the Calibration sample sites is markedly different with samples 2 and 4 being substantially covered by several swaths, sample 1 being covered only by the margins of one swath, and sample 3 receiving 0 % coverage. The lack of sonar coverage over sample 3 is the result of a GPS navigation jump at the time of recording the sample location, which caused Sample 3 to be erratically positioned several hundred metres from the other samples. Unfortunately, this GPS error was not detected until the post-survey processing stage, and thus a replacement sample could not be obtained. In spite of this, sample 3 was retained for analysis as, although its precise location was uncertain, it was known to have been obtained in close proximity to the others, and could therefore be used to support or disprove any trends identified in the surficial sediment of the Calibration site.

In terms of bathymetric data coverage of the $30x30m^2$ area surrounding the other sample locations, the figures in Table 5.2 shows that each area is densely covered with over 15,000 elements.

Shingle Site

This site traversed the shipping channel in Portsmouth harbour in search of pockets of shingle on the seabed. The constant stream of shipping traffic disrupted the survey, preventing the generation of straight-line swath survey track plots and replacing them with continuous-streaming swath survey data, split into three because of data overload. The ground-truthing was also carried out during the continuous-streaming swath survey runs. This factor accounts for the exceptionally high density of the bathymetric data

coverage over each sample site, because the ISIS 100 transducers were still operating whilst the vessel was halted for the retrieval and documentation of the grab samples.

Invincible Site

The Invincible wreck was the focal point of this survey area. A total of seven parallel 100m swath lines were run in a West-East orientation. The sediment sampling programme at this site was confined to four random samples, two either side of the wreck on the West-East trend, because of the apparent homogeneity of the acoustic backscatter amplitudes shown on the side-scan images.

The figures for bathymetric data coverage listed in Table 5.2 show a large variety in density. Although this is partly related to the random nature of the sediment sampling program, the data densities tend to reflect the number of swath lines which have covered the area, thus the higher figures represent samples taken from well inside the Invincible survey area. This is clearly demonstrated by samples 20, 21 and 22, which as a direct result of their close proximity to the focal point of the survey, the Invincible wreck, have been subjected to an excessive coverage of nearly 270000 elements – all within a $30x30m^2$ area.

A1 Submarine Site

The swath sonar survey focused around the submarine wreck. Four main lines of 100m in length were run in a West-East orientation over the site. The bathymetric results suggested that the submarine was standing a few metres proud of the seabed, and thereby inducing a large acoustic shadow zone. The presence of the shadow zones necessitated the addition of three cross-lines running practically perpendicular to the main lines to fill in the backscatter gaps.

In order to increase the chances of collecting the visually different sediments which divers stated could be found in this area, the random sampling technique was replaced by a more regimented and methodical sampling technique at the submarine site.

A total of five sample locations were earmarked, with four of the five forming the corners of a 100m x 50m box around the wreck, as illustrated in Figure 5.19, and the final sample being taken only metres from the wreck itself.

The bathymetric data coverage over the grab samples in this area followed a similar pattern to that found at the Invincible site, with those surrounding the wreck (samples 17, 18 and 19) being covered by over 150000 elements. However, the regular distribution of samples 12, 13, 14, 15 and 16, have resulted in a more even coverage rate per location, of between 6000 and 9000 elements.

5.6. Conclusion

The aim of obtaining high-density coverage of ISIS 100 raw swath data over the ground-truthed sample sites has been successful for all but sample 3. The next step is to fully evaluate the quality of information that has been collected both by the ISIS 100 survey and the ground-truthing survey, as the analysis of acoustic-sediment relationships can only be performed once all of this data has been processed.

A full account of the post-processing analyses for the sonar and ground-truthed data can be found in Chapters 6 and 7 respectively.

CHAPTER 6:

DIGITAL DATA ANALYSIS

6.1. Introduction to ISIS100 post-processing techniques

This chapter will begin by outlining the existing capabilities of the ISIS 100 and the associated software in terms of the data output. It will then show how that information can be processed/modified to derive/suit the requirements of the trigonometric and sonar parameters within the sonar equation. Illustrations accompany each section to show the across-swath trends of each parameter using the equations provided.

The generation of numerical values for each parameter is followed up by a description of the data filtering methodology employed to enhance the data quality within the swath file.

6.2. System (ISIS) output

For internal data processing within the ISIS system, there are several options open to the user. Output swath files generated from survey lines may be given 'depth only', 'amplitude only' or combined 'depth and amplitude' data. Evidently, the file required for both trigonometric and sonar equation analysis must contain both depth (trigonometric analysis) and amplitude (sonar equation analysis) information.

In combining the depth and amplitude data, the ISIS software simply adds an amplitude value to each (X, Y, Z) depth element. This data amalgamation is achieved by calculating the range to the depth element, and then identifying and grouping all the amplitude values whose range lies between halfway from the previous depth element until halfway to the next element. This processing technique works on the assumption that the amplitude data has been collected at a higher rate than the depth data. The software then averages the amplitude values in each group, and registers the average

value with the relevant depth element – a process referred to as 'co-registering.' The resultant co-registered depth and amplitude files therefore contain differing measures of depth and amplitude resolution for each element.

The reason for this is that although the ISIS samples depth and amplitude data at similar rates (Geen, 1997), the depth values tend to be down-sampled by data filtering prior to the amplitude averaging within the ISIS software.

The important factor to note from this processing technique is that whilst the depth and amplitude data may be termed as 'co-registered' it is not 'simultaneously sampled.'

The existing 'depth and amplitude' swath files created by the standard ISIS100 software contain the following information:-

Table 6.1 Table illustrating the contents of the 'depth and amplitude' Swath files

1.	Ping Number	- numerical record of ping sequence
2.	Element Number	- numerical record of order of detection relative to each ping
3.	Time	- precise time of recording, for relating tide data
4.	Date	- aid to tide data
5.	Qualifier	- Quality Control figure for ISIS processing
6.	Heading	- derived from vessel's compass
7.	Roll	- derived by Motion Reference Unit
8.	Pitch	- derived by Motion Reference Unit
9.	Tide	- supplied by operator in post-processing
10.	Transducer Depth	- below water level, measured during survey
11.	Transducer Eastings	- derived by DGPS
12.	Transducer Northings	- derived by DGPS
13.	Transducer Side	- Transducer responsible for that ping
14.	Type of file	- 'depth', 'amplitude' or 'depth and amplitude'
15.	Element Eastings	- location of element relative to transducer
16.	Element Northings	- location of element relative to transducer
17.	Element range (eastings)	- Eastings off-set between element & transducer
18.	Element range (northings)	- Northings off-set between element & transducer
19.	Weighting	- loose 'quality control' measurement
20.	Status	- quality control included for swath mosaics
21.	Depth of element	- depth below transducer or depth below datum
22.	Amplitude of return	- represented by a 16-bit number, but not simultaneously sampled with depth

The information contained in most fields is self-explanatory, given the brief descriptions, although the methodology behind the derivation of some fields such as Element Location and Depth require a fuller explanation.

6.2.1. Review of ISIS data processing for Depth and Amplitude Information

The X,Y,Z co-ordinates of each element are calculated in relation to the three dimensional location of the source, as determined by the DGPS Eastings (X) and Northings (Y), and the elevation data (Z) derived from the tide and transducer depth data. Given the transducer location, the element location can be derived from a combination of (1) the shortest distance between the source and the element, and (2) the phase angle of the acoustic wave returning from the element (Figure 6.1).

Figure 6.1 Schematic illustrating the trigonometric relationship between the source and the target (element)

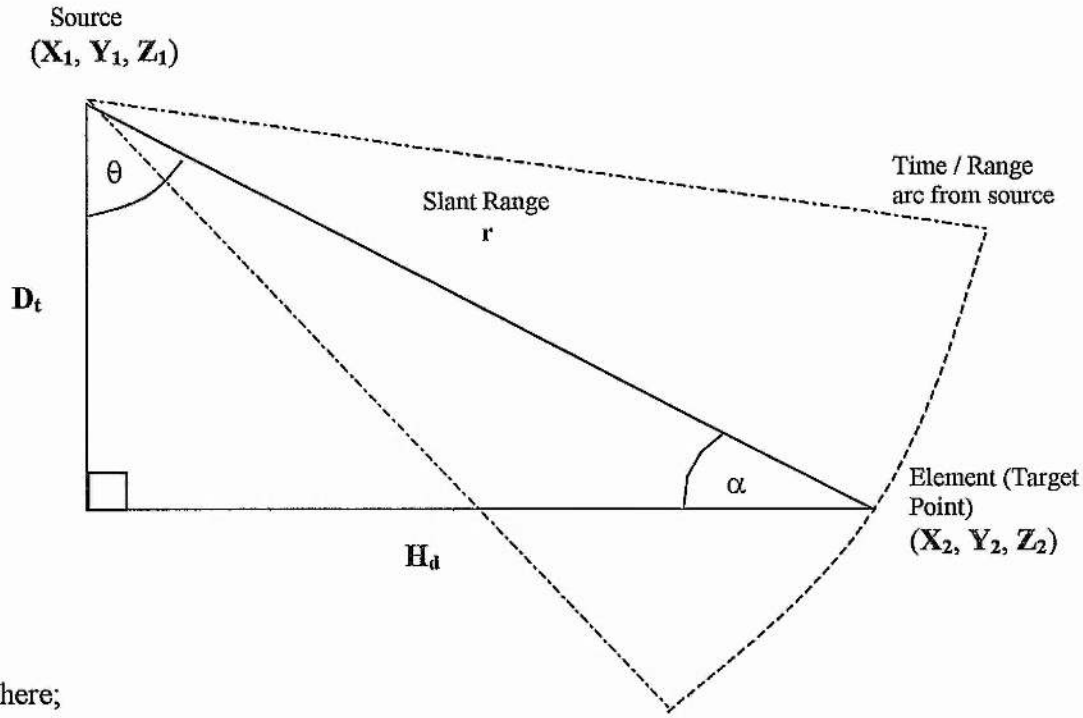

Where;

H_d = Distance from source to element in X,Y plane

D_t = Distance from source to element in Z plane

r = Distance from source to element in X,Y & Z plane

(1) the distance/range from the source to the element is determined by;-

$$r = v_1 \cdot t / 2$$

Where;

r = Range (slant range) from source to element

v_1 = Speed of sound in water

t = Total 2-way travel time

eg. 1490.0 ms^{-1} x t /2 secs where t = total 2-way travel time

NB. As this travel time is stripped out early within the ISIS processing preventing it appearing in the swath file, the element range from the source must be re-calculated from the X,Y,Z values of the transducer and element locations (See section 6.3.3.1).

(2) the angle of return (phase angle) is measured across a stave of receivers set at pre-determined distances apart (determined by the wavelength of the acoustic signal) to pinpoint the target on the time (distance) arc from the source (Figure 6.1). This then determines the X,Y,Z co-ordinates of the element, in relation to the location and orientation of the source (transducer).

6.2.2. Re-formatting of System Output

All of the information in Table 6.1 is compiled within, and output from, the ISIS software in a combined ASCII and binary code format, designed to reduce the overall swath file size. In this format the output file is incompatible with most spreadsheet data processing packages which may be used to analyse and process the raw numerical data. To reformat the output file into an all ASCII format, it was necessary to develop an additional software program known simply as a 'Swath Converter Program.' This program was specifically written in collaboration with Submetrix to meet the digital data requirements of this research by providing universal software access to all of the angular and spatial data recorded by the ISIS, as detailed in Chapter 2. This conversion

or reformatting process generated ASCII swath files that were five to six times larger (up to approximately 20Mb) than the original swath files, thus exacerbating the problem of processing such high data volumes.

The development and testing of this Swath Converter Program proved to be a very arduous task. The initial conversion program resulted in the output ASCII datasets containing data which were grouped into 1-3m thick bands of alternating high and low data densities, as illustrated in Figure 6.2. In Figure 6.2 the 'banding' is evident throughout the entire swath, although it becomes more visible in the outer reaches of the swath where the data density is lower than in the centre of the swath. This is simply because the size and shape of the pixels used to mark the location of each element exceed the true element dimensions, and so can visually mask the banding phenomenon in areas of high data density.

Figure 6.3 provides a clearer image to support this statement by illustrating the spatial distribution of the elements along the depth profile of a solitary ping.

Figure 6.2 **Diagram illustrating the effects of the Banding phenomenon, generated by initial Swath Converter Program, upon the distribution of elements over the seabed.**
This example is taken from the Inv003 swath file.

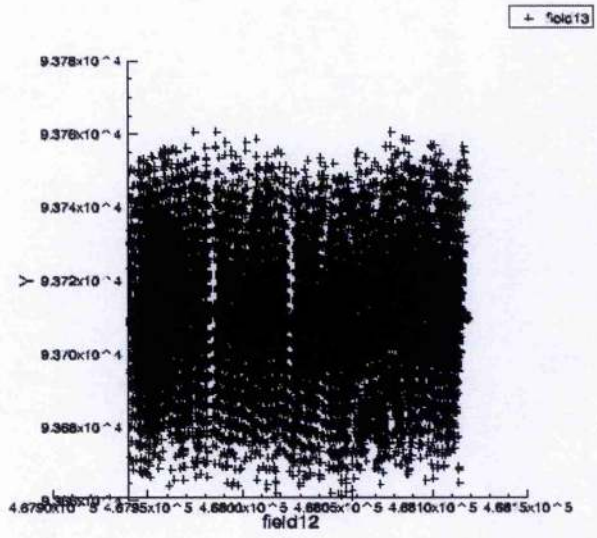

Figure 6.3 **Effects of banding phenomenon upon the depth profile of an individual ping.** This example is taken from Ping 318 in the Inv003 swath file.

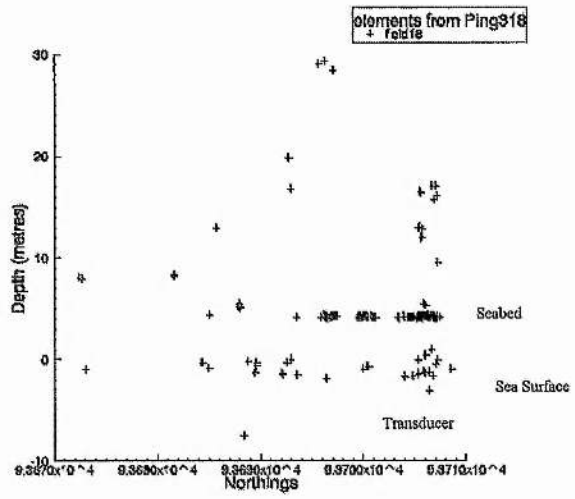

Investigations into the banding phenomenon explored all of the possible causes that could theoretically have induced the uneven distribution of reflection points across the seabed. These included (1) real-time navigational problems, (2) phase angle rounding-off or averaging, (3) acoustic wave interference patterns leading to both constructive and destructive zones, (4) slant range rounding-off or averaging, and (5) errors in number fields read in by lines of code within the Swath Converter program itself.

After much research and inter-disciplinary discussion, the cause of the banding was found to be of a post-processing nature, and was subsequently isolated within the Swath Converter Program. It was discovered that the several lines of code, relating to the reading and reformatting of the locational data (Eastings and Northings) belonging to each element, were in fact 'reading' an incorrect number of integers from the eastings and northings field. This error was enough to displace the elements from their recorded positions and relocate them within high-density bands, as illustrated in Figures 6.2 and 6.3.

Once the errors in the conversion program were eliminated, and correctly converted ASCII swath files were being generated, the analysis then progressed on to the post-processing of the digital data.

It is worthy of note that the process of converting the swath file also facilitated the removal of data points that failed the ISIS 100's in-built 'weightings' filter. There is virtually no documented information available regarding the theory behind this 'weightings' filter. In general, it is believed to be a filter that removes data points which do not conform closely enough to the 'expected' acoustic receive time pattern or sequence, determined as a function of the horizontal distance between the transducer and the reflector. In assuming that this is indeed the case, then the presence of this filter will only impact upon the density, without affecting the quality, of data available for analysis.

6.3. Processing of the ISIS swath output

6.3.1. Introduction

The processing of the acoustic response requires detailed knowledge of the geometric and trigonometric relationships between the source (transducer) and the reflection point (element) on the seafloor, before values can be obtained for the parameters within the sonar equation. Thus the main body of this section has been be divided into two classes of analysis, namely trigonometric analysis and sonar analysis.

The trigonometric analysis focuses upon the spatial relationship between the location of the source (transducer) and the location of the element (reflection point) upon the seabed. It also comprehensively analyses the trigonometric properties of the reflection plane (seabed), relative to the location and orientation of the transducer.

The values obtained from the trigonometric analysis are then used to derive values for each of the variables within the sonar analysis. This is done to account for, and evaluate,

all the possible acoustic losses between the emission of the signal and the detection of backscattering at the transducer. The application of the trigonometric values within the sonar analysis enables a direct comparison between the source signal level, the received signal level and the proportion of the signal lost at the water-sediment interface.

In the trigonometric analysis, it is important to note that the numerical values for the parameters required by the sonar equation are calculated on the assumption that all the values output in the ISIS swath file are correct.

In the sonar analysis, most of the equations used are modified from those described in Chapter 2, whilst all the specifications of the ISIS 100 listed in Chapter 4 section 4.2.2, have been obtained directly from the manufacturers, and are assumed to be correct.

The methodology can be summarised by Figure 6.4.

Figure 6.4 Basic Data Processing Outline

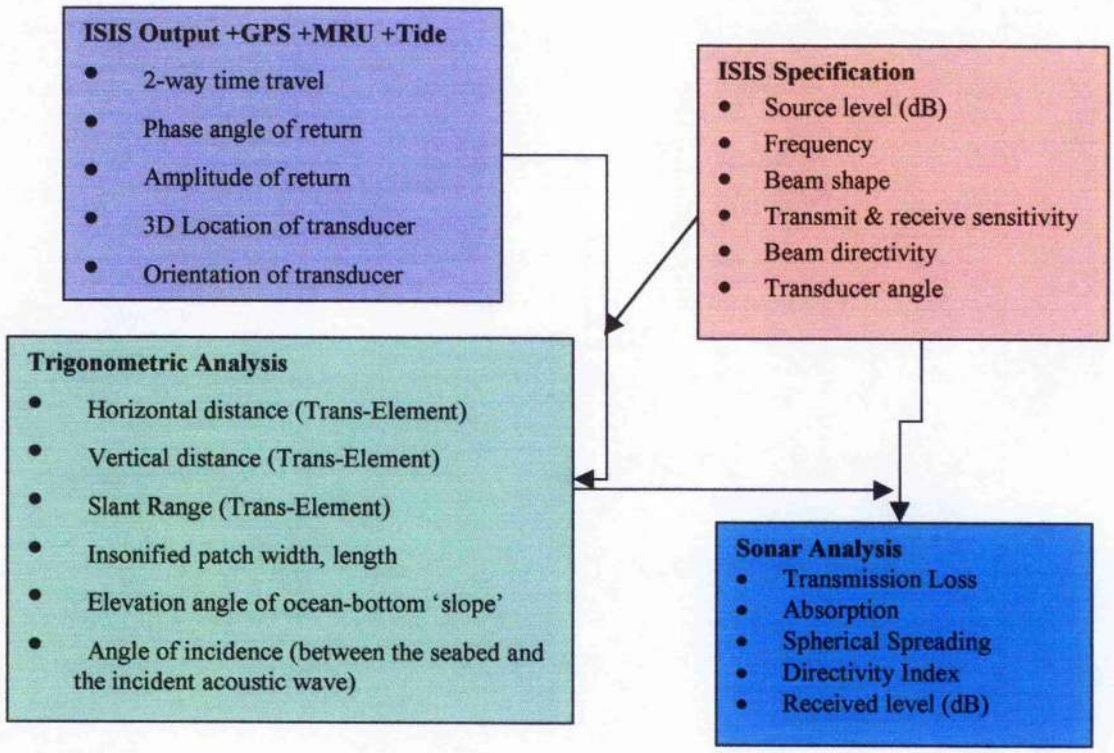

6.3.2. Processing Software

The processing of the swath files for sonar analysis requires the ability to read ASCII data in order to calculate values for new parameters from original data fields, to restructure the data file, and to facilitate the filtering of the entire data file. In addition, the processing package must be capable of producing a graphical analysis of each parameter at any given time as a quality control measure.

The primary software package tested for compatibility to the processing demands was Microsoft Excel. Although Excel spreadsheet processing is not the fastest and most efficient way of handling large data files, it was found to satisfy all of the processing requirements as well as facilitating the step-by-step monitoring of each stage in the processing. Therefore, since Microsoft Excel was found to match the criteria for data processing, and given its user-friendly nature, it was viewed as the most appropriate software package for the processing of ISIS data.

The only drawback was the limitation of file size that can be handled by Excel. Although Excel has a maximum spreadsheet limit of approximately 64000 lines equating to 64000 elements, it falls short of the hundreds of thousands of data lines output by an average swath. In order to minimise the effects of this limitation, the swath files were reduced to a manageable size for Excel by focusing the digital data upon the areas in close proximity to the grab sample sites.

This data reduction process utilised locational filters to obtain the relevant data. The locational filtering process of the ASCII swath files was initially carried out using a FORTRAN 'Stripper' program, which was superseded by a PERL 'Filter' program. Whilst the 'Stripper' program was successful in filtering the data, it struggled to cope with shifts in the sizes of data fields as every space, integer and decimal place in the input file must be accounted for in the 'read' instructions of a FORTRAN program. This

problem was enhanced by the presence of 'navigation jumps' – loss, or partial loss, of navigational data from satellites – which caused a significant change in the size of the locational fields in the swath file. In addition, the resultant knock-on effect was that the majority of fields following on from the locational fields in the input string, were 'read' incorrectly.

Despite adapting the Swath Converter to enlarge the spacings between the swath file output fields in an attempt to eliminate the overlapping of data columns induced by shifting, problems persisted. This led to the design and development of an alternative software program to filter the swath files.

The replacement program utilised the PERL language in place of FORTRAN because the 'read' and 'write' commands of PERL are much more flexible. In the context of this exercise, PERL requires only the names of the fields and at least one space as a separator, whereas FORTRAN requires a rigid definition of the exact number of digits before and after each decimal place, as well as the number of spacings present between fields.

The locational filtering was carried out by defining squared zones centred around the grab sample locations. In setting the dimensions of these zones it was imperative to encompass the locational error margins of ±1m radius incurred by the grab sampling methodology (Chapter 5 section 5.3.3.4). Beyond this zone, it was also desirable to try to maximise the data volume available for processing in order to construct a more comprehensive analysis.

Through trial and error, the maximum file sizes for processing the digital data in Excel related to a optimal zone of 30m x 30m. These 30mx30m zones were delimited by taking each grab sample location and extending both the north-south and east-west ranges by plus and minus 15 metres.

For example, the Eastings (X) and Northings (Y) range for the zone associated with sample location (X, Y) would be;-

Maximum Eastings	= (X + 15) E	Maximum Northings	= (Y + 15) N
Minimum Eastings	= (X – 15) E	Minimum Northings	= (Y – 15) N

A combination of the FORTRAN and PERL programs were used to strip the swath files of data lying outwith the zones surrounding the grab sample sites. A summary of the spatial limits of the digital data sample zones and the associated number of depth recordings within each zone are presented in Table 5.2.

The locational filtering programs were also designed to incorporate a broad depth filter, in order to extract soundings from reflectors or scatterers other than the seabed. In order to delimit the range of acceptable depth values, the depth profiles (Figure 6.5) of several pings within each swath must be plotted. From these profiles, it is possible to classify the causes of acoustic reflections into three distinct groups. Broadly speaking, the elements found grouped around the transducer can be attributed to acoustic noise. Moving down through the water column, the next element group is represented by a coherent/linear pattern of depth soundings marking the seabed, whilst those forming a secondary linear pattern deeper than the first can be classed as multiple reflections.
The distribution of the elements in Figure 6.5 show that by analysing the average depths at which each class occurs within a swath it is possible to apply broad filters to remove the majority of the unwanted elements caused by noise and multiple reflection. In this example, elements with depths of less than 5m in Figure 6.5 can be attributed to acoustic noise or matter within the water column, and thus filtered out. In the same figure, multiple reflections, such as those found between –10m and –15m on the horizontal scale, may be removed by setting a maximum depth filter of one and a half

times the average seabed depth (15m in this case) as determined from the ping profiles (Figure 6.5).

Figure 6.5 **Sample profile of an ISIS ping – taken from the A1 Submarine site.** The submarine wreck induces a 2-3m rise above the seabed at between –15 and -20m on the horizontal scale. The transducer location is represented by the white square.

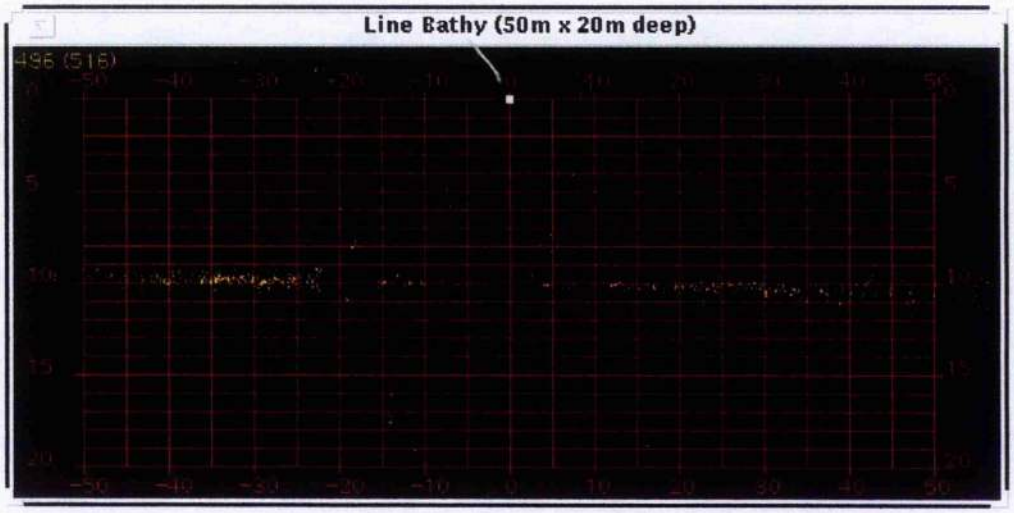

Once the broad filters have been applied, the remaining element locations are plotted to ensure that the depth filter has not removed any large areas of elements within the selected zone, which may relate to an anomalous structural high such as a shipwreck. Remnants of noise or multiple reflections may still exist, but these will be removed by the more advanced filtering techniques of Section 6.5. In the context of the ISIS, it should be noted that this broad depth filtering process effectively replaces the inbuilt ISIS 'weighting' filter, due to uncertainties over the techniques employed to derive the weighting values. After the removal of the excessive and unwanted data, the further processing of the swath file data becomes a more focused and manageable operation.

6.3.3. Trigonometric Processing

The trigonometric relationship between source and element forms the basis for the entire analysis, as all the parameters measured by the ISIS 100 and all other acoustic survey systems, are relative to the location of the signal source (transducer). In establishing and accepting this spatial relationship, it then becomes possible to derive numerical values for all the additional factors that must be accounted for within this analysis.

The trigonometric parameters also form the basis of the acoustic parameter analysis, as all acoustic measurements are relative to some spatial definition.

6.3.3.1. Spatial relationship between transducer and element

As highlighted in Chapter 2, one of the most important spatial parameters between the source and element is that of straight-line range. Although the ISIS has already derived the slant range (r) using the time travel and the speed of sound in water, neither the slant range nor time travel values are output within the swath file. This necessitates the re-calculation of the slant range value based upon the spatial relationship between the source and element as output in the swath file. This process uses the locational data of the source and element to derive the horizontal (X,Y) plane and vertical (Z) plane components (Figure 6.1) of the spatial relationship between source and element area using trigonometry, prior to calculating a value for the slant range through the X,Y and Z planes.

6.i.	Horizontal distance from Transducer to Element	$\mathbf{H_d}$
6.ii.	Vertical distance from Transducer to Element	$\mathbf{D_t}$
6.iii.	Slant Range from Transducer to Element	$\mathbf{r}$

NB. All distance measurements are made in metres

Using the illustration of the source to element trigonometry Figure 6.1, these trigonometric parameters can be calculated by the following equations 6.i, 6.ii and 6.iii.

6.i. Horizontal Distance (H_d)

The H_e is measured in the X,Y plane, using the eastings (X) and northings (Y) values output within the swath file, to generate the horizontal offset between the transducer and the element.

$$H_d = \sqrt{[(X_2 - X_1)^2 + (Y_2 - Y_1)^2]} \qquad \textbf{Equation 6.i}$$

Where;

H_d = Horizontal distance from transducer to element
X_1 = Easting location of transducer
X_2 = Easting location of element
Y_1 = Northing location of transducer
Y_2 = Northing location of element

6.ii. Vertical Distance (D_t)

D_t represents the vertical (Z plane) offset between the transducer and the element, detected by the sonar transducer. This measurement will not require adjustment where it is preserved within the swath output file. In some cases however, the swath output file may contain the depth below the lowest astronomical tide recorded (D_{RP}), and will require the reversal of the conversion equation presented in Chapter 4 section 4.4.2 to derive the desired value of D_t.

$$D_t = (D_{RP} + T) - T_d \qquad \textbf{Equation 6.ii}$$

6.iii. Slant Range Distance (r)

Having derived values for both H_d and D_t, the slant range (r) between the transducer and element in the X,Y and Z planes can be calculated using Equation 6.iii.

$$r^2 = [H_d]^2 + [D_t]^2$$

$$r = \sqrt{\{[(X_2 - X_1)^2 + (Y_2 - Y_1)^2] + [D_t]^2\}} \qquad \textbf{Equation 6.iii}$$

Where; r = Slant range from transducer to element

D_t = Depth below transducer = $(D_{RP} + T) - T_d$

The spatial relationship between transducer and element can be illustrated using the slant range variable between the two points. The addition of this slant range field to a swath file shows a general increase in slant range with increasing horizontal distance between transducer and element, assuming a relatively flat seabed.

At this point, attention must be drawn to the ordering within the swath output file prior to calculating further trigonometric parameters. On output from the ISIS, the swath file is ordered by the data in the first two fields of each line, namely Ping number and Element Number. This places the elements in the succession in which they are recorded, and not in relation to the expected order of increasing horizontal distance along the seabed profile. The effects of using this data ordering to create a planar profile of the seabed are illustrated in Figure 6.6.

Figure 6.6 Illustration of the planar profile generated using elements ordered by Ping number and element detection number

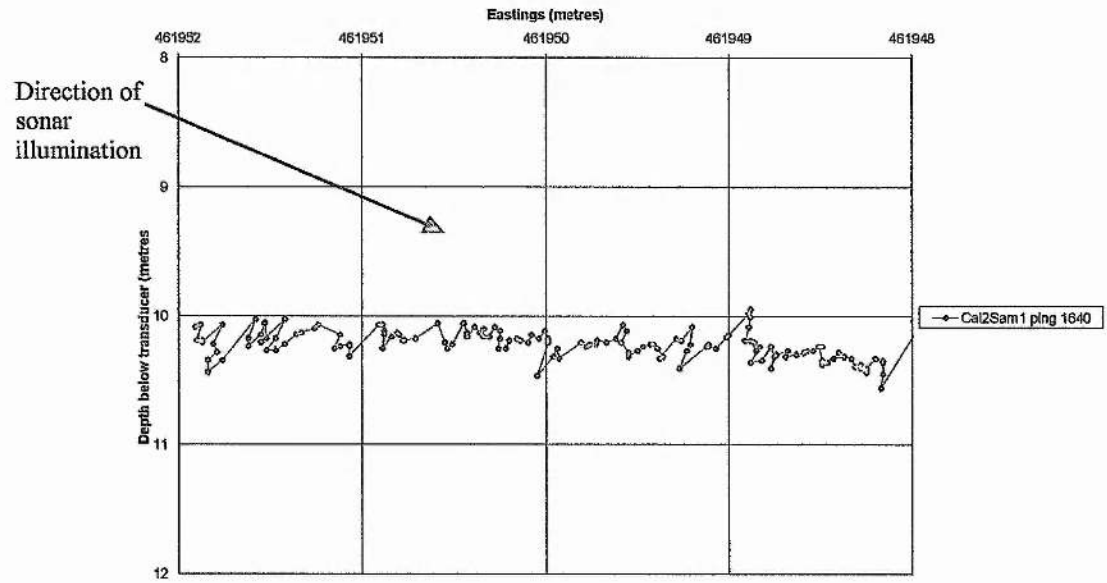

Although this topographic trend implies the presence of multiple overhangs, such structures are highly improbable in soft sediments, and even if they were present, the preceding topographic relief would prevent the sonar signal from reaching the troughs, thereby resulting in 'acoustic shadowing.' Figure 6.6 clearly shows that with this ordering the seabed profile assumes a skewed form, with the skewed angle tending towards the perpendicular of the direction of travel of the sonar signal. This problem was overcome by re-sorting the data, based upon the horizontal distance values derived by applying equation 6.i.

The re-sorted profile of the ping in Figure 6.6 can be seen in Figure 6.7, which generates a more realistic aspect to the topographic profile.

Figure 6.7 Planar profile of a ping re-ordered using the horizontal distance parameter

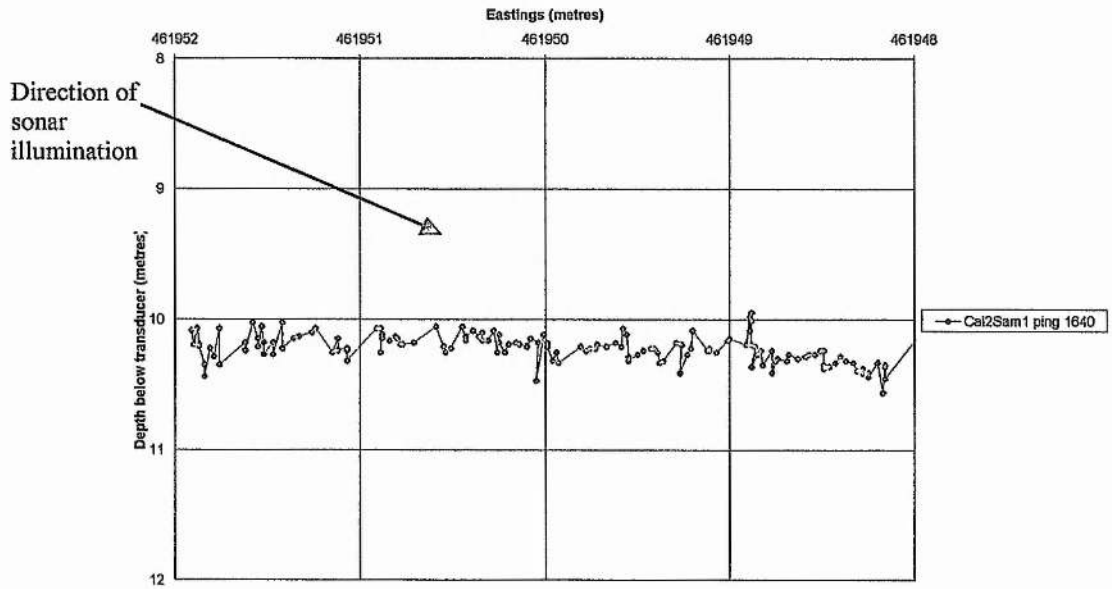

This step is essential for the trigonometric calculations of the spatial relationships between adjacent elements, whose distribution represent the topographic profile of the seabed.

6.3.3.2. Dimensions of the Element (or insonified area)

As discussed in Chapter 2, the dimensions of the area of seabed insonified by the sonar pulse must be known in order to evaluate both the Lambertian scattering and the overall Target Strength parameter. For example, the target strength is determined by the size of the insonified target patch factored by the backscatter coefficient of the seabed, with an allowance made for the backscatter angle.

The size of the insonified area relating to each element is calculated from the length and width components of the acoustic beam, as projected onto the seabed (Figure 6.8).

The parameters under analysis here are outlined below;

6.iv.	Width of Insonified Patch/Element	$\mathbf{E_w}$
6.v.	Length of Insonified Patch/Element	$\mathbf{E_L}$
6.vi.	Area of Insonified Patch/ Element	$\mathbf{E_{area}}$ **(also denoted by *dA*)**

Figure 6.8 Illustration of insonified element dimensions projected upon the seabed.

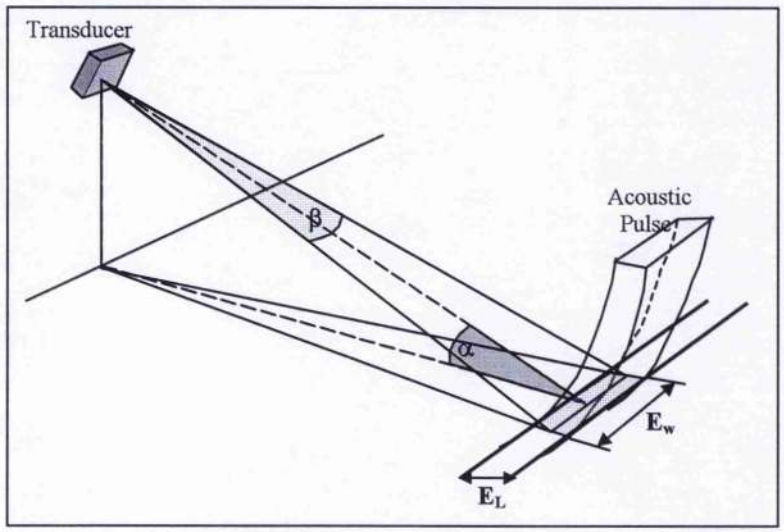

6.iv. Width of Element (E_w)

The width of the insonified area representing each element is dependent upon the azimuth of the transmitted beam and the slant range over which the beam travels. The

beam azimuth is defined as the angle over which the signal falls from its maximum to half of this maximum intensity (Mitchell, 1992), and is therefore measured to –3dB points, or 3dB down.

$$E_w = r \,.\, \tan \beta \qquad \textbf{Equation 6.iv}$$

Where;

E_w = Element width (metres)

r = Slant range from transducer to element (metres)

β = Beam azimuth (degrees)

The manufacturers specification states that the beam azimuth for the ISIS 100 234kHz system is;

β = 1.0^0 to –3 dB points for the 234kHz system

6.v. Length of Element (E_L)

The length of the element is dependent upon the pulse length (P_L) of the acoustic signal and also the angle at which it is projected /resolved upon the seabed. As can been seen in Figure 6.9, the angle of incidence dictates the projected length of the element on the seabed.

The manufacturers specifications state that the smallest practical pulse of the ISIS 100 is roughly ten wavelengths of the sonar frequency (Geen, 1997). This equates to a pulse time (P_t) of 4.274×10^{-5} seconds for the 234kHz ISIS, calculated from the following equation;

Pulse time = 10 / sonar frequency

The pulse length is then defined by:-

Pulse Length = (Speed of Sound in Water) x (Pulse time)

$P_L = v_1 \,.\, P_t$

In assuming an average speed of sound in water of $1490ms^{-1}$, the pulse length is found to be:

$$\mathbf{P_L} = 1490\ ms^{-1} \times (4.274 \times 10^{-5}\ s) = \mathbf{0.064m}\ \textit{for 234 kHz}$$

The length of the pulse in effect determines the smallest possible resolvable across-track dimension on the seabed. In order to calculate the true resolution (E_L) at any given point along the ping profile however, this pulse length must be projected onto the seabed using equation 6.v:

$$\mathbf{E_L = [(P_L) / (\cos \alpha)]} \qquad \textbf{Equation 6.v}$$

Where;

E_L = Element length (metres)

P_L = Pulse Length (metres)

α = Total grazing angle (See Equation 6.x)

6.vi. Area of Element (E_{area})

The overall area of the rectangular element is simply defined by;

$$\mathbf{E_{area} = E_L \cdot E_w} \qquad \textbf{Equation 6.vi}$$

Where;

E_{area} = Area of element (m^2)

E_L = Length of element (metres)

E_w = Width of element (metres)

The application of Equations 6.iv, 6.v and 6.vi to a swath file, enable the generation of a plot of element area variability across a swath.

6.3.3.3. Grazing angle between acoustic wave and water-sediment interface

The following parameters must be calculated in order to establish the total grazing angle:-

6.vii.	Slope length between elements E_{n-1} and E_{n+1}	$\mathbf{Sl_e}$
6.viii.	Grazing angle assuming a flat, horizontal seabed	α_H
6.ix.	Elevation angle of seabed slope between elements E_{n-1} and E_{n+1}	α_S
6.x.	Total grazing angle of acoustic wave at the water-sediment interface	α

Figure 6.9 illustrates the method by which the 2-dimensional slope angle can be derived. This cross-section of the water-sediment interface represents the seabed slope angle along a line perpendicular to the transducer face. The slope angle across element E_n can be calculated by analysing the (X,Y,Z) locations of elements E_{n-1} and E_{n+1} , to give as precise a localised slope angle at point E_n as is possible with the sonar system.

Figure 6.9 **Schematic illustrating the ability of swath bathymetry systems to derive the total grazing angle of the acoustic pulse (α) at the water-sediment interface.** (NB. The lengths of the arrows represent relative acoustic scattering strengths)

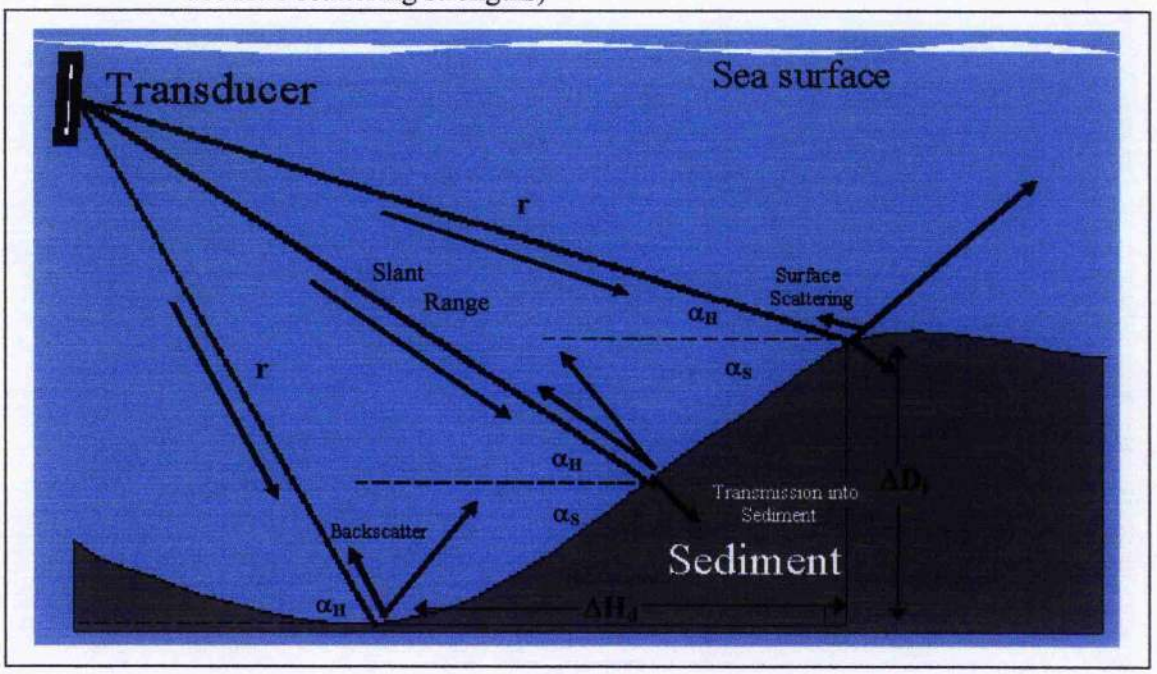

Care must be taken during this process as although $Hd_{n+1} - Hd_{n-1}$ (ΔH) will always be positive, this may not be the case for the ΔD values ($Dt_{n+1} - Dt_{n-1}$) as depth values may rise and fall across a ping section.

In order to eliminate the possibility of negative values within the derivation of angle 'α_S', it is recommended that α_S be calculated using the slope length and the horizontal distance between the elements E_{n-1} and E_{n+1}.

6.vii. Slope length (Sl_e) between elements E_{n-1} and E_{n+1}

The slant range between E_{n-1} and E_{n+1} is be calculated using their respective $\mathbf{H_d}$ and $\mathbf{D_t}$ values, to provide a form of quality control by measuring the length of the section of slope which is providing the slope angle data. Although this is of more relevance in section 6.4, the derivation equation is offered here as the value of Sl_e can also be used in the calculation of α.

$$\mathbf{Sl_e} = \sqrt{\left[(\mathbf{Dt_{n+1}} - \mathbf{Dt_{n-1}})^2 + (\mathbf{Hd_{n+1}} - \mathbf{Hd_{n-1}})^2 \right]} \qquad \textbf{Equation 6.vii}$$

Where;

Sl_e = Slope length between elements E_{n-1} and E_{n+1}
Dt_{n+1} = Depth of Element E_{n+1}
Dt_{n-1} = Depth of Element E_{n-1}
Hd_{n+1} = Horizontal Distance from Transducer to E_{n+1}
Hd_{n-1} = Horizontal Distance from Transducer to E_{n-1}

6.viii. Grazing angle of incidence assuming a flat, horizontal seabed (α_H)

Figure 6.10 illustrates the angle of incidence of an acoustic wave at the water-sediment interface, assuming a flat, horizontal seabed.

Figure 6.10 Schematic illustrating the systems ability to derive the 'grazing' angle of incidence, i.e. assuming a flat, horizontal seabed

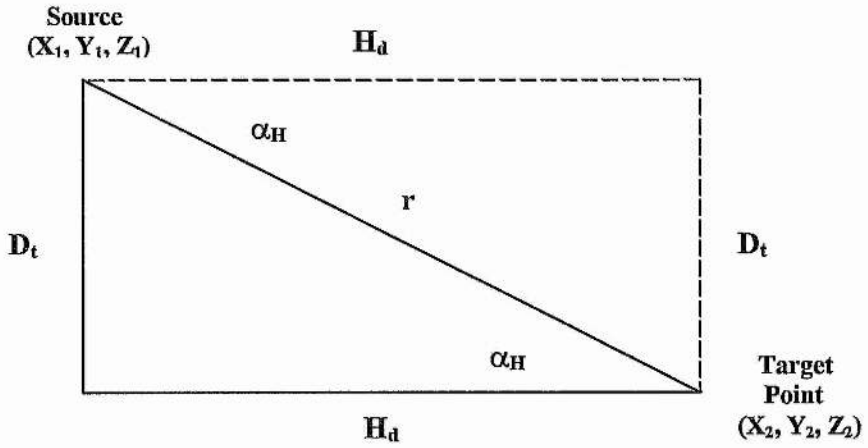

The value of 'α_H' is derived by the simply trigonometric equation below; -

$$\cos \alpha_H = H_d / r$$

$$\alpha_H = \cos^{-1} (H_d / r) \qquad \textbf{Equation 6.viii}$$

Where;

α_H = Grazing angle of incidence assuming a flat, horizontal seabed

H_d = Horizontal distance from transducer to element

r = Slant Range between transducer and element

In terms of the angle of elevation, this is clearly obtained from the above data, although the elevation angle in relation to the seabed must have an additional factor that represents the effects of slope angle on the seabed itself (Figure 6.9).

6.ix. Elevation angle of seabed slope (α_S)

The derivation of the seabed slope angle appears relatively straightforward in theory, but in practice its application to an entire swath file required the ability to cope with both positive and negative offsets in the horizontal and vertical locations of E_n.

Thus angle 'α_S' can be defined by;

$$\alpha_S = \tan^{-1} [(Dt_{n+1} - Dt_{n-1}) / (Hd_{n+1} - Hd_{n-1})] \qquad \textbf{Equation 6.ix}$$

Where;

α_S = 2 dimensional Elevation angle of seabed slope at E_n

$\mathbf{Dt}_{n+1}$ = Vertical Distance from Transducer to E_{n+1}

$\mathbf{Dt}_{n-1}$ = Vertical Distance from Transducer to E_{n-1}

$\mathbf{Hd}_{n+1}$ = Horizontal Distance from Transducer to E_{n+1}

$\mathbf{Hd}_{n-1}$ = Horizontal Distance from Transducer to E_{n-1}

The resultant values of 'α_S' are found to be positive when the seabed between E_{n+1} and E_{n-1} is sloping away from the transducer, and negative when the same slope is sloping towards the transducer.

In an attempt to enhance the quality of the data derived by this calculation, the application of this equation was controlled by a range limit on the horizontal distance between E_{n-1} and E_{n+1}. This range limit was set at 1 metre because the averaging of the seabed slope angle over distances beyond that was regarded as unreliable, and un-complementary with respect to the bathymetric resolution of the ISIS.

6.x. The total grazing angle (α) of the acoustic wave with the seabed at E_n

This can be determined by the following equation: -

$$\alpha = \alpha_H - \alpha_S \qquad \textbf{Equation 6.x}$$

Where;

α = Total grazing angle

α_H = Grazing angle assuming a flat, horizontal seabed

α_S = 2 dimensional angle of elevation of the seabed

6.3.4. Derivation of Acoustic Parameters

Once the trigonometric calculations have been completed, the next step is to apply these dimensions to the acoustic parameters, thus deriving numerical values for most of the parameters within the sonar equation.

In order to calculate the values of these acoustic parameters, the following additional parameters from the system specification must be known, (a) Receive sensitivity, (b) Detection threshold, and (c) Transducer angle.

The receive sensitivity of the transducers in the ISIS systems is required for the conversion of the Received Voltage (RV) into Received Level (RL). In the case of the 234kHz version of the ISIS, the manufacturers specifications state that the receive sensitivity is:-

$$\mathbf{R_{sens} = -196\ dB\ re\ uPa/V\ @\ 1m} \qquad \textbf{for the 234kHz system}$$

The detection threshold is an inherent cut-off point within the system, below which the receiver will not detect a target. The use of this detection threshold helps to reduce the sensitivity of the receivers to the background noise, and other weak signals with low levels of reliability. In the case of the 234kHz ISIS, the detection threshold is set at **10dB**.

The offset angle of the transducer face (**TA**) from the vertical is one of the parameters required to calculate the directivity index of the acoustic pulse. This angular offset refers to the angle of the bracket used to mount the transducer, and is normally predetermined by the manufacturer. Although the angle of the transducer face may vary during surveys due to the angular nature of the installation, and vessel motion, such factors are accounted for by the calibration procedure and the MRU respectively.

The ISIS manufacturers specifications state that the vertical offset of the transducer face associated with the transducer mounting bracket is a **fixed 30^0**.

Once these values have been obtained from the system specification and the survey set-up, then analysis of the acoustic parameters may be carried out.

Numerical values are required for the following parameters;

6.xi	Absorption of Sound within the water column	**Ab**
6.xii	Spherical Spreading within the water column	**SS**
6.xiii	Total transmission loss within the water column	**TTL**
6.xiv	Beam Directivity	**DI**
6.xv	Elevation Angle	ϕ
6.xvi	Directivity Index	$\mathbf{DI_{ping}}$
6.xvii	Received Voltage	**RV**
6.xviii	Received Level	**RL**
6.xix	Target Strength	**TS**
6.xx	Echo Level	**EL**
6.xxi	Acoustic Loss	$\mathbf{AL_{ws}}$

6.xi. Absorption of Sound within the water column

The absorption coefficient of sound within the water column is dependent upon the sonar frequency and the composition and characteristics of the water, as discussed in Chapter 2 section 2.2.2.2. The absorption coefficient (K_{ab}) values applicable to the 234kHz version of the ISIS 100 systems operating in salt water, are taken directly from Figure 2.9 (Fisher & Simmons, 1977) and converted into dB/m measurements:-

$$\mathbf{K_{ab} = 0.072\ dB / metre \quad for\ 234\ kHz\ frequency}$$

This value is noted to corroborate with the values suggested by Urick (1983).

This absorption coefficient ($\mathbf{K_{ab}}$) is then multiplied by the distance travelled by the acoustic wave through the water column (**r**), as in equation 2.iv, to derive a decibel value for **Ab**.

$$\mathbf{Ab = K_{ab} \cdot r} \qquad \textbf{Equation 6.xi}$$

6.xii. Spherical Spreading (SS) of the acoustic wave within the water column

The degree of spherical spreading is calculated using Equation 2.iii, which relates the degree of spherical spreading to the distance travelled from the source:-

$$SS = 20 \log r \qquad \textbf{Equation 6.xii}$$

6.xiii. Total Transmission Loss within the water column (TTL)

The numerical value of TTL refers to the two-way travel of the acoustic signal, and is thus derived by multiplying Equation 2.v by two, to give Equation 2.vi.

$$TTL = 2 (SS + Ab) \qquad \textbf{Equation 6.xiii}$$

The overall effect of transmission losses within the water column is calculated in relation to the location of each element. This parameter can then be applied to the entire swath to generate a transmission loss variability map of the swath (Figure 6.11).

Figure 6.11 Map of transmission loss variability across an actual swath
This map is generated using data from the Inv003 swath file, with the red arrow representing the general track plot of the vessel.

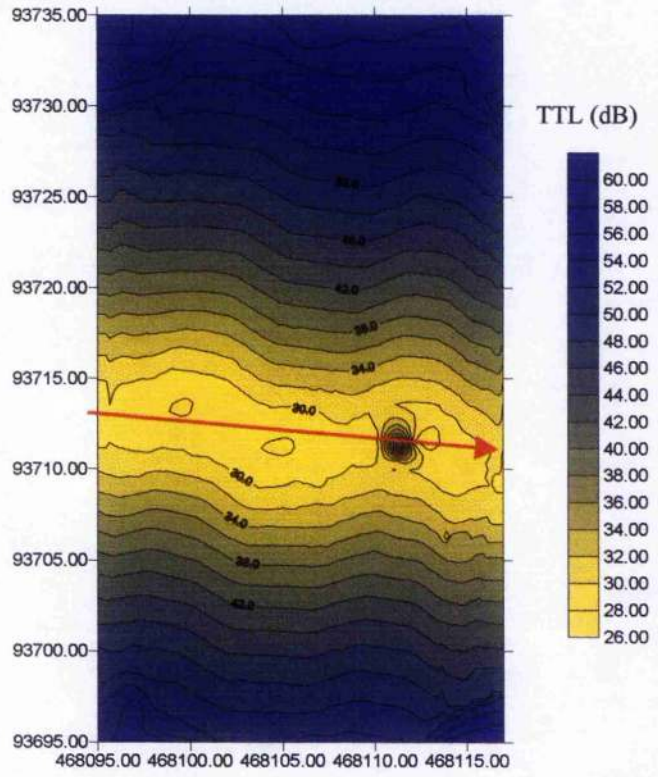

The level of transmission is seen to increase with horizontal distance from the transducer, over the flat seabed in Inv003. The wavy nature of the transmission loss contours can be attributed to either the lateral movement of the vessels track plot or more likely, the roll of the vessel. The anomaly at 468112E 93711N is caused by an erratic deep-lying element (possibly as the result of a multiple reflection).

6.xiv. Beam Directivity (BD)

The beam directivity refers to the degree of focusing applied to concentrate the source energy, thereby limiting the spread of the acoustic pulse. Equation 2.vii is used to determine the beam directivity of the ISIS 100 234kHz system, where $\phi = 61^0$ and $\beta = 1^0$. When these values are substituted into the equation below, the beam directivity for the ISIS 100 234kHz system is found to be;

$$\mathbf{BD} = \mathbf{10 \log [(4\pi) / (\phi . \beta)]} \qquad \textbf{Equation 6.xiv}$$

$$\mathbf{BD} = \mathbf{28.415\ dB} \qquad \text{for the ISIS 100 234kHz system}$$

6.xv. Elevation Angle (EA)

The elevation angle is the angle of return measured at the transducer face, and equates to what is often referred to as the angle relative to normal incidence (θ), as shown in Figure 6.12. This calculation is simplified as the values of α_H have already been calculated. The elevation angle is therefore determined by: $\mathbf{EA = (90 - \alpha_H) = \theta}$

Figure 6.12 Illustration of Elevation Angle

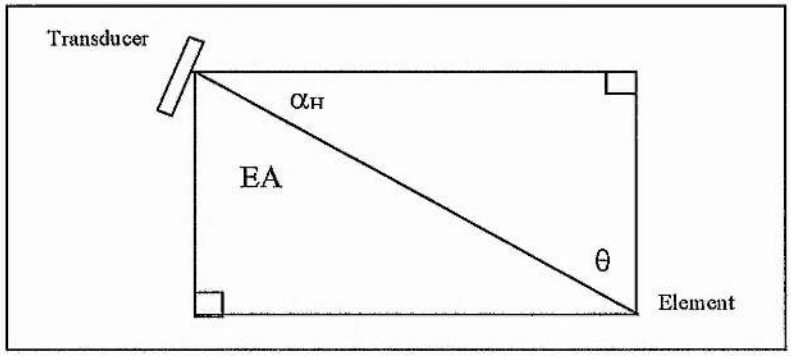

6.xvi. Directivity Index (DI)

The beam directivity must be modified to account for the beam drop-off experienced at any given angle from the main beam directivity which lies along a path perpendicular to the face of the transducer. This is done by applying Equation 2.viii, which adds the transducer transmit response (TR) and the transducer receive response (RR) parameters, to the beam directivity:-

$$\mathbf{DI} = \mathbf{BD} + \mathbf{TR} + \mathbf{RR}$$

The values of TR and RR correspond to the response of the transducers at the angle of return measured relative to the perpendicular from the transducer face, referred to as Kseg (K). In deriving a value for K, the angular analysis must take into account the angle of return of the signal as well as the angle of the transducer face, in order to relate the K value to the perpendicular plane from the transducer, as illustrated in Figure 6.13.

Figure 6.13 Derivation of Kseg

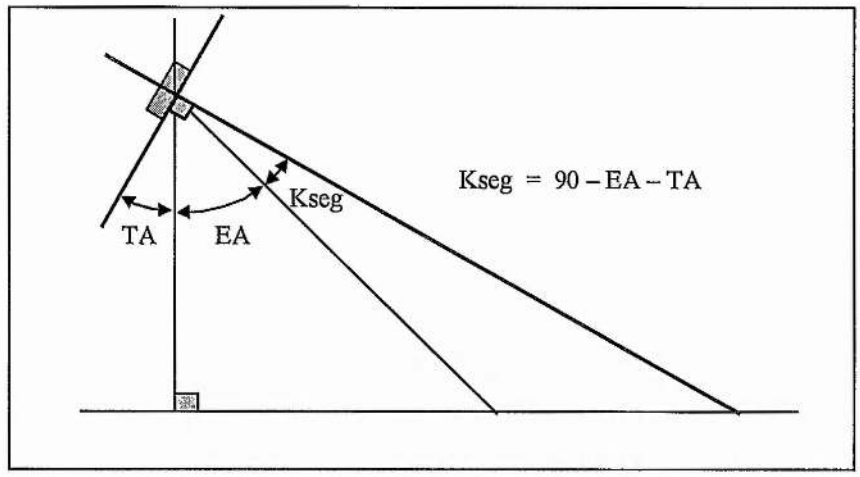

This angular relationship is also mimicked above the perpendicular line, to cover large values of EA, but for simplicity only the lower section is used in this explanation.

Figure 6.13 shows that the angular value of 'Kseg' can be derived by simply subtracting EA and TA from 90^0. This relationship means that the closer the angular response is to the perpendicular, the lower the associated value of Kseg. This Kseg value is then

divided by ten in order to equate the angle to the average responses measured by the manufacturers in 9^0 intervals, eg. $0\text{-}9^0$, $9\text{-}18^0$, etc. This is done using the following equation:-

$$\mathbf{K = (90 - EA - TA + 5)/10} \qquad \textbf{Equation 6.xv}$$

Where;

K = Kseg measurement split into 10 equal sections

EA = Elevation Angle in relation to the transducer

TA = Angle of transducer face from the vertical

The value of '5' is used to compensate for the inherent angular offset between the beam directivity and the angle of the transducer face.

Once this angular value of K has been derived, then the response values for TR and RR can be calculated using the calibration data for the transducers as supplied by the manufacturers.

The transducer transmit response (**TR**) as calibrated by the manufacturers can be plotted against the ten divisions of the **K** range (0 to 9), as shown in Figure 6.14.

Figure 6.14 Graph of manufacturers K measurements plotted against transducer transmit response

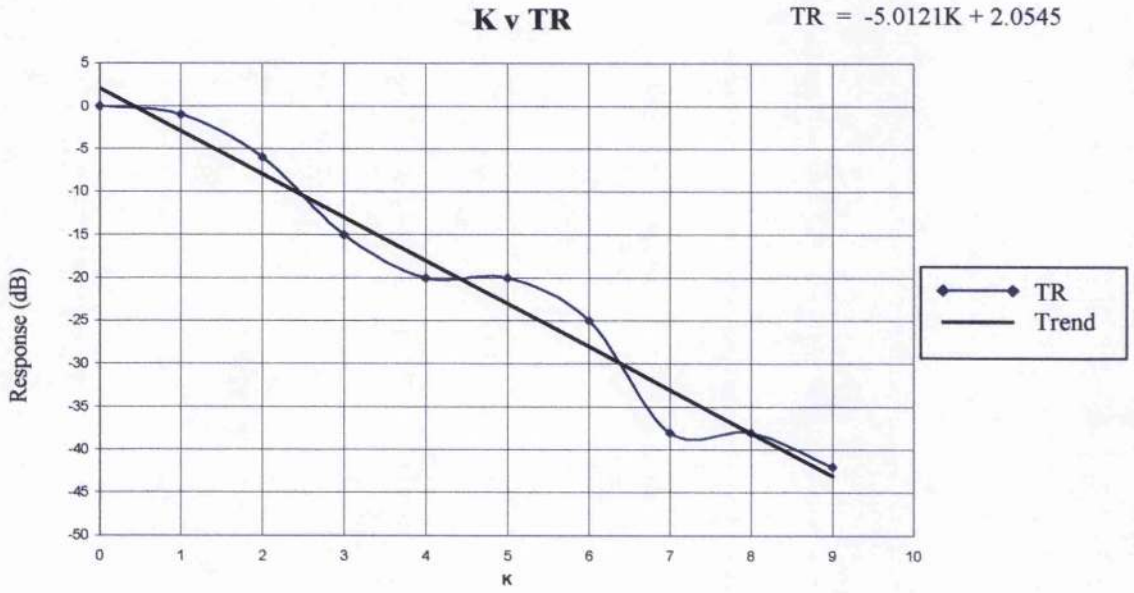

This plot shows that the transmit response will be strongest where K=0, and will drop to around –43dB as K nears 9.

The trend of the transducer transmit response can be crudely equated to the straight line equation:

$$\mathbf{TR = -5.0121(K) + 2.0545} \qquad \textbf{Equation 6.xvi}$$

as shown in Figure 6.14. The equation provides a decibel measurement of the response of the transducers during transmission at the angle K.

In a similar manner, Figure 6.15 shows how an equation is generated for the derivation of a decibel value for the receiver response (RR) at the angle K, where K ranges from 0 to 9.

Figure 6.15 Graph of manufacturers K measurements plotted against transducer receive response

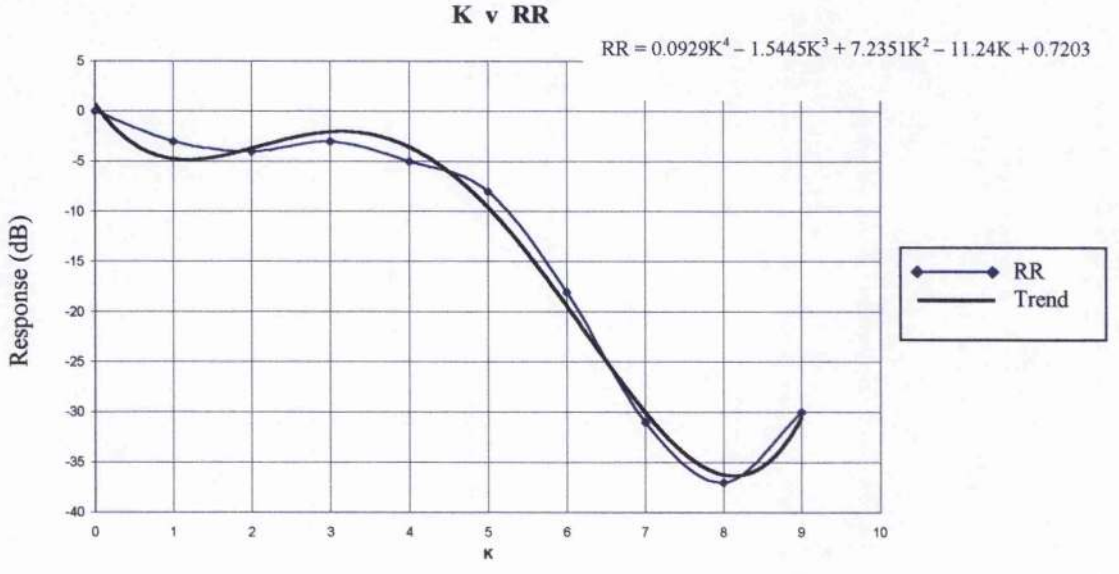

The receive response (RR) can be seen to correlate strongly with the trend line and thus a value for RR may be obtained by substituting a value for K into the linear equation of the trend line:-

$$\mathbf{RR = 0.0929(K^4) - 1.5445(K^3) + 7.2351(K^2) - 11.24(K) + 0.7203} \qquad \textbf{Equation 6.xvii}$$

The pattern of receive response is similar to that of the transmit response, with a maximum receive response where K=0, and a minimum response where K= 8.

The complete directivity index values can be generated by substituting the equations for TR and RR in to the equation for DI, to provide a measure of directivity strength across the entire swath in relation to K. Thus:-

$$\mathbf{DI = BD + TR + RR} \qquad \textbf{Equation 6.xviii}$$

Where;

DI = Directivity Index relative to K, measured in dB

BD = Beam directivity = 28.415dB for the ISIS 100 234kHz system

TR = Transmit Response = $-5.0121(K) + 2.0545$

RR = Receive Response = $0.0929(K^4) - 1.5445(K^3) + 7.2351(K^2) - 11.24(K) + 0.7203$

The complete directivity index of the ISIS 100 234kHz system can be plotted against K, as illustrated in Figure 6.16, to show how the intensity of the beam will vary according to the deviation of the response angle from the main directivity (perpendicular to the transducer face). Figure 6.16 also illustrates the full 180^0 directivity index (K range = -9 to 9) across the transducer face.

Figure 6.16 shows that the highest directivity index of 28.415dB is found along the perpendicular axis from the transducer face, where K=0. As the value of K increases and decreases from zero, the directivity index drops off relatively gently to K=4 or –4, before declining more rapidly between K=4 or –4 and K=8 or –8 respectively.

Figure 6.16 Graph of ISIS 100 234kHz beam intensity relative to the response angle, where K=0 represents the centre of the beam, along the perpendicular axis to the transducer face.

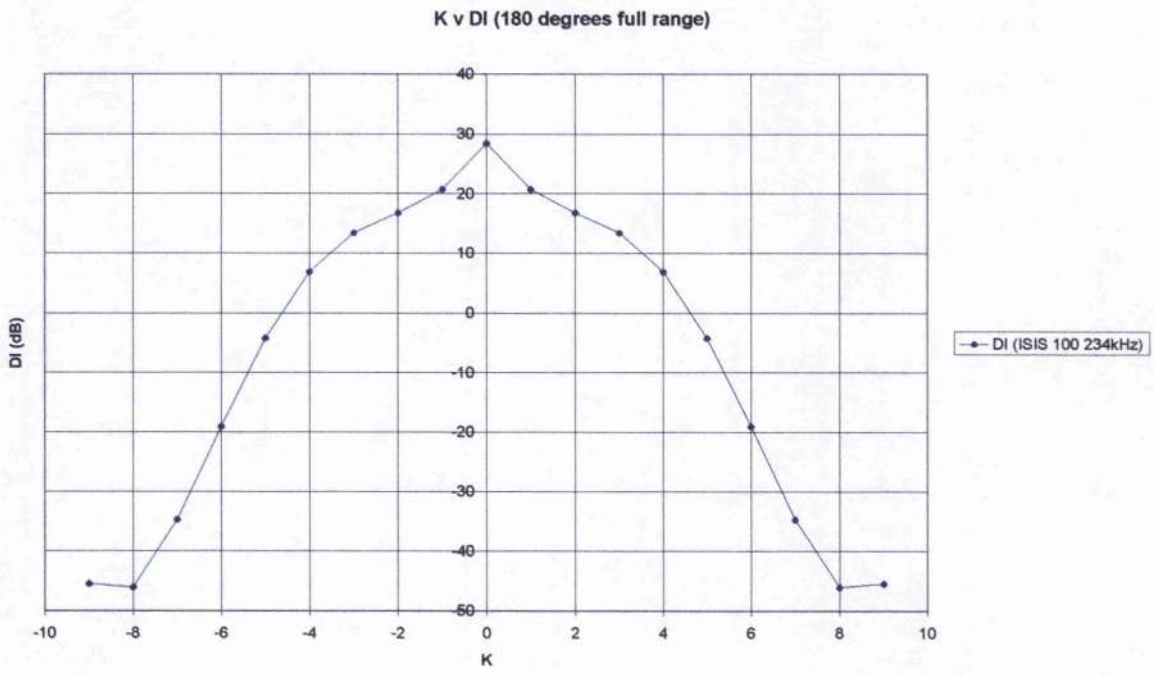

6.xvii. Received Voltage (RV)

The sound level detected by the receivers is initially measured as a sound pressure level across the receivers, before being converted into a voltage reading by the transducer. In order to enhance the accuracy of the returned signal strength as detected by the transducer, this voltage reading is then converted into a 16-bit number and then attached to the corresponding depth element within the swath file.

In post-processing, this 16-bit amplitude number must be converted back into a voltage reading before it can be transformed into an acoustic decibel measurement. This re-conversion was performed using a linear conversion equation derived from the manufacturers laboratory test results of the voltage to 16-bit conversion (Figure 6.17).

Figure 6.17 Graph showing linear conversion from 16-bit amplitude number to milli-Volts (mV)

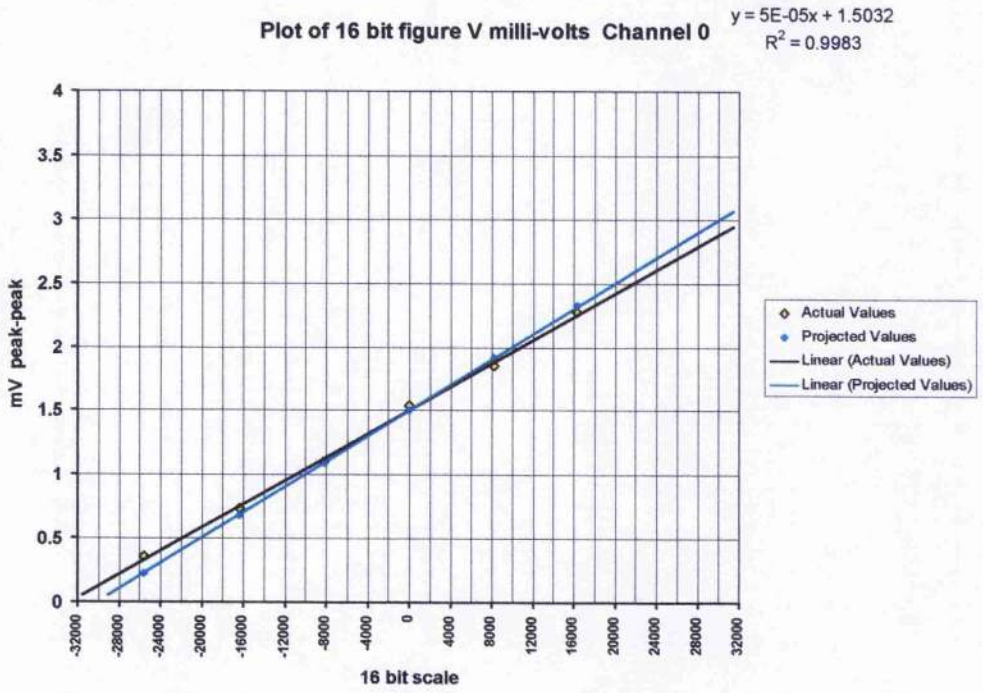

The straight-line equation of the trend line in Figure 6.17 provides a very close approximation to the equation used to convert between the 16-bit amplitude units and milli-volts. Thus the Received Voltage (RV) can be solved by entering the 16-bit amplitude number into the following equation:-

$$\mathbf{RV = [(4.5874 \times 10^{-8}) . Amp] + 0.0015032} \qquad \textbf{Equation 6.xix}$$

Where;

RV = Received Voltage (measured in volts)

Amp = 16-bit Amplitude number

6.xviii. Received Level (RL)

This received voltage (RV) can then be converted into a decibel measurement of the Received Level (RL) to determine the strength of the returned acoustic signal, using Equation 6.xix.

$$\mathbf{RL = [20\ Log_{10}\ (RV)] - [R_{sens}]} \qquad \textbf{Equation 6.xx}$$

Where;

RL = Received Level (dB)

RV = Received Voltage (Volts)

R_{sens} = Receiver Sensitivity (dB re 1V/uPa @ 1m)

The plotting of the raw RL detected back at the transducers may be likened to producing a side-scan imagery measured in decibels.

6.xix. Target Strength (TS)

The Target Strength (TS) of each element is defined by 'Lamberts Law' for interface scattering, following the recommendations made in Chapter 2. This target strength parameter is calculated using Equation 2.xx, which derives the decibel measurement of Lamberts Law for the backscattering strength (S_B) at an interface.

$$S_B = 10 \log \mu + 10 \log dA \sin^2\alpha$$

In addition, this equation requires the inclusion of a compensation factor to account for the backscatter variations induced by changes in the sonar frequency (Urick, 1983). For this purpose, Urick (1983) graphed backscatter results for varying sonar frequencies at set angles of incidence, to illustrate the effects of sonar frequency variations upon backscatter values.

These results were extrapolated and then normalised by Geen (1997) for application to the ISIS sonar frequency, giving a normalised backscatter value (Bsk_0) of –18.979 dB for the 234kHz system. This normalised backscatter value can then be used to replace the logarithm of the proportionality constant (μ) giving:-

$$TS = Bsk_0 + 10.\log[dA \,.\, \sin^2 \alpha]$$

$$TS = -18.979 + 10.\log[dA \,.\, \sin^2 \alpha] \qquad \textbf{Equation 6.xxi}$$

Where;

TS = Target Strength of the element

Bsk_0 = Backscatter value normalised to 0^0

***d*A** = Area of element = E_{area}

α = Total grazing angle

The target strength parameter defined by Equation 6.xx. can be applied to every element within a swath, in order to produce maps of predicted target strength variations.

6.xx. Echo Level (EL)

The Echo Level is defined as being the "expected" received value measured in decibels once all of the sonar factors have been accounted for, in accordance with the sonar equation.

$$\mathbf{EL} = \mathbf{SL} - \mathbf{TTL} + \mathbf{DI_{ping}} + \mathbf{TS} \qquad \textbf{Equation 6.xxii}$$

Where;

EL = Echo Level (value in dB)

SL = Source Level

This Echo Level equation allows the theoretical impact of the combined effects of transmission loss, directivity and target strength upon the sonar pulse to be predicted. Figure 6.18 shows a map of echo level variation across a sample of the Invincible area.

In assuming that all the equations for transmission loss and directivity are correct, any discrepancies viewed must be attributed to inaccuracies in the theoretical target strength value derived by Lambert. As Lamberts Law for interface scattering assumes the scattering or reflecting surface is flat, it becomes apparent that the likely cause of any discrepancies between the expected and actual receive levels will be related to the roughness of the reflecting plane.

Figure 6.18 Map of expected Echo Level associated with each element, taken from the Inv003 swath. The yellow arrow represents the general track plot of the vessel.

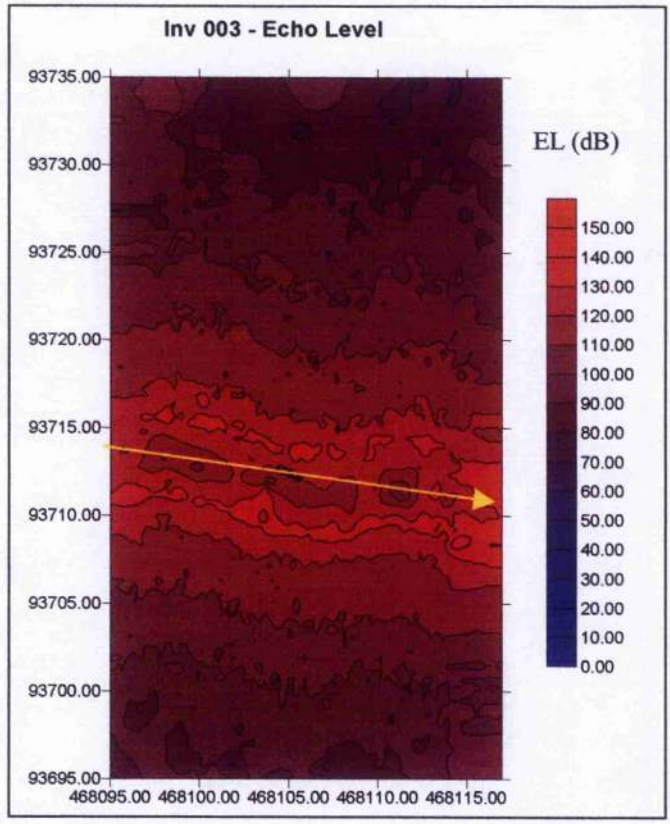

6.xxi. Actual Scattering strength at the water sediment interface (AS)

If the discrepancies are assumed to occur at the water-sediment interface, then it is necessary to derive an actual scattering strength to compare with the theoretical scattering strength provided by Lambert. This actual scattering strength can be measured by simply re-arranging the sonar equation (Equation 2.i) to solve for TS. In order to distinguish between the actual and theoretical scattering strength parameters, the actual scattering strength is referred to simply as the Actual Scattering at the water-sediment interface, and is denoted by AS.

The Actual Scattering can be defined as the loss attributed to the fate of the acoustic signal at the water-sediment interface.

$$\mathbf{AS = RL + TTL - SL - DI} \qquad \textbf{Equation 6.xxiii}$$

Where;

AS = Actual Scattering strength at the water-sediment interface
RL = Received Level
TTL = Total Transmission Loss
SL = Source Level
DI = Directivity Index

The use of the true received level (RL) instead of the echo level is critical to the derivation of the actual scattering strength. In applying this equation to every element, it becomes possible to directly compare and contrast the values of TS and AS, in which the scale of the discrepancy can be inextricably linked to the roughness of the seabed within each element area.

6.xxii. Roughness Indicator (Ri)

Although the degree of roughness is partly determined by the element area and the angle of incidence, the comparative values for TS and AS derived for the same element will be subjected to the same area and angle of incidence factors. This means that an evaluation of the bed roughness within each element can be carried out by simply subtracting AS from TS, or vice versa. If TS is assumed to be the normal scattering strength for a flat surface, then TS can be regarded as the 'normal,' and AS as the deviation from the normal, giving an indication of bed roughness provided by the following equation:-

$$\mathbf{Ri = TS - AS} \qquad \textbf{Equation 6.xxiv}$$

Where;

Ri = Roughness indicator
TS = Target Strength (theoretical)
AS = Actual Scattering strength

Thus the value derived for Ri offers a digital parameter for the evaluation of bed roughness.

In order to derive a relationship between the digital roughness parameter and the true roughness, the value of Ri must be compared to the bed roughness implied by the sediment analysis.

Before proceeding to the sediment analysis, it is imperative that the digital data be subjected to refined filtering in order to ensure the digital values for RI are as accurate and reliable as possible.

6.4. Data Quality Enhancement through Refined Filtering

6.4.1. Introduction

Although the application of the broad depth filters to remove multiple reflections and noise from around the transducers (as described in section 6.3.2) was clearly successful, a glance at the broadly filtered raw depth profile in Figure 6.7 suggests the presence of more discrete bathymetric anomalies within the profile. This concern is highlighted in Figure 6.19 which provides a close-up view of a short section from the same ping.

This section will outline the techniques used in the refined filtering of the ISIS datasets to remove elements that do not conform to the general element pattern or distribution produced by each ping. This stage in the processing is critical to the enhancement of the precision and accuracy of the topographic profile of the seabed, which forms the basis for the derivation of the acoustic data applied within the seabed classification analysis.

The intricacies of the identification and elimination of these non-conforming, anomalous elements must be performed on an element by element scale across the depth profile to maintain the precision of the datasets. The refined filtering processes are thus based upon the three dimensional location of elements in relation to adjacent elements within the same ping, with the evaluation being carried out through the examination of

several trigonometric parameters generated from the spatial relationship between elements.

Figure 6.19 Close-up view of a section from Ping 1640 from Cal2Sam1

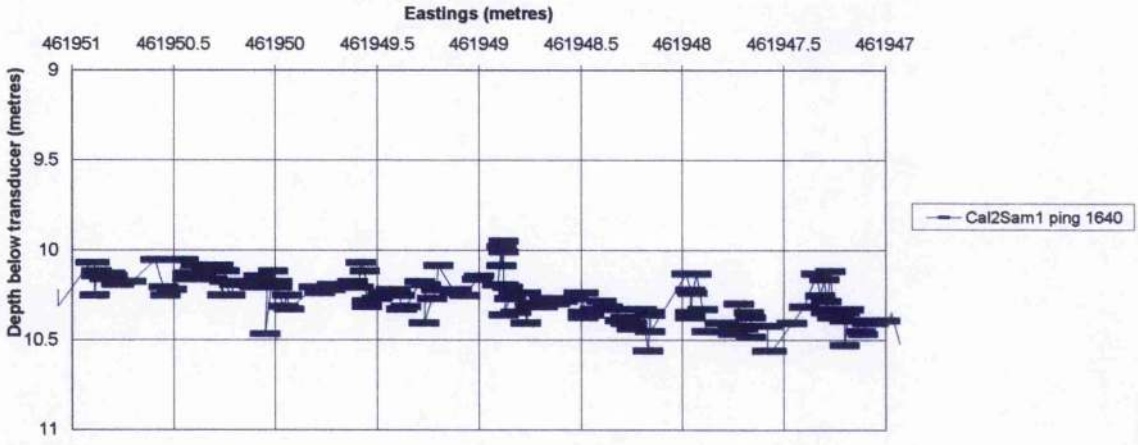

A detailed investigation resulted in the identification of four separate trigonometric parameters; **(1) Depth (D_t), (2) Slope angle (α_S), (3) Total grazing angle (α)**, and **(4) grazing angle assuming a flat, horizontal seabed (α_H);** which could be used to carry out the refined filtering of elements.

The plot in Figure 6.19 can be used to broadly visualise how each of these parameters calculated from the spatial distribution of adjacent elements can be used to determine the likelihood and reliability of both the parameter value, and the position of the element itself.

It should be noted that every stage of the filtering process involves only the complete elimination of unwanted elements, and does not entail any form of averaging or interpolation, thereby preventing any loss of data precision or reliability.

6.4.2. Depth Filtering

The filtering of swath files based upon depth data is probably the most common form of data filtering within sonar processing. The general principle applied involves the

analysis of height differences between adjacent elements within the same ping, which once calculated, are filtered using a maximum tolerance value as defined by the user.

The maximum tolerance of vertical offset between adjacent elements was set at 1 metre within the depth filter, and applied throughout the swath file. The application of this filter was complicated by the presence of shipwrecks, given the nature of the survey sites. In order to prevent the deletion of elements representing existing anomalies on the seabed, such as shipwreck debris, this filtering required a condition of application. The depth filtering was therefore confined in application to points where the horizontal distance between each element was less than 1 metre, as a one metre height difference over a metre horizontal distance was deemed 'possible' given the wrecks and debris present within the survey sites. As the presence of wreck debris prevented the complete smoothing of the depth data, the slope angle parameter was used to further cleanse the dataset.

The elements that fall out-with the maximum tolerance are normally 'smoothed' during bathymetric processing, but in this case are deleted completely. In avoiding the generation of interpolated values during the 'smoothing' process, the data which remains is regarded as being as accurate and true as the system's precision permits.

In summary, this technique allowed a refined filter of the more subtle erratic depth samples in a 2-dimensional sense (across-track / along-ping). Once the unwanted elements had been removed the spreadsheet recalculated all the trigonometric values using the new element distribution to derive refined spatial relationships prior to further filtering.

6.4.3. Slope Length Filter

This filter was applied in order to limit the spatial range between the elements involved in the trigonometric calculations. In setting a maximum slope length of one metre, this

prevented the large scale averaging of seabed slope angles over areas with sparse data coverage, and thus increased the level of confidence in the slope angle calculation.

6.4.4. Slope Angle Filter

Although in most cases bathymetric datasets are simply filtered by the height difference factor alone, a method of relating the height difference to the horizontal distance between each element using the slope angle of the seabed between elements is proposed here. This seabed slope angle parameter, derived from the element depth and horizontal distance, provides an additional technique for the filtering of elements based upon their relative depths. The slope angles between elements (α_S) can highlight areas where the user may 'expect' to find an acoustic shadow zone caused by seabed undulations or seabed anomalies. If elements are indeed found in this area, then it suggests that the height or nature of the object casting the acoustic shadow may not be as first thought.

The slope angle filter was given both upper and lower limits with which to filter the elements within the swath files. Where the slope angle is positive, the slope is regarded as facing away from the transducer, and where negative, it is regarded as facing towards the transducer, as discussed in section 6.ix. The upper limit of the positive values was set equal to the grazing angle 'α_H', as where the slope angle equals or exceeds 'α_H' the incident pulse would run tangentially to the seabed surface and there should be no incidence between the slope and the acoustic pulse.

The lower limit of the negative values was set at -50^0 so as to eliminate the unrealistically steep slopes facing the transducer. The spreadsheet was again set to re-calculate the trigonometric parameters to encompass the data refining offered by this filter. This was the final stage of re-calculation.

It should be noted that this slope angle filter operates only in 2-dimensions, as a result of the slope angle calculation itself being based upon elements within the same ping.

6.4.5. Total Angle of Incidence Filter

This filter is primarily designed to remove any elements with erratic incidence angle values. The maximum value of α was set at 140^0 in order to encapsulate the topography of slopes facing towards the transducers, whilst the minimum value was set at 20^0 to remove the erratic data obtained from very acute angles of incidence, following the practice of Urick (1983).

In addition, this filter can also be used to focus the acoustic analysis upon interface scattering by eliminating the elements whose associated 'α' values lie either within the 'spectral reflection' range (near 90^0) or beyond the critical angle. This necessitated the rejection of an intermediate range of between 80^0 and 100^0 due to the possible dominance of spectral reflection, whilst the minimum value of 20^0 set by Urick (1983) was deemed sufficient to cover anomalies induced beyond any potential critical angle.

The inclusion of elements with α values between 100^0 and 150^0 within the analysis was based on the assumption that their interface scattering properties would mirror those elements with α values between 80^0 and 30^0 respectively, as predicted by Lambert's Law.

In summary, this filter helped to enhance the quality of the dataset, whilst also focusing the acoustic analysis upon elements whose acoustic response is dominated by interface scattering.

6.4.6. Grazing angle (assuming a flat seabed) filter

The grazing angle parameter was used to delimit the acceptance of high-range element data due to the increase in system error margins with increasing range, as described in Chapter 4 section 4.5. This filter was used in place of a simple range filter, because since the depth below the transducer is a factor in the derivation of this parameter, it means that it is automatically corrected for varying water depths, unlike the range filter.

This grazing angle filter may be regarded as operating on both the trigonometric and the sonar level, as the filter extracts both the low reliability bathymetric data at far-range and also the erratic sonar scattering results associated with low grazing angles.

In addition, this filter was also used to complement the directivity index of the sonar by setting the minimum acceptance angle to be equal to the transducer angle at that moment in time. This enabled acceptance of the elements up to a maximum range determined by the angular nature of the peak directivity of the sonar, which as demonstrated in section 6.xvi., relates to a grazing angle that is equal to the angle of the transducer face from the vertical.

This resulted in a minimum angular acceptance level of approximately 30^0.

6.4.7. Filtered digital data coverage over ground-truthed locations

The result of the refined data filtering process is an enhancement of the quality and reliability of the remaining element data. Each element present at this stage will have its own unique set of values for the trigonometric and acoustic parameters, with the confidence in the data having been enhanced by the re-calculation of the values following the first two stages of filtering. This means that each element can be treated as one sample of the acoustic analysis.

The effectiveness of this acoustic sampling coverage can be visualised in Figures 6.20 to 6.24, by the plotting of these remaining elements within the critical ±1m Eastings and Northings range of the grab sample locations. The sample locations plotted have been selected to permit a direct comparison with the raw data coverage plots provided in Chapter 5. The same scaling has been applied to each plot, and the dimensions and orientations of the elements plotted within each area have been scaled and angled to match the trigonometric and geometric fields relating to each element.

Figure 6.20 Filtered element coverage within ±1m range of Sample Site 2 (Cal2Sam2)

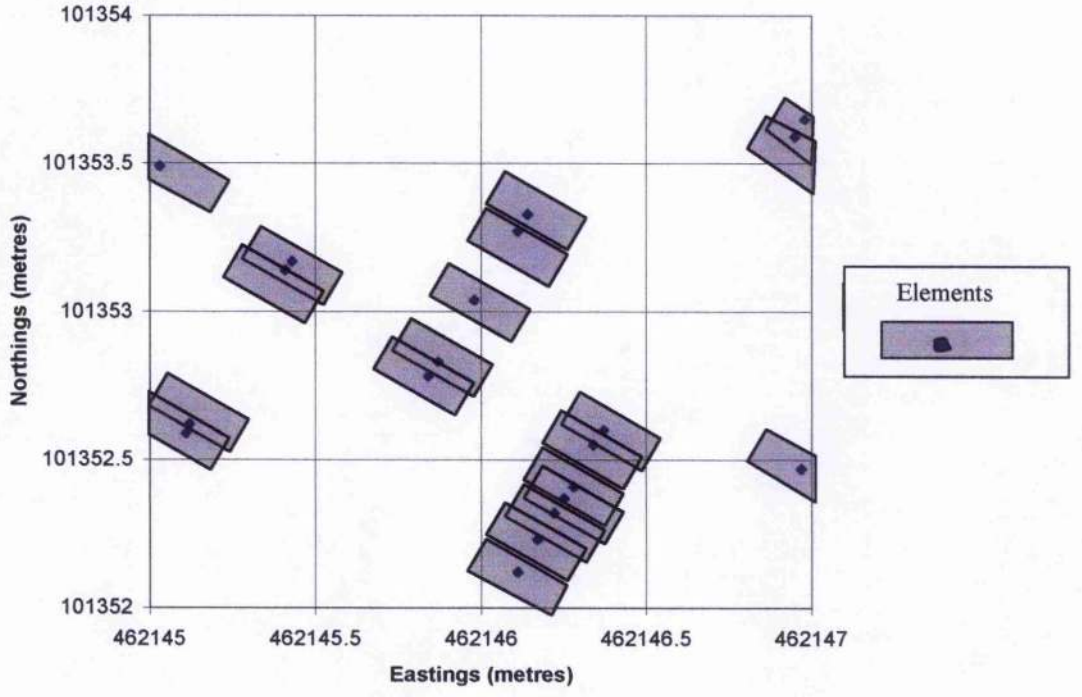

Figure 6.21 Filtered element coverage within ±1m range of Sample Site 5 (Shingle1Sam5 W-E section only)

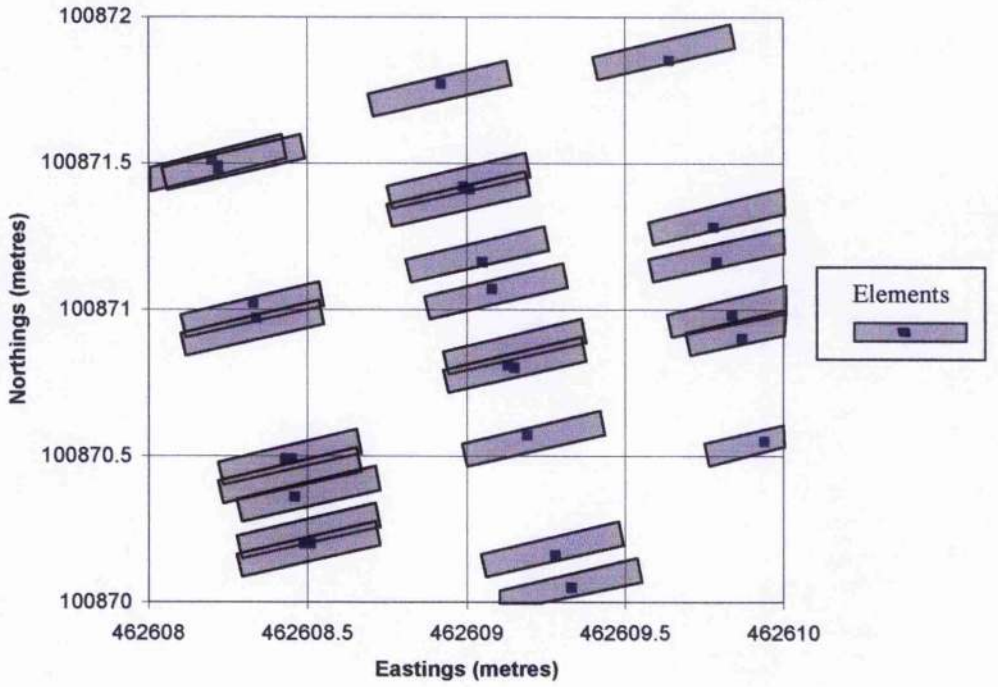

Figure 6.22 Filtered element coverage within ±1m range of Sample Site 11 (Inv000.5swath only)

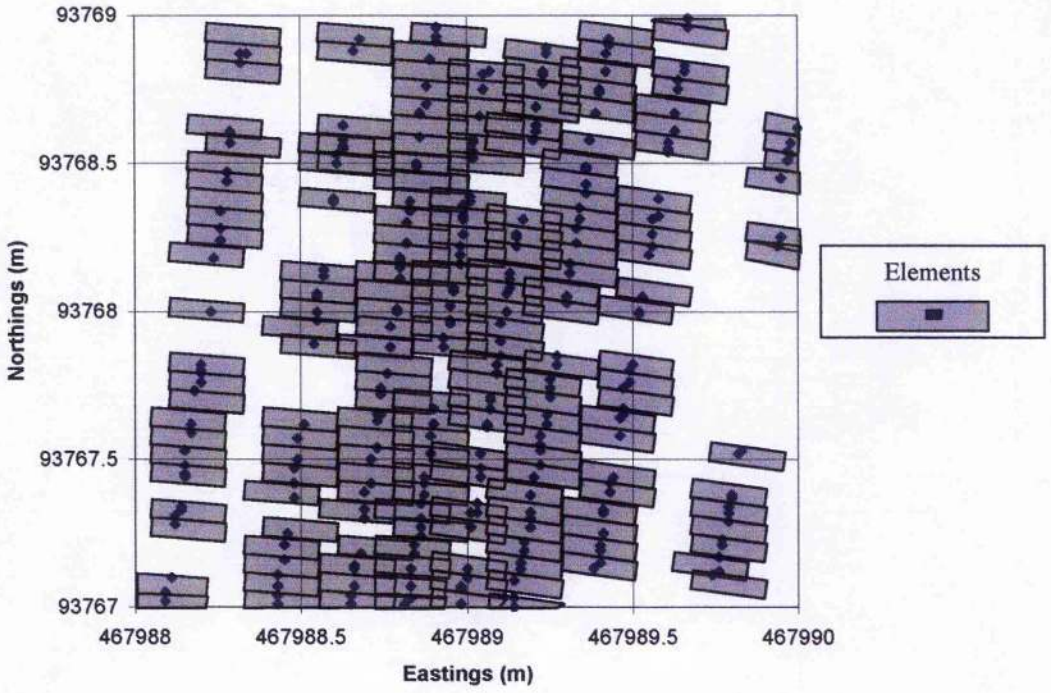

Figure 6.23 Filtered element coverage within ±1m range of Sample Site 14 (SubxlSam14 swath only)

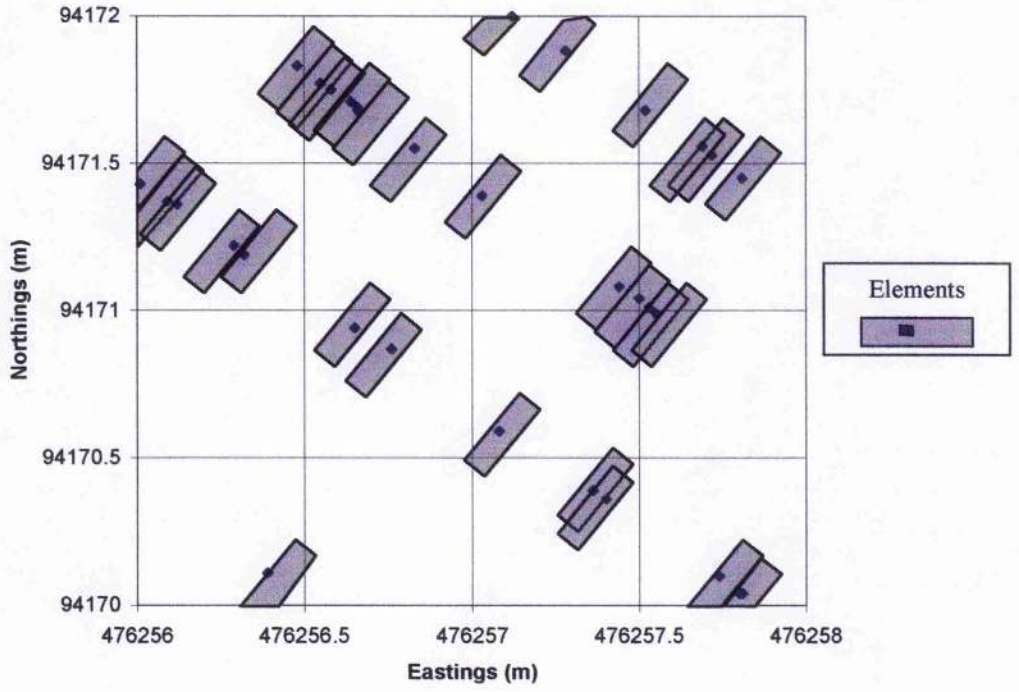

Figure 6.24 Filtered element coverage within ±1m range of Sample Site 15 (Sub000a and Subxlc swaths only)

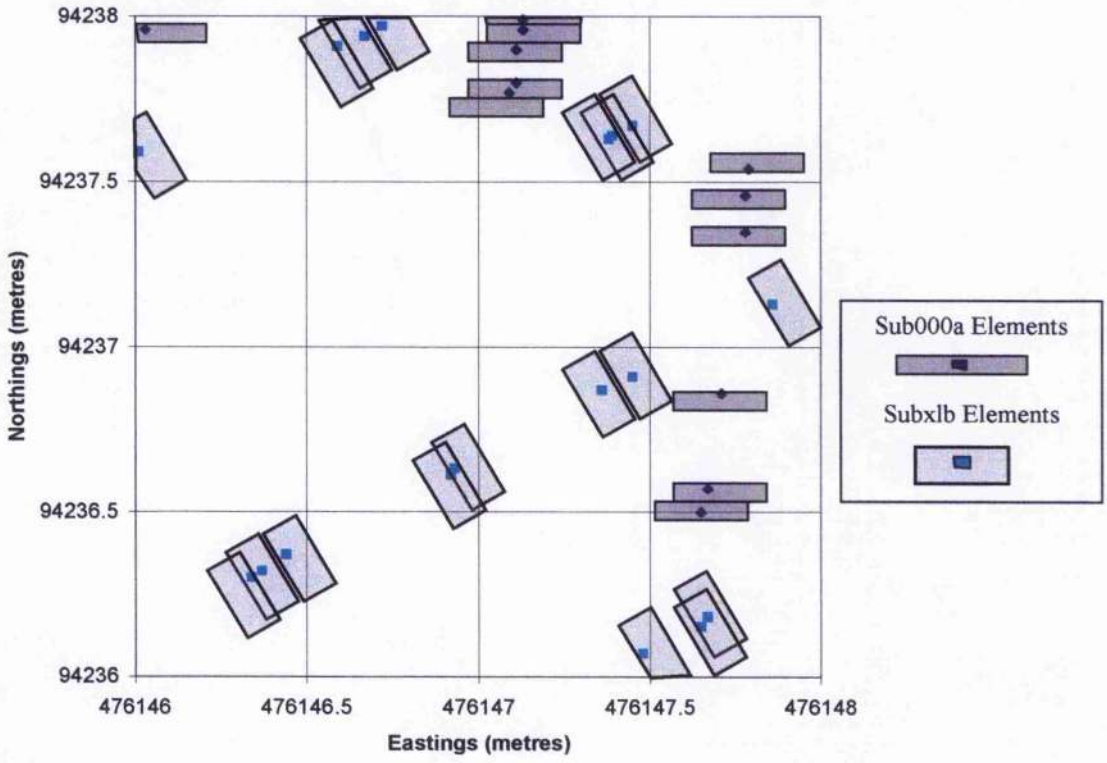

These plots show that even after refinement of the datasets using a variety of filers, a high rate of refined digital sampling within ±1m of the grab sample locations is maintained.

The low density of elements within Figure 6.20 is attributed to the occurrence of many near-normal grazing angles of incidence, as the sample location lies very close to the vessel track-plot (Figure 5.23).

The data coverage in Figure 6.21 is taken from a different section of the swath than that of Figure 5.24, and thus does not truly represent the same data densities that could be expected. This change in swath section was carried out because the shear density of the data in Figure 5.24, proved so dense that it masked the visual objective of the plot.

Figure 6.22 shows that the Invincible site was also subjected to a dense covering of high data quality elements. The along-track ping density reflects a higher ping rate within the

site, as shallow waters and a short range reduced the 'listening' period required by the sonar.

The plots in Figures 6.23 and 6.24 provide a perfect example of the changes in the survey aspect, achieved by the addition of cross-lines (Subxl, Subxlb and Subxlc), can alter the orientation of the elements on the seafloor.

6.4.8. Summary of filtering process

The refined filtering processes applied to the swath files can clearly clarify the topographic profile of each ping, without the need for extrapolation or interpolation of the dataset. This means that the enhancement of the bathymetric data quality recorded by the ISIS is done simply by extracting the elements which have a low reliability, as performed by the depth and slope angle filters.

Once this bathymetric profile has been refined and finalised, the filters applied to α and α_H are used to ensure that only the elements whose acoustic response is dominated by interface scattering will be applied to the sediment-acoustic analysis.

These filtering techniques are regarded as satisfying the requirements for the digital data quality and precision demanded by the sediment-acoustic analysis.

In spite of this, it must be acknowledged that the incorporation of an along-track angular dimension within the trigonometric analysis would obviously provide a higher level of quality control and a higher precision of the angular impact upon the degree of scattering. At present, the trigonometric analysis is carried out only in a 2-dimensional, across-track sense, and is therefore subject to the assumption that each element represents a valid/true point of reflection on the seafloor.

One adaptation that would have helped to counter this problem is the construction of a 3-dimensional chart of the seabed prior to processing the angular calculations within the

trigonometric analysis. Although attempts were made to create a three dimensional filter, the fact that this had to be done using raw data meant that serious logistical problems were encountered due to the excessive number of data points within each swath file (as tabulated in Tables 5.2 and 5.3).

It is hypothesised that a combination of across-track and along-track quality controls would have simplified the methodology for determining the level of confidence attributed to the location of each element, as well as enhancing the accuracy of the angular relationships at the water-sediment interface.

6.5. Conclusion

This chapter has shown how the derivation of values for all the parameters identified and evaluated within the trigonometric and sonar analysis can furnish the sediment acoustician with enough information to analysis the acoustic interaction at the water-sediment interface beyond any precision or resolution previously achievable.

This analysis has also shown that by deriving and successfully preserving the orientation and dimensions of each element, the digital data can be used to provide more than simply multiple acoustic samplings within each $2m^2$ area of seabed. In addition, the utilisation and analysis of the orientation and element dimension data may also be used to demonstrate the effects of varying the sonar aspect, and varying angles of incidence and roughness scales, through the cross-analysis of elements sampled over the same seabed type.

The processing techniques employed within the trigonometric and sonar analysis have also generated three secondary benefits;

(1) a mechanism for automating slant range corrections on 'side-scan' images, which can be achieved through recompensating each element field for the acoustic losses incurred by transmission through the water column

(2) a mechanism for accurately examining the seabed slope angles in two dimensions, using Sl_e

(3) the facility to produce accurate swath variability maps of all the trigonometric and sonar parameters

This chapter has ultimately enabled a direct comparison between the theoretical interface scattering strength (TS), derived by Lamberts Law, and the actual interface scattering strength (AS) derived through the trigonometric and sonar analysis. In assuming that Lamberts Law accurately accounts for the interface scattering induced by a flat surface, where the grazing angle is α and the area of insonification is represented by, $d\mathbf{A}$, then any discrepancy between TS and AS must be directly related to the only parameter unaccounted for by the digital data analysis – that of the degree of surface roughness within each element area. In order to evaluate the seabed roughness the attention must turn to the analysis of the material sampled at each site.

SUMMARY OF EQUATIONS

Equation 6.i. $H_d = \sqrt{[(X_2 - X_1)^2 + (Y_2 - Y_1)^2]}$

Equation 6.ii. $D_t = (D_{RP} + T) - T_d$

Equation 6.iii. $r = \sqrt{\{[(X_2 - X_1)^2 + (Y_2 - Y_1)^2] + [D_t]^2\}}$

Equation 6.iv. $E_w = r \cdot \tan \beta$

Equation 6.v. $E_L = [(P_L) / (\cos \alpha)]$

Equation 6.vi. $E_{area} = E_L \cdot E_w$

Equation 6.vii. $Sl_e = \sqrt{[(Dt_{n+1} - Dt_{n-1})^2 + (Hd_{n+1} - Hd_{n-1})^2]}$

Equation 6.viii. $\alpha_H = \cos^{-1} (H_d / r)$

Equation 6.ix. $\alpha_S = \tan^{-1} [(Dt_{n+1} - Dt_{n-1}) / (Hd_{n+1} - Hd_{n-1})]$

Equation 6.x. $\alpha = \alpha_H - \alpha_S$

Equation 6.xi. $Ab = K_{ab} \cdot r$

Equation 6.xii. $SS = 20 \log r$

Equation 6.xiii. $TTL = 2 (SS + Ab)$

Equation 6.xiv. $BD = 10 \log [(4\pi) / (\phi \cdot \beta)]$

Equation 6.xv. $K = (90 - EA - TA + 5)/10$

Equation 6.xvi. $TR = -5.0121(K) + 2.0545$

Equation 6.xvii. $RR = 0.0929(K^4) - 1.5445(K^3) + 7.2351(K^2) - 11.24(K) + 0.7203$

Equation 6.xviii. $DI = BD + TR + RR$

Equation 6.xix. $RV = [(4.5874 \times 10^{-8}) \cdot Amp] + 0.0015032$

Equation 6.xx. $RL = [20 \text{Log}_{10} (RV)] - [R_{sens}]$

Equation 6.xxi. $TS = -18.979 + 10.\log[dA \cdot \sin^2 \alpha]$

Equation 6.xxii. $EL = SL - TTL + DI_{ping} + TS$

Equation 6.xxiii $AS = RL + TTL - SL - DI$

Equation 6.xxiv $Ri = TS - AS$

CHAPTER 7:

SEDIMENT DATA ANALYSIS

7.1. Introduction

The textural characterisation of the sediment samples collected from each of the field areas examined for acoustic scattering is discussed in this chapter.

In Chapters 2 and 3 the effects of surface roughness, adjusted for angle of incidence and resolution, were highlighted as the main determinants of the acoustic scattering strength of a reflecting surface - as illustrated in both theoretical and practical models.

The surface roughness parameter is refined by the digital data processing in Chapter 6 which illustrates how the ISIS data can be used to derive accurate measurements of depth/range, planar orientation (total angle of incidence) and element dimensions (resolution) for each insonified area. In measuring these additional parameters, the scattering surface area can be placed in elevation and orientation (relative to the transducers), and the dimensions of the area can be adjusted for localised seabed slope angles. This digital data processing thus leaves the surface roughness within the insonified area as the only factor unaccounted for in the scattering process described in Chapter 2.

Before the roughness factor can be evaluated, it is essential to examine the relationship between bathymetric resolution and surface topography in order to determine the scale of the surface roughness under analysis.

The surface roughness factor is traditionally assessed on two different scales, namely 'micro-topographic variation' (surface features/patterns) and 'bed roughness' (particulate roughness). As stated in Chapter 4, the use of the high resolution ISIS system enables the bathymetric measuring of the micro-topographic variations of bedforms, and so any surface roughness analysis must focus upon the 'bed roughness'

which is present within the insonified area, and undetected by the bathymetric data. This 'bed roughness' parameter is assumed to relate directly to the nature and composition of the material found at the surface of the scattering plane (seabed). The sediment analysis will examine the full roughness range of the reflecting surface as precisely as possible, by measuring the particulate nature of the surface sediments and assessing the influence of particle size upon the roughness of the insonified area. It is essential that this process incorporates mobile sediment within the assessment of the material properties and composition of the surface sediment, as all particles contribute to the roughness of the surface. It should be noted that the grain size analysis of the sediments will determine the true bed roughness of the sediment, and not that perceived by the angle of incidence and the size of the insonified area.

The refined aim of this chapter is to identify and measure the roughness characteristics of the seabed sediment that can be accurately measured from grab samples, as well as discussing additional characteristics that can be inferred from the actual sediment analysis results. This primary data will form the basis for an evaluation of the surface roughness or texture associated with each sediment sample collected. It should be noted that the textural analyses of sediments cannot be confined to an analysis of the particle size however, as biological factors can also influence the surface roughness at the water-sediment interface through the presence of shell fragments and organic matter. This means that the laboratory analysis of the sediments must take account of particle size, carbonate content and also organic content.

7.2. Impact of sample acquisition methodology upon sediment characteristic analysis

Although Chapter 5 provides a comprehensive explanation of the sample acquisition methodology, it is important to evaluate the impact of the acquisition methodology upon the precision and limitations of the detailed analysis of sediment properties.

Chapter 5 states that the van Veen method of sediment sampling retrieves material, but very little else in the way of sediment properties from the bottom, because of disruptions to the sub-surface sediment structure and a significant loss of water content. Such disruptions and alterations inhibit a direct analysis of density and porosity values from the retrieved sediments. Indeed, the British Engineering Standards state categorically that, in order to measure saturated sediment density 'all methods require physical access to the sediment *in situ,*' except in the case of very cohesive sediments. In light of this, the van Veen sampling technique only permits the direct analysis of particle size and material content of the upper layer of sediment.

Another limitation is induced through the combination of the random nature and small scale sampling of the sediments. Such a sampling technique is susceptible to the collection of 'unrepresentative' samples of the local surficial material. Whilst confidence can be applied to the more stable sediment body, it is necessary to be more cautious with regard to the spatial distribution of the more unstable surficial materials. This problem is accentuated in areas where the hydrodynamic levels are variable over a small area. For example, the random grab sampler may or may not contact a small-scale dead shell assemblage, especially in the vicinity of an underwater obstruction where currents are disrupted.

The van Veen sampling technique may disrupt the in-situ properties, the structure of the sediment, and be limited in its spatial representation, but it is still possible to learn much about the characteristics of the material. The refined sampling of the top 10mm of seabed sediment (discussed in Chapter 5) enables precise measurements of particle size distribution, sediment composition and a crude assessment of the surficial material. This refined sampling also allows verbal descriptions of the sea floor to be used in conjunction with the laboratory test results, to aid in the comparison of sediment

variability, partially clarifying the picture despite the random nature of the sampling programme.

7.3. Laboratory Analysis of Sediment Textures

7.3.1. Sample Preparation

Each sediment sample was divided into four representative portions to enable the independent analysis of the three sediment parameter variables highlighted above, with one quarter being curated for future reference. This quartering procedure was carried out upon the wet samples because each methodology of sediment property analysis required different preparation techniques. For example, Buller and McManus (1979) warn against drying sediments containing more than a few percent of clay as this can create a hard crust of clay on the surface of the sample, which even if broken down can still cause the occurrence of synthetic platy particles. The quartering of the wet sediment was also vital in the curation of a representative sample that preserved all of the original sediment properties. Surface shell fragments are often excluded from the particle size distribution analysis, and are instead treated as mobile sediments, since their platy, flakey, nature makes them very susceptible to water motion. In this case both clastic and carbonate particles must be incorporated because the overall aim is to relate the small-scale 'roughness' element of the seabed, caused by both clastic and carbonate surface scatterers, to variations in acoustic loss at the water-sediment interface.

The quartering procedure follows the recommendations of Buller and McManus (1979), where the sample is "coned" by pouring it into the middle of a flat-bottomed container, and then quartered. Although this method is primarily intended for dry samples, it was found to be just as effective for the wet samples collected in this analysis.

As the aim of the laboratory analysis was to measure the properties of the sediments as they occurred in nature, the samples were not 'washed'. This prevented the removal of

salts from the interstitial waters, thereby preserving the dynamic characteristics of the clay particles, and allowing flocculated particles to be incorporated in the particle size analysis.

7.3.2. Particle Size Analysis

The particle size analysis of each sample was carried out using a two-stage process. The samples were wet-sieved down to a size of 0.71mm, to extract and preserve the coarser fractions. This 0.71mm sieve was used as the minimum sieving stage because below 0.71mm, it was possible to replace the sieving technique with a faster and more precise electronic particle sizing and counting system known as a laser Coulter Counter. This change in technique at 0.71mm effectively acted as a divide between the coarse and fine fractions. Further information on the Coulter methodology and operating techniques can be found in Sheldon and Parson (1967), and McCave and Jarvis (1973).

The laser Coulter Counter is an industrially and academically accepted method of providing a simple, rapid, and very detailed analysis of the finer particle size-volume distributions within sediments.

The final particle size distribution results were generated by combining the sieve analysis and Coulter analysis measurements, to produce a complete particle volume-size distribution curve encapsulating both the coarse and fine fractions for each sample.

7.3.3. Carbonate Content Analysis

As particle size is the main sediment characteristic under investigation, the carbonate component was included within the particle size analysis. In order to assess the overall sediment composition, the analysis required the additional measurement of the percentage content of carbonates within each sample.

The following procedure was used to calculate the percentage weight of the carbonate content. In preparation for the carbonate testing, each sample was dried at 60^0C for 18 hours to remove all moisture present. Once the samples were reduced to their solid material content, the dry weight of each sample was recorded. 10mls of HCl (of known weight) was then added to each sample in order to dissolve the carbonate content. The same volume of HCl was also added to an empty container to act as a 'control' for evaporation loss. The samples were re-weighed after 12 hours to determine the post-reaction weight of each sample. The recorded weights were adjusted for the weight of HCl added, and also for the evaporation loss detected by the control HCl, to enable the derivation of weight loss directly attributed to the carbonate content.

The final weight of the carbonate content is expressed as a weight percentage of the initial sample in the results section.

7.3.4. Organic Content Analysis

The organic content of each sample was also measured as part of the assessment of the material composition of the surficial sediments.

The samples were prepared for the organic content analysis by being dried at 60^0C for 18 hours to remove the water content, after which the dry weight was recorded. The dried samples were then placed into the furnace at a temperature of 400^0C in order to burn off the organic matter. After 6 hours the samples were removed from the furnace and re-weighed to establish the weight loss attributable to the organic content.

The organic content of each sample is expressed as a weight percentage of the initial sample in the results section.

7.4. Interpretation of Textural Analyses

The textural classification and characterisation of seabed sediments is determined primarily by the nature of the particle size distribution. The simplest form of interpretation involves the size grading of each particle, as classed by Wentworth (1922).

The universally accepted Wentworth (1922) classification, describes the nature or grade of particles based upon measurements of the particle size or diameter, as illustrated in Table 7.1.

The classification of particle sizes by Wentworth (1922) has since been used by sedimentologists such as Trefethen (1950), Shepard (1954), and Folk (1954), as the basis for textural sediment classification schemes. These classification schemes are based upon the relative weight percentage compositions within Wentworth's major particle classification categories of gravel, sand, silt and clay.

In cases where gravels are present, silts and clays are amalgamated into a 'mud' grade, to enable a low-resolution textural classification using a Gravel-Sand-Mud ternary plot (Figure 7.1a). If no gravels are present, then the Sand-Silt-Clay grades are applied to the ternary diagram to determine the high-resolution textural class (Figure 7.1b).

These ternary systems have become the most frequently used form of textural characterisation for sediments containing substantial amounts of clasts either coarser or finer than sand (Smith & McConnaughey, 1999).

The Folk (1954) textural classification was selected from the various alternatives because it offers a more refined Gravel-Sand-Mud classification, as demonstrated in Figure 7.1.

Table 7.1 Wentworth Sediment Type Classification from Particle Size

WENTWORTH SEDIMENT TYPE CLASSIFICATION		PARTICLE SIZE RANGE		
		Metres	Milli-metres	Microns
		0.2	200	200000
COBBLES				
		0.06	60	60000
GRAVEL	COARSE			
		0.02	20	20000
	MEDIUM			
		0.006	6	6000
	FINE			
		0.002	2	2000
SAND	COARSE			
		0.0006	0.6	600
	MEDIUM			
		0.0002	0.2	200
	FINE			
		0.00006	0.06	60
SILT	COARSE			
		0.00002	0.02	20
	MEDIUM			
		0.000006	0.006	6
	FINE			
		0.000002	0.002	2
CLAY				

Figure 7.1 Comparative textural classifications of Folk (1954) and Shepard (1954) using ternary plots

a. Folk (1954) Low resolution classes

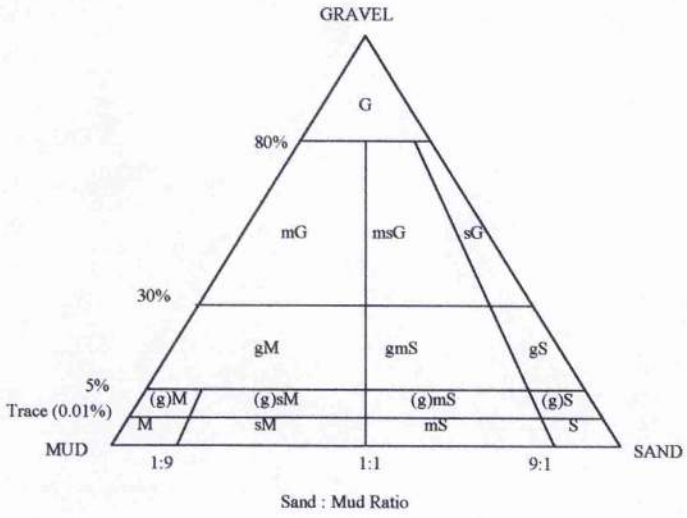

Shepard (1954) low resolution classes

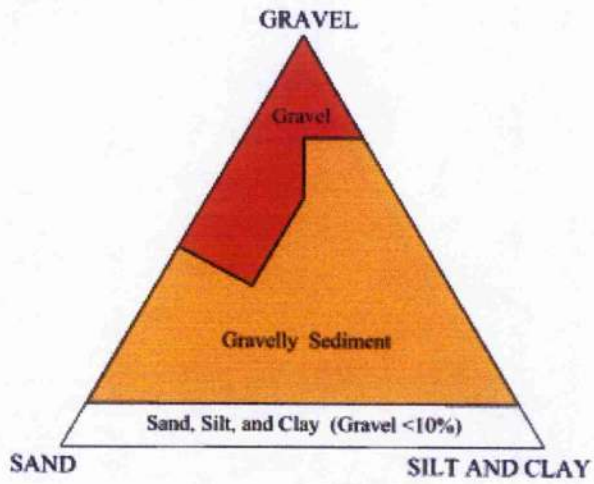

b. Folk (1954) high resolution classes **Shepard (1954) high resolution classes**

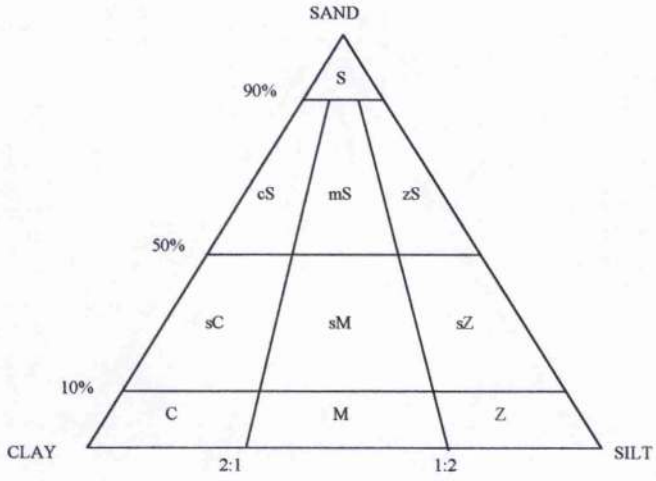

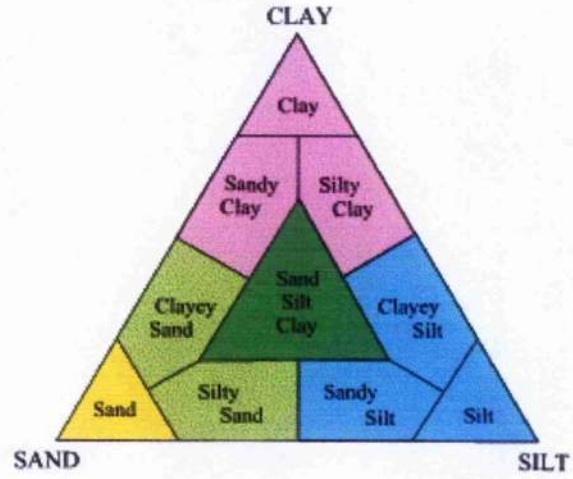

The greater discrimination of Gravel-Sand-Mud textures by Folk (1954) complements the evaluation of surface roughness, which necessitates the encapsulation of the larger, rougher, particles within the samples.

Table 7.2 provides a key to the classification symbology used in Figure 7.1.

Table 7.2 Terms applied by Folk (1954) to Gravel, Sand, Silt and Clay textural classifications

Gravel-Sand-Mud Ternary Plot	
Sediment Symbol	Major Textural Class
G	Gravel
sG	Sandy gravel
msG	Muddy sandy gravel
mG	Muddy gravel
gS	Gravelly sand
gmS	Gravelly muddy sand
gM	Gravelly mud
(g)S	Slightly gravelly sand
(g)mS	Slightly gravelly muddy sand
(g)sM	Slightly gravelly sandy mud
(g)M	Slightly gravelly mud
S	Sand
mS	Muddy sand
sM	Sandy mud
M	Mud

Sand-Silt-Clay Ternary Plot	
Sediment Symbol	Major Textural Class
S	Sand
zS	Silty sand
mS	Muddy sand
cS	Clayey sand
sZ	Sandy silt
sM	Sandy mud
sC	Sandy clay
Z	Silt
M	Mud
C	Clay

More sophisticated forms of textural analyses involve the application of graphical statistical methods to the textural spectrum in order to quantitatively assess the particle size distribution. These particle size distributions are traditionally displayed graphically as both 'cumulative frequency' and 'frequency weight percentage' plots.

The cumulative frequency curves graph the weight percentage trend of the samples by summing the sediment weights at each size interval below the selected particle size, and plotting the percentage weight of the sample that falls below this size value. These cumulative frequency 'weight percentage less than' curves provide all the necessary information for the statistical characterisation of sediments (See Folk & Ward, 1957, Inman, 1952).

The frequency weight percentage graphs, plotted against the Wentworth class divisions, are ideal for showing trends in frequencies of individual size grades and are especially useful in illustrating the verbal description of the samples (Buller & McManus, 1979).

Krumbein (1934) states that in order to maximise the precision of the statistical analysis, the particle size scale must be measured in the logarithmic units of Phi (ϕ). In accordance, all the metric (mm) units used in the sieve analysis were converted to Phi (ϕ) units using the conversion of $\phi = -log_2(particle\ diameter\ in\ millimetres)$, suggested by Krumbein (1934).

Once the cumulative-frequency and frequency-as-a-weight-percentage plots have been graphed using the Phi (ϕ) scale, all the necessary values can be derived for the statistical analysis.

The main statistical characterisation is carried out using four key measures (Buller & McManus, 1979);

1. Average Values – such as ***mean***, ***median*** and ***mode***, are designed to provide values around which all others cluster
2. Data scatter – such as ***dispersion***, ***standard deviation*** and ***sorting*** are used to measure the spread of data around the average values
3. Skewness - measures the degree of symmetry around the average values
4. Kurtosis - measures the degree of peakedness of the distributions.

There have been many proposed methodologies for these statistical measures, but the success of each statistical methodology is entirely dependent upon the extent of the distribution data available, and also upon the statistical resolution required by the user. Three of the most popular methods;

- Friedman (1962)
- Inman (1952)
- Folk and Ward (1957)

were examined for their suitability to the needs of this project.

The 'method of moments' proposed by Friedman (1962) is generally accepted as one of the most comprehensive statistical techniques, but its effectiveness is entirely dependent upon a 'closed' distribution, where every single particle has been encapsulated. This 'open' or 'closed' nature of the distribution concerns the ability of the analytical technique to account precisely for the extremities of the particle size range, an ability which itself is subject to debate (Inman, 1952).

There exist two schools of thought, with regard to the use of the distribution 'tails' in the statistical analysis techniques.

The 'inclusive' school of thought, supported by Folk & Ward (1957), Folk (1968) and Visher (1969), favours the inclusion of the distribution tails because they are viewed as highlighting the most critical differences between samples, and also as being the most sensitive indicators of the depositional environment. The application of this method is reserved for the analysis of 'closed' distributions, due to the high dependency upon information within the tails of the distribution. For example, the Folk and Ward (1957) analysis utilises 90% of the distribution, from the 5^{th} to the 95^{th} percentile, and the method of moments' technique requires the analysis of the full distribution.

In contrast, the 'exclusive' school of thought regards the distribution tails as reflecting the errors in the analysis technique, and being unreliable because they reflect different mechanisms of deposition. This theory is supported by Inman (1952) who proffers the most comprehensive, and universally applicable, statistical analysis for 'open' distributions (Buller & McManus, 1979). Inmans' analysis focuses upon the central 68% of the distribution, from the 16^{th} to the 84^{th} percentile, in order to avoid the 'tails' of the distribution.

The decision of which method to use hinges upon the fact that the coarse fraction is the most important fraction in terms of its impact upon surface roughness.

In assessing the cumulative frequency particle size distributions graphs for each sediment sample, it became clear that the statistical techniques of Folk and Ward (1957) offered the most accurate, and reliable, method of numerically evaluating the coarse fraction within the textural analysis. In covering the 5^{th} to the 95^{th} percentile, the Folk and Ward techniques encapsulated a substantially coarser fraction than that achieved using the 16^{th} - 84^{th} percentiles analysed by Inman (1952).

In focusing upon the extremities of the coarse distribution, the omission of the 0-5^{th} percentiles in the Folk and Ward method was found to decrease the susceptibility to errors in the analysis techniques, thereby providing a more reliable method to the

method of moments. In any case, the statistical values derived by both the 'Folk and Ward' and the 'method of moments' techniques are found to be very similar (Folk, 1968; Green, 1974).

In selecting the methods of Folk and Ward (1957) the Phi-scale statistical analysis of the particle size distributions consisted of the following equations;

Mean phi particle size (M_z) $$M_z = \frac{\varphi_{16} + \varphi_{50} + \varphi_{84}}{3}$$

Median particle size (M_d) $$Md = \varphi_{50}$$

Inclusive graphic standard deviation (σ_I) $$\sigma_I = \frac{\varphi_{84} - \varphi_{16}}{4} + \frac{\varphi_{95} - \varphi_5}{6.6}$$

Inclusive graphic skewness (Sk_I) $$Sk_I = \frac{\varphi_{16} + \varphi_{84} - (2\varphi_{50})}{2(\varphi_{84} - \varphi_{16})} + \frac{\varphi_5 + \varphi_{95} - (2\varphi_{50})}{2(\varphi_{95} - \varphi_5)}$$

Inclusive graphic kurtosis (K_G) $$Kg = \frac{\varphi_{95} - \varphi_5}{2.44(\varphi_{75} - \varphi_{25})}$$

The calculation of the mean particle size for each sample enables the inclusion of two additional sediment properties based upon the empirical relationships documented by Hamilton and Bachman (1982), derived from the analysis of sediment cores from the Bering Sea, North Sea, Mediterranean Sea, and older datasets from several other locations.

Richardson and Briggs (1993) also derived similar empirical relationships from the inverse approach to Hamilton's, by using sediment physical properties to predict sediment geoacoustic properties. The linear relationship between porosity and mean particle size plotted in Figure 7.2 offers a rough approximation to the percentage porosity where the mean particle size is known. Hamilton and Bachman (1982) also documented a linear relationship between mean grain size and the saturated bulk density, with density increasing as the mean particle size increases (Figure 7.3).

Figure 7.2 **Plot of relationship between porosity and mean grain size as observed by Hamilton and Bachman (1982)**

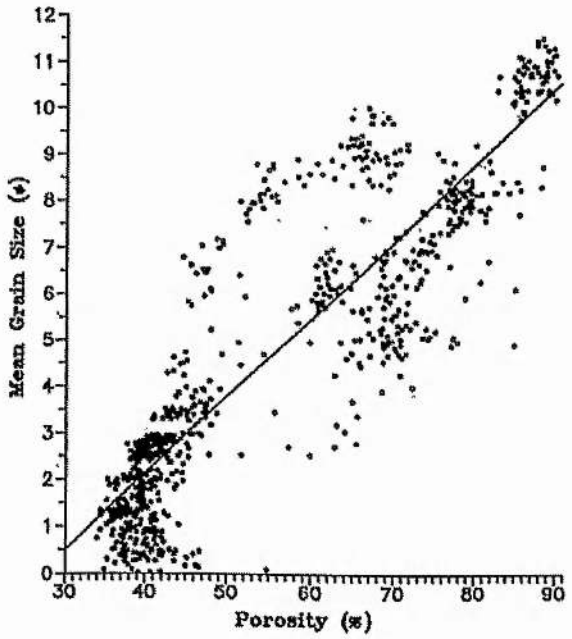

These empirical relationships enable the inclusion of approximate density and porosity values, based upon statistically derived M_z values, within the results of this analysis. It should be noted that the data concentrations in two regions corresponds to sands and muds, whilst the wide dispersion of the intervening data corresponds to various mixtures of coarse and fine sediments.

Figure 7.3 **Plot of relationship between density and mean grain size as observed by Hamilton and Bachman (1982)**

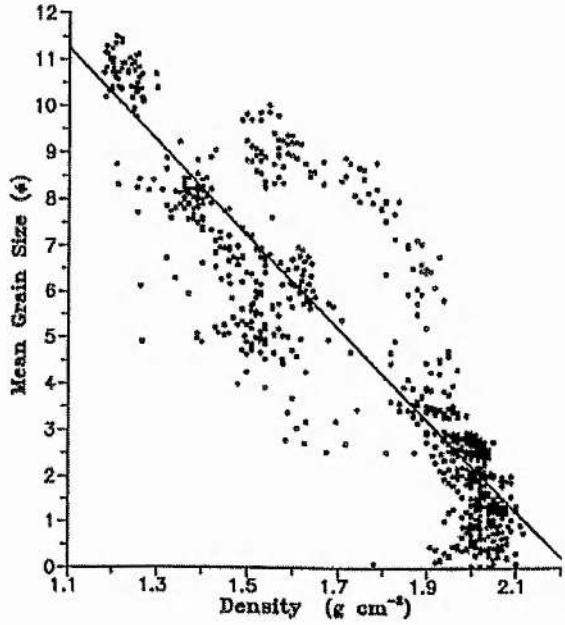

7.5. Results of Textural Analysis

The sieving preparation of the samples for particle size analysis permitted the generation of Table 7.3, which shows the breakdown of the upper ranges of particle sizes, and details descriptions of the sediments appearance within each size range. This table offers a quick reference to the nature of materials found in excess of the maximum particle size limit of the Coulter Counter, and also enables an enhanced analysis of their composition. The appearance of the material within each major size range, >2mm, 2mm>p>0.71mm, and <0.71mm, as separated by the sieving process, is documented by the photographs in Plates 7.1 to 7.22. These photographs clearly illustrate the material variation within the coarse fraction.

The particle size analysis results for each sample have been tabulated in numerical form highlighting the mean and median particle size diameters, and also the percentage compositions of the four main sediment classes, gravel, sand, silt and clay. The distribution results are also displayed as cumulative frequency curves and frequency weight percentage graphs.

Frequency weight percentage graphs can also illustrate clearly the verbal descriptions of sediments such as the mode, the degree of sorting, and general skewness and kurtosis figures.

The weight percentage values of gravels, sands, silts and clays have also been plotted on ternary diagrams to illustrate the textural classification results derived from Folk (1954).

The material content of the coarse fraction has been described at each stage of the analysis to indicate where carbonates out-weigh the clastics. In cases where the particle size range is dominated by carbonates, this fact has been denoted by an asterisk (*), and where carbonates account for 100% of the particles in a size range then a double

asterisk (**) is used. In descriptive terms, the presence of a '*' results in 'gravelly' being replaced by 'shelly,' and '**' results in 'gravel' being replaced by 'shell.'

The purpose of the textural analysis is to classify the sediment type as determined by the nature of the particulate size distribution within the upper layers of the surface sediment, which may impact upon the micro-topographic 'roughness' of the surface.

In addition to all of the statistical results, approximate values for density and porosity are proposed based upon the empirical relationships, between mean particle size and density, and mean particle size and porosity, provided by Hamilton and Bachman (1982). The derivations of percentage carbonates and percentage organics are also tabulated to complement the comprehensive sediment classification results.

Table 7.3 Sieving descriptions of the Sediment samples obtained using the van Veen Grab Sampler

	Sample Number	Total Weight of Sample (in grams)	Weight of Fraction >2mm (in grams)	Weight of Fraction 2mm>*P*>0.71mm (in grams)	Weight of Fraction <0.71mm (in grams)	Total Weight of Sample (in grams)	Percentage >2mm	Percentage 2>*P*>0.71mm	Percentage <0.71mm	Visual Description of Particles (*P*)		
										P > 2mm	2mm > *P* >0.71mm	*P* < 0.71mm
Calibration	1	6.18	0.52	0.05	5.61	6.18	8.41	0.81	90.78	pebble	shell and grains	silt and clay
	2	6.11	0.07	0.05	5.99	6.11	1.15	0.82	98.04	shell	shell and grains	silt and clay
	3	5.7	0.00	0.00	5.70	5.70	0.00	0.00	100.00	n/a	n/a	silt and clay
	4	8.72	1.87	0.18	6.67	8.72	21.44	2.06	76.49	shell	shell	silt and clay
Shingle	5	13.2	3.14	0.04	10.02	13.20	23.79	0.30	75.91	shell	shell and platy minerals	silt and clay
	6	8.01	4.67	0.23	3.11	8.01	58.30	2.87	38.83	shell	shell and minerals	minerals, silt and clay
	7	10.55	3.94	0.08	6.53	10.55	37.35	0.76	61.90	shell and flint	flint and grains	silt and clay
Invincible	8	17.33	0.00	0.04	17.29	17.33	0.00	0.23	99.77	n/a	shell and flint	silt and clay
	9	12.71	0.00	0.00	12.71	12.71	0.00	0.00	100.00	n/a	n/a	sand
	10	16.8	0.00	0.00	16.80	16.80	0.00	0.00	100.00	n/a	n/a	sand
	11	16.03	0.00	0.00	16.03	16.03	0.00	0.00	100.00	n/a	n/a	sand
A1 Submarine	12	1.26	0.00	0.01	1.25	1.26	0.00	0.79	99.21	n/a	shell	silt and clay
	13	3.45	0.18	0.04	3.23	3.45	5.22	1.16	93.62	clay nodule	shell	silt and clay
	14	9.11	0.00	0.00	9.11	9.11	0.00	0.00	100.00	n/a	n/a	silt and clay
	15	8.26	0.05	0.06	8.15	8.26	0.61	0.73	98.67	quartz minerals	shell and minerals	silt and clay
	16	6.79	0.08	0.07	6.64	6.79	1.18	1.03	97.79	shell	shell and minerals	silt and clay
	17	6.24	0.00	0.06	6.18	6.24	0.00	0.96	99.04	n/a	shell	silt and clay
	18	7.82	0.04	0.07	7.71	7.82	0.51	0.90	98.59	shell	shell	silt and clay
	19	12.5	0.00	0.00	12.50	12.50	0.00	0.00	100.00	n/a	n/a	sand and silt
Invincible	20	18.56	0.00	0.01	18.55	18.56	0.00	0.05	99.95	n/a	shell fragment	sand
	21	18.81	0.00	0.01	18.80	18.81	0.00	0.05	99.95	n/a	grains	sand
	22	22.78	0.00	0.00	22.78	22.78	0.00	0.00	100.00	n/a	n/a	sand

Plates 7.1 to 7.22 show photographic evidence of sediment composition at each sieving stage. It should be noted that these sediments have been dried to enhance their particulate appearance, and also that the relative quantities presented at each stage is determined only by the aesthetics of the imaging, and is not representative of the overall proportionate composition of the sediment sample.

The samples are presented within a 5cm^2 area marked out on millimetre square graph paper to provide a clear scale of measurement.

Plate 7.1 Sample 1 - Calibration Area

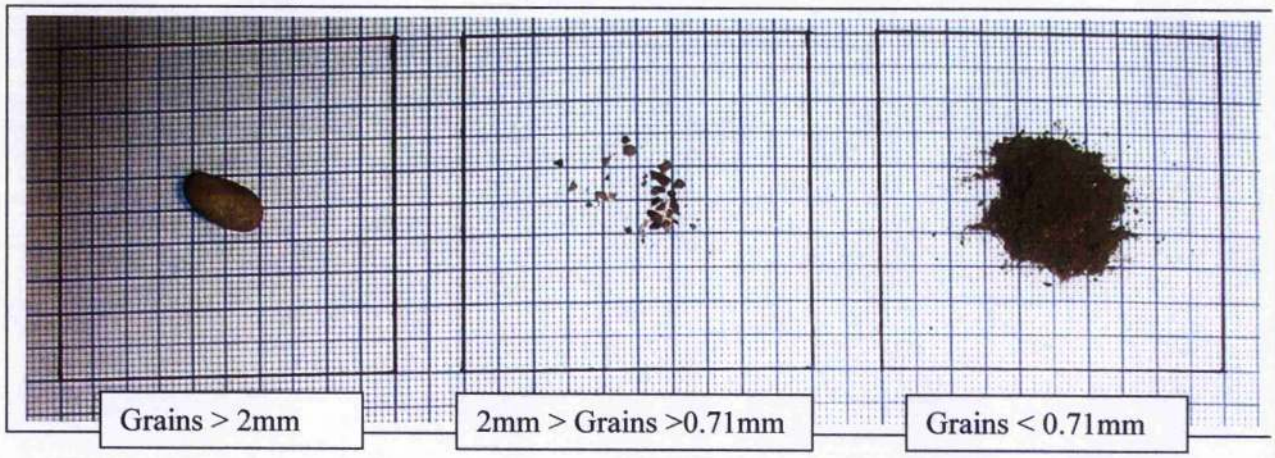

Plate 7.2 Sample 2 - Calibration area

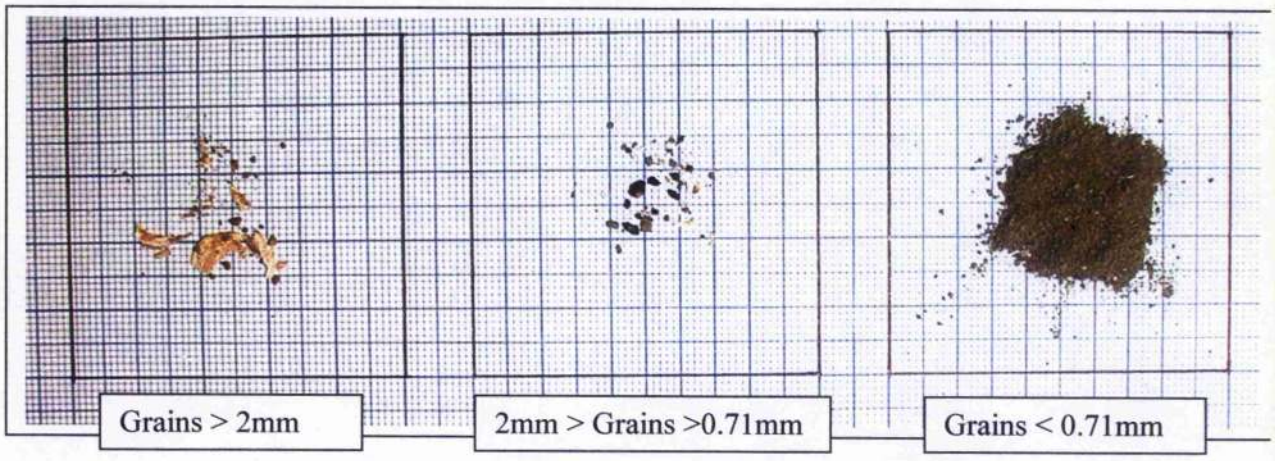

Plate 7.3 Sample 3 - Calibration area

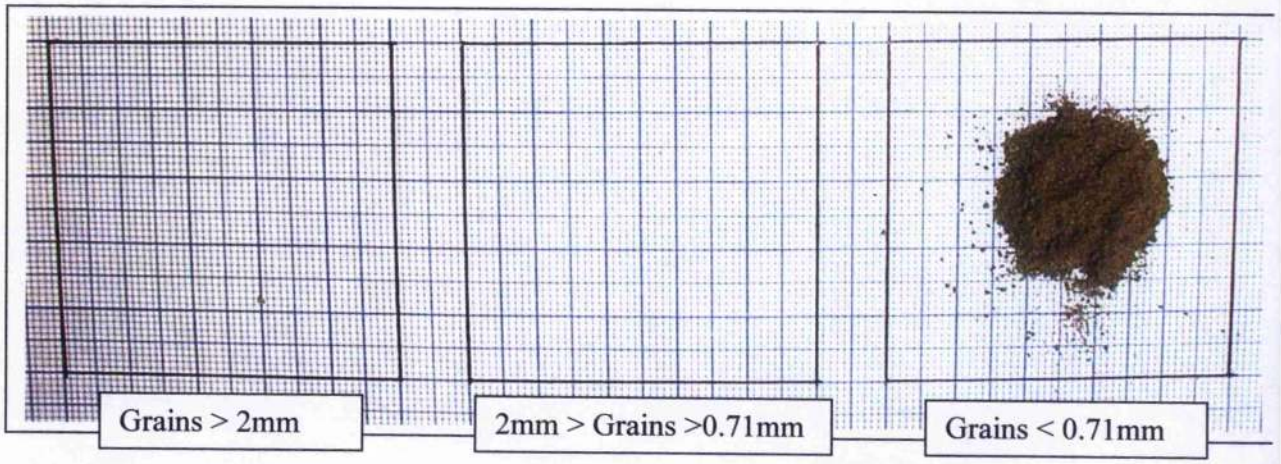

Plate 7.4 Sample 4 - Calibration area

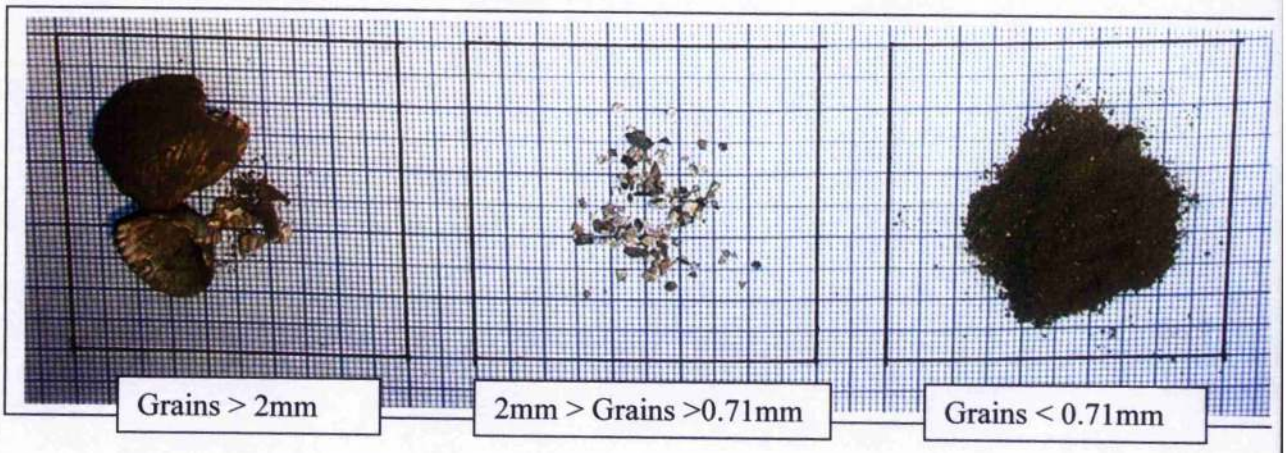

Plate 7.5 Sample 5 - Shingle area

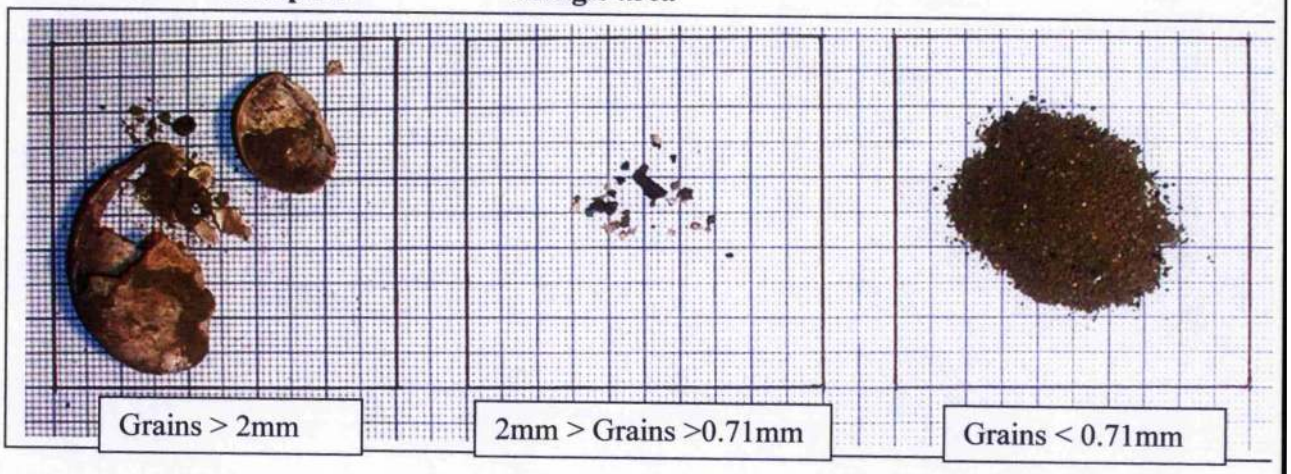

Plate 7.6 Sample 6 - Shingle area

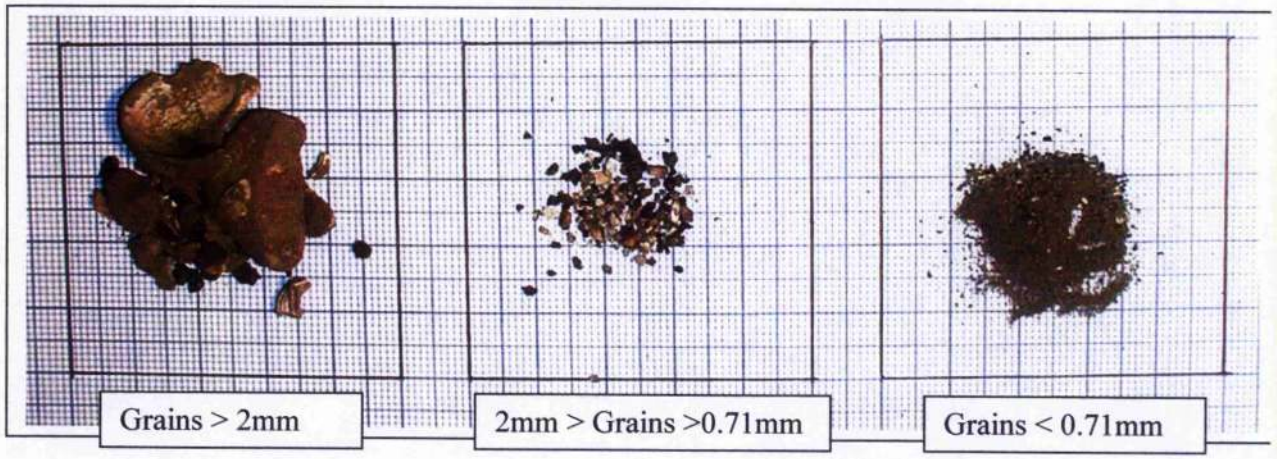

Plate 7.7 Sample 7 - Shingle area

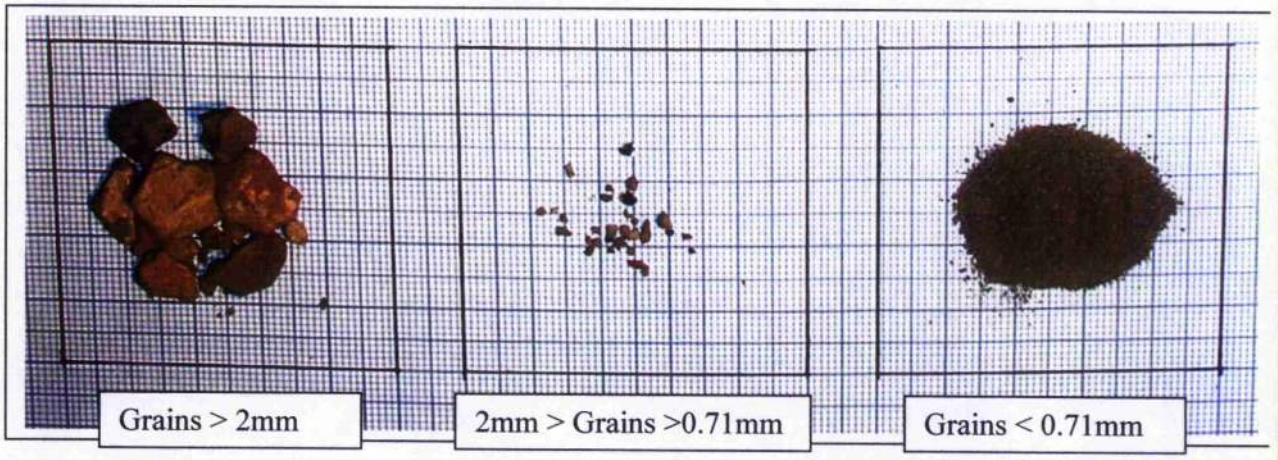

Plate 7.8 Sample 8 - Invincible area

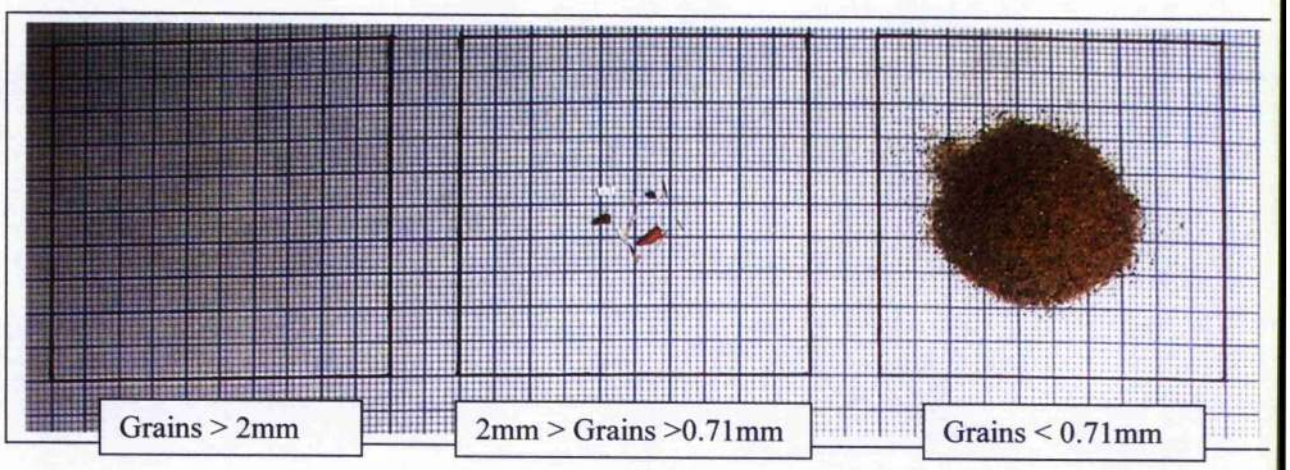

Plate 7.9 Sample 9 - Invincible area

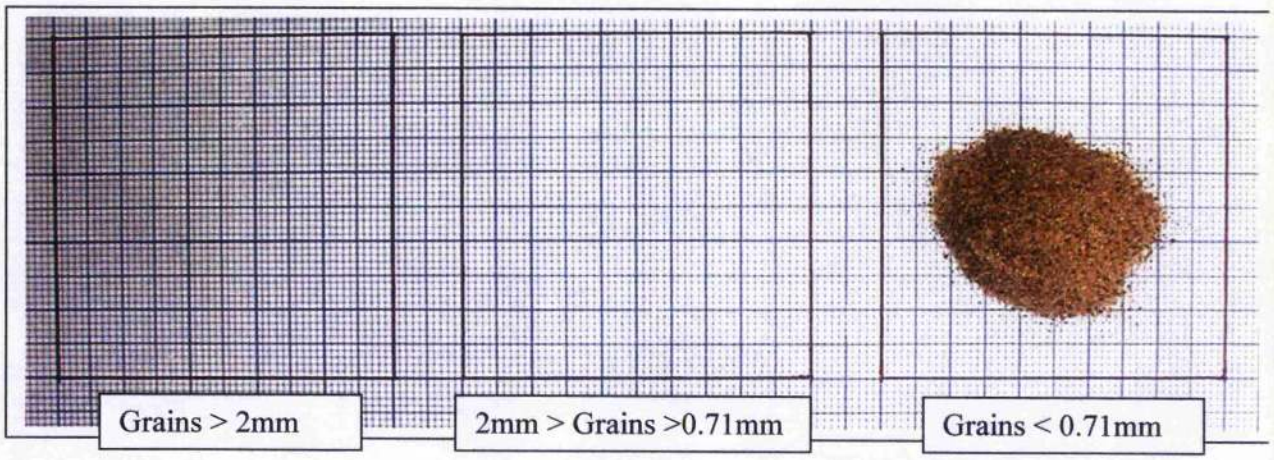

Plate 7.10 Sample 10 - Invincible area

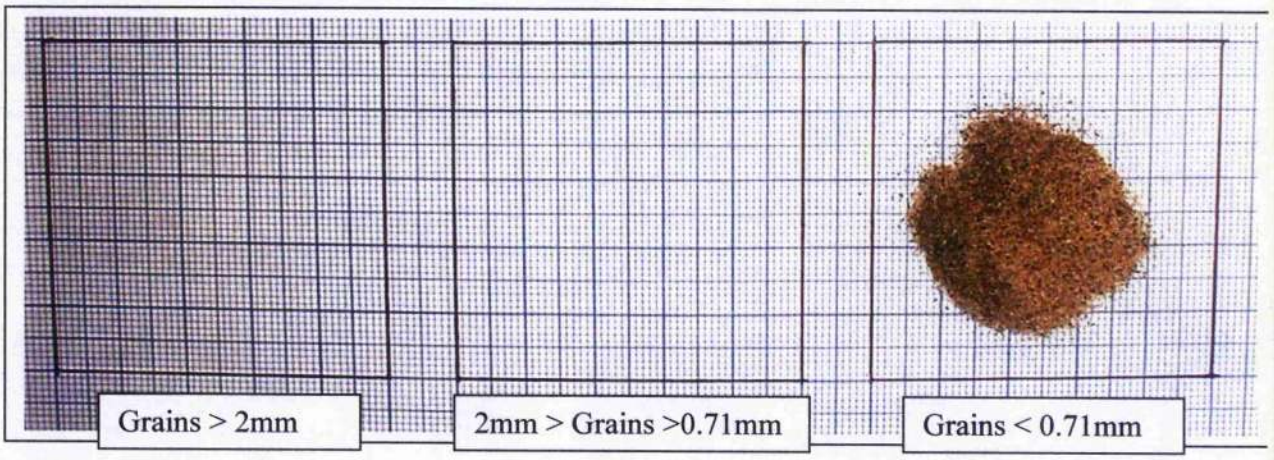

Plate 7.11 Sample 11 - Invincible area

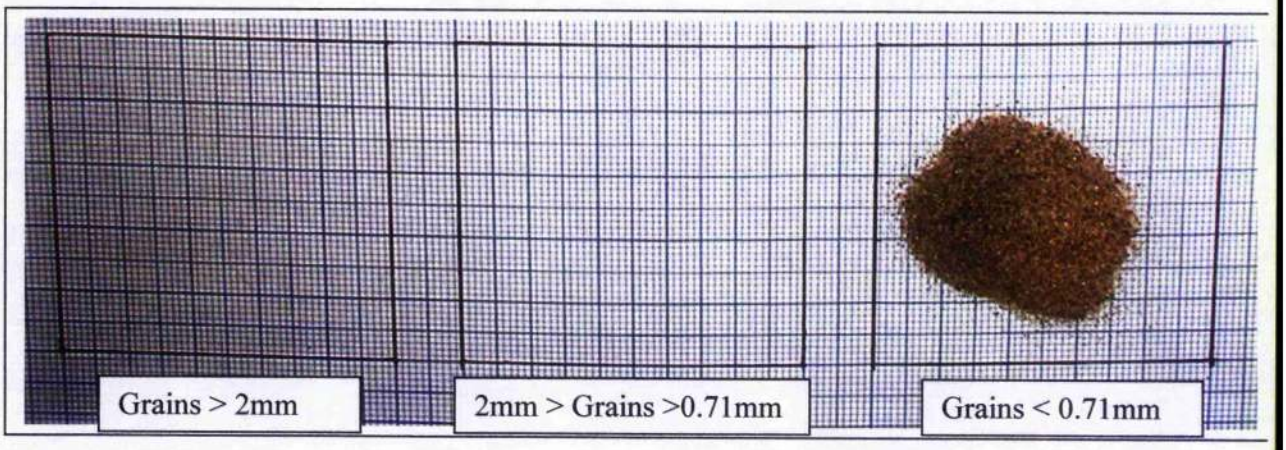

Plate 7.12 Sample 12 - A1 Submarine area

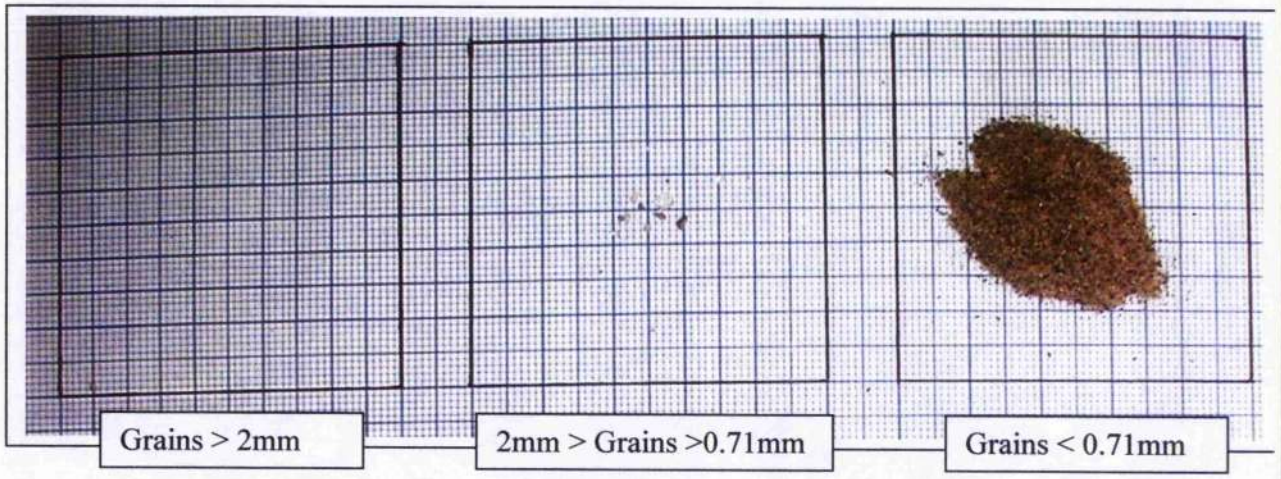

Plate 7.13 Sample 13 - A1 Submarine area

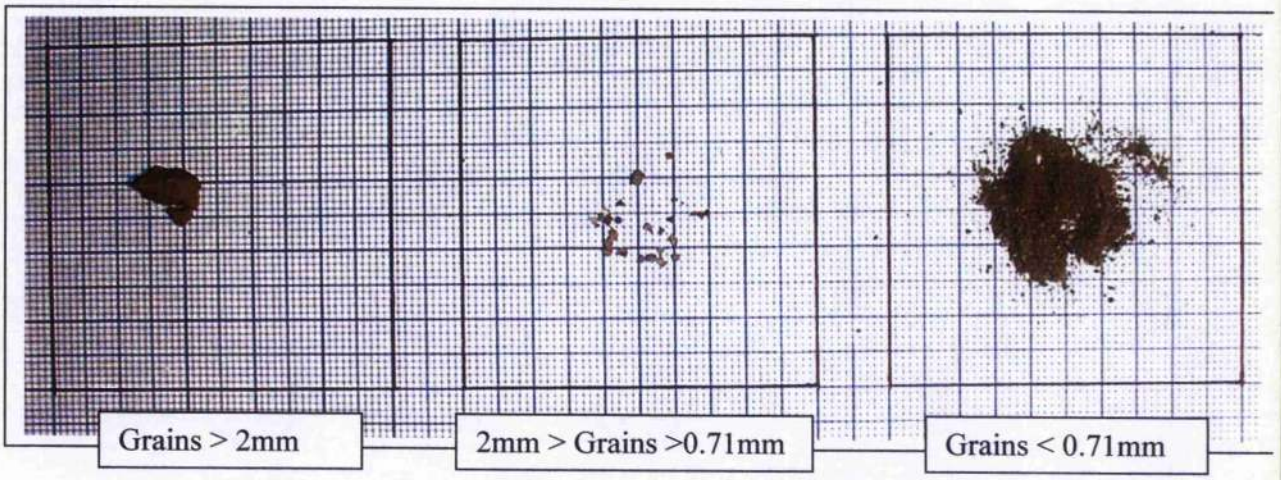

Plate 7.14 Sample 14 - A1 Submarine area

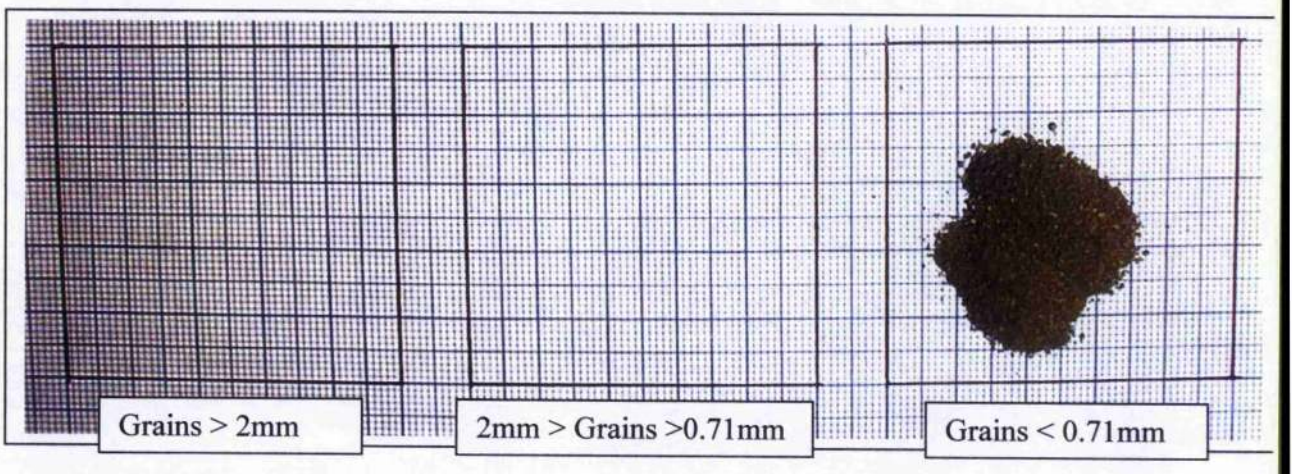

Plate 7.15 Sample 15 - A1 Submarine area

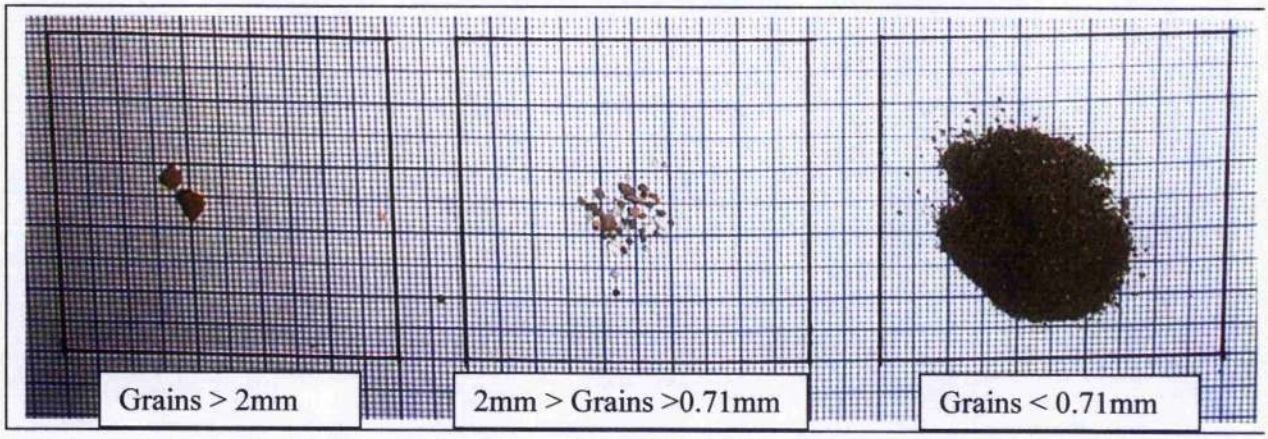

Plate 7.16 Sample 16 - A1 Submarine area

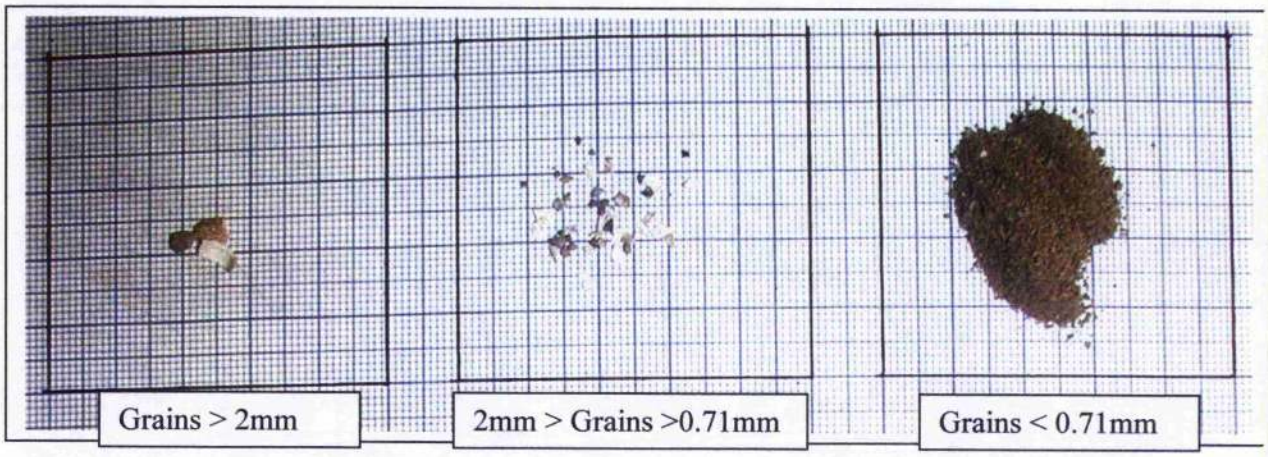

Plate 7.17 Sample 17 - A1 Submarine area

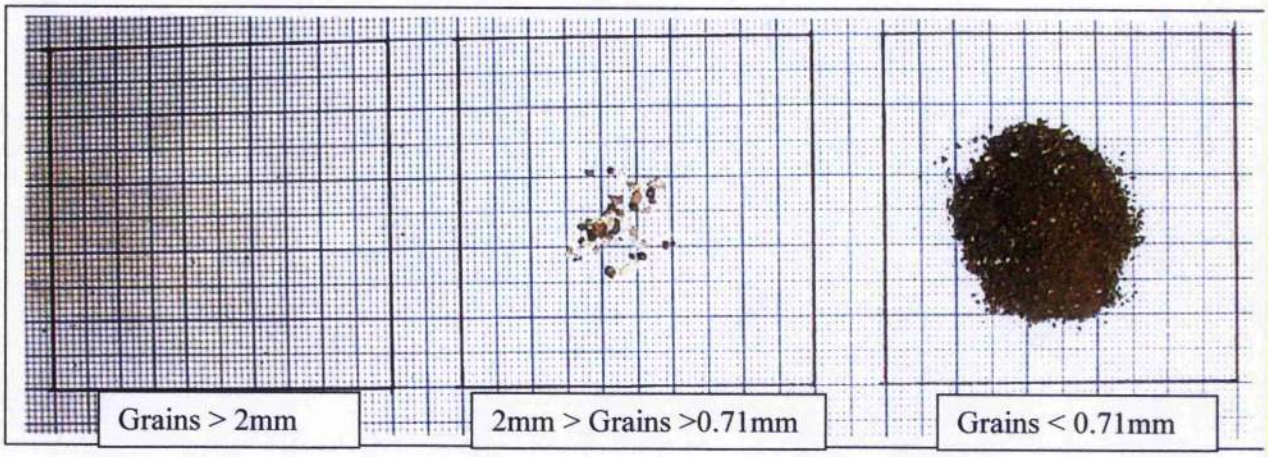

Plate 7.18 Sample 18 - A1 Submarine area

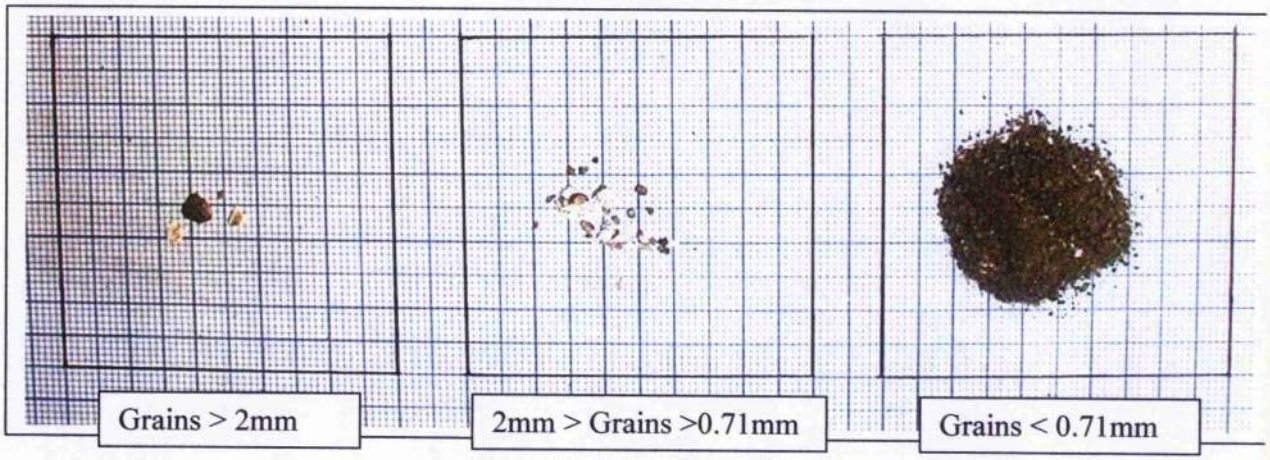

Plate 7.19 Sample 19 - A1 Submarine area

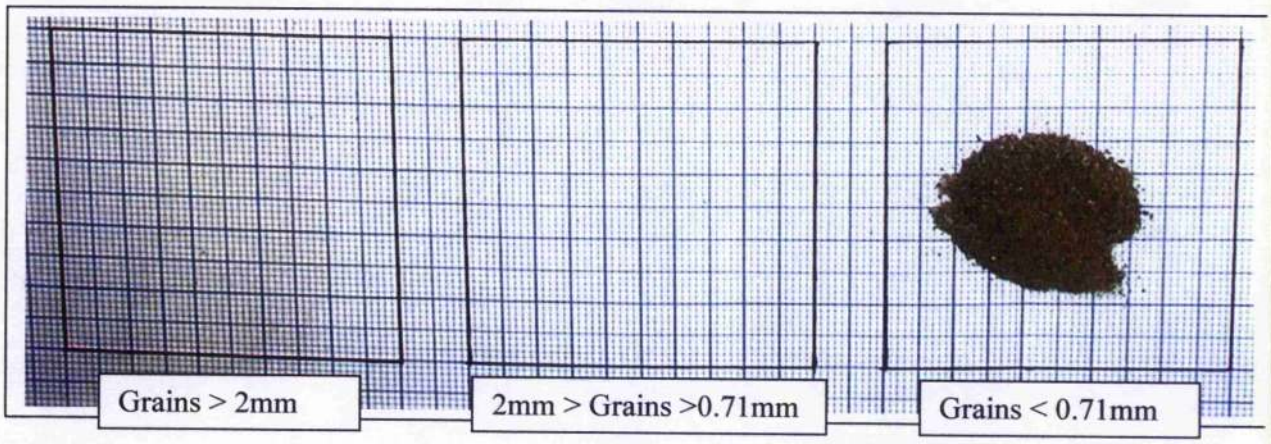

Plate 7.20 Sample 20 - Invincible area

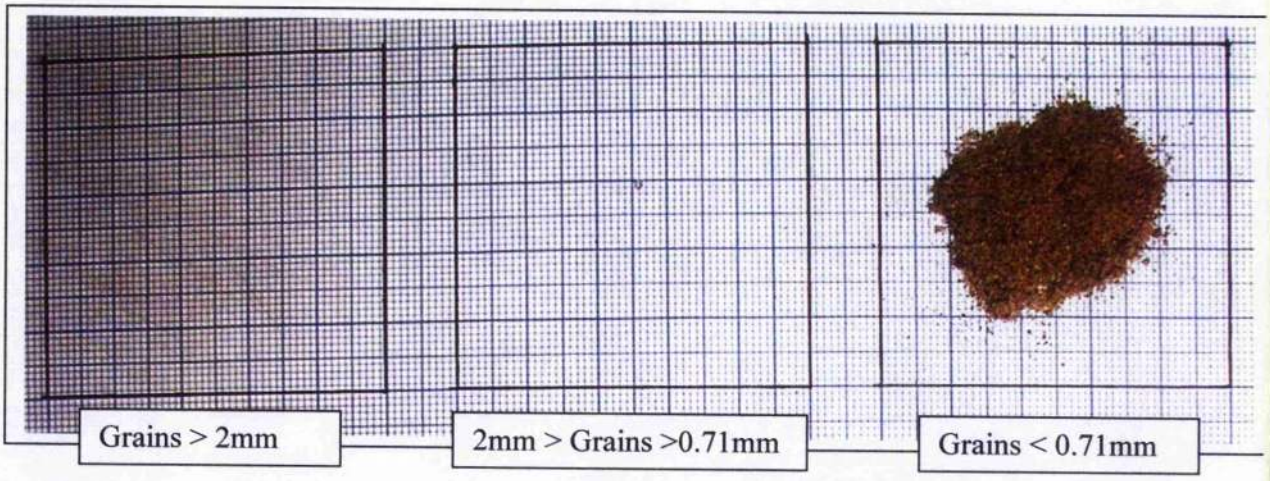

Plate 7.21 Sample 21 - Invincible area

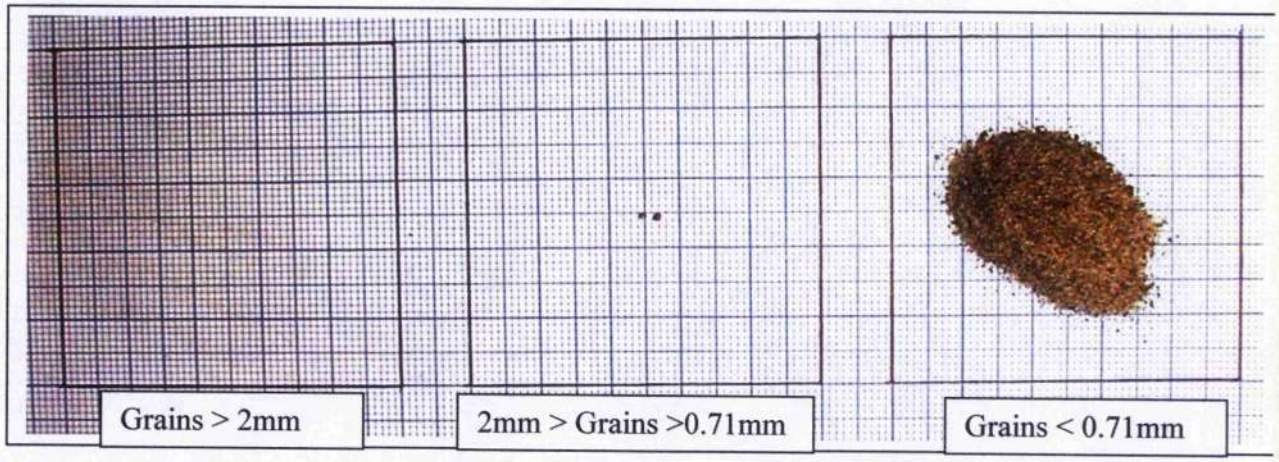

Plate 7.22 Sample 22 - Invincible area

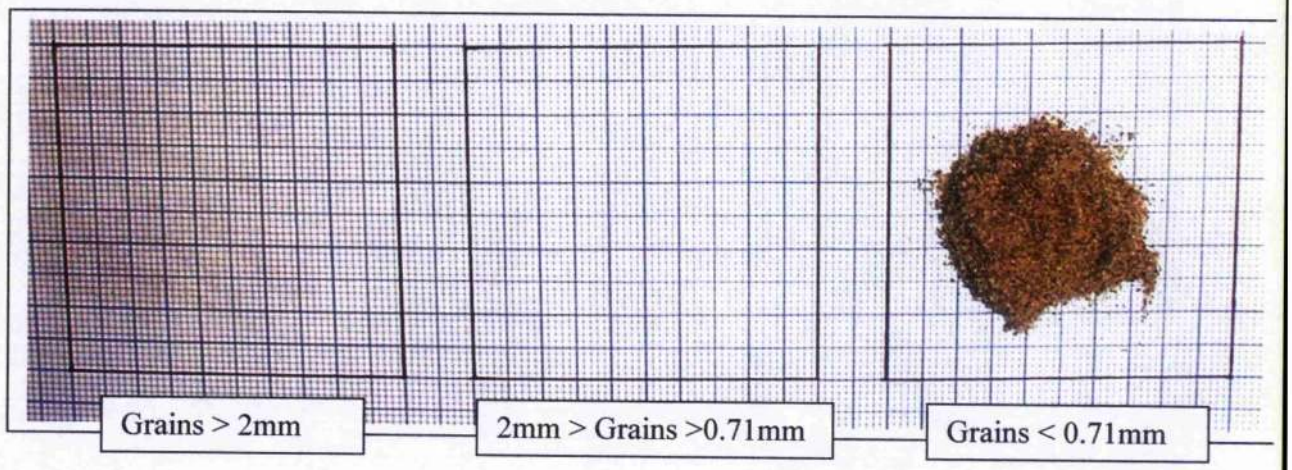

7.5.1. Textural analysis for the Calibration site samples

TABLE 7.4 Particle Size Analysis for Calibration Sediment Samples 1-4

Sample Number	SIEVE ANALYSIS					COULTER ANALYSIS								
	Total Weight of Sample	Wt of Sample 64mm>p>4mm	Wt of Sample 4mm>p>2mm	Wt finer than 2mm	Weight 2>p>0.71mm	Wt finer than 0.71mm	Wt of Sample > 0.6mm	Weight 2mm>p>0.6mm	Wt finer than 0.6mm	Wt finer than 0.2mm	Wt finer than 0.06mm	Wt finer than 0.02mm	Wt finer than 0.006mm	Wt finer than 0.002mm
SAM 1	6.18	0.52	0	5.66	0.05	5.61	0.08	0.13	5.53	5.20	4.66	3.48	1.74	0.54
SAM 2	6.11	0.04	0.03	6.04	0.05	5.99	0.05	0.10	5.94	5.49	4.59	3.31	1.59	0.49
SAM 3	5.70	0	0	5.70	0	5.70	0.05	0.05	5.65	5.42	4.51	3.16	1.54	0.47
SAM 4	8.72	1.79	0.08	6.85	0.18	6.67	0.10	0.28	6.57	6.16	5.43	4.04	2.21	0.77

SAMPLE 1						
Wt of Sample coarser than (mm)	(phi)	Wt recorded	Total sam wt	% by wt	Skewness	Kurtosis
64	-6	0	6.18	0	-.36 phi	1.53 phi
4	-2	0.52	6.18	8.41	Mean (phi) =	5.58
2	-1	0.52	6.18	8.41		
0.6	0.74	0.65	6.18	10.46	Median (phi) =	6.06
0.2	2.32	0.98	6.18	15.80		
0.06	4.06	1.52	6.18	24.66	% Clay	8.71
0.02	5.64	2.70	6.18	43.65	% Silt	66.63
0.006	7.38	4.44	6.18	71.80	% Sand	16.24
0.002	8.97	5.64	6.18	91.29	% Gravel	8.41

SAMPLE 2						
Wt of Sample coarser than (mm)	(phi)	Wt recorded	Total sam wt	% by wt	Skewness	Kurtosis
64	-6	0	6.11	0	-.12 phi	.97 phi
4	-2	0.04	6.11	0.65	Mean (phi) =	5.75
2	-1	0.07	6.11	1.15		
0.6	0.74	0.17	6.11	2.80	Median (phi) =	5.92
0.2	2.32	0.62	6.11	10.15		
0.06	4.06	1.52	6.11	24.81	% Clay	8.07
0.02	5.64	2.80	6.11	45.87	% Silt	67.13
0.006	7.38	4.52	6.11	73.99	% Sand	23.66
0.002	8.97	5.62	6.11	91.93	% Gravel **	1.15

SAMPLE 3						
Wt of Sample coarser than (mm)	(phi)	Wt recorded	Total sam wt	% by wt	Skewness	Kurtosis
64	-6	0.00	5.70	0	-.03 phi	.92 phi
4	-2	0.00	5.70	0	Mean (phi) =	5.96
2	-1	0.00	5.70	0		
0.6	0.74	0.05	5.70	0.89	Median (phi) =	6.00
0.2	2.32	0.28	5.70	4.99		
0.06	4.06	1.19	5.70	20.94	% Clay	8.31
0.02	5.64	2.54	5.70	44.51	% Silt	70.75
0.006	7.38	4.16	5.70	73.06	% Sand	20.94
0.002	8.97	5.23	5.70	91.69	% Gravel	0.00

SAMPLE 4						
Wt of Sample coarser than (mm)	(phi)	Wt recorded	Total sam wt	% by wt	Skewness	Kurtosis
64	-6	0	8.72	0	-.45 phi	.90 phi
4	-2	1.79	8.72	20.53	Mean (phi) =	3.56
2	-1	1.87	8.72	21.44		
0.6	0.74	2.15	8.72	24.63	Median (phi) =	5.31
0.2	2.32	2.56	8.72	29.35		
0.06	4.06	3.29	8.72	37.71	% Clay	8.86
0.02	5.64	4.68	8.72	53.68	% Silt	53.44
0.006	7.38	6.51	8.72	74.64	% Sand	16.26
0.002	8.97	7.95	8.72	91.15	% Gravel **	21.44

Weight % of Grain Diameter Range measured in Phi						
Range (mm)	Grain size (Phi)	SAMPLE 1	SAMPLE 2	SAMPLE 3	SAMPLE 4	Average Phi
256 to 64	-8 to -6	0	0	0	0	-7
64 to 4	-6 to -2	8.41	0.65	0	20.53	-4
4 to 2	-2 to -1	0	0.49	0	0.92	-1.5
2 to 0.71	-1 to 0.494	0.81	0.82	0	2.06	-0.25
0.71 to 0.6	0.494 to 0.737	1.23	0.83	0.89	1.12	0.62
0.6 to 0.2	0.737 to 2.322	5.34	7.35	4.10	4.71	1.53
0.2 to 0.06	2.322 to 4.059	8.86	14.66	15.95	8.36	3.19
0.06 to 0.02	4.059 to 5.644	18.99	21.07	23.57	15.98	4.85
0.02 to 0.006	5.644 to 7.381	28.15	28.12	28.55	20.96	6.51
0.006 to 0.002	7.381 to 8.966	19.49	17.94	18.63	16.51	8.17
<0.002	8.966 and above	8.71	8.07	8.31	8.85	9.83
		0	0	0	0	12
Total		100	100	100	100	

ALL WEIGHT MEASUREMENTS IN GRAMS

* DENOTES PARTICLE SIZE RANGES COMPRISING OF >50% SHELL

** DENOTES PARTICLE SIZE RANGES COMPRISING OF 100% SHELL

Figure 7.4 Cumulative Frequency Particle Size Distribution Graphs for the Calibration Samples 1-4

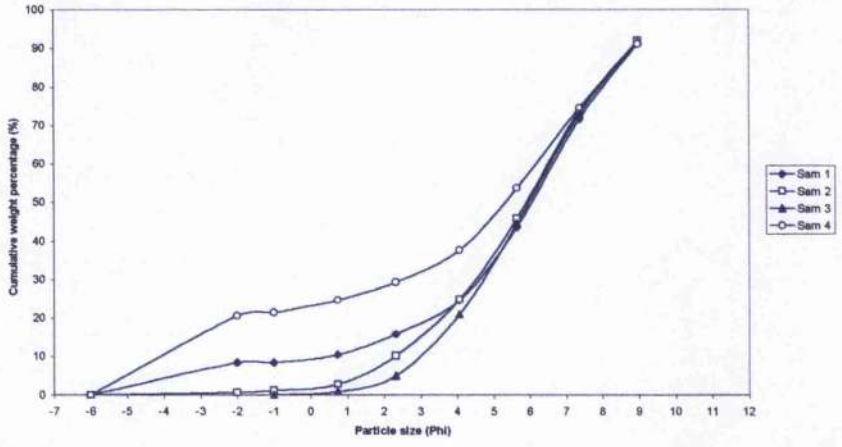

Figure 7.5 Frequency Weight Percentage versus Particle Diameter plots for the Calibration Samples 1-4

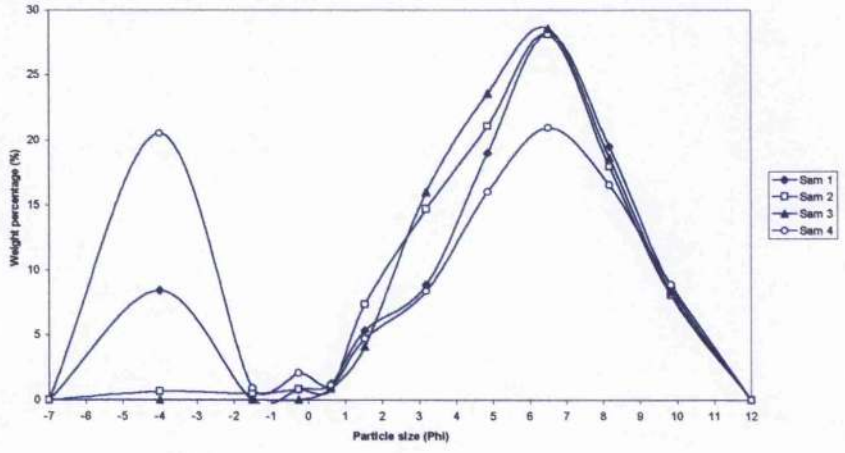

Figure 7.6 Textural Classification plots for Calibration samples 1-4

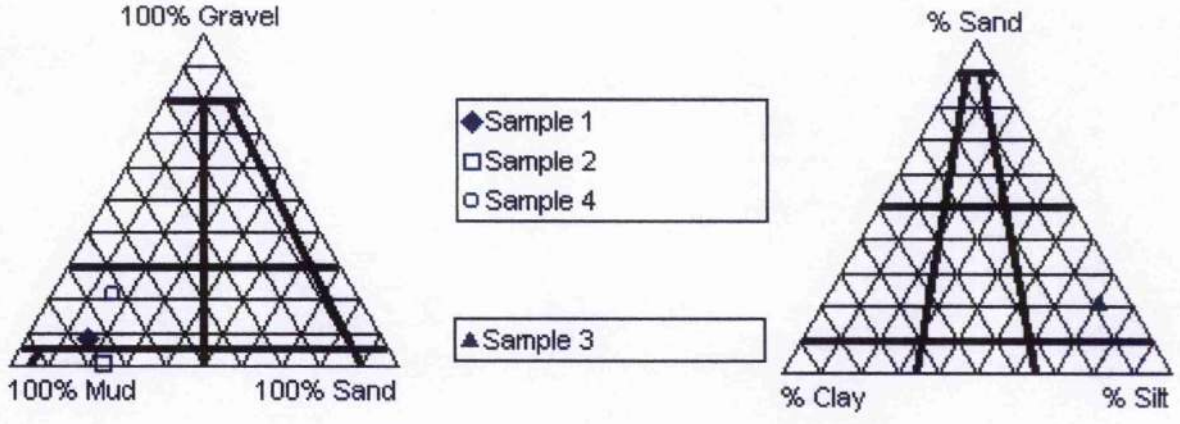

Discussion of Calibration samples 1-4

The Calibration samples all exhibit similar cumulative particle size distribution and frequency weight percentage trends, but samples 1 and 4 are observed to contain a significantly higher coarse content percentage than samples 2 and 3. This is supported by the bi-modal nature of the frequency weight percentage plots for samples 1 and 4, and skewness values of -0.36 and -0.45 respectively. Tables 7.5 and 7.6 suggest that this is caused by an 8.41% gravel content in Sample 1, and a 21.44% coarse shell content in Sample 4. All the samples are regarded as being very, to extremely, poorly sorted.

The irregular undulations at 0.62φ and –0.25φ on the frequency weight percentage plots are found to relate to the point at which the sieve data and the Coulter data are combined.

The overall Folk (1954) textural classifications outlined in Table 7.5 suggest that sample 4 and then sample 1 will have the highest degrees of textural roughness due to the presence of gravels and shells, decreasing to sample 2 (slightly shelly, sandy) and then sample 3 (sandy).

The carbonate analysis found the samples comprised of between 4% and 8% carbonates, which supports the general findings of small shell fragments during the sieving analysis. The fact that the percentage carbonate values do not appear to mirror the shell content in the particle size compositions (Table 7.5), is attributed to the fact that the low number of large particles prevented an even and representative division using the cone and divide technique.

Table 7.5 Summary of Sediment Composition and Classification for Calibration Samples 1-4

Sample Number	Particle Class Composition				Textural Classification from Folk (1954)	Carbonates (%)	Organics (%)	Density* (g/cm^3)	Porosity* (%)
	% Gravel	% Sand	% Silt	% Clay					
1	8.41	16.24	66.63	8.71	gravelly mud	6.27	10.84	1.65	61
2	1.15	23.66	67.13	8.07	slightly shelly sandy mud	6.82	10.49	1.63	62
3	0	20.94	70.75	8.31	sandy silt	4.43	11.8	1.61	63
4	21.44	16.26	53.44	8.85	shelly mud	7.42	11.88	1.86	48

* derived from the empirical relationships suggested by Hamilton & Bachman (1982)

Table 7.6 Statistical Summary of Particle Size Analysis for Calibration Samples 1-4

Sample Number	Md (phi)	Mz (phi)	Modal Size			SD (phi)	Sk_a (phi)	K_g (phi)
			1st (phi)	2nd (phi)	3rd (phi)			
1	6.06	5.58	6.51	-4	n/a	5.00	-0.365	1.526
2	5.92	5.75	6.44	n/a	n/a	3.78	-0.116	0.975
3	6.00	5.96	6.33	n/a	n/a	3.40	-0.033	0.921
4	5.31	3.56	6.55	-4	n/a	7.79	-0.452	0.903

7.5.2. Textural analysis for the Shingle site samples

TABLE 7.7 Particle Size Analysis for Shingle Sediment Samples 5-7

Sample Number	SIEVE ANALYSIS					COULTER ANALYSIS								
	Total Weight of Sample	Wt of Sample 64mm>p>4mm	Wt of Sample 4mm>p>2mm	Wt finer than 2mm	Weight 2>p>0.71mm	Wt finer than 0.71mm	Wt of Sample > 0.6mm	Weight 2mm>p>0.6mm	Wt finer than 0.6mm	Wt finer than 0.2mm	Wt finer than 0.06mm	Wt finer than 0.02mm	Wt finer than 0.006mm	Wt finer than 0.002mm
SAM 5	13.20	3.08	0.06	10.06	0.04	10.02	0.14	0.18	9.89	7.11	5.54	4.12	2.26	0.71
SAM 6	8.01	2.91	1.76	3.34	0.23	3.11	0.00	0.23	3.11	3.01	2.59	1.92	1.04	0.35
SAM 7	10.55	3.48	0.46	6.61	0.08	6.53	0.09	0.17	6.44	5.58	4.73	3.48	1.86	0.62

SAMPLE 5

Wt of Sample coarser than (mm)	(phi)	Wt recorded	Total sam wt	% by wt	Skewness	Kurtosis
64	-6	0	13.20	0	-.12 phi	1.03 phi
4	-2	3.08	13.20	23.33	Mean (phi) =	2.31
2	-1	3.14	13.20	23.79		
0.6	0.74	3.32	13.20	25.11	Median (phi) =	2.77
0.2	2.32	6.09	13.20	46.16		
0.06	4.06	7.66	13.20	58.05	% Clay	5.34
0.02	5.64	9.08	13.20	68.78	% Silt	36.61
0.006	7.38	10.94	13.20	82.89	% Sand	34.27
0.002	8.97	12.50	13.20	94.66	% Gravel **	23.79

SAMPLE 6

Wt of Sample coarser than (mm)	(phi)	Wt recorded	Total sam wt	% by wt	Skewness	Kurtosis
64	-6	0	8.01	0	.46 phi	.68 phi
4	-2	2.91	8.01	36.33	Mean (phi) =	0.44
2	-1	4.67	8.01	58.30		
0.6	0.74	4.90	8.01	61.17	Median (phi) =	-1.37
0.2	2.32	5.00	8.01	62.42		
0.06	4.06	5.42	8.01	67.65	% Clay	4.37
0.02	5.64	6.09	8.01	76.03	% Silt	27.98
0.006	7.38	6.97	8.01	87.02	% Sand	9.35
0.002	8.97	7.66	8.01	95.63	% Gravel *	58.30

SAMPLE 7

Wt of Sample coarser than (mm)	(phi)	Wt recorded	Total sam wt	% by wt	Skewness	Kurtosis
64	-6	0	10.55	0	-.19 phi	.62 phi
4	-2	3.48	10.55	32.99	Mean (phi) =	2.13
2	-1	3.94	10.55	37.35		
0.6	0.74	4.11	10.55	38.97	Median (phi) =	2.96
0.2	2.32	4.97	10.55	47.12		
0.06	4.06	5.82	10.55	55.13	% Clay	5.91
0.02	5.64	7.07	10.55	67.04	% Silt	38.97
0.006	7.38	8.70	10.55	82.42	% Sand	17.78
0.002	8.97	9.93	10.55	94.09	% Gravel	37.35

ALL WEIGHT MEASUREMENTS IN GRAMS

*** DENOTES PARTICLE SIZE RANGES COMPRISING OF >50% SHELL**

**** DENOTES PARTICLE SIZE RANGES COMPRISING OF 100% SHELL**

Weight % of Grain Diameter measured in Phi

Range (mm)	Grain size (Phi)	SAMPLE 5	SAMPLE 6	SAMPLE 7	Average Phi
256 to 64	-8 to -6	0	0	0	-7
64 to 4	-6 to -2	23.33	36.33	32.99	-4
4 to 2	-2 to -1	0.45	21.97	4.36	-2
2 to 0.71	-1 to 0.494	0.30	2.87	0.76	-0.25
0.71 to 0.6	0.494 to 0.737	1.02	0.00	0.86	0.62
0.6 to 0.2	0.737 to 2.322	21.05	1.25	8.15	1.53
0.2 to 0.06	2.322 to 4.059	11.89	5.23	8.01	3.19
0.06 to 0.02	4.059 to 5.644	10.73	8.38	11.91	4.85
0.02 to 0.006	5.644 to 7.381	14.11	10.99	15.37	6.51
0.006 to 0.002	7.381 to 8.966	11.77	8.61	11.68	8.17
<0.002	8.966 and above	5.34	4.37	5.91	9.83
		0	0	0	12
Total		100	100	100	

Figure 7.7 Cumulative Frequency Particle Size Distribution Graphs for the Shingle Samples 5-7

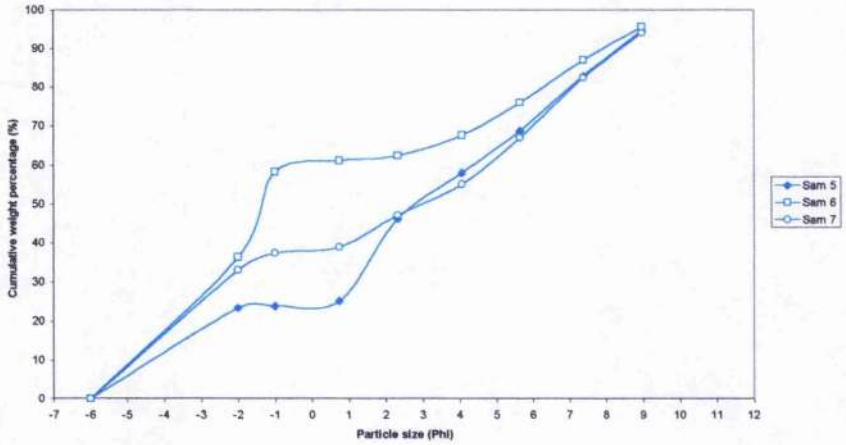

Figure 7.8 Frequency Weight Percentage versus Particle Diameter plots for the Shingle Samples 5-7

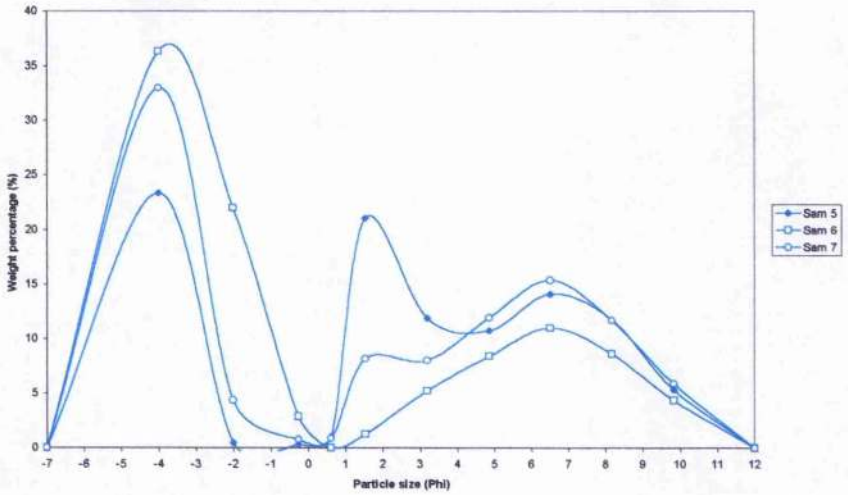

Figure 7.9 Textural Classification plots for Shingle samples 5-7

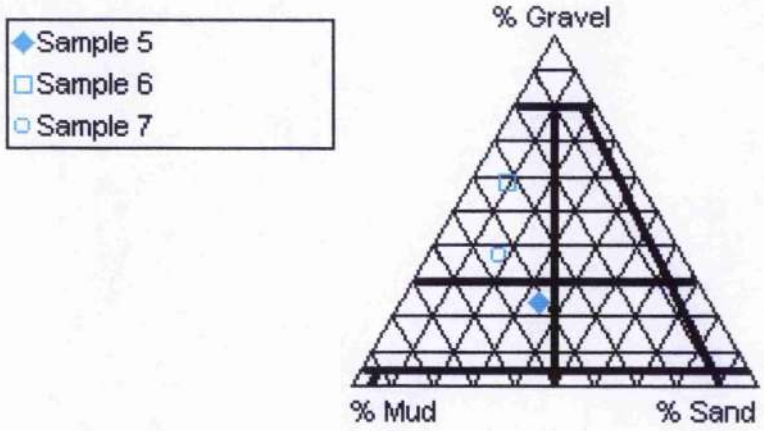

Discussion of Shingle samples 5-7

The Shingle samples are all characterised by a high coarse content, although the materials responsible for the high values are markedly different in each sample. The gravel class for samples 5 to 7 change in composition from 100% shell to 100% gravel content, with sample 5 having 100% coarse shell content, sample 6 containing both gravel and coarse shell, and sample 7 characterised by 100% gravel. The variations in the gravel class cause the samples to be spread out in the ternary plot, and illustrate a decrease in textural roughness from sample 6, to sample 7 and to sample 5.

The high coarse contents are also reflected in the mean particle sizes of between 2.31φ for sample 5, and 0.44φ for sample 6, and in the skewness values ranging from -0.12 to 0.46.

It is notable that the mean grain size of sample 6 is essentially meaningless, as there are virtually no grains of this size present.

The standard deviation values suggest extremely poor sorting, and this is supported by the bi-modal nature of samples 6 and 7, and also by the unusual tri-modal nature of sample 5.

It is worthy of note that the samples from the Shingle area contain large fragments of shell, as is emphasised by the sieving data (Tables 7.3 & 7.7). Sample 6 must also be highlighted because, with a carbonate content of over 13%, it contained over twice as much carbonate as any other sample from within the harbour. Sample 6, with 15.27%, also contained approximately one and a half times the organic content of samples 5 and 7.

Tables 7.8 and 7.9 provide a summary of the textural and statistical analyses for each Shingle sample.

Table 7.8 Summary of Sediment Composition and Classification for Shingle samples 5-7

Sample Number	Particle Class Composition				Textural Classification from Folk (1954)	Carbonates (%)	Organics (%)	Density* (g/cm^3)	Porosity* (%)
	% Gravel	% Sand	% Silt	% Clay					
5	23.79	34.27	36.61	5.34	shelly mud	3.9	9.17	1.96	42
6	58.30	9.35	27.98	4.37	muddy shelly gravel	13.25	15.27	2.17	30
7	37.35	17.78	38.97	5.91	muddy gravel	4.76	10.59	2.00	39

* derived from the empirical relationships suggested by Hamilton & Bachman (1982)

Table 7.9 Statistical Summary of Particle Size Analysis for Shingle samples 5-7

Sample Number	Md (phi)	Mz (phi)	Modal Size			SD (phi)	Sk_a (phi)	K_g (phi)
			1st (phi)	2nd (phi)	3rd (phi)			
5	2.77	2.31	-3.96	1.650	6.65	7.58	-0.123	1.028
6	-1.37	0.44	-3.70	6.520	n/a	7.71	0.458	0.679
7	2.96	2.13	-3.96	6.500	1.84	8.01	-0.186	0.621

7.5.3. Textural analysis for the Invincible site samples

TABLE 7.10 Particle Size Analysis for Invincible Sediment Samples 8-11

Sample Number	SIEVE ANALYSIS					COULTER ANALYSIS								
	Total Weight of Sample	Wt of Sample 64mm>p>4mm	Wt of Sample 4mm>p>2mm	Wt finer than 2mm	Weight 2>p>0.71mm	Wt finer than 0.71mm	Wt of Sample > 0.6mm	Weight 2mm>p>0.6mm	Wt finer than 0.6mm	Wt finer than 0.2mm	Wt finer than 0.06mm	Wt finer than 0.02mm	Wt finer than 0.006mm	Wt finer than 0.002mm
SAM 8	17.33	0	0	17.33	0.04	17.29	0	0.04	17.29	4.06	0	0	0	0
SAM 9	12.71	0	0	12.71	0	12.71	0	0	12.71	2.70	0	0	0	0
SAM 10	16.80	0	0	16.80	0	16.80	0	0	16.80	2.79	0	0	0	0
SAM 11	16.03	0	0	16.03	0	16.03	0	0	16.03	3.93	0	0	0	0

SAMPLE 8

Wt of Sample coarser than (mm)	(phi)	Wt recorded	Total sam wt	% by wt	Skewness	Kurtosis
2	-1	0	17.33	0	.31 phi	1.06 phi
0.6	0.74	0.04	17.33	0.23	Mean (phi) =	1.78
0.2	2.32	13.27	17.33	76.60	Median (phi) =	1.66
0.06	4.06	17.33	17.33	100	% Clay	0.00
0.02	5.64	17.33	17.33	100	% Silt	0.00
0.006	7.38	17.33	17.33	100	% Sand	100.00
0.002	8.97	17.33	17.33	100	% Gravel	0

SAMPLE 9

Wt of Sample coarser than (mm)	(phi)	Wt recorded	Total sam wt	% by wt	Skewness	Kurtosis
2	-1	0	12.71	0	.29 phi	1.12 phi
0.6	0.74	0	12.71	0	Mean (phi) =	1.73
0.2	2.32	10.01	12.71	78.79	Median (phi) =	1.64
0.06	4.06	12.71	12.71	100	% Clay	0.00
0.02	5.64	12.71	12.71	100	% Silt	0.00
0.006	7.38	12.71	12.71	100	% Sand	100.00
0.002	8.97	12.71	12.71	100	% Gravel	0

SAMPLE 10

Wt of Sample coarser than (mm)	(phi)	Wt recorded	Total sam wt	% by wt	Skewness	Kurtosis
2	-1	0	16.8	0	.25 phi	1.08 phi
0.6	0.74	0	16.8	0	Mean (phi) =	1.63
0.2	2.32	14.01	16.8	83.41	Median (phi) =	1.57
0.06	4.06	16.8	16.8	100	% Clay	0.00
0.02	5.64	16.8	16.8	100	% Silt	0.00
0.006	7.38	16.8	16.8	100	% Sand	100.00
0.002	8.97	16.8	16.8	100	% Gravel	0

SAMPLE 11

Wt of Sample coarser than (mm)	(phi)	Wt recorded	Total sam wt	% by wt	Skewness	Kurtosis
2	-1	0	16.03	0	.32 phi	1.07 phi
0.6	0.74	0	16.03	0	Mean (phi) =	1.80
0.2	2.32	12.10	16.03	75.47	Median (phi) =	1.67
0.06	4.06	16.03	16.03	100	% Clay	0.00
0.02	5.64	16.03	16.03	100	% Silt	0.00
0.006	7.38	16.03	16.03	100	% Sand	100.00
0.002	8.97	16.03	16.03	100	% Gravel	0

Weight % of Grain Diameter Range measured in Phi

Range (mm)	Grain size (Phi)	SAMPLE 8	SAMPLE 9	SAMPLE 10	SAMPLE 11	Average Phi
64 to 4	-6 to -2	0	0	0	0	-4
4 to 2	-2 to -1	0	0	0	0	-1.5
2 to 0.71	-1 to 0.494	0.23	0	0	0	-0.25
0.71 to 0.6	0.494 to 0.737	0	0	0	0	0.62
0.6 to 0.2	0.737 to 2.322	76.36	78.79	83.41	75.47	1.53
0.2 to 0.06	2.322 to 4.059	23.40	21.21	16.59	24.53	3.19
0.06 to 0.02	4.059 to 5.644	0	0	0	0	4.85
0.02 to 0.006	5.644 to 7.381	0	0	0	0	6.51
0.006 to 0.002	7.381 to 8.966	0	0	0	0	8.17
<0.002	8.966 and above	0	0	0	0	9.83
		0	0	0	0	12
Total		100	100	100	100	

ALL WEIGHT MEASUREMENTS IN GRAMS

* DENOTES PARTICLE SIZE RANGES COMPRISING OF >50% SHELL

** DENOTES PARTICLE SIZE RANGES COMPRISING OF 100% SHELL

Figure 7.10 Cumulative Frequency Particle Size Distribution Graphs for the Invincible Samples 8-11

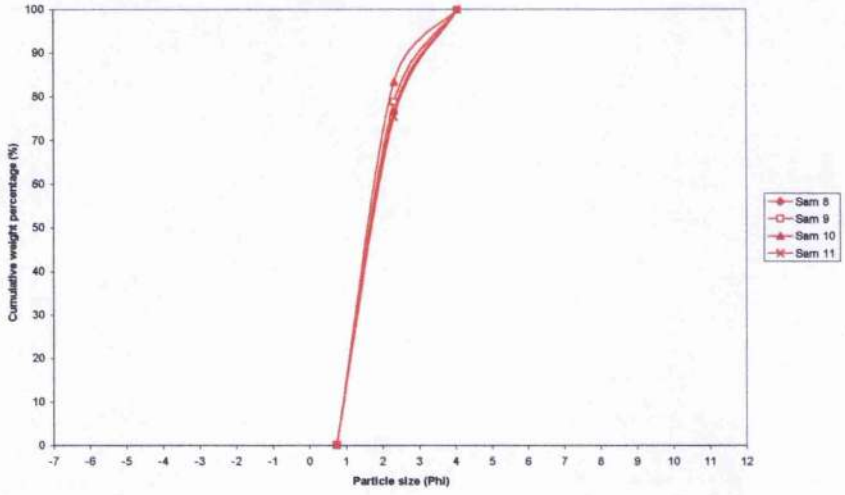

Figure 7.11 Frequency Weight Percentage versus Particle Diameter plots for the Invincible Samples 8-11

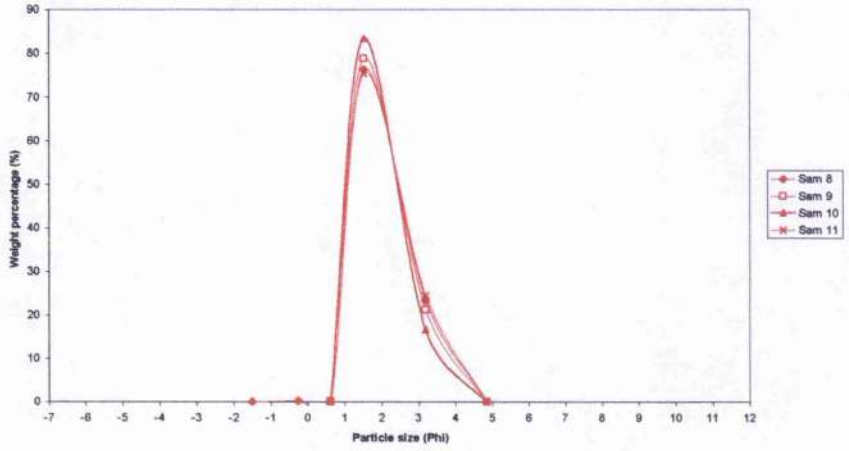

Figure 7.12 Textural Classification plots for Invincible samples 8-11 & 20-22

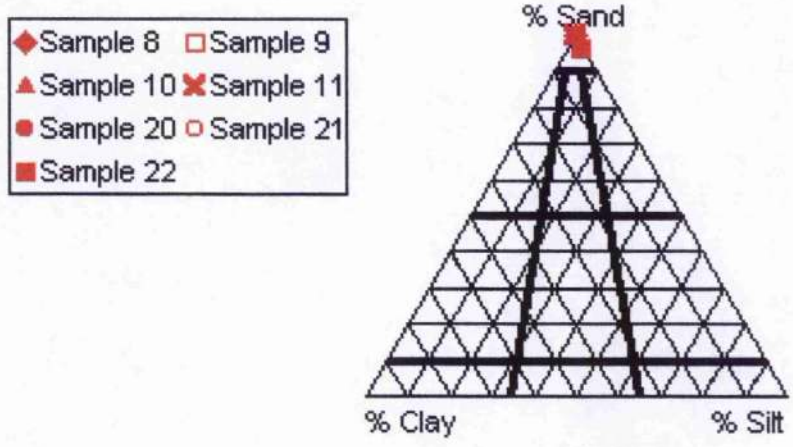

TABLE 7.11 Particle Size Analysis for Invincible Sediment Samples 20-22

Sample Number	SIEVE ANALYSIS					COULTER ANALYSIS								
	Total Weight of Sample	Wt of Sample 64mm>p>4mm	Wt of Sample 4mm>p>2mm	Wt finer than 2mm	Weight 2>p>0.71mm	Wt finer than 0.71mm	Wt of Sample > 0.6mm	Weight 2mm>p>0.6mm	Wt finer than 0.6mm	Wt finer than 0.2mm	Wt finer than 0.06mm	Wt finer than 0.02mm	Wt finer than 0.006mm	Wt finer than 0.002mm
SAM 20	18.56	0	0	18.56	0.01	18.55	0	0.01	18.55	3.16	0	0	0	0
SAM 21	18.81	0	0	18.81	0.01	18.80	0	0.01	18.80	3.68	0.52	0.40	0.20	0.05
SAM 22	22.78	0	0	22.78	0	22.78	0	0	22.78	8.10	0.91	0.57	0.31	0.09

SAMPLE 20

Wt of Sample coarser than (mm)	(phi)	Wt recorded	Total sam wt	% by wt	Skewness	Kurtosis
2	-1	0	18.56	0	.28 phi	1.09 phi
0.6	0.74	0.01	18.56	0.05	Mean (phi) =	1.65
0.2	2.32	15.40	18.56	82.97	Median (phi) =	1.58
0.06	4.06	18.56	18.56	100	% Clay	0
0.02	5.64	18.56	18.56	100	% Silt	0
0.006	7.38	18.56	18.56	100	% Sand	100.00
0.002	8.97	18.56	18.56	100	% Gravel	0

SAMPLE 21

Wt of Sample coarser than (mm)	(phi)	Wt recorded	Total sam wt	% by wt	Skewness	Kurtosis
2	-1	0	18.81	0	.32 phi	1.16 phi
0.6	0.74	0.01	18.81	0.05	Mean (phi) =	1.71
0.2	2.32	15.13	18.81	80.44	Median (phi) =	1.61
0.06	4.06	18.29	18.81	97.24	% Clay	0.27
0.02	5.64	18.41	18.81	97.87	% Silt	2.50
0.006	7.38	18.61	18.81	98.94	% Sand	97.24
0.002	8.97	18.76	18.81	99.73	% Gravel	0

SAMPLE 22

Wt of Sample coarser than (mm)	(phi)	Wt recorded	Total sam wt	% by wt	Skewness	Kurtosis
2	-1	0	22.78	0	.28 phi	.89 phi
0.6	0.74	0	22.78	0	Mean (phi) =	2.06
0.2	2.32	14.68	22.78	64.44	Median (phi) =	1.90
0.06	4.06	21.87	22.78	96.01	% Clay	0.40
0.02	5.64	22.21	22.78	97.50	% Silt	3.60
0.006	7.38	22.47	22.78	98.64	% Sand	96.01
0.002	8.97	22.69	22.78	99.60	% Gravel	0

Weight % of Particle Diameter Range measured in Phi

Range (mm)	Grain size (Phi)	SAMPLE 20	SAMPLE 21	SAMPLE 22	Average Phi
64 to 4	-6 to -2	0	0	0	-4
4 to 2	-2 to -1	0	0	0	-1.5
2 to 0.71	-1 to 0.494	0.05	0.05	0	-0.25
0.71 to 0.6	0.494 to 0.737	0	0	0	0.62
0.6 to 0.2	0.737 to 2.322	82.90	80.40	64.44	1.53
0.2 to 0.06	2.322 to 4.059	17.05	16.78	31.57	3.19
0.06 to 0.02	4.059 to 5.644	0	0.66	1.48	4.85
0.02 to 0.006	5.644 to 7.381	0	1.07	1.16	6.51
0.006 to 0.002	7.381 to 8.966	0	0.78	0.96	8.17
<0.002	8.966 and above	0	0.26	0.39	9.83
		0	0	0	12
Total		100	100	100	

ALL WEIGHT MEASUREMENTS IN GRAMS

* DENOTES PARTICLE SIZE RANGES COMPRISING OF >50% SHELL

** DENOTES PARTICLE SIZE RANGES COMPRISING OF 100% SHELL

Figure 7.13 Cumulative Frequency Particle Size Distribution Graphs for the Invincible Samples 20-22

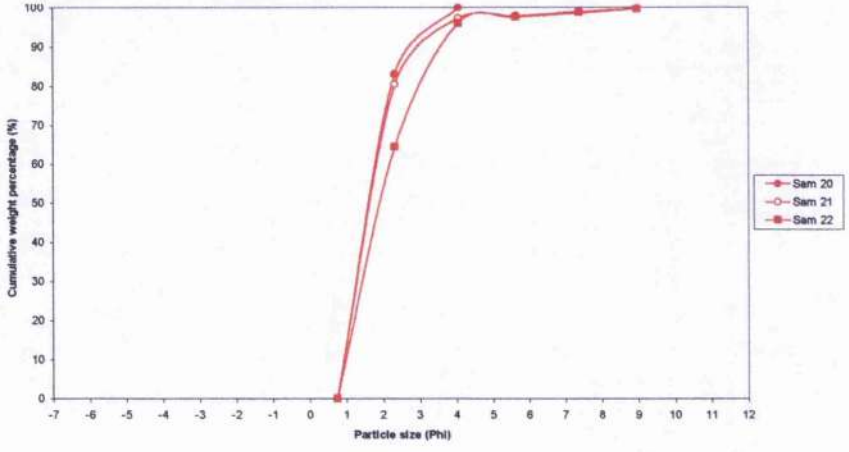

Figure 7.14 Frequency Weight Percentage versus Particle Diameter plots for the Invincible Samples 20-22

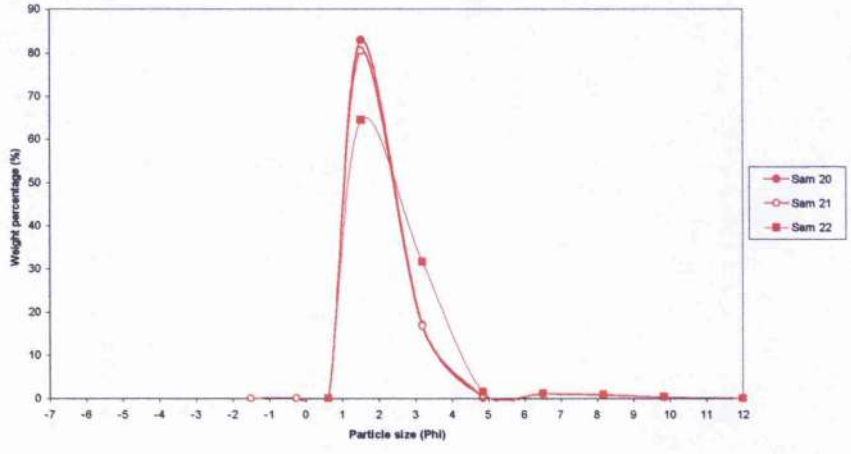

See Figure 7.12 for textural classification plots for Invincible samples 20-22

Discussion of Invincible samples 8-11 and 20-22

All six samples from within the Invincible site are undisputedly classed as sands (Figure 7.12), or more specifically fine sands according to the Wentworth scale. The range of M_z values within the six samples is only from 1.65φ to 2.06φ, with the M_d values ranging from 1.57 to 1.9φ. Samples 21 and 22 are noted as being the only samples to contain particles outwith the sand fraction.

This shows a very high level of consistency throughout the Invincible area, given that the laser Coulter Counter cannot clearly distinguish between all six.

Despite the relative peakedness, the standard deviation values of 1.02 to 1.51 suggest a poorly sorted sediment, skewed towards the fines in each case. The almost identical modal values suggest that the only variable within this site is illustrated by subtle changes in the slope of the fines tail. The samples from this site appear to contain no trace of carbonates. The only discrepancy arises from the sieve analysis, with two small shell fragments were found in samples 8 and 20. As there is no further trace of carbonates, these 'random' shell fragments may be classed as anomalous occurrences. In terms of organics, it is may be worthy of note that the samples located very close to the wreck site (20, 21 and 22) contained twice the organic content of the other samples taken from the surrounding area.

The projected density and porosity values are also very static across the site.

Tables 7.12 and 7.13 enable a direct comparison of the textural and statistical variations across the Invincible site.

Table 7.12 Summary of Sediment Composition and Classification for Invincible samples 8-11 & 20-22

Sample Number	Particle Class Composition				Textural Classification from Folk (1954)	Carbonates (%)	Organics (%)	Density* (g/cm^3)	Porosity* (%)
	% Gravel	% Sand	% Silt	% Clay					
8	0	100	0	0	Sand	0	1.05	2.03	37
9	0	100	0	0	Sand	0	0.76	2.04	36
10	0	100	0	0	Sand	0	0.57	2.05	35
11	0	100	0	0	Sand	0	0.72	2.03	37
20	0	100	0	0	Sand	0	1.24	2.05	35
21	0	97.24	2.50	0.27	Sand	0	1.2	2.04	36
22	0	96.01	3.60	0.40	Sand	0	1.48	2.01	39

* derived from the empirical relationships suggested by Hamilton & Bachman (1982)

Table 7.13 Statistical Summary of Particle Size Analysis for Invincible samples 8-11 & 20-22

Sample Number	Md (phi)	Mz (phi)	Modal Size			SD (phi)	Ska (phi)	Kg (phi)
			1st (phi)	2nd (phi)	3rd (phi)			
8	1.66	1.78	1.60	n/a	n/a	1.21	0.306	1.056
9	1.64	1.73	1.58	n/a	n/a	1.15	0.287	1.117
10	1.57	1.63	1.55	n/a	n/a	1.02	0.252	1.081
11	1.67	1.80	1.60	n/a	n/a	1.22	0.321	1.071
20	1.58	1.65	1.58	n/a	n/a	1.04	0.275	1.088
21	1.61	1.71	1.57	n/a	n/a	1.15	0.321	1.159
22	1.90	2.06	1.64	n/a	n/a	1.51	0.277	0.895

7.5.4. Textural analysis for the A1 Submarine site samples

TABLE 7.14 Particle Size Analysis for A1 Submarine Sediment Samples 12-16

Sample Number	SIEVE ANALYSIS					COULTER ANALYSIS								
	Total Weight of Sample	Wt of Sample 64mm>p>4mm	Wt of Sample 4mm>p>2mm	Wt finer than 2mm	Weight 2>p>0.71mm	Wt finer than 0.71mm	Wt of Sample > 0.6mm	Weight 2mm>p>0.6mm	Wt finer than 0.6mm	Wt finer than 0.2mm	Wt finer than 0.06mm	Wt finer than 0.02mm	Wt finer than 0.006mm	Wt finer than 0.002mm
SAM 12	1.26	0	0	1.26	0.01	1.25	0	0.01	1.25	1.17	0.28	0.21	0.12	0.05
SAM 13	3.45	0.13	0.05	3.27	0.04	3.23	0.03	0.07	3.20	3.05	2.63	1.77	0.96	0.33
SAM 14	9.11	0	0	9.11	0	9.11	0	0	9.11	8.90	7.54	4.90	2.62	0.92
SAM 15	8.26	0	0.05	8.21	0.06	8.15	0	0.06	8.15	7.70	5.19	2.80	0.99	
SAM 16	6.79	0.04	0.04	6.71	0.07	6.64	0	0.07	6.64	6.49	5.55	3.84	2.10	0.76

SAMPLE 12

Wt of Sample coarser than (mm)	(phi)	Wt recorded	Total sam wt	% by wt	Skewness	Kurtosis
64	-6	0	1.26	0	.59 phi	2.29 phi
4	-2	0	1.26	0	Mean (phi) =	3.92
2	-1	0	1.26	0		
0.6	0.74	0.01	1.26	0.79	Median (phi) =	3.33
0.2	2.32	0.09	1.26	7.38		
0.06	4.06	0.98	1.26	77.42	% Clay	3.64
0.02	5.64	1.05	1.26	83.24	% Silt	18.94
0.006	7.38	1.14	1.26	90.27	% Sand	77.42
0.002	8.97	1.21	1.26	96.36	% Gravel	0

SAMPLE 13

Wt of Sample coarser than (mm)	(phi)	Wt recorded	Total sam wt	% by wt	Skewness	Kurtosis
64	-6	0	3.45	0	-.14 phi	1.26 phi
4	-2	0.13	3.45	3.77	Mean (phi) =	5.74
2	-1	0.18	3.45	5.22		
0.6	0.74	0.25	3.45	7.25	Median (phi) =	5.72
0.2	2.32	0.40	3.45	11.54		
0.06	4.06	0.82	3.45	23.79	% Clay	9.69
0.02	5.64	1.68	3.45	48.59	% Silt	66.52
0.006	7.38	2.49	3.45	72.24	% Sand	18.57
0.002	8.97	3.12	3.45	90.31	% Gravel	5.22

SAMPLE 14

Wt of Sample coarser than (mm)	(phi)	Wt recorded	Total sam wt	% by wt	Skewness	Kurtosis
64	-6	0	9.11	0	.1 phi	.89 phi
4	-2	0	9.11	0	Mean (phi) =	6.10
2	-1	0	9.11	0		
0.6	0.74	0	9.11	0	Median (phi) =	5.90
0.2	2.32	0.21	9.11	2.27		
0.06	4.06	1.57	9.11	17.23	% Clay	10.12
0.02	5.64	4.21	9.11	46.16	% Silt	72.65
0.006	7.38	6.49	9.11	71.21	% Sand	17.23
0.002	8.97	8.19	9.11	89.88	% Gravel	0

SAMPLE 15

Wt of Sample coarser than (mm)	(phi)	Wt recorded	Total sam wt	% by wt	Skewness	Kurtosis
64	-6	0	8.26	0	.13 phi	.79 phi
4	-2	0	8.26	0	Mean (phi) =	6.56
2	-1	0.05	8.26	0.61		
0.6	0.74	0.11	8.26	1.33	Median (phi) =	6.36
0.2	2.32	0.11	8.26	1.33		
0.06	4.06	0.56	8.26	6.77	% Clay	12.02
0.02	5.64	3.07	8.26	37.14	% Silt	81.21
0.006	7.38	5.46	8.26	66.15	% Sand	6.16
0.002	8.97	7.27	8.26	87.98	% Gravel	0.61

SAMPLE 16

Wt of Sample coarser than (mm)	(phi)	Wt recorded	Total sam wt	% by wt	Skewness	Kurtosis
64	-6	0	6.79	0	-.05 phi	.88 phi
4	-2	0.04	6.79	0.59	Mean (phi) =	5.91
2	-1	0.08	6.79	1.18		
0.6	0.74	0.15	6.79	2.21	Median (phi) =	6.06
0.2	2.32	0.30	6.79	4.40		
0.06	4.06	1.24	6.79	18.24	% Clay	11.17
0.02	5.64	2.95	6.79	43.38	% Silt	70.80
0.006	7.38	4.69	6.79	69.08	% Sand	17.06
0.002	8.97	6.03	6.79	88.83	% Gravel **	1.18

Weight % of Grain Diameter measured in Phi

Range (mm)	Grain size (Phi)	SAMPLE 12	SAMPLE 13	SAMPLE 14	SAMPLE 15	SAMPLE 16	Average Phi
256 to 64	-8 to -6	0	0	0	0	0	-7
64 to 4	-6 to -4	0	3.77	0	0	0.59	-4
4 to 2	-2 to -1	0	1.45	0	0.61	0.59	-1.5
2 to 0.71	-1 to 0.494	0.79	1.16	0	0.73	1.03	-0.25
0.71 to 0.6	0.494 to 0.737	0	0.87	0	0	0	0.62
0.6 to 0.2	0.737 to 2.322	6.59	4.30	2.27	0	2.19	1.53
0.2 to 0.06	2.322 to 4.059	70.04	12.25	14.96	5.44	13.84	3.19
0.06 to 0.02	4.059 to 5.644	5.82	24.80	28.93	30.37	25.14	4.85
0.02 to 0.006	5.644 to 7.381	7.02	23.65	25.05	29.01	25.70	6.51
0.006 to 0.002	7.381 to 8.966	6.09	18.07	18.67	21.84	19.75	8.17
<0.002	8.966 and above	3.64	9.69	10.12	12.02	11.17	9.83
		0	0	0	0	0	12
Total		100	100	100	100	100	

ALL WEIGHT MEASUREMENTS IN GRAMS

* DENOTES PARTICLE SIZE RANGES COMPRISING OF >50% SHELL

** DENOTES PARTICLE SIZE RANGES COMPRISING OF 100% SHELL

Figure 7.15 Cumulative Frequency Particle Size Distribution Graphs for the A1 Submarine Samples 12-16

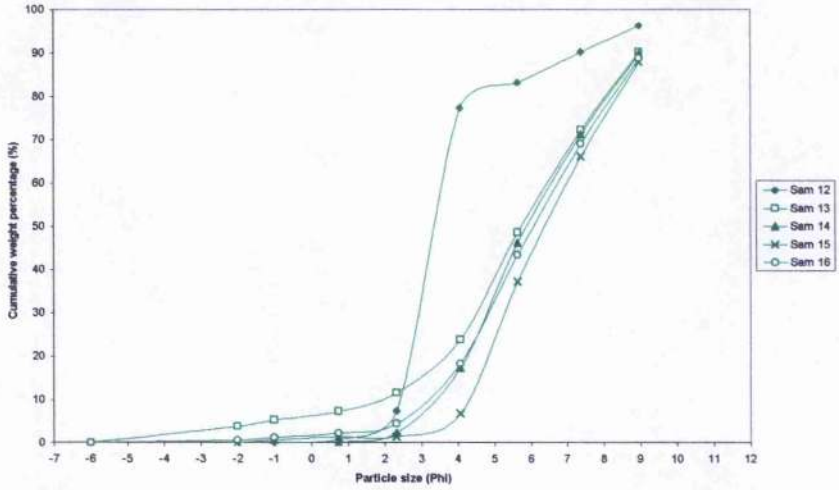

Figure 7.16 Frequency Weight Percentage versus Particle Diameter plots for the A1 Submarine Samples 12-16

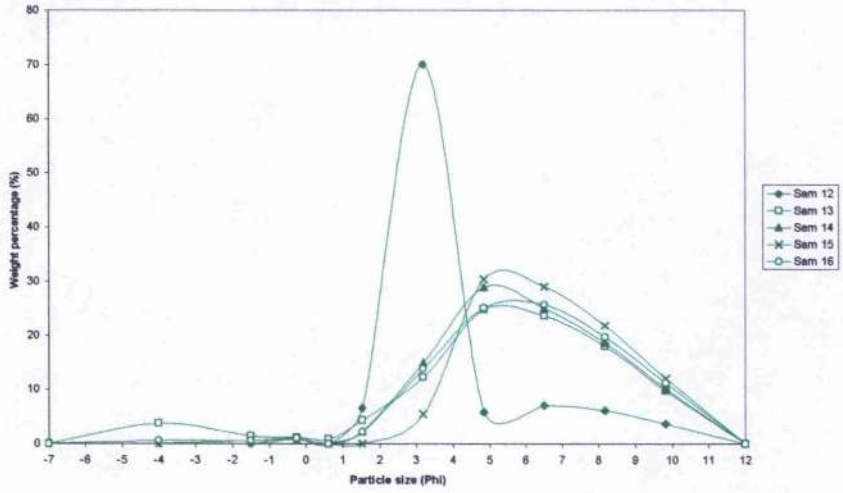

Figure 7.17 Textural Classification plots for A1 Submarine samples 12-16 & 17-19

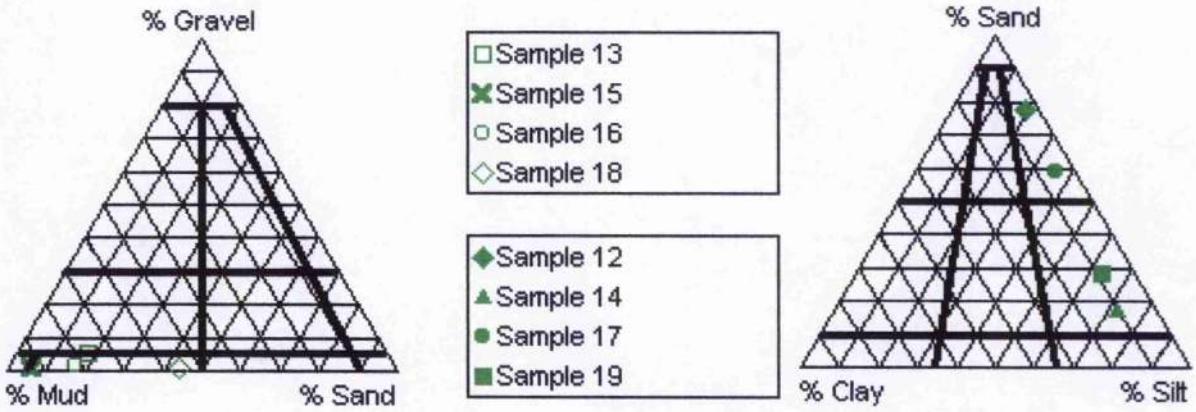

TABLE 7.15 Particle Size Analysis for A1 Submarine Sediment Samples 17-19

Sample Number	SIEVE ANALYSIS					COULTER ANALYSIS								
	Total Weight of Sample	Wt of Sample 64mm>p>4mm	Wt of Sample 4mm>p>2mm	Wt finer than 2mm	Weight 2>p>0.71mm	Wt finer than 0.71mm	Wt of Sample > 0.6mm	Weight 2mm>p>0.6mm	Wt finer than 0.6mm	Wt finer than 0.2mm	Wt finer than 0.06mm	Wt finer than 0.02mm	Wt finer than 0.006mm	Wt finer than 0.002mm
Sample 17	6.24	0	0	6.24	0.06	6.18	0.17	0.23	6.01	5.42	2.56	1.81	0.95	0.30
Sample 18	7.82	0	0.04	7.78	0.07	7.71	0.13	0.20	7.58	6.91	4.36	3.10	1.67	0.55
Sample 19	12.50	0	0	12.50	0	12.50	0.17	0.17	12.33	11.73	8.91	5.53	2.96	1.08

SAMPLE 17

Wt of Sample coarser than (mm)	(phi)	Wt recorded	Total sam wt	% by wt	Skewness	Kurtosis
64	-6	0	6.24	0	.42 phi	.97 phi
4	-2	0	6.24	0	Mean (phi) =	4.46
2	-1	0	6.24	0		
0.6	0.74	0.23	6.24	3.69	Median (phi) =	3.67
0.2	2.32	0.82	6.24	13.14		
0.06	4.06	3.68	6.24	58.97	% Clay	4.81
0.02	5.64	4.43	6.24	70.99	% Silt	36.22
0.006	7.38	5.29	6.24	84.78	% Sand	58.97
0.002	8.97	5.94	6.24	95.19	% Gravel	0

SAMPLE 18

Wt of Sample coarser than (mm)	(phi)	Wt recorded	Total sam wt	% by wt	Skewness	Kurtosis
64	-6	0	7.82	0	.25 phi	.81 phi
4	-2	0	7.82	0	Mean (phi) =	5.02
2	-1	0.04	7.82	0.51		
0.6	0.74	0.24	7.82	3.07	Median (phi) =	4.51
0.2	2.32	0.91	7.82	11.64		
0.06	4.06	3.46	7.82	44.25	% Clay	7.03
0.02	5.64	4.72	7.82	60.36	% Silt	48.72
0.006	7.38	6.15	7.82	78.64	% Sand	43.73
0.002	8.97	7.27	7.82	92.97	% Gravel **	0.51

SAMPLE 19

Wt of Sample coarser than (mm)	(phi)	Wt recorded	Total sam wt	% by wt	Skewness	Kurtosis
64	-6	0	12.50	0	.14 phi	.86 phi
4	-2	0	12.50	0	Mean (phi) =	5.55
2	-1	0	12.50	0		
0.6	0.74	0.17	12.50	1.36	Median (phi) =	5.29
0.2	2.32	0.77	12.50	6.16		
0.06	4.06	3.59	12.50	28.72	% Clay	8.64
0.02	5.64	6.97	12.50	55.76	% Silt	62.64
0.006	7.38	9.54	12.50	76.32	% Sand	28.72
0.002	8.97	11.42	12.50	91.36	% Gravel	0

Weight % of Particle Diameter measured in Phi

Range (mm)	Grain size (Phi)	SAMPLE 17	SAMPLE 18	SAMPLE 19	Average Phi
256 to 64	-8 to -6	0	0	0	-7
64 to 4	-6 to -4	0	0	0	-4
4 to 2	-2 to -1	0	0.51	0	-1.5
2 to 0.71	-1 to 0.494	0.96	0.90	0	-0.25
0.71 to 0.6	0.494 to 0.737	3	1.70	1	0.62
0.6 to 0.2	0.737 to 2.322	9.41	8.52	4.77	1.53
0.2 to 0.06	2.322 to 4.059	45.89	32.60	22.59	3.19
0.06 to 0.02	4.059 to 5.644	12.03	16.08	27.04	4.85
0.02 to 0.006	5.644 to 7.381	13.69	18.31	20.57	6.51
0.006 to 0.002	7.381 to 8.966	10.45	14.33	15.00	8.17
<0.002	8.966 and above	4.83	7.06	8.65	9.83
		0	0	0	12
Total		100	100	100	

ALL WEIGHT MEASUREMENTS IN GRAMS

* DENOTES PARTICLE SIZE RANGES COMPRISING OF >50% SHELL

** DENOTES PARTICLE SIZE RANGES COMPRISING OF 100% SHELL

Figure 7.18 Cumulative Frequency Particle Size Distribution Graphs for the A1 Submarine Samples 17-19

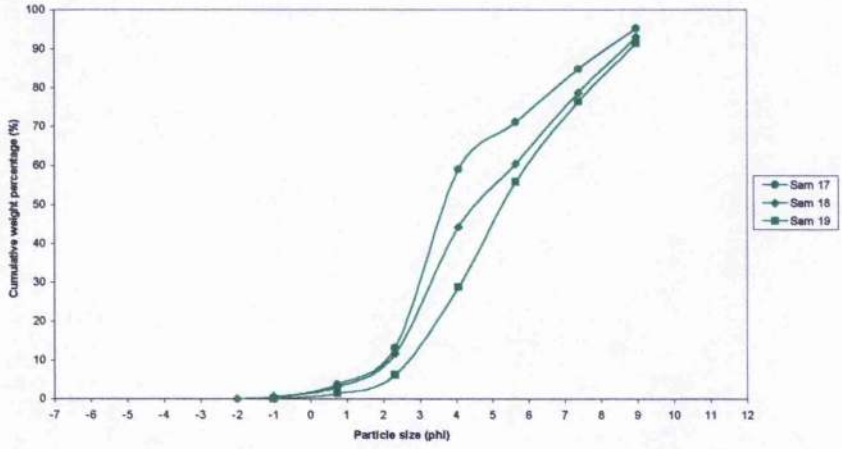

Figure 7.19 Frequency Weight Percentage versus Particle Diameter plots for the A1 Submarine Samples 17-19

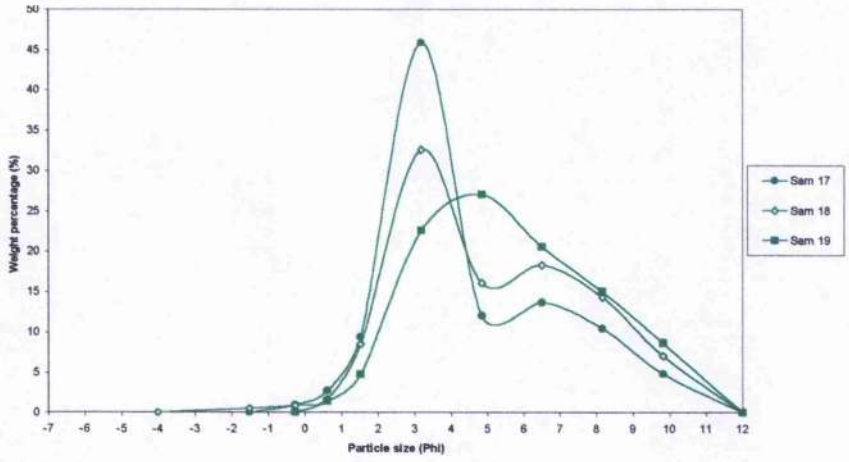

Discussion of A1 Submarine samples 12-16 & 17-19

The graphs of the particle size distribution show a rather large degree of variability within this A1 Submarine site. The M_z values are spread over a 2φ range, from 3.92φ in sample 12, to 6.56φ in sample 15. The M_d values mirror this spread, ranging from 3.33φ in sample 12 to 6.36φ in sample 15. The inclusion of gravel or coarse shells in four of the eight samples, and illustrated by the Sk_a values, has induced a low-resolution textural classification for samples 13, 15, 16 and 18 (Figure 7.17 and Table 7.16), and divides the samples between the gravelly muds and slightly gravelly muds of samples

13 and 15, and the slightly shelly sandy muds of samples 16 and 18. In ignoring the 0-5th percentiles the skewness values are unable to reflect the coarse content in samples 15 and 18, but do succeed in attributing negative skewness values to samples 13 and 16. In the high-resolution textural analysis, samples 12 and 17 are clearly dominated by the sand fraction, giving rise to silty sands. Samples 14 and 19 on the other hand, are classed as sandy silts due to the predominant silt fraction.

The carbonate and organic contents of the samples 17-19 taken from the vicinity of the wreck are found to be approximately half that of the values recorded in samples 12-16. Sample 12 may be highlighted as anomalous as its 7.29% organic content is at least 4% below the values found in the other samples taken from the surrounding area.

It is worthy of note that the most significant observation was that of a "rough crust" which has formed on the seabed surface over sample sites 13, 14, 15, and 16. This silty crust was very rigid and had to be broken up in order to obtain a sample.

A summary of these statistical and textural variations is provided by tables 7.16 and 7.17 below.

Table 7.16 Summary of Sediment Composition and Classification for A1 Submarine samples 12-16 & 17-19

Sample Number	Particle Class Composition				Textural Classification from Folk (1954)	Carbonates (%)	Organics (%)	Density* (g/cm^3)	Porosity* (%)
	% Gravel	% Sand	% Silt	% Clay					
12	0	77.42	18.94	3.64	silty sand	18.52	7.29	1.79	52
13	5.22	18.57	66.52	9.69	gravelly mud	21.66	15.38	1.62	61
14	0	17.23	72.65	10.12	sandy silt	10.43	11.45	1.58	64
15	0.61	6.16	81.21	12.02	slightly gravelly mud	12.26	12.38	1.55	66
16	1.18	17.06	70.60	11.17	slightly shelly sandy mud	13.21	13.59	1.60	62
17	0	58.97	36.22	4.81	silty sand	0	7.69	1.78	54
18	0.51	43.73	48.72	7.03	slightly shelly sandy mud	5.57	7.34	1.73	57
19	0	28.72	62.64	8.64	sandy silt	4.74	4.66	1.68	60

* as derived from the empirical relationships suggested by Hamilton & Bachman (1982)

Table 7.17 Statistical Summary of Particle Size Analysis for A1 Submarine samples 12-16 & 17-19

Sample Number	Md (phi)	Mz (phi)	Modal Size			SD (phi)	Ska (phi)	Kg (phi)
			1st (phi)	2nd (phi)	3rd (phi)			
12	3.33	3.92	3.18	6.750	n/a	2.59	0.592	2.286
13	5.72	5.74	5.31	-3.9	n/a	4.26	-0.138	1.259
14	5.90	6.10	5.15	n/a	n/a	3.27	0.101	0.886
15	6.36	6.56	5.35	n/a	n/a	2.88	0.130	0.793
16	6.06	5.91	5.74	n/a	n/a	3.79	-0.051	0.883
17	3.67	4.46	3.19	6.570	n/a	3.57	0.422	0.972
18	4.51	5.02	3.27	6.500	n/a	3.84	0.246	0.809
19	5.29	5.55	4.70	n/a	n/a	3.58	0.143	0.860

7.6. Discussion of overall textural and compositional analysis

In general terms, the values of M_Z across all the sample sites appears to suggest that the Invincible site possesses the coarsest average sediment, followed by the Shingle site, and then the Calibration and A1 Submarine sites together. The one exception to this statement is sample 6 which actually has the coarsest average sediment of all. Given the relationship between M_Z and porosity, the data also suggests an increase in the percentage porosity from 30-40% at the Invincible area, up to approximately 60% at the Calibration and A1 Submarine areas.

This M_Z observation is also mirrored almost exactly by the M_d values. The primary modal values break from this pattern by placing all of the shingle samples at the coarsest end of the spectrum, followed by the Invincible site, the A1 Submarine site and finally the Calibration site.

The textural analysis of all the samples, displayed collectively in Figure 7.20, provides an alternative measure of the 'roughness' for each sample. The coarse 'gravel' contents are fully accounted for by plotting the compositions on the ternary plot for Gravel-Sand-Mud. This plot is regarded as having a low textural resolution, but in terms of encompassing the coarse 'gravel' fraction, the Gravel-Sand-Mud plot may actually be viewed as increasing the resolution.

Figure 7.20 Textural classification summary for all the samples analysed

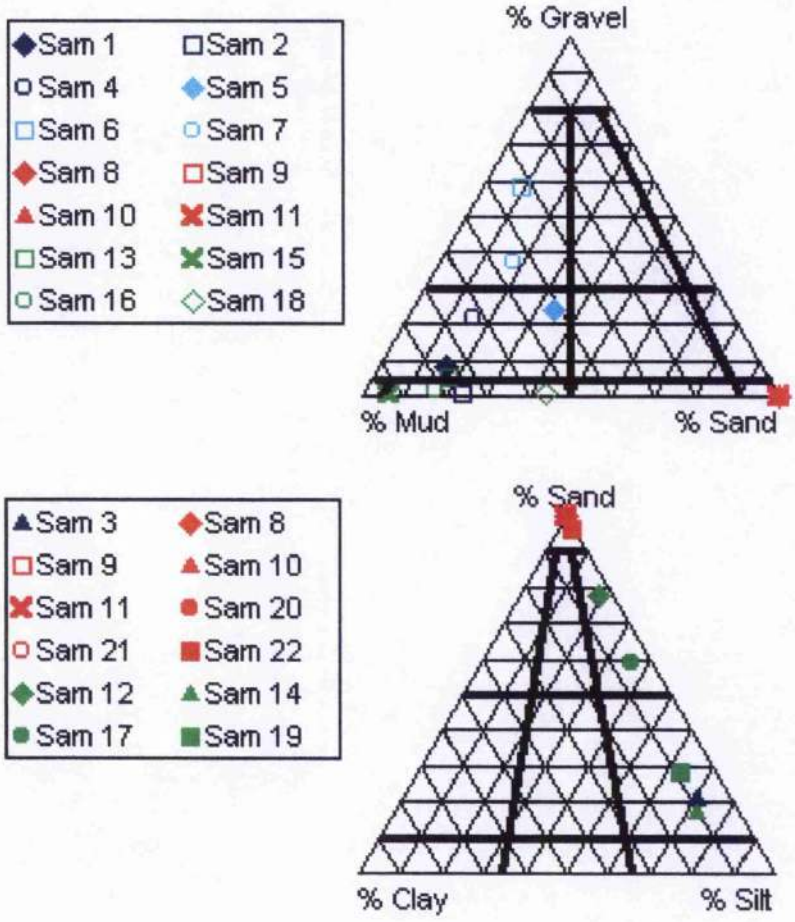

The textural analysis suggests that there is a broad range of sediment types between each site. The Calibration site has a dominant mud matrix throughout, but is found to contain a variety of gravels, shells and sands within the coarse fractions. From the ternary plots, the samples can be listed with decreasing roughness or coarseness, from sample 4, to sample 1, to sample 2 and finally sample 3. Shingle sediments are found to be a mixture of gravels, shells and muds, with most variation coming in the gravel and sand grades. The ternary plots suggest that the textural roughness is highest in sample 6 (muddy shelly gravel), followed by sample 7 (muddy gravel) and then sample 5 (shelly mud). The Invincible samples illustrate very little textural variety, with each one clearly falling within the textural classification of sand on both the low and high resolution ternary plots. In contrast, the A1 Submarine samples show a much more complex

textural picture, with the sediment matrix varying between sand and mud. The small percentage of coarse material found within samples 13, 15, 16 and 18 were enough to place them on the low-resolution ternary plot, but the lack of a substantial sand fraction in relation to the other samples means that they cannot be automatically regarded as texturally coarser. The direct comparison of samples 12 and 16 can be used to illustrate this point. For example, although sample 16 has a gravel content of 1.18% compared to 0% in sample 12, sample 12 is found to have over four times the weight percentage of sand that is present in sample 16.

In general, samples 13, 15, 16, and 18 reflect the compositions found within the Calibration site, with muds dominating the particle class composition and gravels and coarse shell accounting for less than 5% of the material. The high-resolution ternary plot in Figure 7.20 shows that the other four samples follow a progression of decreasing textural roughness from sample 12, through samples 17 and 19, to sample 14, as the sand fraction becomes replaced by a silt fraction.

The results of the carbonate content analysis revealed a marked contrast between survey areas, with generally little variation within each site, other than in the immediate vicinity of wrecks.

In broad terms, the A1 Submarine site contains the highest carbonate content, with between 10% and 22% carbonates in the exposed areas away from the wreck. The surface sediments in the Calibration and Shingle sites contain comparable levels of carbonates ranging from 4 - 8%, with the exception of Sample 6 which contains an anomalously high 13.25%. As for the Invincible site, all seven samples recorded 0% trace of carbonates. In truth, the laboratory results actually showed an apparent weight gain in the Invincible samples following the carbonate analysis. This minute gain is explained, and discounted, because the HCl evaporation rate in the sands is less than in

the control beaker due to percolation into the sand material, thereby causing an over-compensation for the weight lost to evaporation.

The organic analysis results suggested a high degree of variability between the sites. The Calibration site samples were found to contain a very consistent level of 11-12% organic content, which is attributed to the settling from suspension of organic matter in the shallow, slow-moving water at the margins of the estuary. The Shingle samples taken from within the centre of the estuary however, also recorded relatively high levels of between 9% and 15%. The seven samples across the Invincible site recorded very low, and almost negligible, levels of organic content. The results from the A1 Submarine site show a much higher organic content, ranging from 5-8% near the wreck, to 11-16% in the surrounding area.

As the projected density and porosity values are directly related to the mean particle size, the variability of both parameters mimics the pattern illustrated by the variations in mean particle size.

The final sediment analysis results have been summarised in Table 7.18.

Table 7.18 Summary of sediment analysis results

Sample Number	Mean GS (phi)	Median GS (phi)	Modal (1st) (phi)	Finest Mode (phi)	Gravel (%)	Sand (%)	Silt (%)	Clay (%)	Density (g/cm^3)	Porosity (%)
1	5.58	6.06	6.51	6.51	8.41	16.24	66.63	8.71	1.65	61
2	5.75	5.92	6.44	6.44	1.15	23.66	67.13	8.07	1.63	62
3	5.96	6.00	6.33	6.33	0.00	20.94	70.75	8.31	1.61	63
4	3.56	5.31	6.55	6.55	21.44	16.26	53.44	8.85	1.86	48
5	2.31	2.77	-3.96	6.65	23.79	34.27	36.61	5.34	1.96	42
6	0.44	-1.37	-3.70	6.52	58.30	9.35	27.98	4.37	2.17	30
7	2.13	2.96	-3.96	6.50	37.35	17.78	38.97	5.91	2.00	39
8	1.78	1.66	1.60	1.60	0.00	100.00	0.00	0.00	2.03	37
9	1.73	1.64	1.58	1.58	0.00	100.00	0.00	0.00	2.04	36
10	1.63	1.57	1.55	1.55	0.00	100.00	0.00	0.00	2.05	35
11	1.80	1.67	1.60	1.60	0.00	100.00	0.00	0.00	2.03	37
20	1.65	1.58	1.58	1.58	0.00	100.00	0.00	0.00	2.05	35
21	1.71	1.61	1.57	1.57	0.00	97.24	2.50	0.27	2.04	36
22	2.06	1.90	1.64	1.64	0.00	96.01	3.60	0.40	2.01	39
12	3.92	3.33	3.18	6.75	0.00	77.42	18.94	3.64	1.79	52
13	5.74	5.72	5.31	5.31	5.22	18.57	66.52	9.69	1.62	61
14	6.10	5.90	5.15	5.15	0.00	17.23	72.65	10.12	1.58	64
15	6.56	6.36	5.35	5.35	0.61	6.16	81.21	12.02	1.55	66
16	5.91	6.06	5.74	5.74	1.18	17.06	70.60	11.17	1.60	62
17	4.46	3.67	3.19	6.57	0.00	58.97	36.22	4.81	1.78	54
18	5.02	4.51	3.27	6.50	0.51	43.73	48.72	7.03	1.73	57
19	5.55	5.29	4.70	4.70	0.00	28.72	62.64	8.64	1.68	60

7.7. Conclusions

The textural analysis of the sediment samples acquired over the Portsmouth survey areas revealed a considerable variation in the degrees of sediment roughness. The samples varied in the coarseness of the sediment matrix, from the gravel matrix of the Shingle site down to the mud matrix of the Calibration and A1 Submarine sites.

In terms of trying to measure the surface roughness through particle size analysis, the verbal textural classification of Folk (1954) better preserves the characteristics of the coarse fraction than the results derived for the individual statistical measures that were applied. The mean values can be used to provide a good indication of the predominant clast size range within the samples. The median values may be regarded as offering a similar roughness assessment to that of the mean values, although they appear to be more sensitive to the nature of the coarse fraction.

In conclusion, the measurement of sediment roughness must incorporate both the statistical measures and the textural classification in order to accurately represent the full range of clasts present within the seabed sediment.

These results will thus form the basis for the seabed roughness evaluation within the overall acoustic-sediment analysis.

CHAPTER 8:

RESULTS

8.1. Introduction to Results

The purpose of this chapter is to cross-correlate the findings of the digital swath data processing and the ground-truthed sediment analysis, thereby enabling a direct comparison of predicted and actual scattering strengths recorded in relation to known sediment characteristics.

The first stage of the results will present the findings of the digital data processing in Chapter 6, in which the roughness of the water-sediment interface is evaluated using remote sensing sonar techniques. This remote evaluation of the seabed roughness will then be cross-correlated with the actual sediment roughness characteristics presented in Chapter 7, in order to assess the empirical relationships between the remote and ground-truthed roughness measurements.

This cross-correlation will be performed on both an area by area, and a site by site basis, in order to permit the identification of both 'inter-area' and 'intra-area' empirical relationships.

8.2. Digital data processing results

At each of the four survey sites, a representative swath file has been selected to provide an overview of the results from the digital data analysis, thereby enabling a visual comparison of the general sonar characteristics between survey areas. The overview comprises of the mapping of five critical acoustic parameters within a 10m x 10m square grid surrounding the sample locations:-

(1) Bathymetry / Topography (D_t)

(2) Seabed slope angle (α_S)

(3) Total grazing angle (α)

(4) Element area (E_{area} or dA)

(5) Theoretical minus Actual scattering strength (TS-AS)

The key parameter in the sonar analysis of sediment-acoustic relationships is that of TS-AS. As discussed in Chapter 6, the direct comparison of these parameters can be used to describe the acoustic roughness of the surface by creating three different conditions of scattering, TS>AS, TS=AS, and TS<AS.

Where TS=AS then the surface matches Lambert's Law and thus it is assumed to be effectively flat. Where TS>AS, then the actual strength of the scatter is less than that of a flat surface. In such circumstances it may be hypothesised that the shortfall in acoustic scattering is the result of an enhancement of the other acoustic interface forms of reflection or absorption. In assuming that the surface is flat, then the proposed enhancement of reflection or absorption (transmission) will be dependent upon the reflection coefficient and the acoustic impedance contrast at the water-sediment interface. Where TS<AS, then the surface is regarded as causing a higher scattering strength than predicted by Lambert's Law. The theories of scattering at an interface discussed in Chapter 2 state that an enhancement in scattering levels occurs as a direct result of an increase in the roughness of the interface.

The analysis will therefore focus upon the relationships between the TS-AS values generated by the sonar analysis in Chapter 6 and the actual sediment roughness characteristics provided by Chapter 7.

The sediment characteristics derived in Chapter 7 are used to provide a guide to the granular or particulate roughness of the seabed, referred to as 'bed roughness.' As

discussed previously, the scale of bed roughness is entirely dependent upon the scale of analysis, and so the particle size value must be compared to the acoustic scale of analysis defined by the element area and the grazing angle. This is done using the following equation to determine a 'Resolvable Roughness' factor in relation to the roughness perceived by the grazing angle. As the acoustic roughness increases with increasing grazing angle, the Resolvable Roughness calculation is based upon the vertical height differential determined by the tangential of the grazing angle multiplied by the length of the element, as shown below.

$$RR = E_L \cdot \tan \alpha$$

Where;

RR = Resolvable Roughness (vertical)

E_L = Element length

α = Grazing angle

This Resolvable Roughness factor is then multiplied by the area of the element to give a 'Roughness Index,' which defines the actual measurable bed roughness in relation to the sonar signal:-

$$RI = RR \cdot E_{area}$$

Where:

RI = Bed Roughness Index

RR = Resolvable Roughness

E_{area} = Element area

This Roughness Index value can then be plotted against the sonar parameter of TS-AS for every sample site, to enable a direct assessment of 'acoustic scattering strength' versus 'bed roughness' across the entire dataset.

Once this has been achieved for each survey area, the results will be compared between survey areas of broadly different sediment types to assess the more universal ability of

the sediment-acoustic relationships to discriminate between gravels, sands, silts and muds.

The impact of the percentage carbonate and organic contents, and the associated density and porosity values, are also incorporated within the analysis, but are treated as secondary factors because these characteristics focus more upon the sediment matrix composition than on the surface 'roughness' value.

Construction of Maps

The variability maps presented in this chapter were constructed using the Surfer Win-32, Golden Software package. The Kriging technique was used for the gridding of the irregularly spaced X, Y, Z datasets because it is specifically designed for geostatistical gridding of irregularly-spaced data using very low level interpolation, in order to highlight trends rather than anomalies in the dataset (Isaaks & Srivastava, 1989). The minimum interpolation function was used to preserve the accuracy of the high resolution data, thereby enabling true trends to be depicted across each map. The preference for 'trends' rather than 'anomalies' is necessary due to the low-density, and low resolution (Eastings ±1m and Northings ±1m), nature of the ground-truthed sediment data. The area within a 1m radius of each sample location must be assumed, in the absence of further data, to have homogeneous sediment characteristics to that of the sediment sample itself. This restricts the variability maps to focusing upon the overall 'trend' of acoustic data in relation to each fixed sediment parameter within the site, as the assumption of homogeneous sediments would prevent the elimination of sediment variability as a cause of any anomaly highlighted within the area.

Post-processed and filtered digital data coverage of each sample location

The actual cross-correlation of digital data with ground-truthed data is subject to the density of the digital data coverage following the post-processing and filtering stages outlined in Chapter 6. The overall coverage of filtered digital data within ±1m of the sample sites is summarised in Table 8.1.

Table 8.1 Summary of filtered element coverage within a 2m x 2m square surrounding each of the sample locations

SURVEY AREA	Sample No.	No. of Elements
Calibration	1	23
	2	89
	3	0
	4	62
Shingle	5	107
	6	0
	7	371
Invincible	8	307
	9	440
	10	122
	11	706
A1 Submarine	12	49
	13	218
	14	453
	15	82
	16	32

This summary table highlights the fact that although there is not an abundance of sample sites, the digital data relating to each site is more than sufficient to provide a comprehensive analysis of sediment-acoustic relationships.

Sample sites 17-22 have been omitted from the results due to the difficulties encountered during post-processing and filtering due to the close proximity of the anomalous bathymetry relating to each wreck, and also because of the poor locational data associated with the sediment sample retrieval by divers.

8.2.1. Calibration Survey Area (Samples 1-4)

The general sonar characteristics of this survey area are presented using post-processing data from the 'Cal3.swa' swath file to generate maps of D_t, α_S, α, E_{area}, and TS-AS, over Sample Site 4, as illustrated in Figures 8.1-8.5 respectively. For the purpose of evaluating these figures, it should be noted that this area has been illuminated by the sonar in a NE to SW orientation (across-track), with the vessel actually travelling from NW-SE. This is particularly relevant to the maps of angular variability.

Figure 8.1 Map of D_t (bathymetry) variability within a 10m x 10m area surrounding Sample Site 4 (Cal3Sam4)

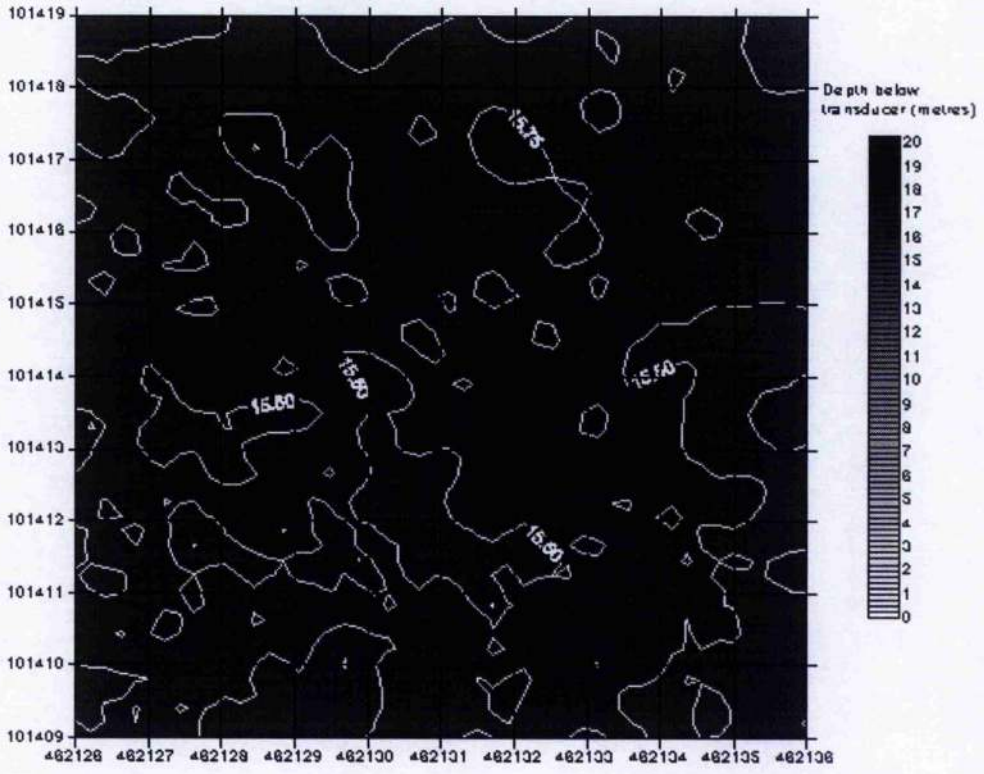

Figure 8.2 **Map of α_S variability within a 10m x 10m area surrounding Sample Site 4 (Cal3Sam4)**

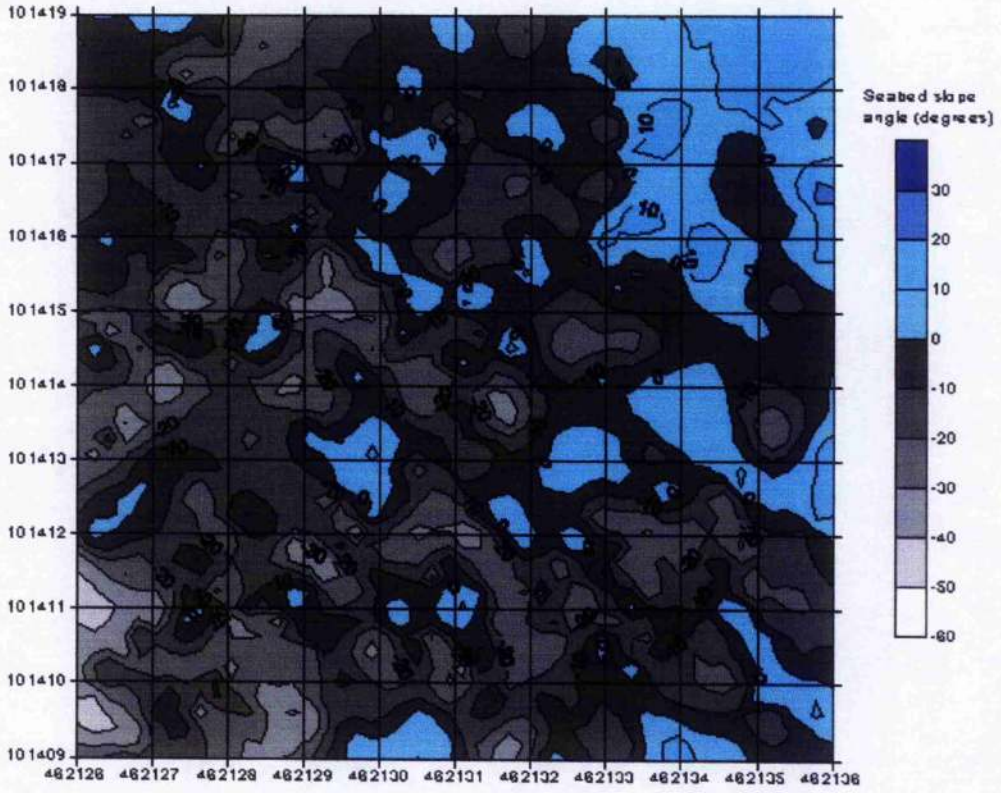

Figure 8.3 **Map of α variability within a 10m x 10m area surrounding Sample Site 4 (Cal3Sam4)**

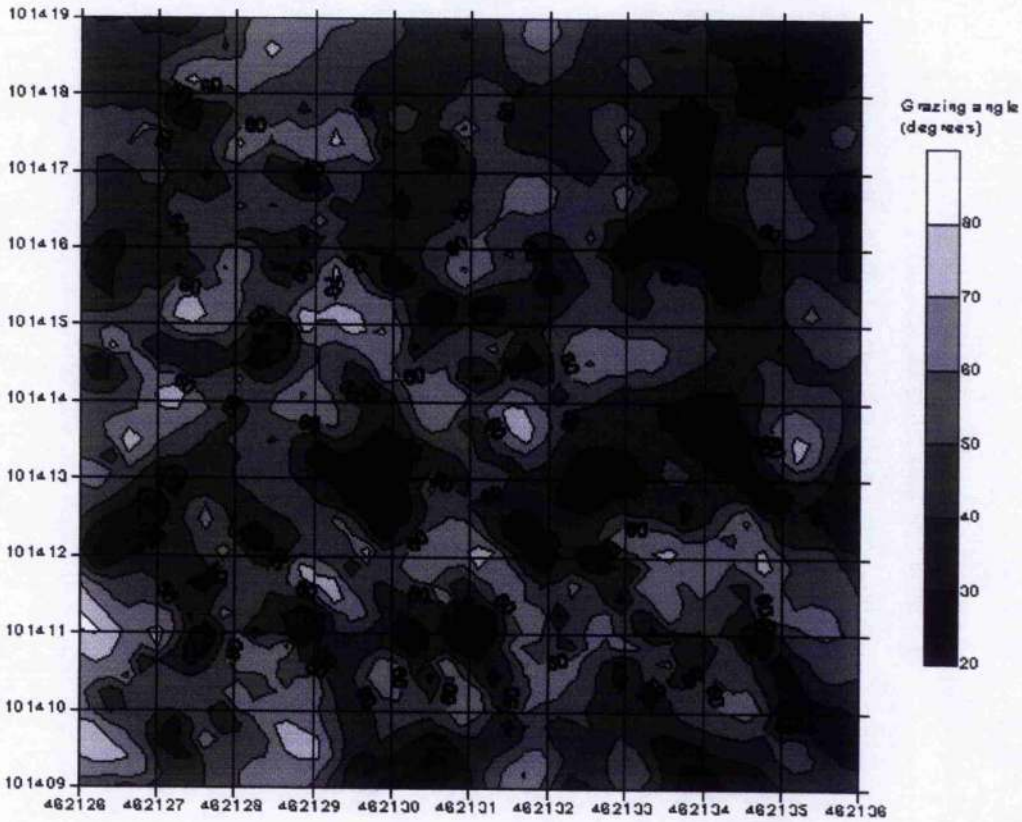

Figure 8.4 **Map of E_{area} variability within a 10m x 10m area surrounding Sample Site 4 (Cal3Sam4)**

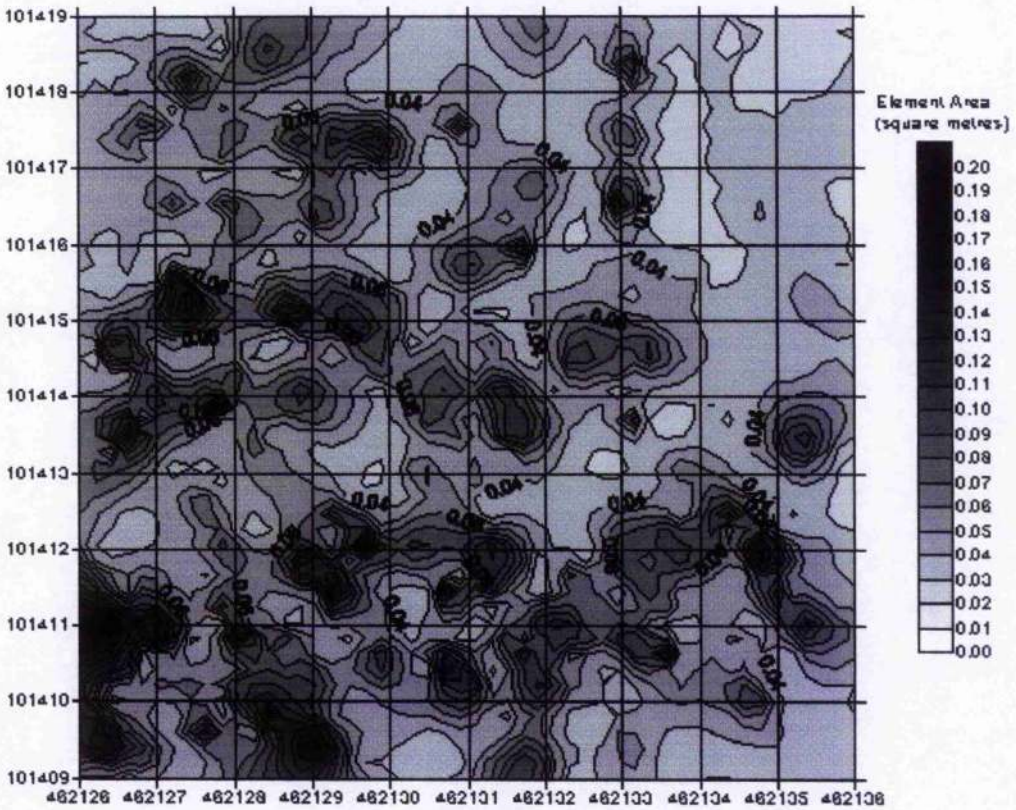

Figure 8.5 **Map of TS-AS variability within a 10m x 10m area surrounding Sample Site 4 (Cal3Sam4)**

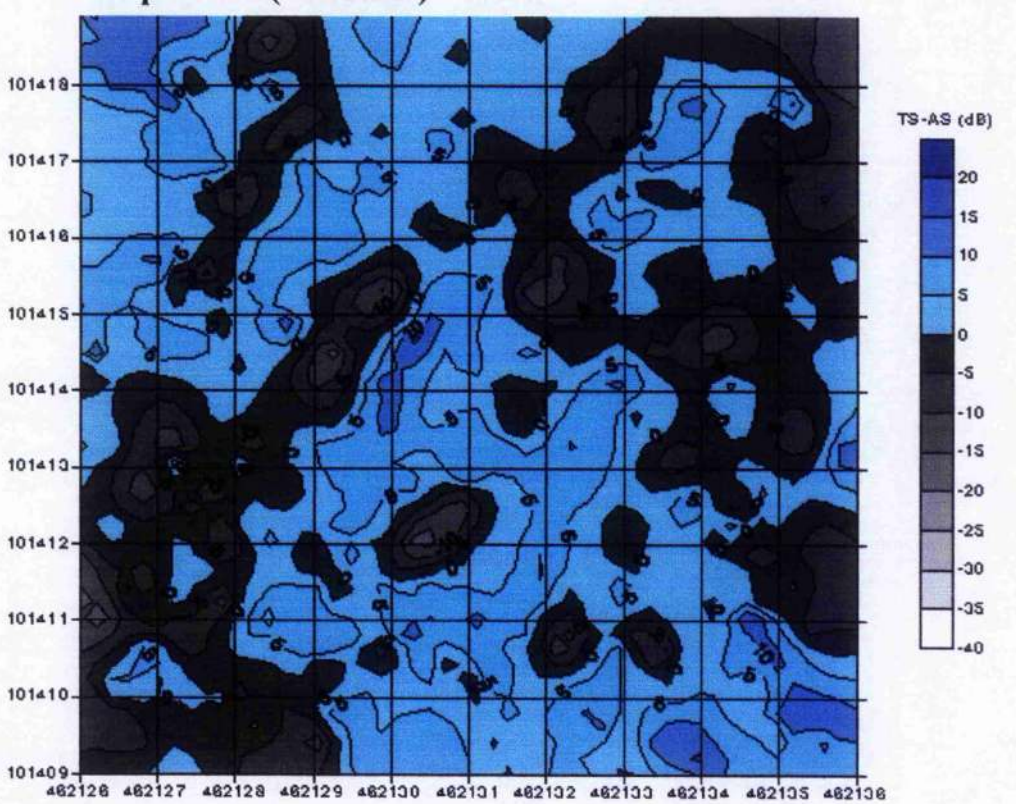

Figure 8.1 shows that the bathymetry is relatively flat and horizontal over sample site 3. Figure 8.2 shows the localised seabed slope trends with the areas where the seabed is sloping away from the transducers being shaded in blue to clarify the trend. The low distribution of the blue shading suggests that, relative to the transducer, the majority of the seabed surface dips towards the vessel. This broadly correlates with Figure 8.1 bearing in mind a NE to SW aspect to the sonar illumination. The impact of the seabed slope angles are translated into the overall grazing angle in Figure 8.3, which shows the presence of uncharacteristically low grazing angles in the NE corner, close to the transducers. A glance at Figure 8.2 shows that this occurs because the localised seabed is sloping away from the transducer. Figure 8.4 shows the general trend of E_{area} increasing with distance from the transducer, with the presence of anomalies induced by variations in the total grazing angle. The cumulative affect of all of these parameters upon the TS-AS relationship is shown by Figure 8.5 to result in a large proportion of the area having a lower scattering strength than predicted by Lambert.

Figure 8.6 Plot of TS-AS versus Grazing angle values for data sampled from the $2m^2$ area surrounding sample sites 1, 2, and 4.

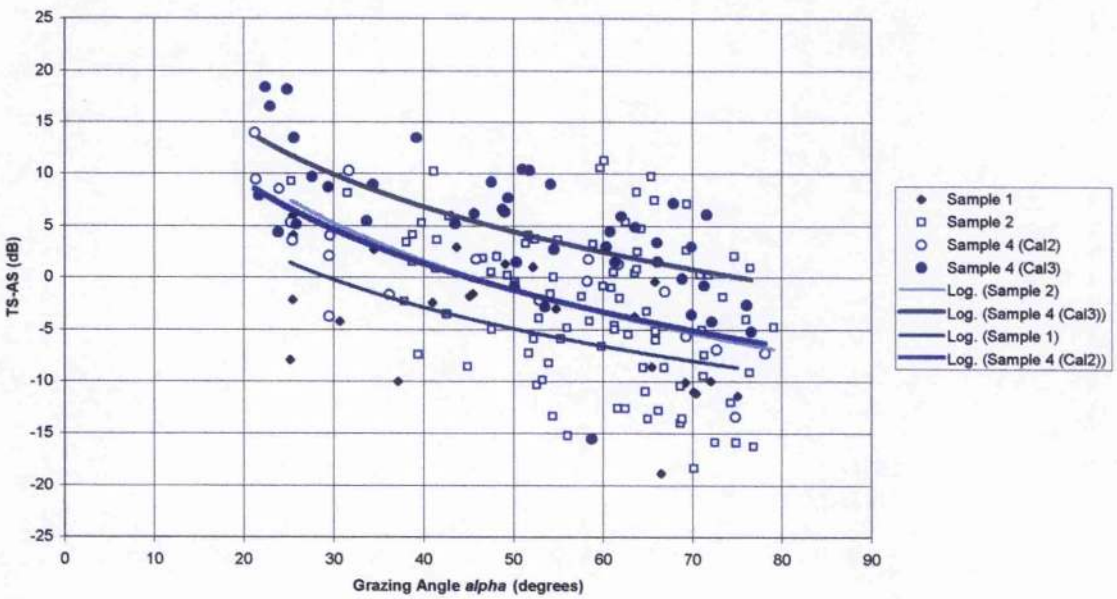

The TS-AS parameter can be analysed in more detail by plotting the values graphically against the sonar factors of grazing angle (Figure 8.6) and element area (Figure 8.7), which affect the strength of the scattering surface.

Figure 8.7 Plot of TS-AS versus Element area values for data sampled from the $2m^2$ area surrounding sample sites 1, 2, and 4.

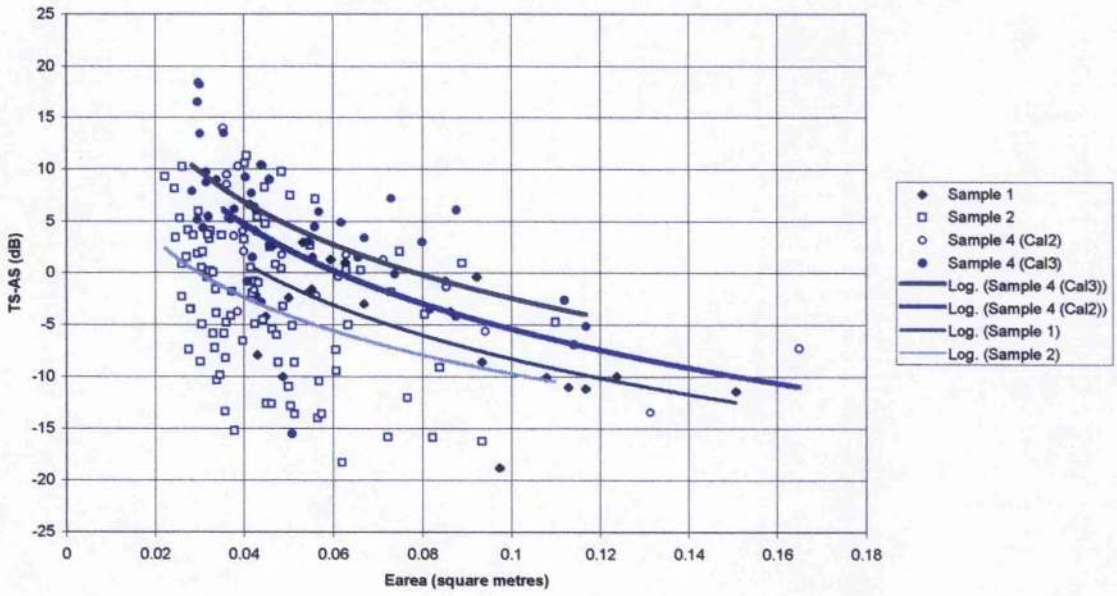

Figures 8.6 shows that as the grazing angle increases, the actual scattering strength is found to increase relative to the theoretical scattering. This trend is also evident in Figure 8.7 with AS increasing in relation to TS as the element area increases.

The combination of these plots suggest that the actual scattering strength increases relative to the theoretical strength as a direct result of increasing the acoustic sensitivity to the bed roughness through increasing α, and an increase in E_{area} enhances the number of scatterers encapsulated within the insonified area.

These logarithmic trends demonstrated by plotting α against TS-AS, and E_{area} against TS-AS, can be assessed by applying the Roughness Index to the sonar data. Figure 8.8 provides a visual comparison of the Roughness Index of the actual seabed sediment, which can be compared directly with the map of TS-AS values in Figure 8.5. It should

be noted that little correlation is expected within the areas where TS>AS because this condition is not roughness dependent.

The comparative analysis between TS-AS and the Roughness Index within a $2m^2$ area around samples 1, 2 and 4 can be shown in more detail by graphing the data of TS-AS versus RI (Figure 8.9). This plot generally shows that as the Roughness Index increases, so the actual scattering strength increases relative to the theoretical strength. Between 0 and 0.05 on the Roughness Index range, the value of TS-AS generally decreases from +5 or +10 down to around –5 to –8. For all samples this decrease in TS-AS appears to be quite steep between RI values of 0 and 0.01, before easing off as the RI increases from 0.01 to 0.05.

Figure 8.8 Map of Roughness Index variability within a 10m x 10m area surrounding Sample Site 4 (Cal3Sam4)

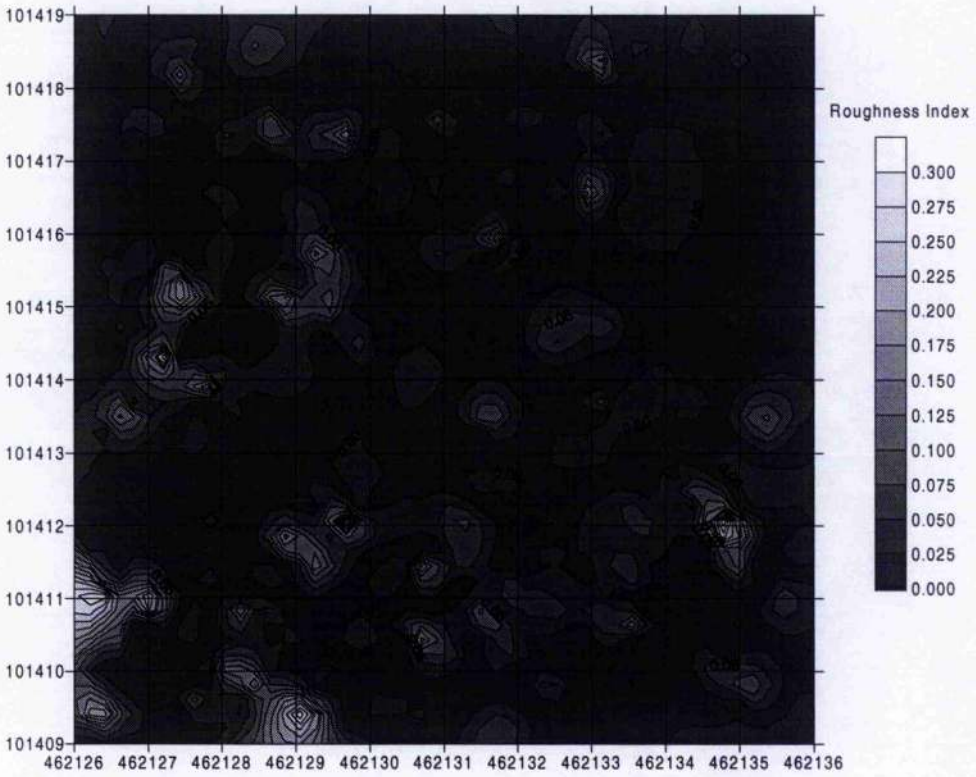

Figure 8.9 Plot of TS-AS versus Roughness Index values for data sampled from the $2m^2$ area surrounding sample sites 1, 2, and 4.

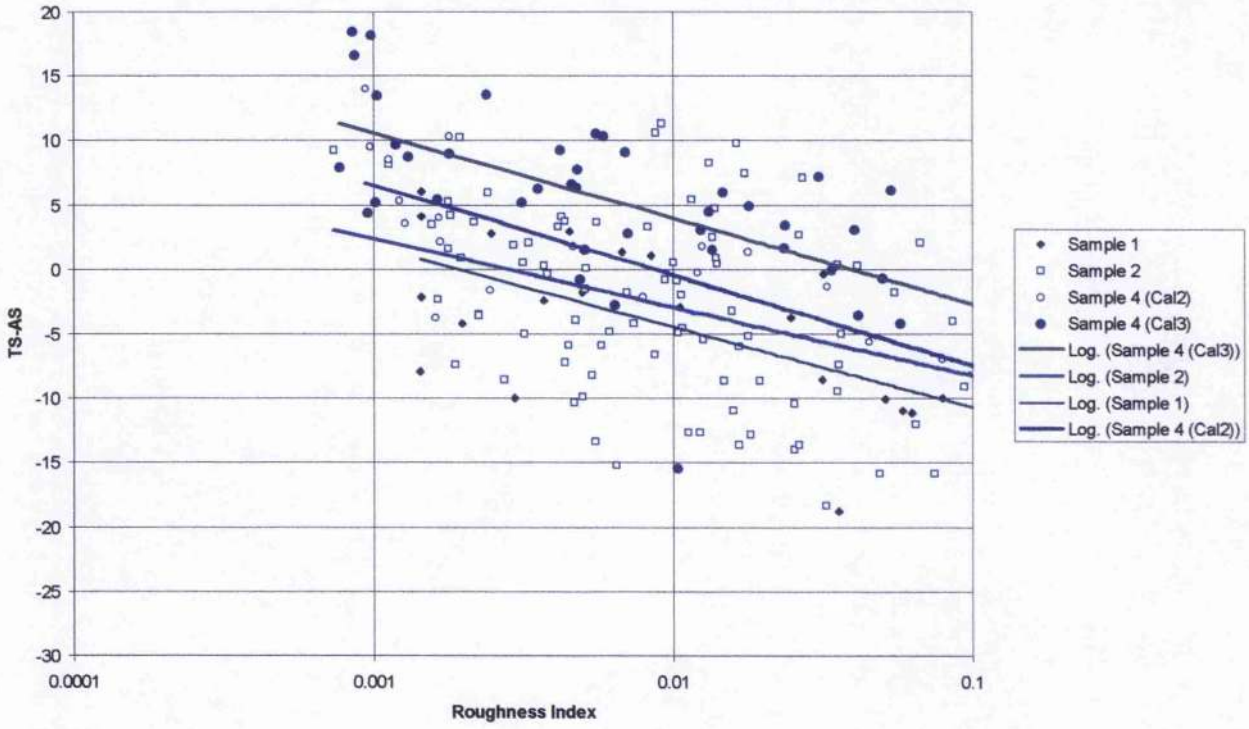

In summary, the TS-AS value is very sensitive to low Roughness Index values, with the sensitivity tailing off as the Roughness Index increases, to give a minimum TS-AS value of –8 for the Calibration survey area.

The relationships between TS-AS and the Roughness Index can be summarised at each site using the log-linear trend lines illustrated in Figure 8.9.

These log-linear relationships show a close correlation between TS-AS and Roughness Index values for each sample site within the Calibration survey area, thereby suggesting a similar nature of sediment at the water-sediment interface. It is also evident that the log-linear relationships are centred around the 'TS-AS = 0' condition, which means that the Lambertian scattering closely represents the actual scattering.

The relative ordering of the data distribution and the log-linear trends in Figure 8.9 suggest that the degree of bed roughness encountered at the water-sediment interface increases from sample site 4, through sample site 2, to sample site 1.

8.2.2. Shingle Survey Area (Samples 5, 6 and 7)

The general sonar characteristics of this survey area are presented using post-processing data from the 'Shingle1.swa' swath file to generate maps of D_t, α_S, α, E_{area}, and TS-AS, over Sample Site 5, as illustrated in Figures 8.10-8.14 respectively. For the purpose of evaluating these figures, it should be noted that this area has been illuminated by the sonar in a North to South orientation (across-track), with the vessel actually travelling from West to East. This is particularly relevant to the maps of angular variability.

Figure 8.10 Map of D_t (bathymetry) variability within a 10m x 10m area surrounding Sample Site 5 (Shingle1Sam5)

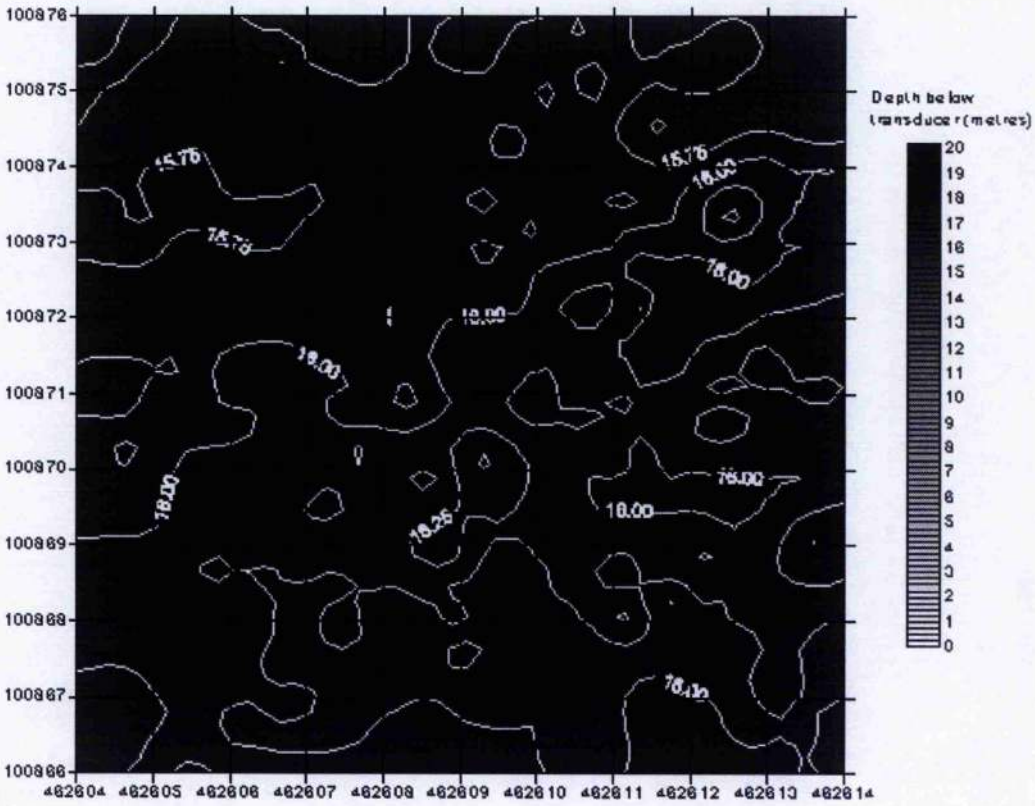

Figure 8.11 Map of α_S variability within a 10m x 10m area surrounding Sample Site 5 (Shingle1Sam5)

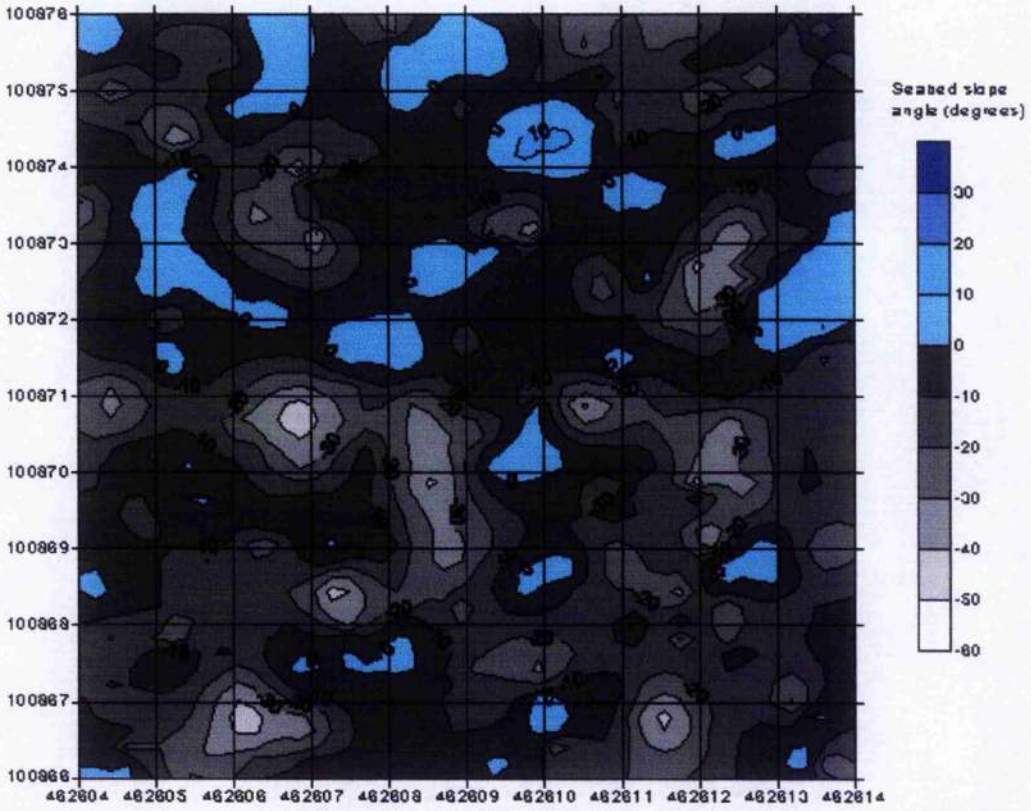

Figure 8.12 Map of α variability within a 10m x 10m area surrounding Sample Site 5 (Shingle1Sam5)

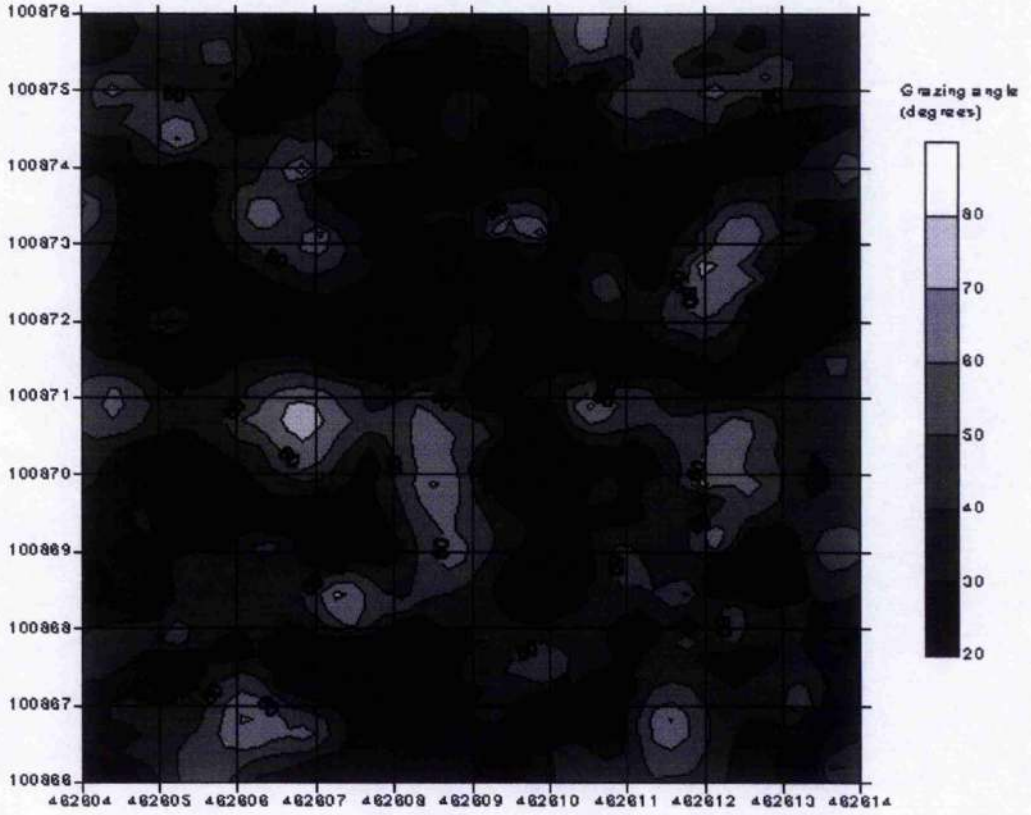

Figure 8.13 Map of E_{area} variability within a 10m x 10m area surrounding Sample Site 5 (Shingle1Sam5)

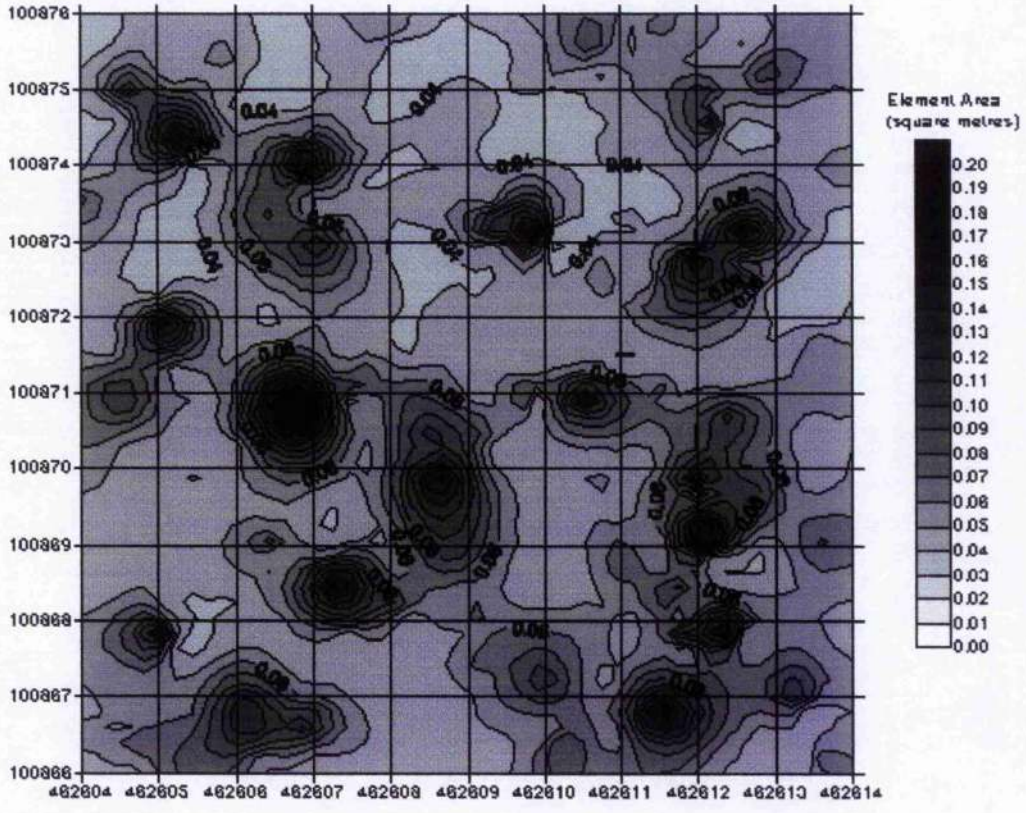

Figure 8.14 Map of TS-AS variability within a 10m x 10m area surrounding Sample Site 5 (Shingle1Sam5)

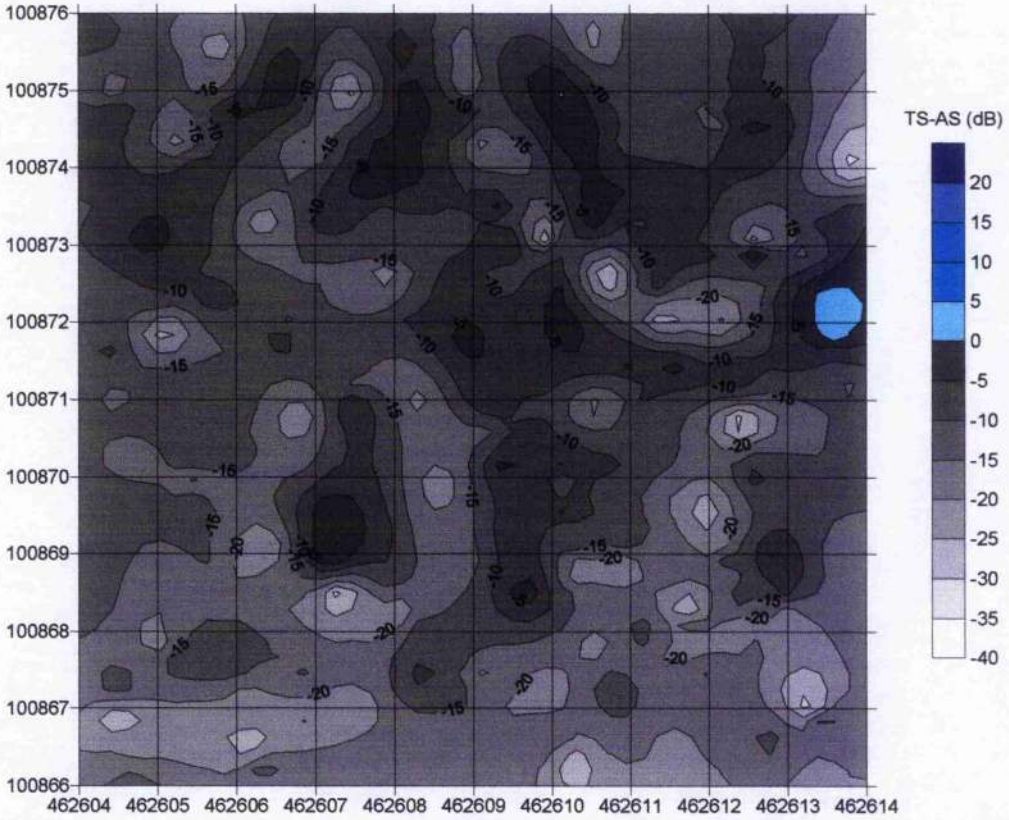

Figure 8.10 shows a relatively flat area of seabed, with depths ranging between 15 and 16.25m over the $10m^2$ area. The blue areas in Figure 8.11 match the areas sloping southwards away from the illumination angle in Figure 8.10, although Figure 8.11 also suggests that the actual angle of illumination is a slightly skewed towards a NNW-SSE direction given the areas of blue occur to the south-east of the bathymetric highs, and north-west of the bathymetric lows. This is again reflected in the total grazing angle map shown in Figure 8.12. The element area map in Figure 8.13 shows a correlation between the seabed slope angles in Figure 8.11, and the element area values.

Figure 8.14 appears to show that although there is a large variation in TS-AS values, the vast majority of the area satisfies the TS<AS condition. The TS-AS parameter can be analysed in more detail by plotting the values graphically against the sonar factors of grazing angle (Figure 8.15) and element area (Figure 8.16), which affect the strength of the scattering surface.

Figure 8.15 Plot of TS-AS versus Grazing angle values for data sampled from the $2m^2$ area surrounding sample sites 5 and 7.

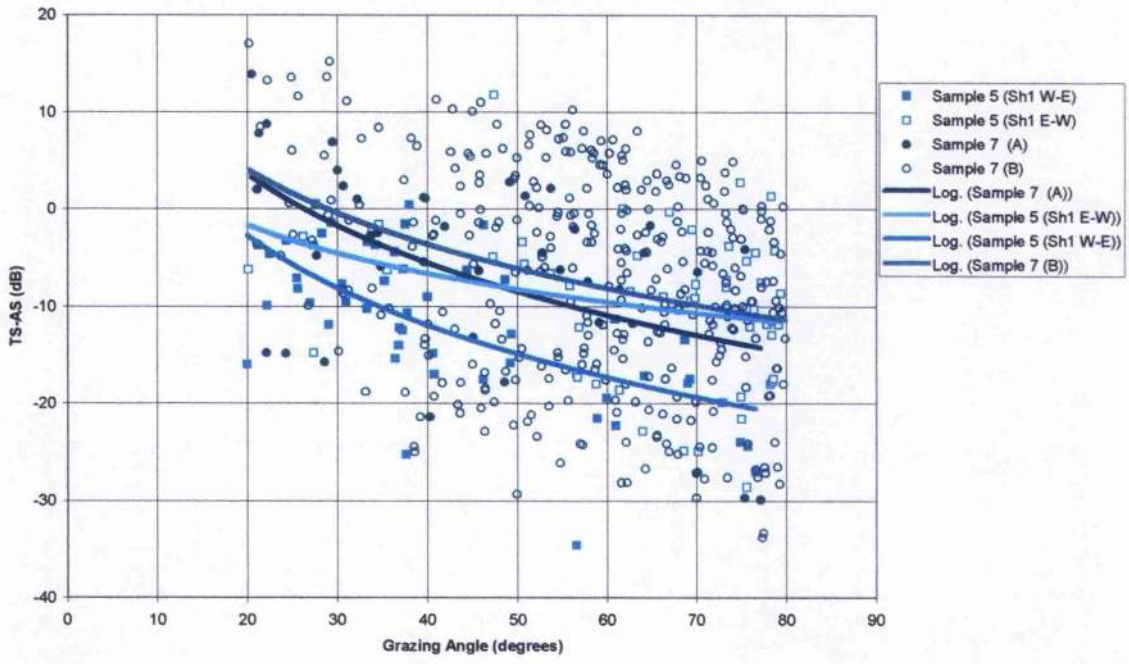

Figure 8.15 shows that each sample site approximately satisfies the TS=AS condition as the grazing angles approach 20^0. It also suggests that sample site 5 is characterised by a lower TS-AS trend than that of sample site 7, under all grazing angle values. Figure 8.16 supports this trend by demonstrating a lower trend line for sample site 5 than for sample site 7.

Figure 8.16 Plot of TS-AS versus Element area values for data sampled from the $2m^2$ area surrounding sample sites 5 and 7.

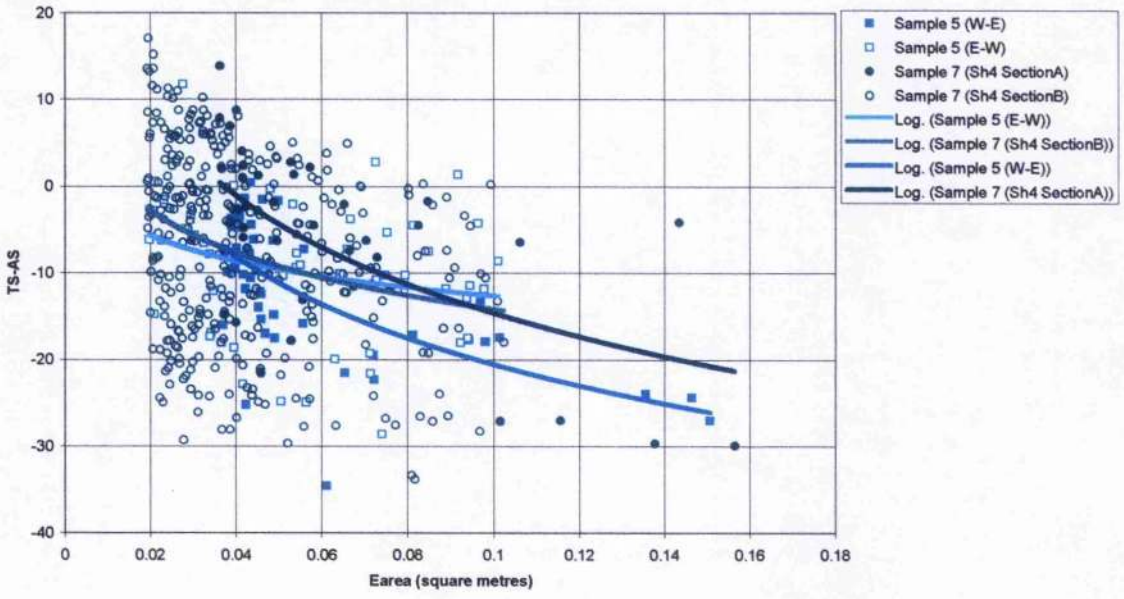

The distribution of the TS-AS values can be further assessed by analysing the spatial distribution trends of the Roughness Index plot in Figure 8.17 relative to the TS-AS plot in Figure 8.14, which also reflects the pattern of the grazing angle and element area plots. The comparison of Figures 8.14 and 8.17 show that where the Roughness Index is low, then TS-AS is high. This observation can be examined in graphical form by directly comparing the values of TS-AS to the Roughness Index, obtained from within 1m range from Sample sites 5 and 7 (Figure 8.18).

Figure 8.17 Map of Roughness Index variability within a 10m x 10m area surrounding Sample Site 5 (Shingle1Sam5)

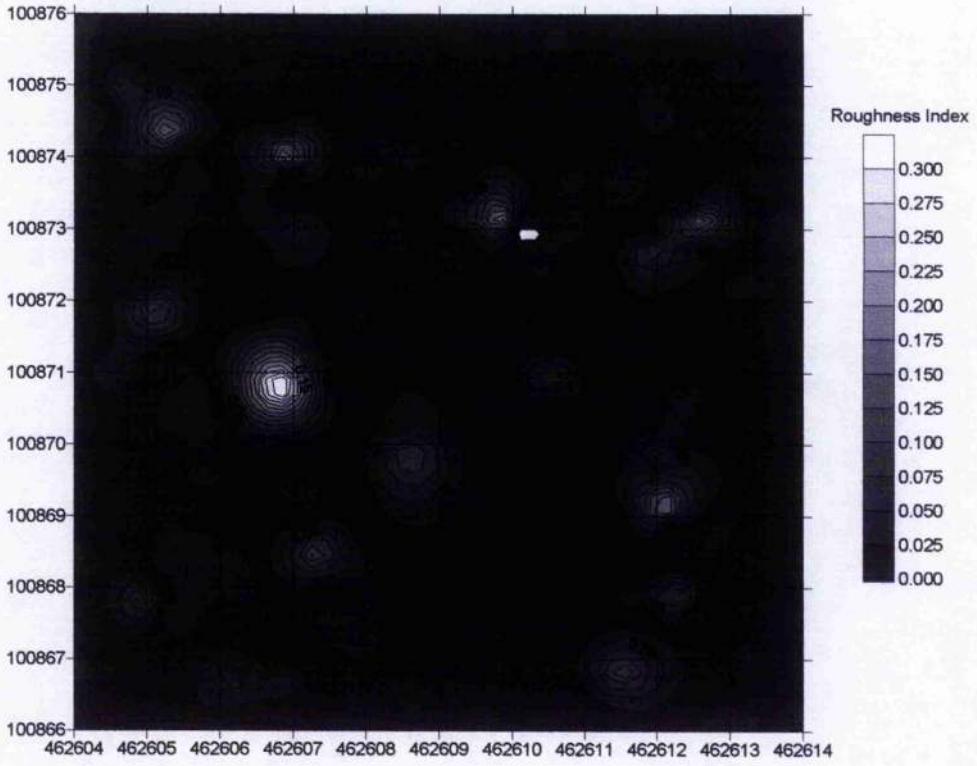

Figure 8.18 Graph of TS-AS against Roughness Index for data sampled from the $2m^2$ area surrounding sample sites 5 and 7.

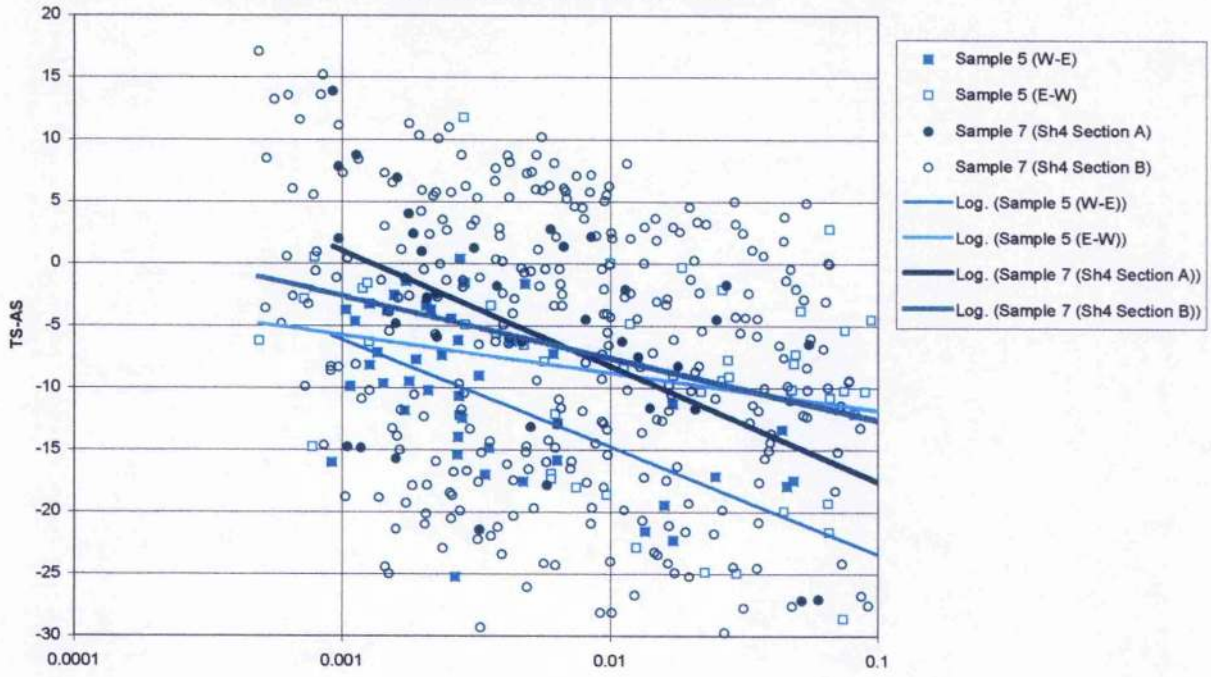

The data presented in Figure 8.18 are divided into two groups with respect to each sample site. This is due to the continuous nature of the swath data collection over the Shingle site, which resulted in both West-East and East-West traverses over each sample site. As these traverses are over a constant sediment type, then the difference in the Roughness Index values must be attributed to the sonar resolution, with the West-East traverses offering a higher resolution than the East-West traverses.

The relationships generated between the TS-AS figures and the Roughness Index at each sample site are summarised by the log-linear trend lines displayed in Figure 8.18. These trend lines also suggest that the roughness of the water-sediment interface is higher at sample site 5 than at sample site 7.

8.2.3. Invincible Survey Area (Samples 8, 9, 10 and 11)

The general sonar characteristics of this survey area are presented using post-processing data from the 'Invincible000.5.swa' swath file to generate maps of D_t, α_S, α, E_{area}, and TS-AS, over Sample Site 11, as illustrated in Figures 8.19-8.23 respectively. For the purpose of evaluating these figures, it should be noted that this area has been illuminated by the sonar in a North to South orientation (across-track), with the vessel actually travelling from East to West. This is particularly relevant to the maps of angular variability.

Figure 8.19 Map of D_t (bathymetry) variability within a 10m x 10m area surrounding Sample Site 11 (Invincible000.5Sam11)

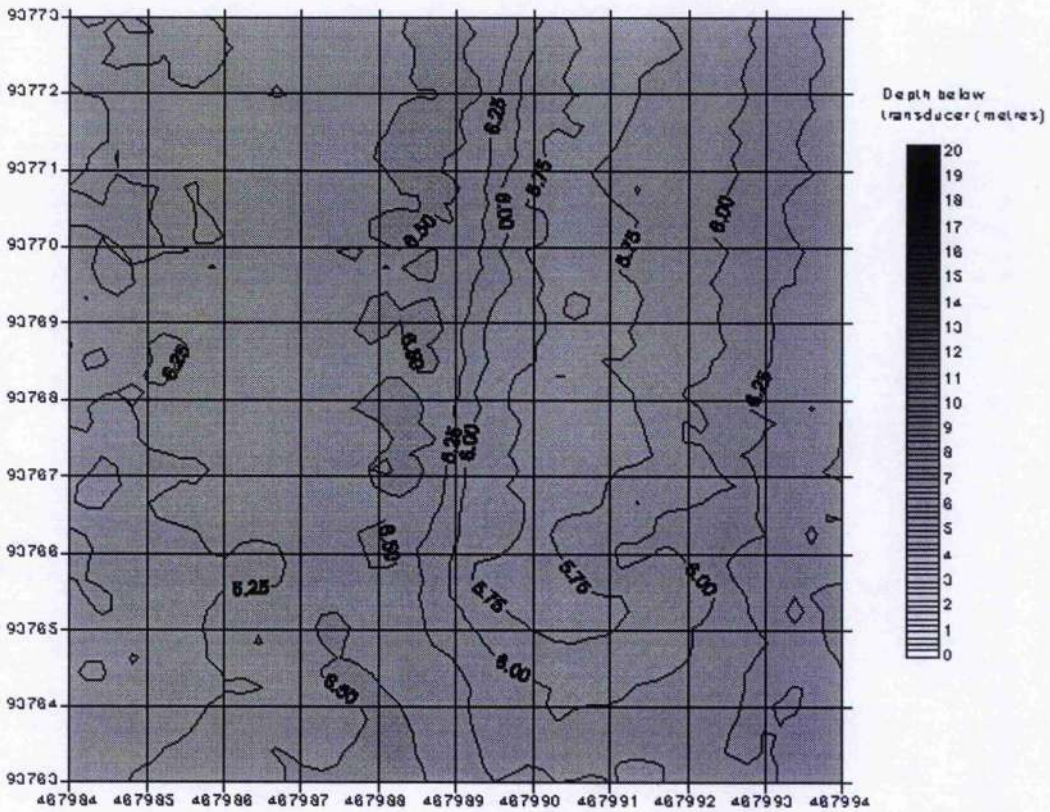

Figure 8.20 **Map of α_S variability within a 10m x 10m area surrounding Sample Site 11 (Invincible000.5Sam11)**

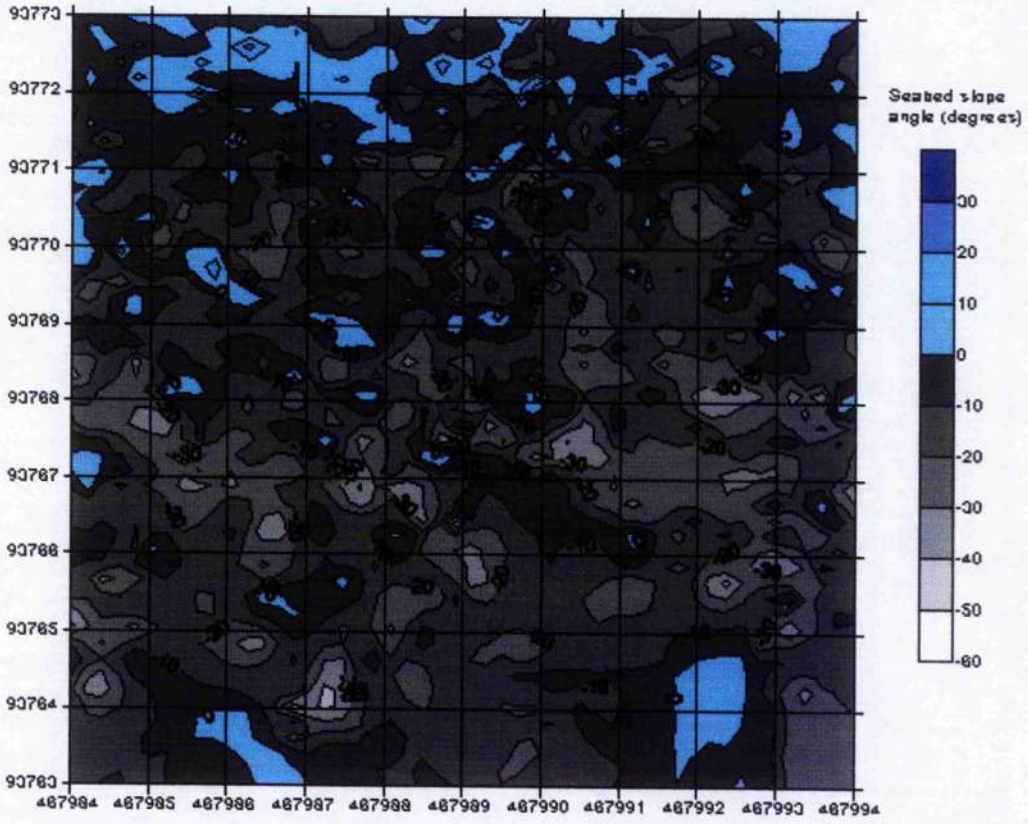

Figure 8.21 **Map of α variability within a 10m x 10m area surrounding Sample Site 11 (Invincible000.5Sam11)**

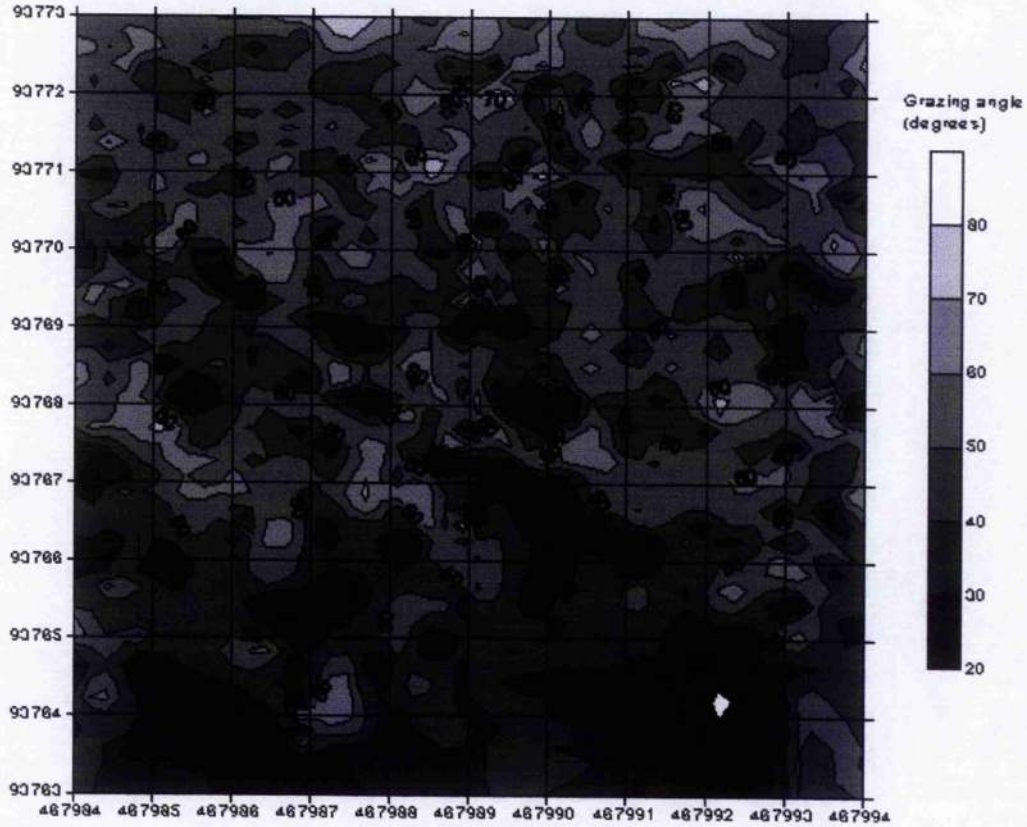

Figure 8.22 Map of E_{area} variability within a 10m x 10m area surrounding Sample Site 11 (Invincible000.5Sam11)

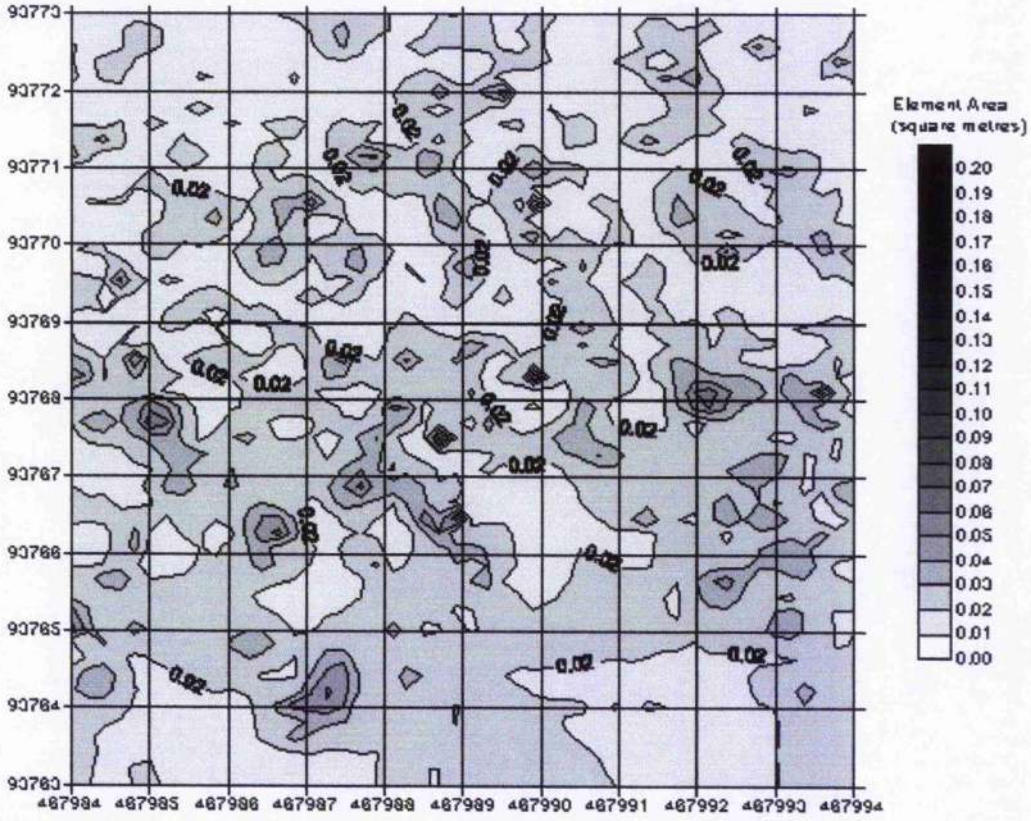

Figure 8.23 Map of TS-AS variability within a 10m x 10m area surrounding Sample Site 11 (Invincible000.5Sam11)

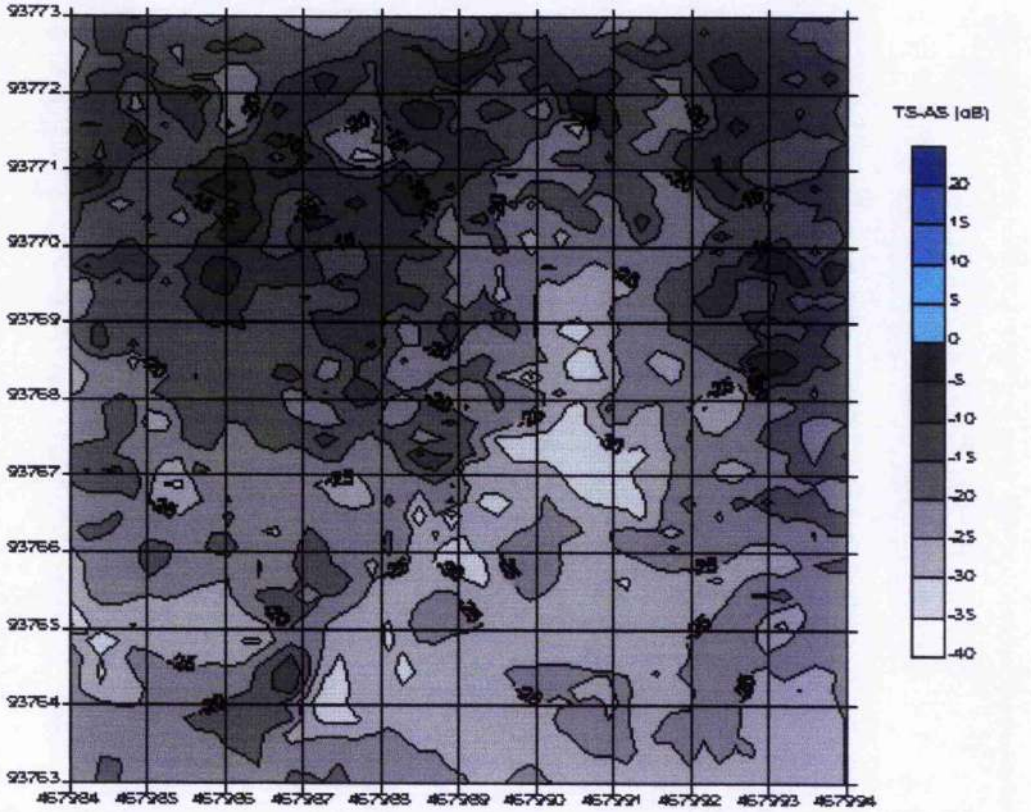

Figure 8.19 shows that Sample Site 11 is characterised by very shallow bathymetry (5-6.5m), and the presence of a ridge running North-South between 467989E and 467992E. In general, the depth below transducer at this site is between a half and a third of that found in the Calibration and Shingle survey areas. Figure 8.20 suggests that in general the seabed slope angles are relatively flat under North-South illumination, with the exception of the blue area at the southern end of the ridge (467992E 93764N) which confirms that the seabed slopes away from the transducers. This correlates with the grazing angle map in Figure 8.21, which shows small fluctuations but no significant pattern across the area. Figure 8.22 illustrates that the area is covered by very high resolution (small element area) sonar data. This is accentuated at far-range in shallow waters, through a combination of low grazing angles (short element lengths) and low horizontal ranges (narrow beam widths).

Figure 8.23 shows that the condition of TS<AS exists over the entire area, with the values of TS-AS appearing to decrease from North to South. The trend of the TS-AS parameter can be analysed in more detail by plotting the values graphically against the sonar factors of grazing angle (Figure 8.24 and 8.25) and element area (Figure 8.26 and 8.27), which affect the strength of the scattering surface.

Figure 8.24 Plot of TS-AS versus Grazing angle values for data sampled from the $2m^2$ area surrounding sample sites 8, 9, and 10.

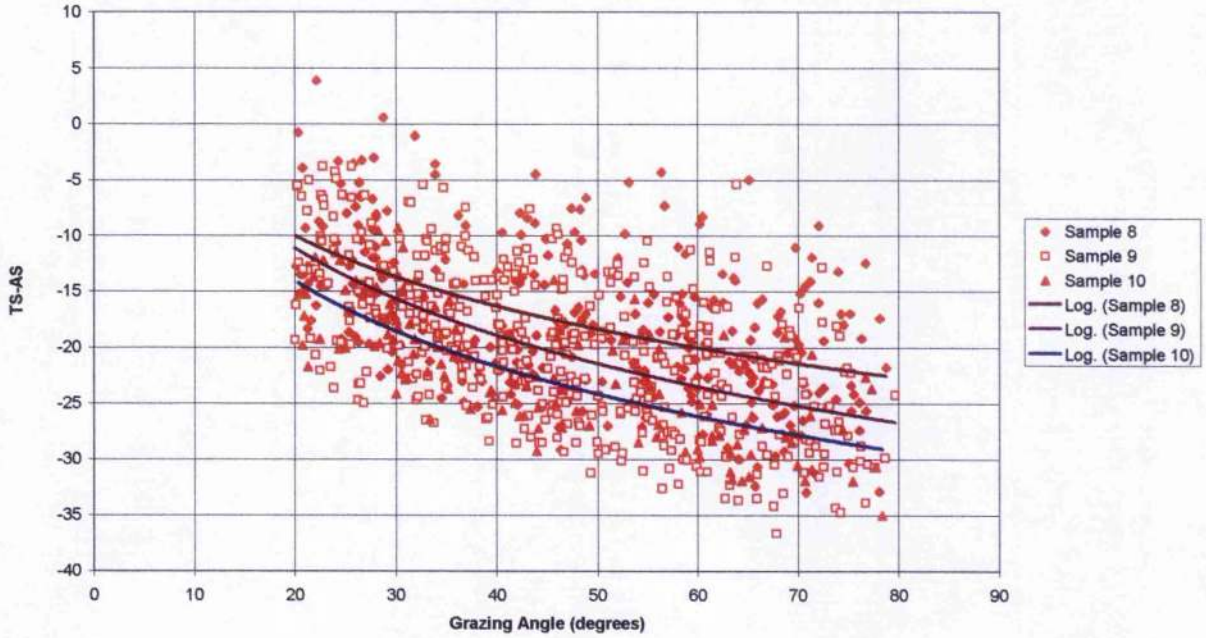

Figure 8.25 Plot of TS-AS versus Grazing angle values for data sampled from the $2m^2$ area surrounding sample site 11.

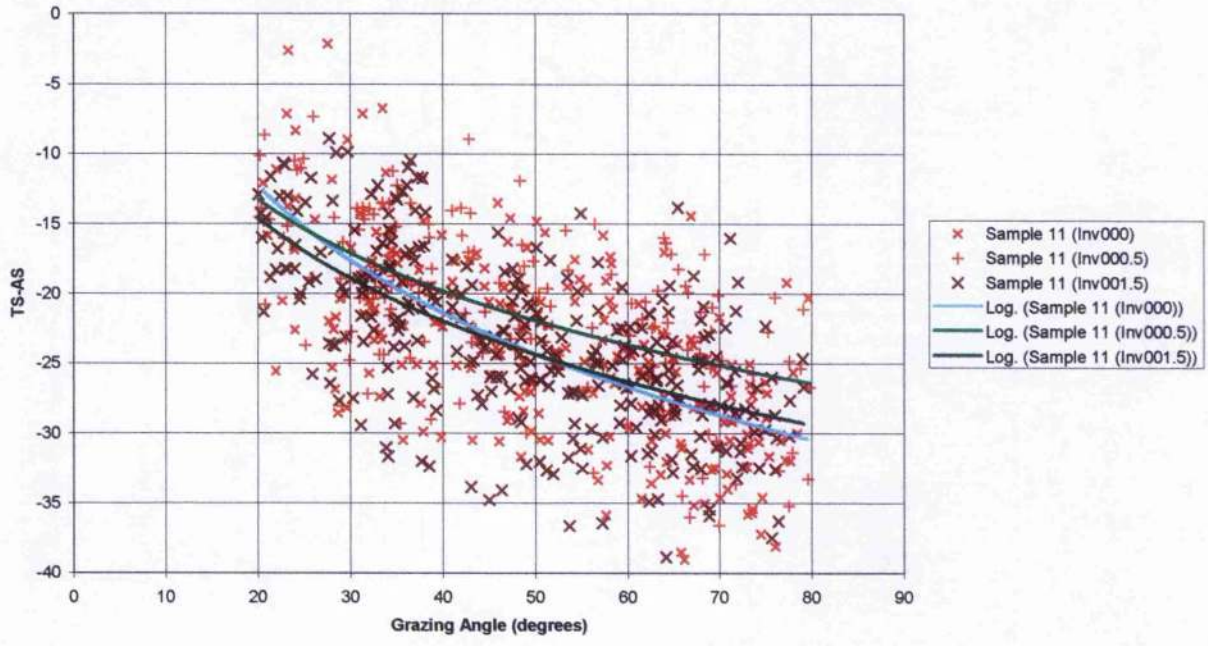

Figure 8.26 Plot of TS-AS versus Element area values for data sampled from the $2m^2$ area surrounding sample sites 8, 9, and 10.

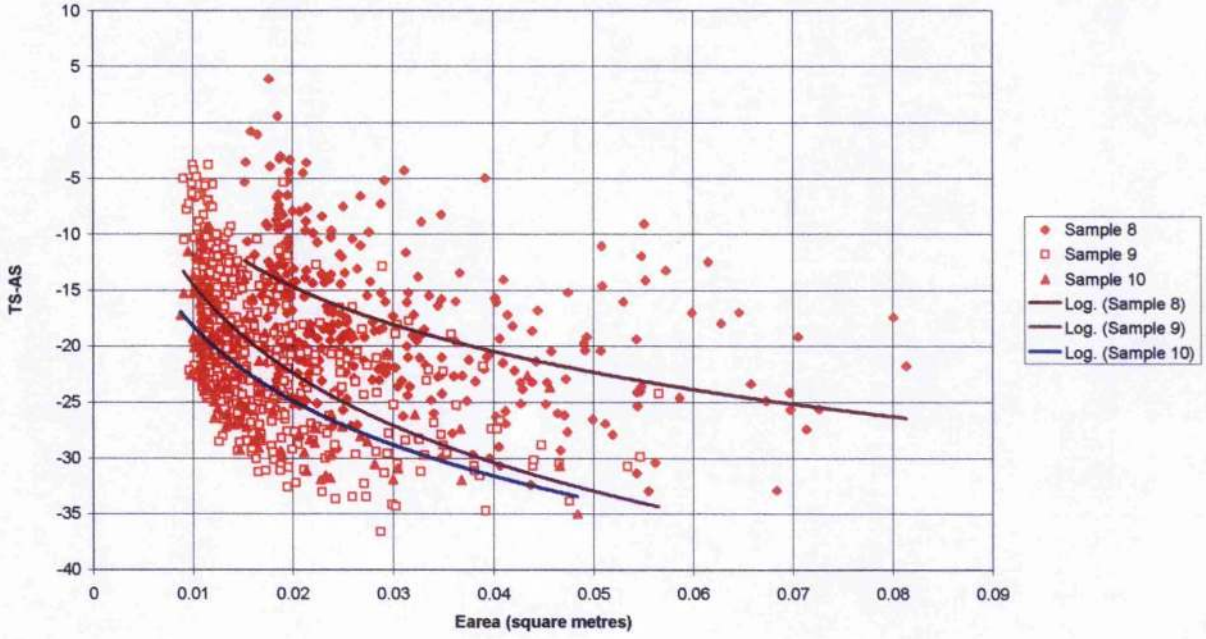

Figure 8.27 Plot of TS-AS versus Element area values for data sampled from the $2m^2$ area surrounding sample site 11.

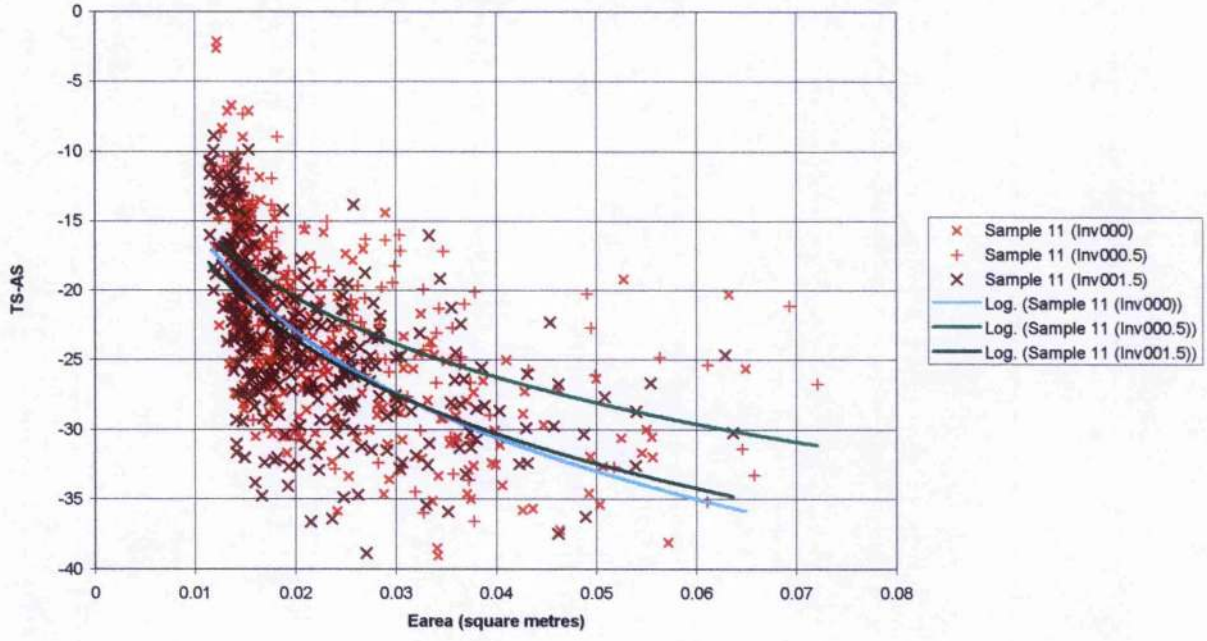

Figures 8.24 and 8.25 show that the TS-AS value is heavily dependent upon the grazing angle of incidence, with TS-AS decreasing as the grazing angle increases. Although each site is evidently covered by a high density of elements from a variety of swaths, it is significant that the overall scattering of these data points conforms to this overall trend. Figure 8.26 and 8.27 suggest that the TS-AS values are also heavily dependent upon the area of the element, as an increase in element area is associated with an increase in the actual scattering relative to the theoretical scattering. This trend is not so clearly illustrated by the data distribution which is strongly skewed towards the low range of the element area axis. This is due to the shallow nature of the survey causing the majority of the elements to have very small areas of insonification.

The overall spatial distribution of the TS-AS variability can be compared to the Roughness Index plotted in Figure 8.28 which, in contrast to the TS-AS map, shows a relatively consistent Roughness Index across the 10x10m survey area. This apparent uniformity is induced by the universal scale applied to the Roughness Index variability maps, which in covering the overall range of RI values has become insensitive to narrow range variations. The true relationship between TS-AS and the Roughness Index can be closely analysed by graphing the TS-AS and RI data from within a $2m^2$ area surrounding each of the Invincible sample sites, 8, 9, 10 (Figure 8.29) and 11 (Figure 8.30).

Figure 8.28 Map of Roughness Index variability within a 10m x 10m area surrounding Sample Site 11 (Invincible000.5Sam11)

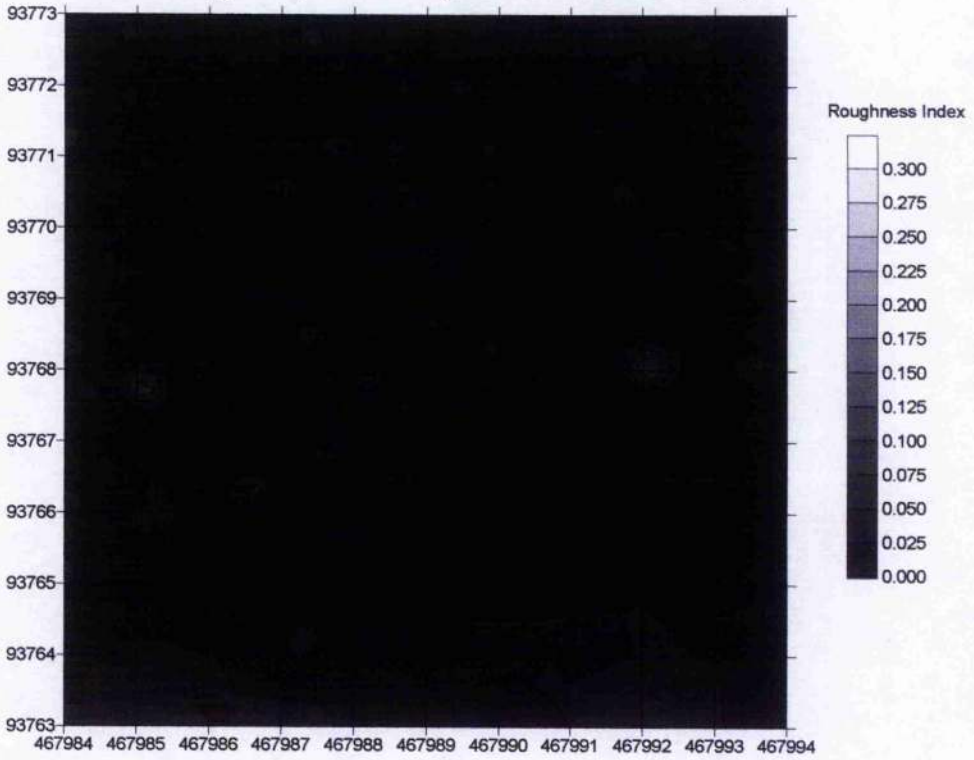

Figure 8.29 Graph of TS-AS against Roughness Index for data sampled from the $2m^2$ area surrounding sample sites 8, 9, and 10.

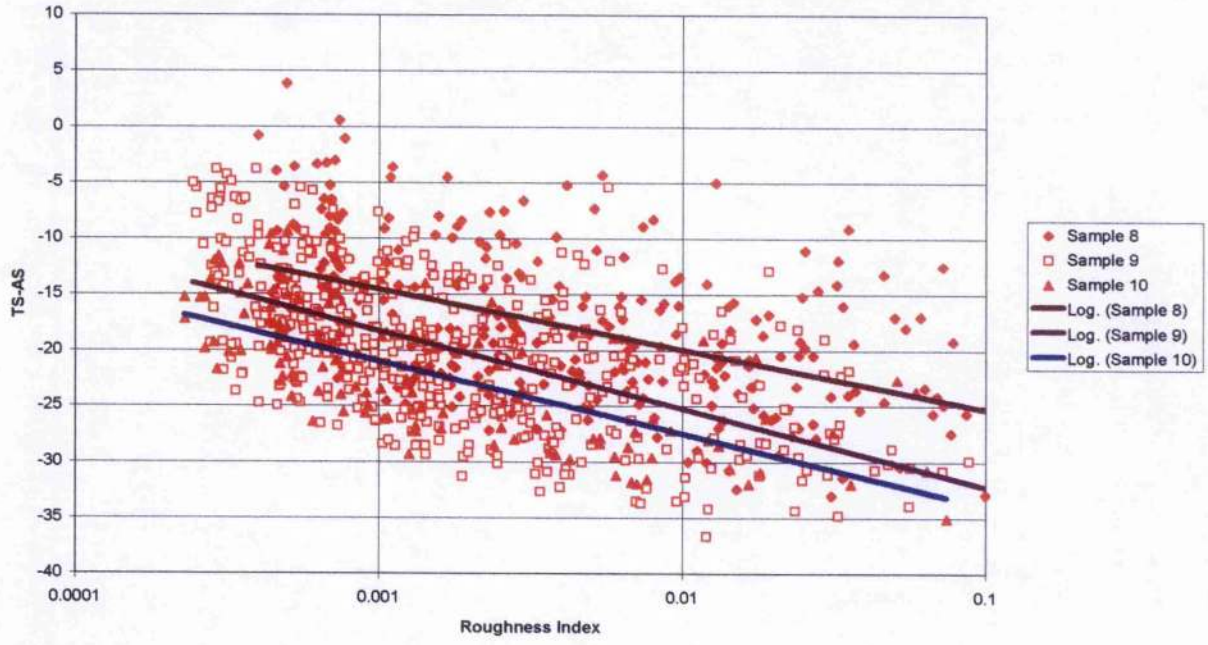

Figure 8.30 Graph of TS-AS against Roughness Index for data sampled from the $2m^2$ area surrounding sample site 11.

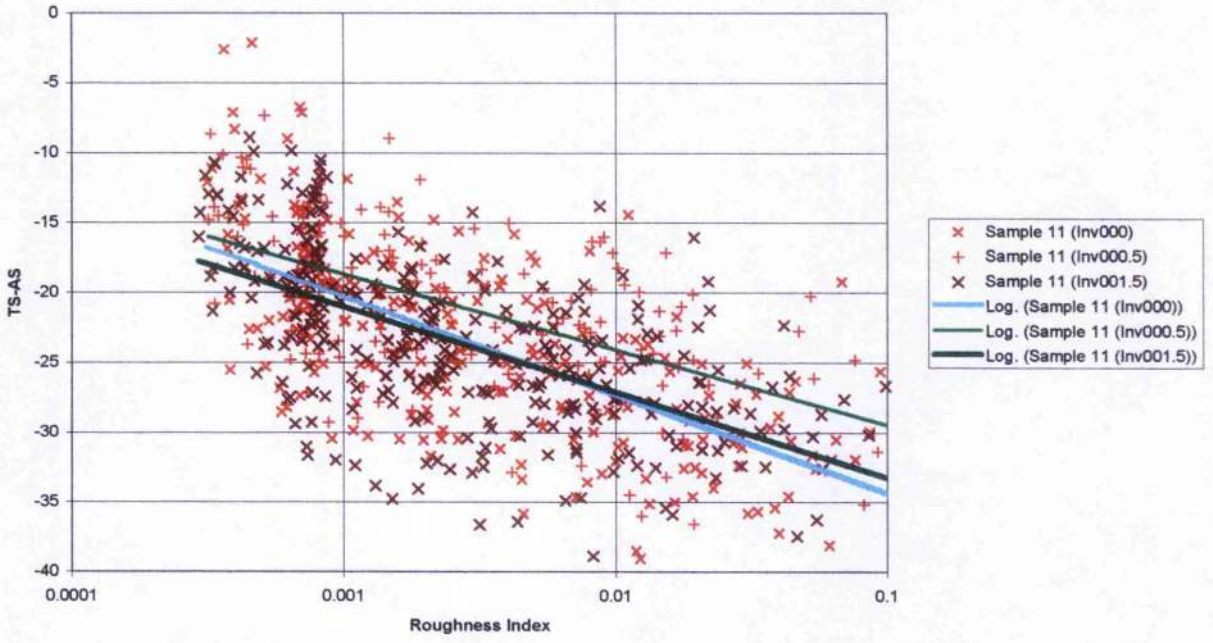

The general trends of the datapoints suggest that there is a relatively strong log-linear relationship between the sonar scattering parameter (TS-AS) and the Roughness Index (RI) across the whole of the Invincible survey site. The log-linear trend lines shown in Figures 8.29 and 8.30 are representative of the relationships between TS-AS and RI at each sample site.

The spatial relationships of the trend-lines suggest that the surface roughness detected by the sonar at each sample site is relatively constant throughout the Invincible area. The only exception may be that of Sample site 8, which appears to produce a slightly lower level of actual scattering strength. This finding appears to conform with the results of Chapter 7, which states that there is very little variation within the sediment parameters across the whole of the Invincible survey area.

8.2.4. A1 Submarine Survey Area (Samples 12, 13, 14, 15 and 16)

The general sonar characteristics of this survey area are presented using post-processing data from the 'Sub002.swa' swath file to generate maps of D_t, α_S, α, E_{area}, and TS-AS, over Sample Site 14, as illustrated in Figures 8.31-8.35 respectively. For the purpose of evaluating these figures, it should be noted that this area has been illuminated by the sonar in a South to North orientation (across-track), with the vessel actually travelling from East to West. This is particularly relevant to the maps of angular variability.

Figure 8.31 Map of D_t (bathymetry) variability within a 10m x 10m area surrounding Sample Site 14 (Sub002Sam14)

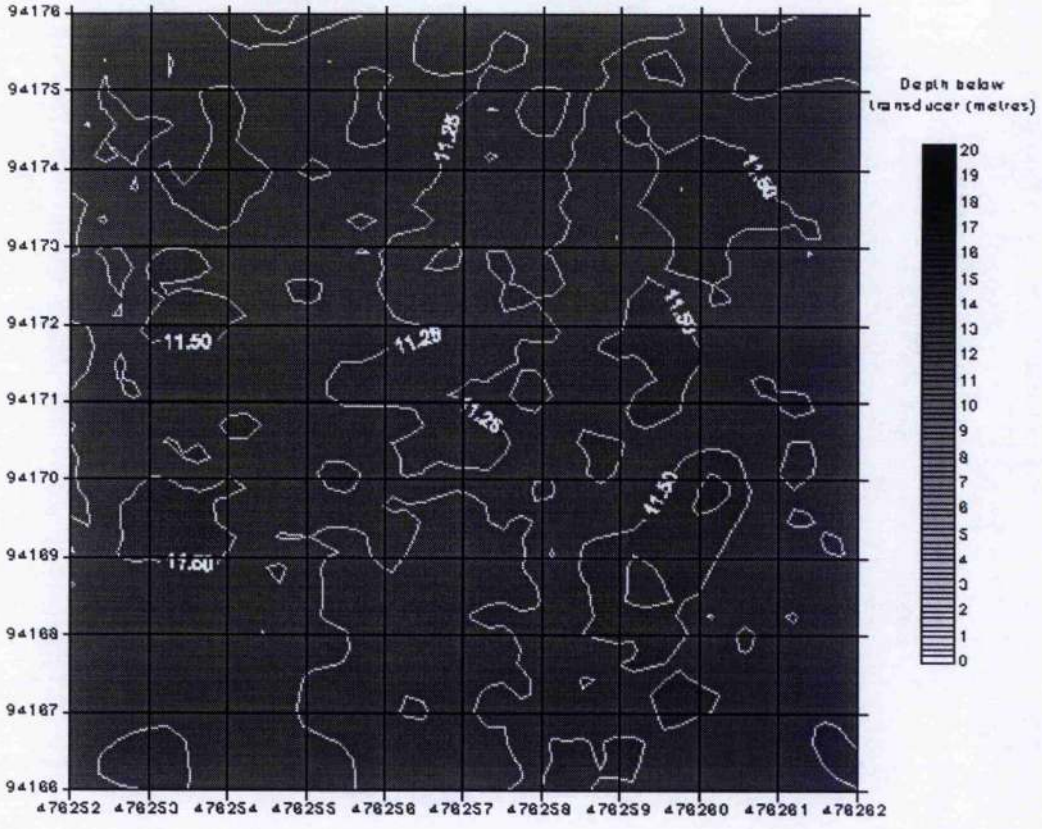

Figure 8.32 Map of α_S variability within a 10m x 10m area surrounding Sample Site 14 (Sub002Sam14)

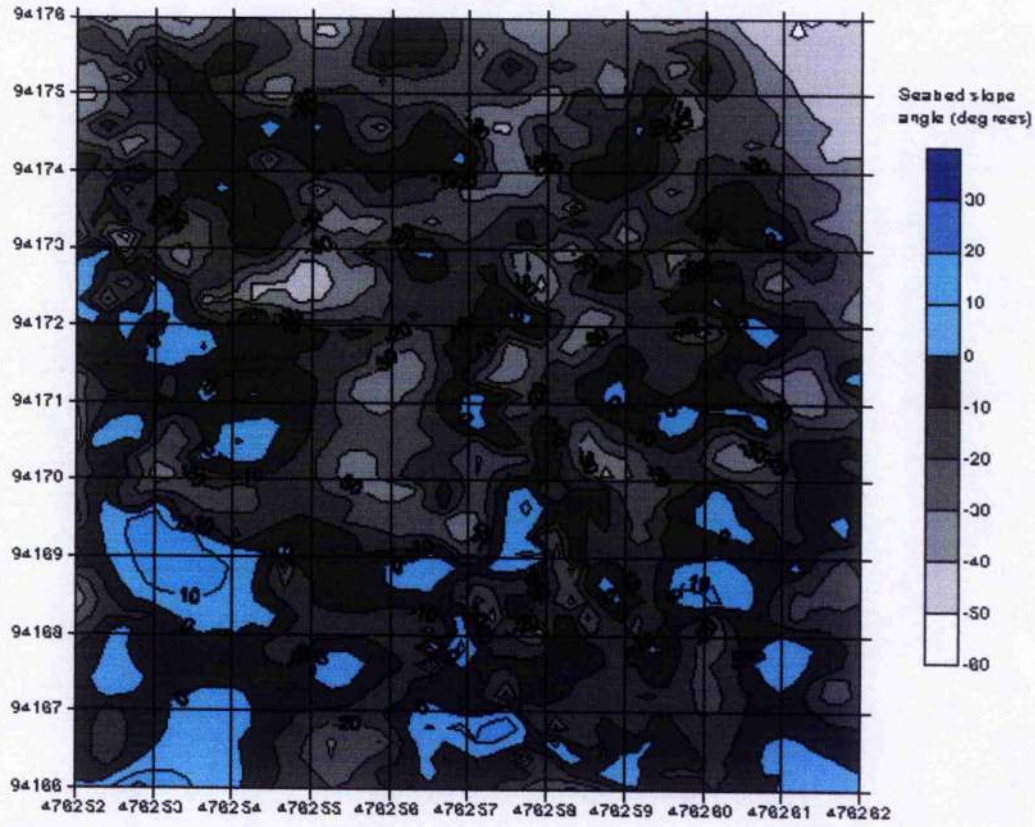

Figure 8.33 Map of α variability within a 10m x 10m area surrounding Sample Site 14 (Sub002Sam14)

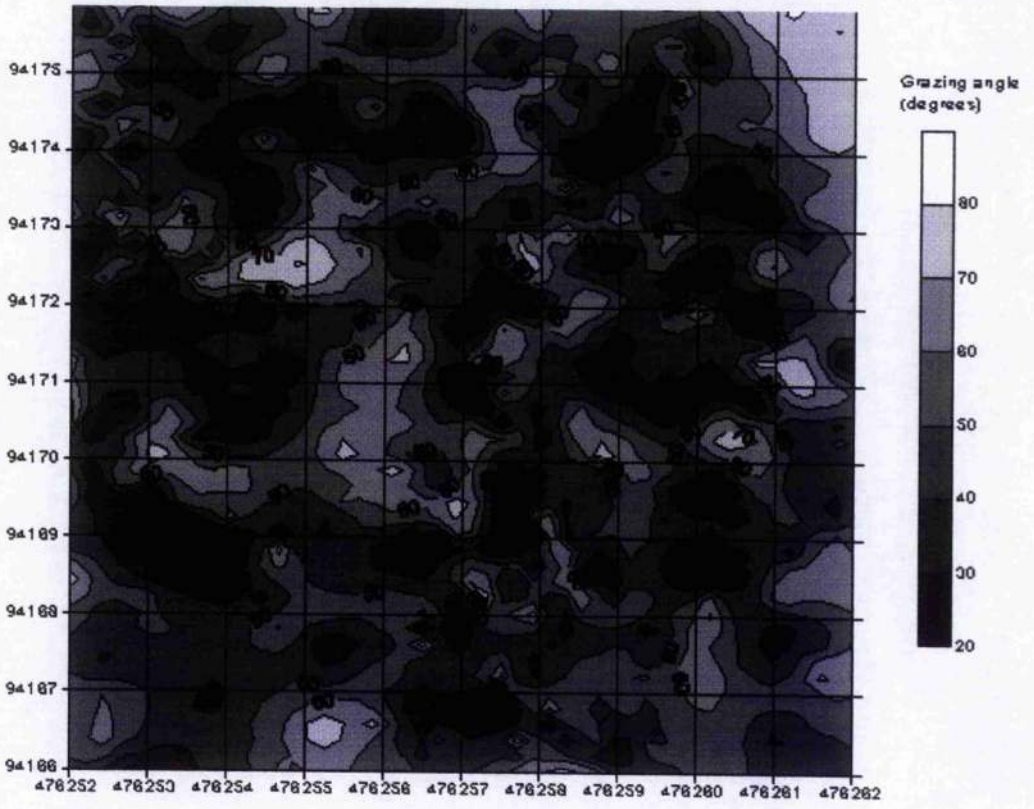

Figure 8.34 Map of E_{area} variability within a 10m x 10m area surrounding Sample Site 14 (Sub002Sam14)

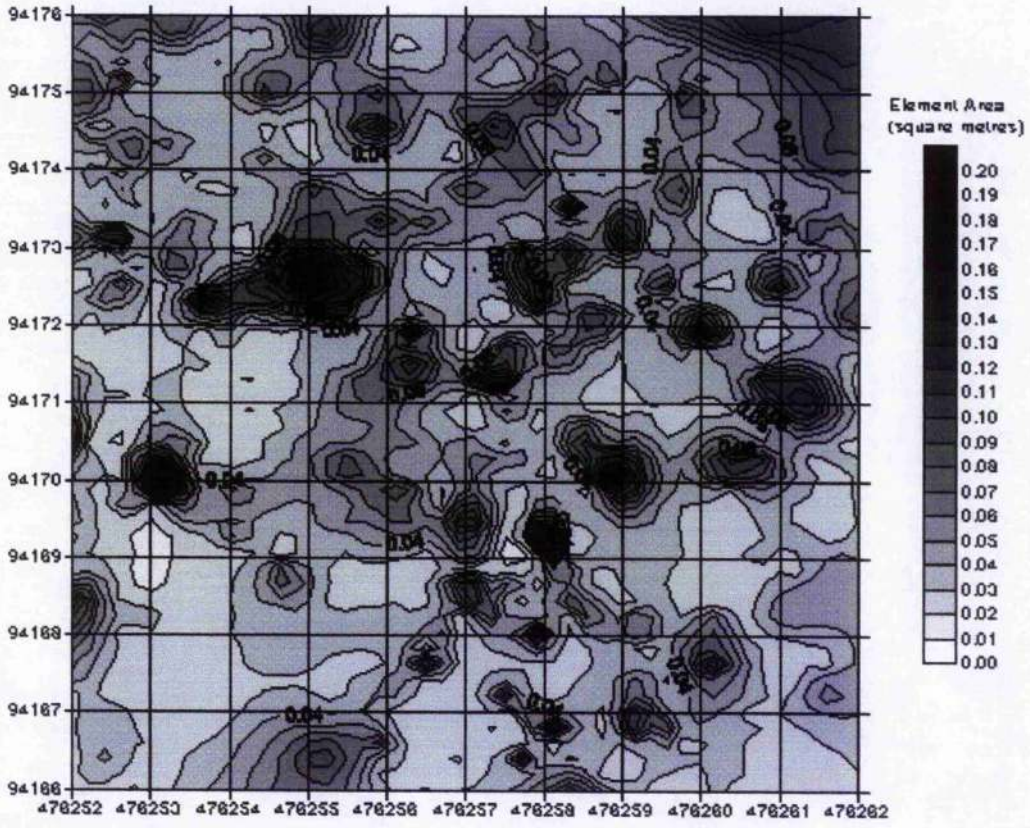

Figure 8.35 Map of TS-AS variability within a 10m x 10m area surrounding Sample Site 14 (Sub002Sam14)

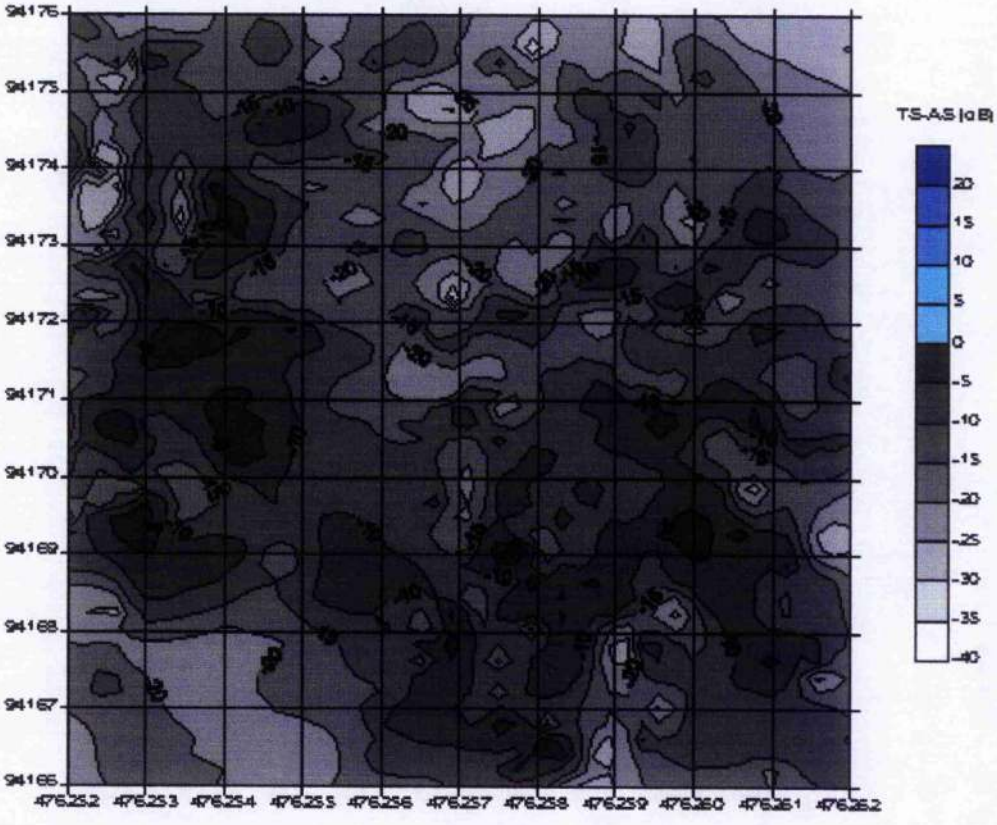

Figure 8.31 shows that this area of seabed is relatively flat, with D_t values ranging between 10.9m and 11.9m. Although the range of D_t values is very narrow, the wide variety and distribution of seabed slope angle contours in Figure 8.32 suggest that the small-scale topography is far from smooth. The presence of small undulations is again supported by the lack of any visible trend in the distribution of grazing angle values in Figure 8.33. The effects of this uneven seabed are also evident in the wide range of element area values displayed in Figure 8.34, from $0.01m^2$ to $0.2m^2$.

The absence of any clear pattern across the survey area is encapsulated in Figure 8.35, which shows an almost random variation in TS-AS values.

The nature of this distribution can be evaluated in more detail by plotting the TS-AS values against the sonar factors of grazing angle (Figures 8.36, 8.37 and 8.38) and element area (Figures 8.39, 8.40 and 8.41), which affect the strength of the scattering surface.

Figure 8.36 Plot of TS-AS versus Grazing angle values for data sampled from the $2m^2$ area surrounding sample sites 12 and 13.

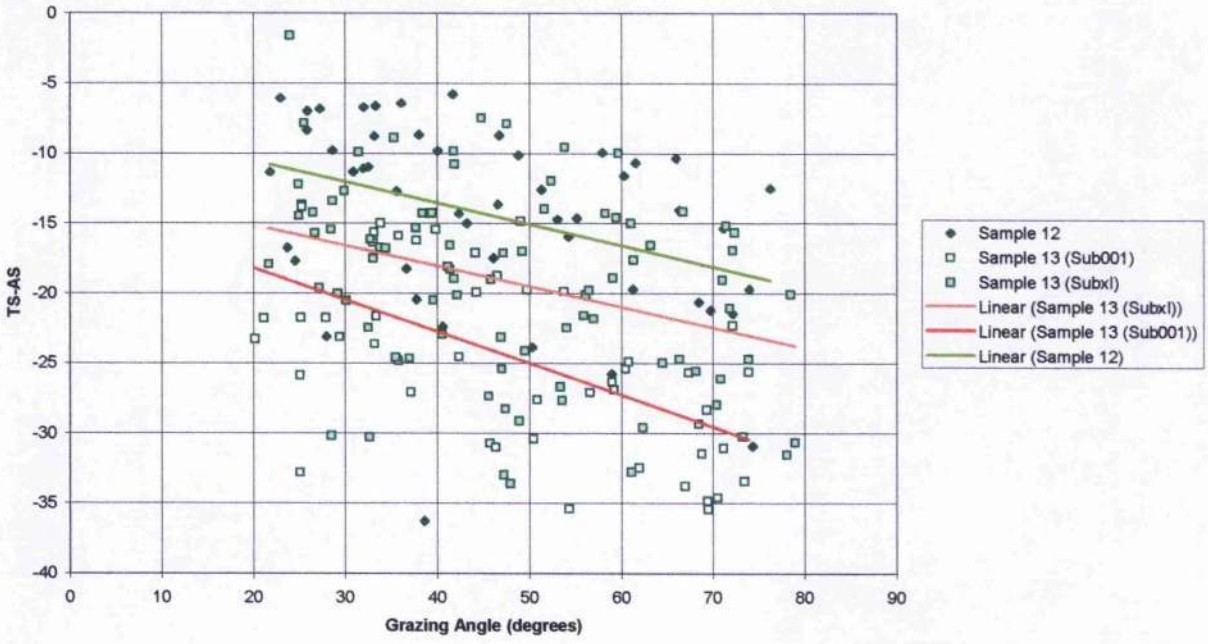

Figure 8.37 Plot of TS-AS versus Grazing angle values for data sampled from the $2m^2$ area surrounding sample site 14.

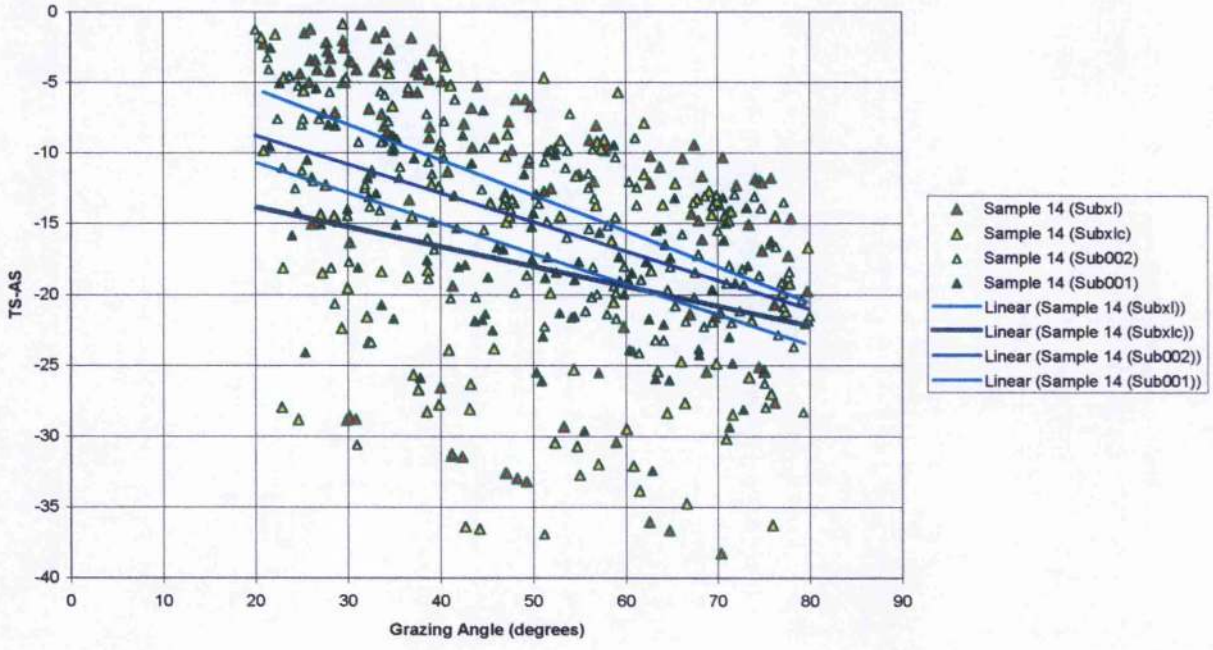

Figure 8.38 Plot of TS-AS versus Grazing angle values for data sampled from the $2m^2$ area surrounding sample sites 15 and 16.

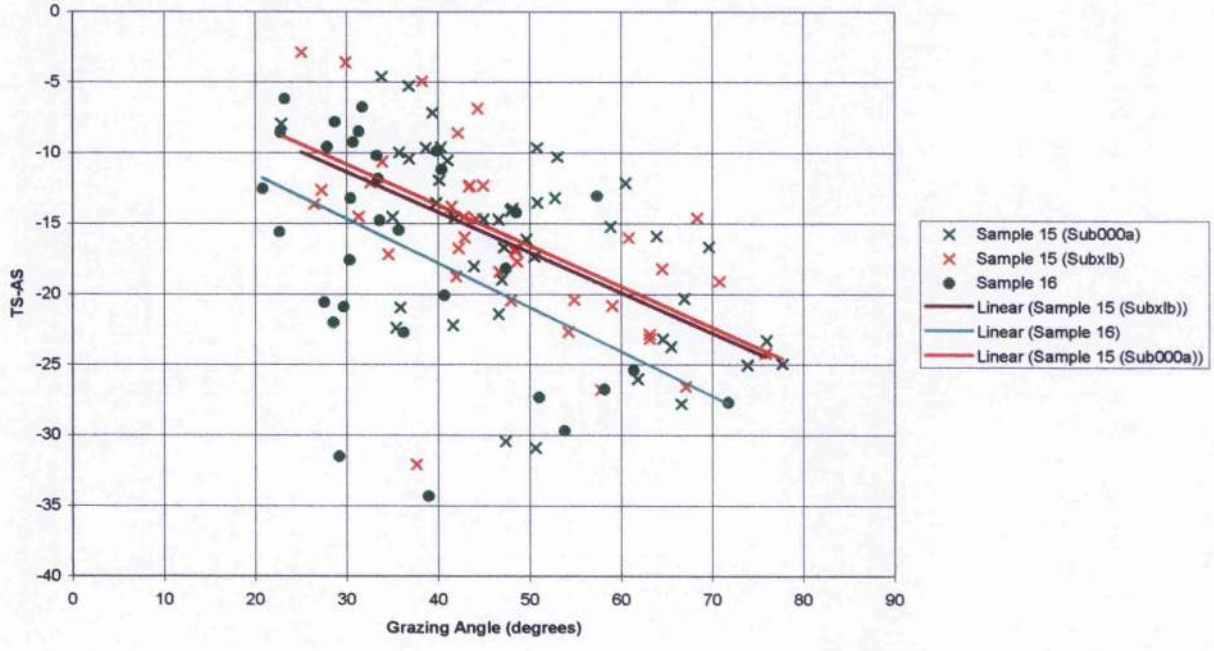

Figure 8.39 Plot of TS-AS versus Element area values for data sampled from the $2m^2$ area surrounding sample sites 12 and 13.

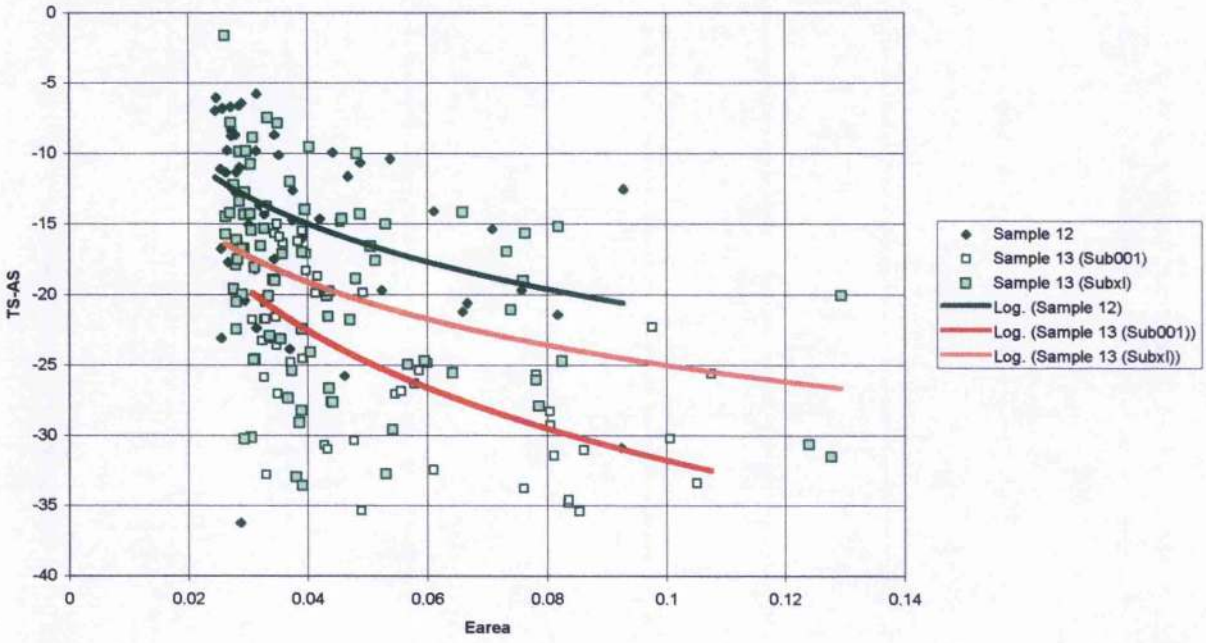

Figure 8.40 Plot of TS-AS versus Element area values for data sampled from the $2m^2$ area surrounding sample site 14.

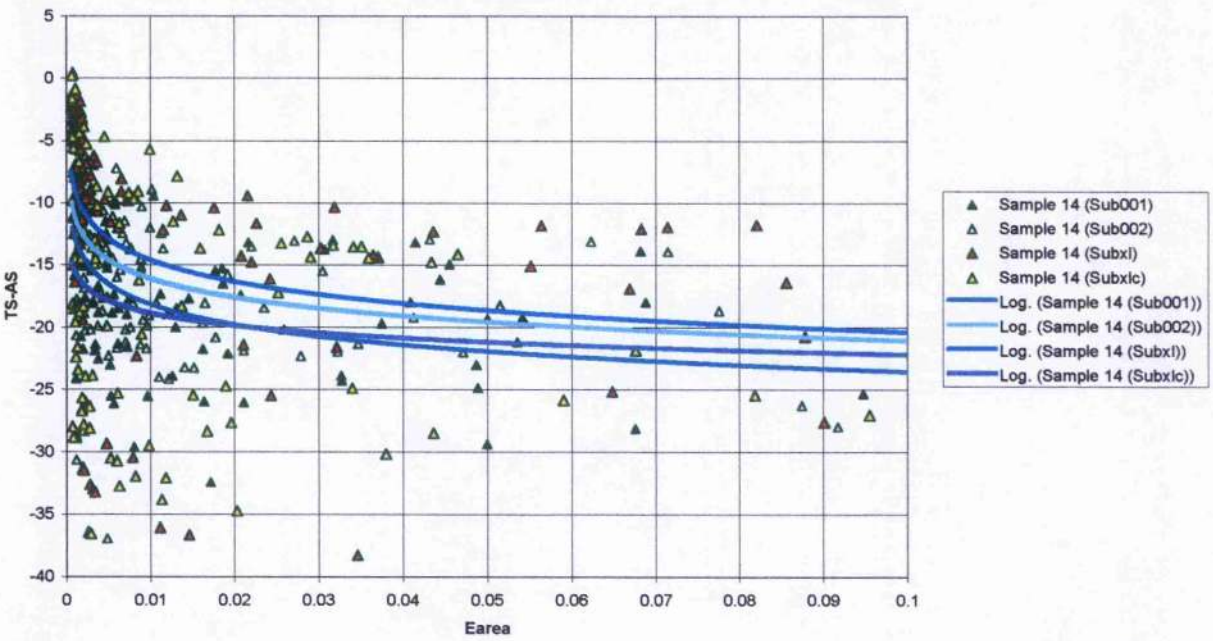

Figure 8.41 Plot of TS-AS versus Element area values for data sampled from the $2m^2$ area surrounding sample sites 15 and 16.

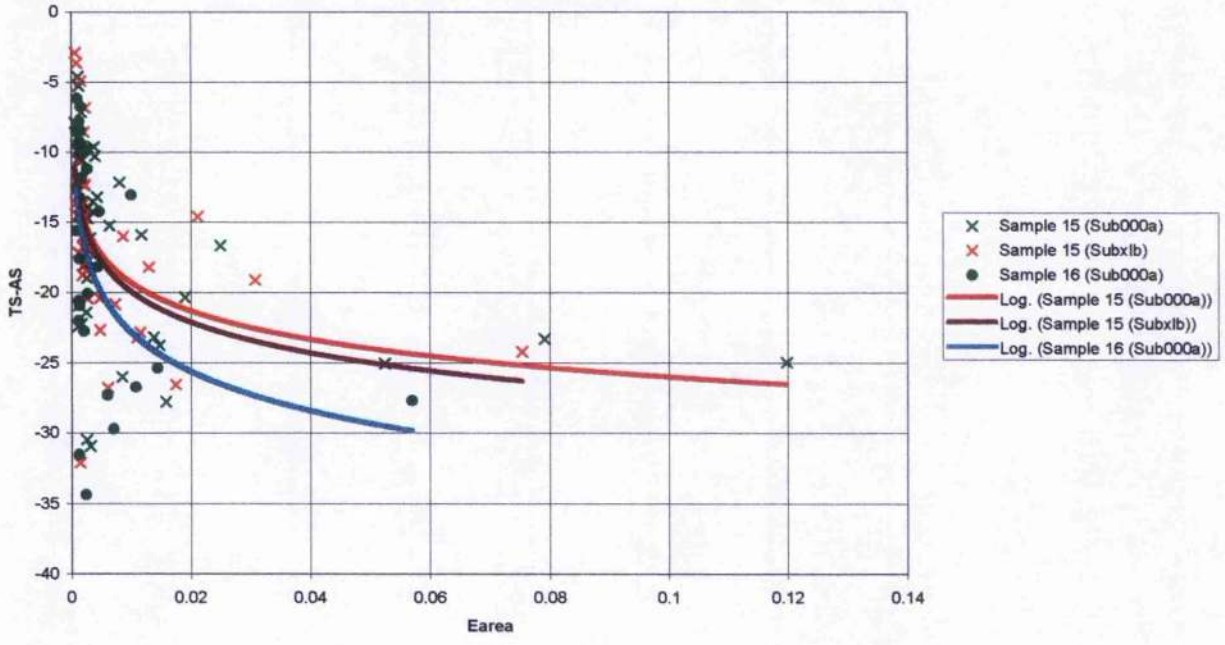

Figures 8.36, 8.37 and 8.38 show that the 'TS-AS v α' log-linear trend lines for all of the A1 Submarine samples have a relatively uniform gradient, with TS-AS values generally decreasing from approximately –10 down to less than –20 as the grazing angle increases from 20^0 to 80^0. Figures 8.39, 8.40 and 8.41 show a similar trend and distribution occurs when plotting TS-AS against E_{area}, with TS-AS decreasing as E_{area} increases.

In comparing the spatial distribution of TS-AS values in Figure 8.35 to the Roughness Index map of Figure 8.42, the areas of low TS-AS values such as can be found at (476261E, 94175N) and (476254E, 94167N) appear to correspond to areas of increased Roughness Index values. This aside, there is little evidence of any trends or significant correlations between the TS-AS and RI distribution charts. The detection of any relationships is therefore dependent upon the use of more detailed graphical plots of TS-AS against RI. The resultant graphical plots compiled from data within $2m^2$ of sample sites 12, 13, 14, 15 and 16, are displayed in Figures 8.43, 8.44 and 8.45.

Figure 8.42 Map of Roughness Index variability within a 10m x 10m area surrounding Sample Site 14 (Sub002Sam14)

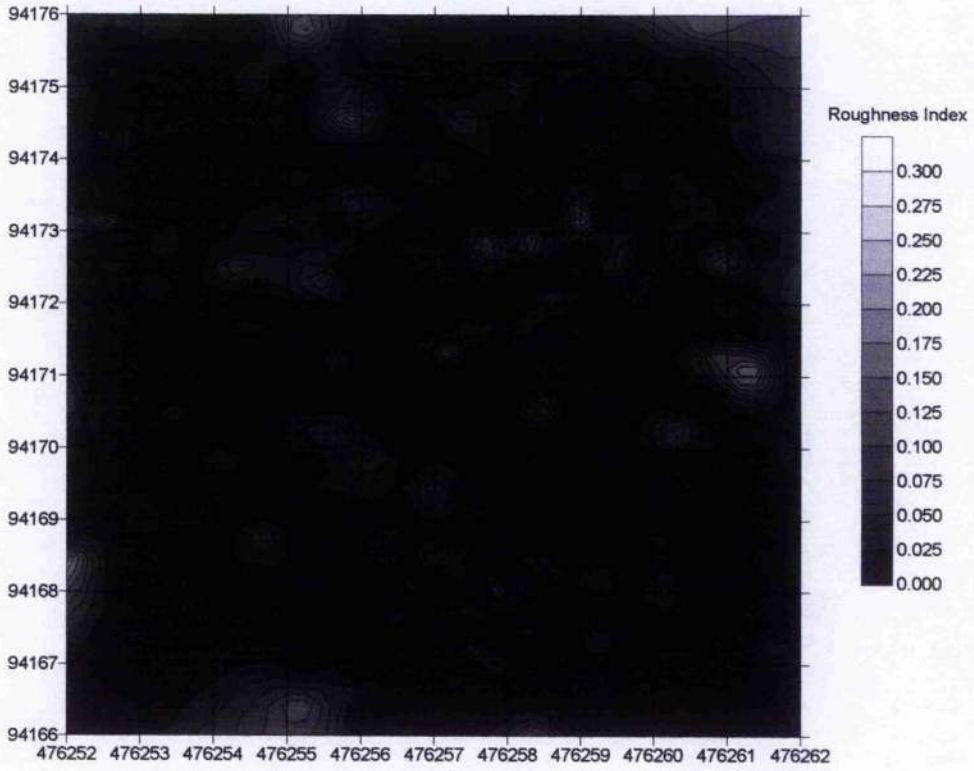

Figure 8.43 Graph of TS-AS against Roughness Index for data sampled from the $2m^2$ area surrounding sample sites 12 and 13.

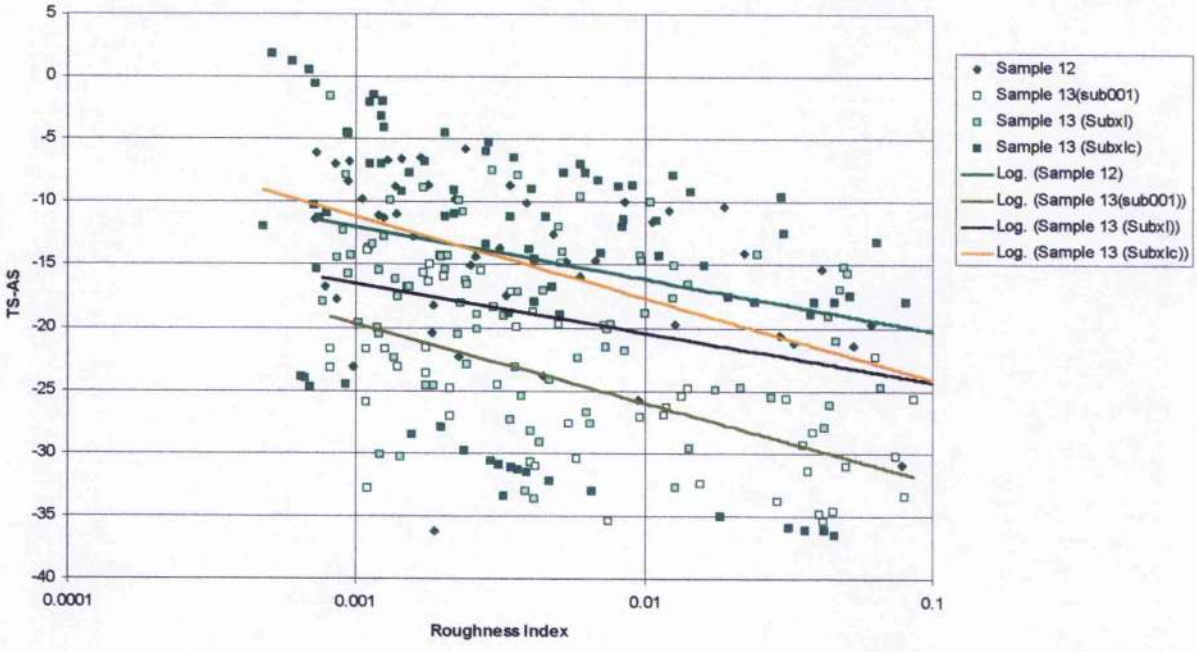

Figure 8.44 Graph of TS-AS against Roughness Index for data sampled from the $2m^2$ area surrounding sample site 14.

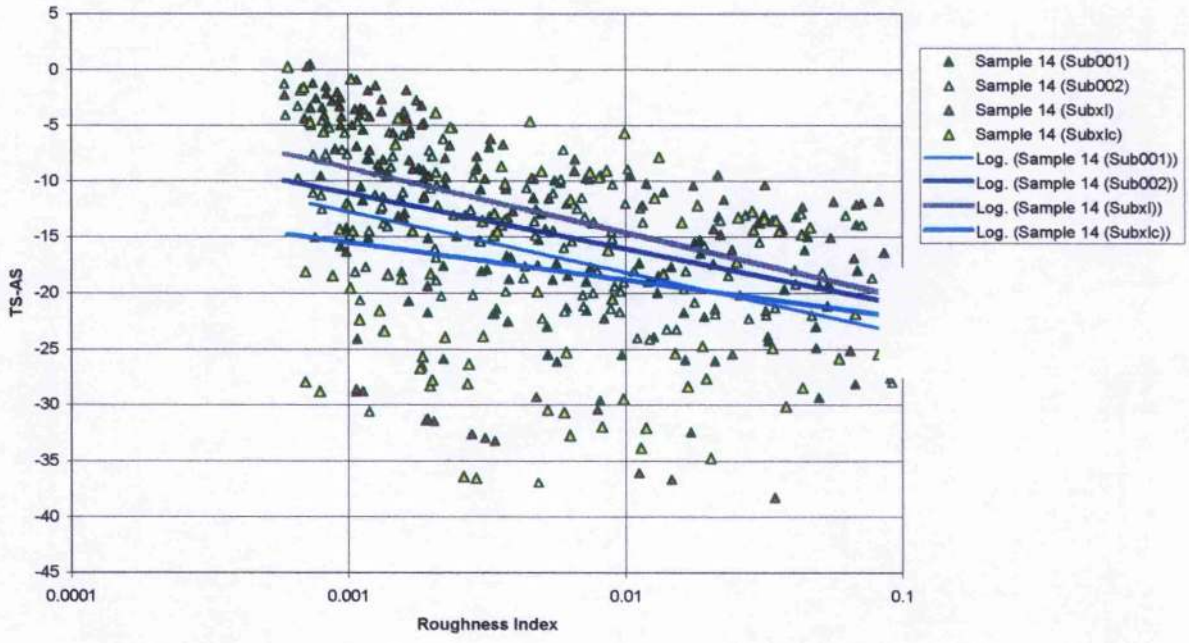

Figure 8.45 Graph of TS-AS against Roughness Index for data sampled from the $2m^2$ area surrounding sample sites 15 and 16.

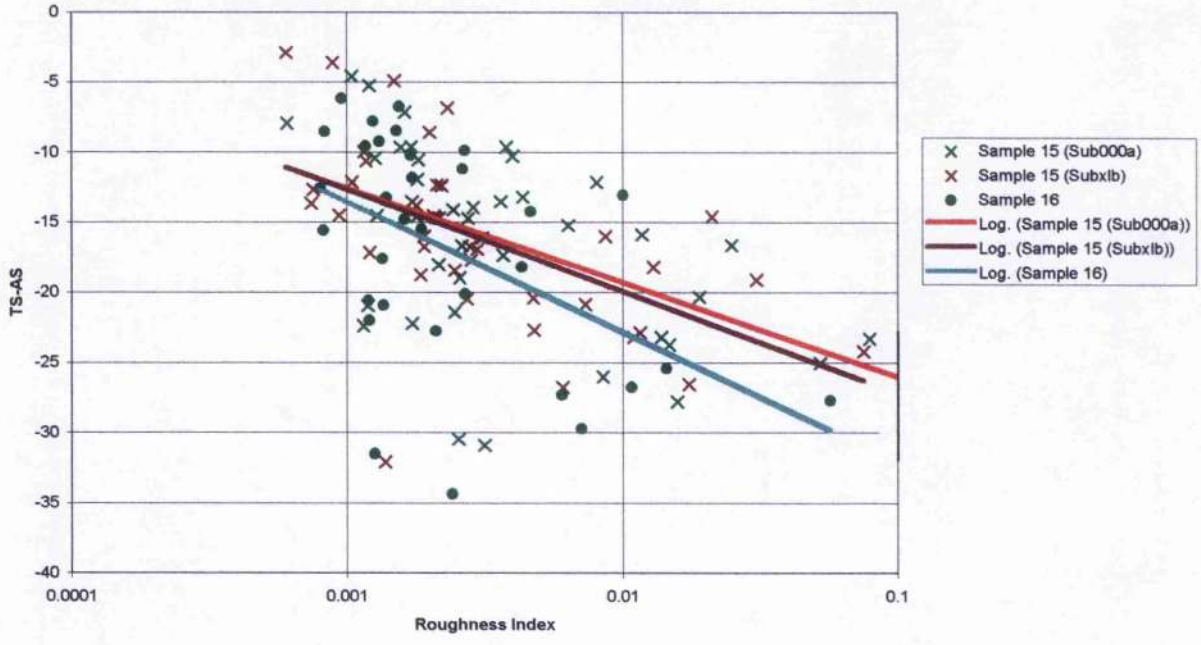

The graphs presented in Figures 8.43, 8.44 and 8.45 show that virtually all of the data from this survey area produces 'TS-AS v RI' trend lines of similar gradients. Although samples 15 and 16 appear to have slightly steeper dipping trend lines, it is thought that

this observation may be less reliable due to the uncertainties associated with the reduced number of data points found within these sites.

The log-linear trends between TS-AS and Roughness Index values for each of the sample sites within the A1 Submarine survey area can be summarised using the log-linear trend lines presented in Figure 8.43, 8.44 and 8.45.

These data trends associated with each sample site appear to suggest a close correlation between the majority of the samples from the A1 Submarine survey area. This is further illustrated by Figure 8.46 which shows a combined plot of all of the data from samples 12, 13, 14, 15, and 16.

Figure 8.46 Graph of TS-AS against Roughness Index for data sampled from the $2m^2$ area surrounding sample sites 12-16.

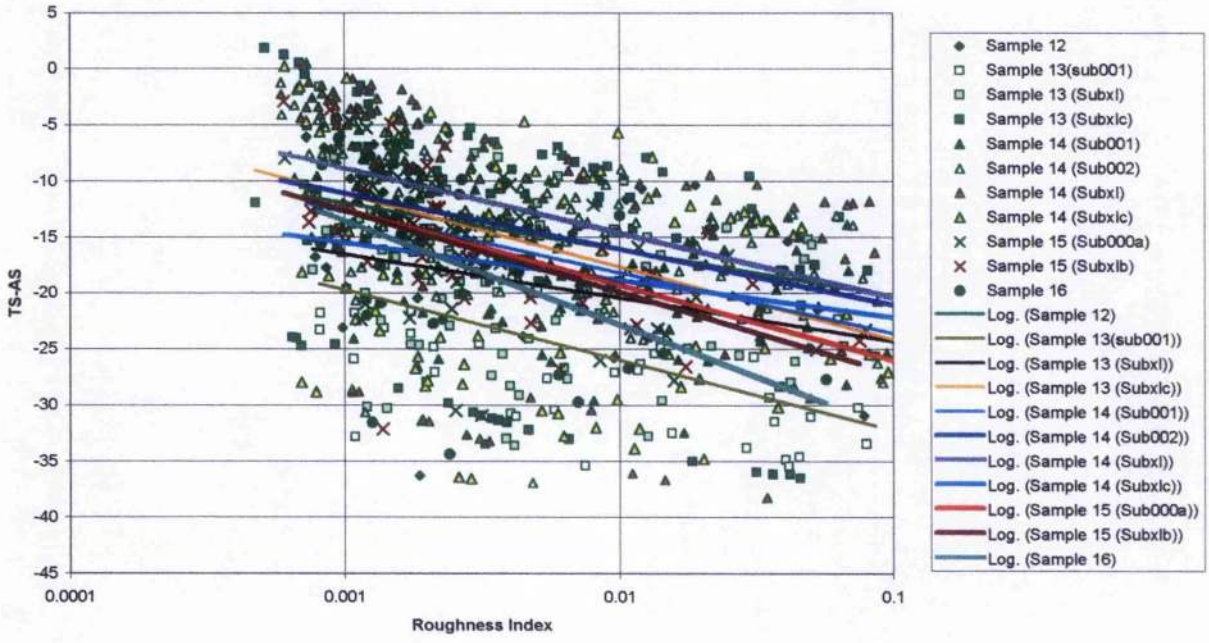

8.2.5. Comparison of TS-AS versus Roughness Index between survey areas

The log-linear equations summarising the relationship between TS-AS values and the Roughness Index for each sample within every survey area can be plotted together in Figure 8.47 in order to aid cross-correlation and comparative analyses.

Figure 8.47 illustrates a grouping of the results from within each survey area. Importantly, it also shows that the TS-AS values relating to any given roughness index value are significantly different between each survey area. Figure 8.47 also suggests that the majority of the trend-lines representing the relationships between TS-AS and the Roughness Index at each site, share a common gradient and therefore a universal sensitivity of TS-AS to the Roughness Index parameter can be proposed.

The distribution of the trend lines in Figure 8.47 suggest that the acoustic scattering from the water-sediment interface was lowest at the Calibration site, and increased through the Shingle site and then the A1 Submarine site, with the highest acoustic scattering being found at the Invincible site.

Figure 8.47 Graph of log-linear trends between TS-AS and the Roughness Index for all of the survey sites – Calibration (Blue), Shingle (Light blue), Invincible (Red), A1 Submarine (Green).

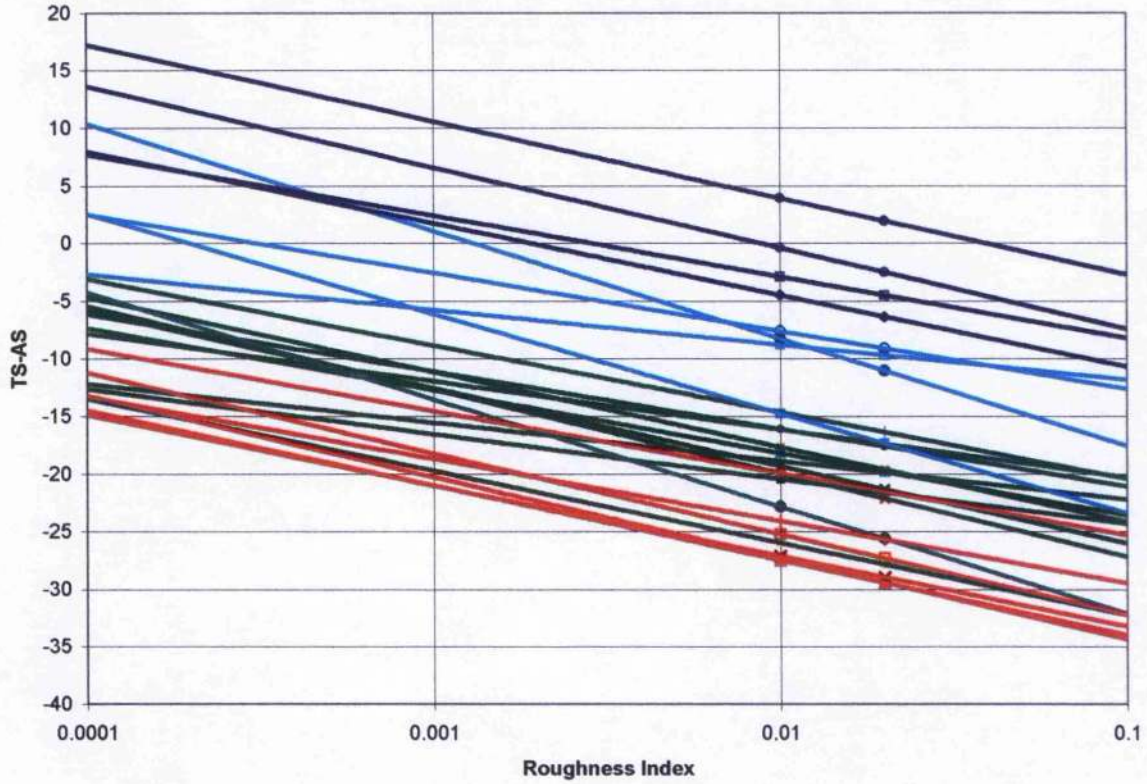

This summary can also be expressed by the overall distribution of the Portsmouth sonar datasets plotted on a single graph, as in Figure 8.48. This shows that even without averaging the trends, there is still a significant variation in the data distribution associated with each survey area.

Figure 8.48 TS-AS v Roughness Index plot illustrating the differences in data scatter between the Portsmouth survey areas (colour coded)

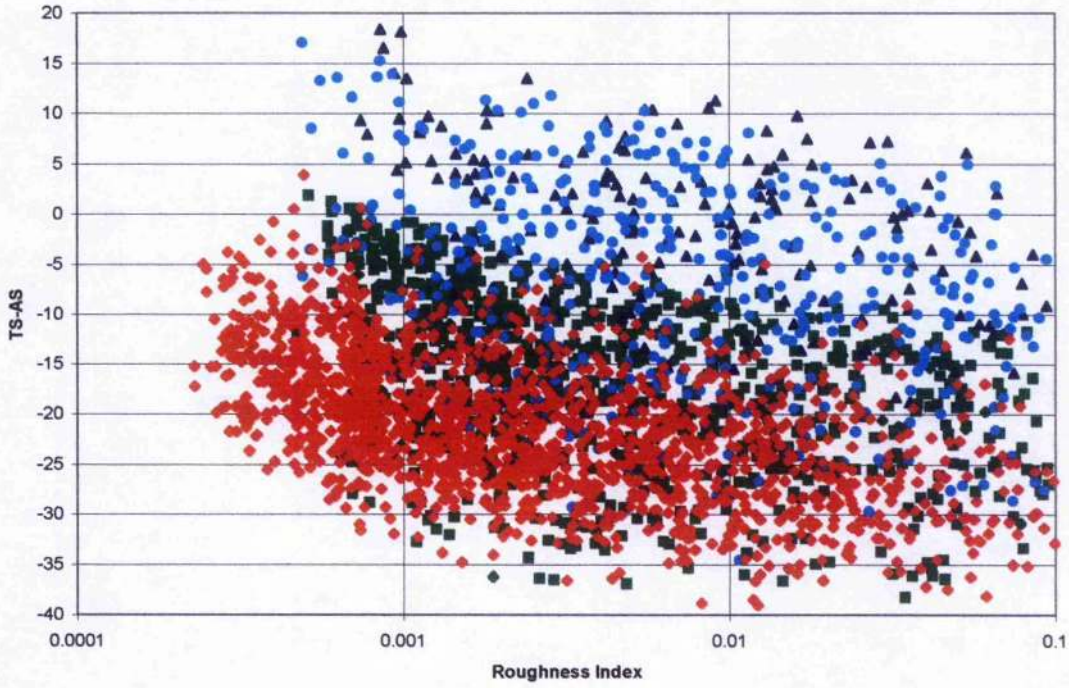

Figure 8.48 suggests that the data distributions of the Invincible and A1 Submarine areas are slightly more concentrated than those of the Calibration and Shingle areas.

The varying degrees of acoustic roughness measured at each sample site can be assessed relative to all of the other sites to provide a more comprehensive order of increasing roughness. This comparative ordering is performed using the assumption that at any given value of RI, the lower the associated value of TS-AS, the higher the actual roughness of the interface. In order to derive an overall roughness assessment at each sample site, the 'TS-AS v RI' data from all of the swaths within each sample location are grouped together to generate an average trend for the relationship between TS-AS and the Roughness Index. Table 8.2 summarises the resulting order of increasing acoustic roughness across all of the sample sites analysed by digital and ground-truthed data.

Table 8.2 Summary of relative degrees of acoustic roughness detected over the Portsmouth survey area

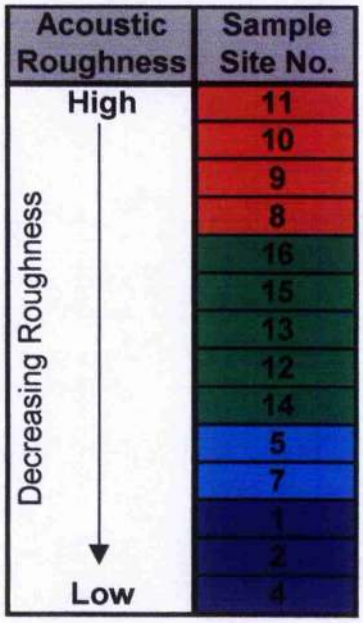

Table 8.2 shows a clear distinction between the degrees of acoustic roughness detected within each survey area, with the Invincible (red) area having the highest degree of acoustic roughness, followed by the A1 Submarine (green) area and then the Shingle area (light blue), and then finally the Calibration area (blue).

This ordering of acoustic roughness can now be directly compared to the findings of the grain size analysis in Chapter 7, in order to assess the correlation between the actual sediment roughness properties and the remote roughness measurements derived from the sonar data.

8.3. Cross-correlation of 'TS-AS versus Roughness Index' results with the actual sediment 'roughness' data between survey areas

The cross-correlation of the acoustic and actual bed roughness results can be visualised in Tables 8.3, 8.4, 8.5, and 8.6 below. These tables are compiled from the results of Section 8.2, and the sediment analysis results reported in Chapter 7. The colour scheme applied to each survey area has been incorporated within Tables 8.3, 8.4, 8.5 and 8.6 in order to simplify the visual comparisons between each area.

The trend of decreasing acoustic roughness values has been used as the basis for the evaluation of the cross-correlation with the sediment characteristics.

Table 8.3 **Cross-correlations between 'acoustic roughness' (Digital data) and 'Ground-truthed' primary sediment statistics (Mz, Md, Modal) results, presented in order of increasing phi (decreasing metric scale) value from top to bottom**

Acoustic Roughness	Sample Site No.	Mz (phi) Increasing	Sam No.	Md (phi) Increasing	Sam No.	Modal (1st) Increasing	Sam No.	Finest Mode Increasing	Sam No.
High	11	1.63	10	1.57	10	-3.96	5	1.55	10
	10	1.73	9	1.64	9	-3.96	7	1.58	9
	9	1.78	8	1.66	8	1.55	10	1.60	8
	8	1.80	11	1.67	11	1.58	9	1.60	11
	16	2.13	7	2.77	5	1.60	8	3.16	12
	15	2.31	5	2.96	7	1.60	11	5.16	14
	13	3.58	4	3.33	12	3.16	12	5.31	13
	12	3.92	12	5.31	4	5.16	14	5.35	15
	14	5.09	1	5.72	13	5.31	13	5.74	16
	5	5.74	13	5.90	14	5.35	15	6.44	2
	7	5.78	2	6.31	2	5.74	16	6.50	7
	1	5.91	16	6.38	1	6.44	2	6.81	1
	2	6.10	14	6.06	16	6.81	1	6.09	4
Low	4	6.56	15	6.36	15	6.53	4	6.65	5

Decreasing Roughness

Table 8.4 **Cross-correlations between 'acoustic roughness' (Digital data) and 'Ground-truthed' secondary sediment statistics and bio-content (SD, Ska, Kg, Carbonate, and Organics) results, presented in order of increasing phi (decreasing metric scale) value from top to bottom, and increasing percentage of bio-content**

Acoustic Roughness	Sample Site No.	SD (phi) Increasing	Sam No.	Ska (phi) Increasing	Sam No.	Kg (phi) Increasing	Sam No.	Carbonate % Increasing	Sam No.	Organics % Increasing	Sam No.
High	11	1.02	10	-0.442	4	0.621	7	0.00	8	0.57	10
	10	1.15	9	-0.305	1	0.793	15	0.00	9	0.72	11
	9	1.21	8	-0.186	7	0.883	16	0.00	10	0.76	9
	8	1.22	11	-0.136	13	0.886	14	0.00	11	1.05	8
	16	2.59	12	-0.123	5	0.901	2	3.90	5	7.29	12
	15	2.68	15	-0.118	2	0.973	3	4.76	7	9.17	5
	13	3.27	14	-0.051	16	1.028	5	5.37	1	10.46	3
	12	3.78	2	0.101	14	1.058	8	5.82	2	10.59	7
	14	3.79	16	0.130	15	1.071	11	7.42	3	10.98	1
	5	4.26	13	0.252	10	1.081	10	10.43	14	11.45	14
	7	5.00	1	0.287	9	1.117	9	12.26	16	11.88	4
	1	7.58	5	0.306	8	1.250	13	13.21	15	12.38	15
	2	7.74	4	0.321	11	1.630	1	18.52	12	13.59	16
Low	4	8.01	7	0.592	12	2.286	12	21.66	13	15.36	13

Decreasing Roughness

Table 8.5 **Cross-correlations between 'acoustic roughness' (Digital data) and 'Ground-truthed' sediment particle size classification (% Gravel, % Sand, % Silt, and % Clay) results, presented in order of decreasing metric value from top to bottom**

Acoustic Roughness	Sample Site No.	% Gravel Decreasing	Sam No.	% Sand Decreasing	Sam No.	% Silt Decreasing	Sam No.	% Clay Decreasing	Sam No.
High	11	37.35	7	100.00	8	81.21	15	12.02	15
	10	23.79	5	100.00	9	72.65	14	11.17	16
	9	21.47	4	100.00	10	70.80	16	10.12	14
	8	8.43	1	100.00	11	61.03	2	9.69	13
	16	5.22	13	77.42	12	44.83	1	3.96	1
	15	1.18	16	34.27	5	66.52	13	3.71	2
	13	1.18	2	20.68	2	63.44	4	3.07	4
	12	0.61	15	18.57	13	38.97	7	5.91	7
	14	0.00	8	17.78	7	36.61	5	5.34	5
	5	0.00	9	17.23	14	18.94	12	3.64	12
	7	0.00	10	17.06	16	0.00	8	0.00	8
	1	0.00	11	16.26	4	0.00	9	0.00	9
	2	0.00	12	16.24	1	0.00	10	0.00	10
Low	4	0.00	14	6.16	15	0.00	11	0.00	11

Decreasing Roughness

Table 8.6 **Cross-correlations between 'acoustic roughness' (Digital data) and 'Ground-truthed' sediment textural classification results, presented in order of decreasing coarse content from top to bottom**

Acoustic Roughness	Sample Site No.	Textural Classification Decreasing coarseness	Sample No.
High	11	muddy Gravel	7
	10	Sand	11
	9	Sand	10
	8	Sand	9
	16	Sand	8
	15	silty Sand	12
	13	gravelly Mud	1
	12	gravelly Mud	13
	14	shelly Mud	5
	5	shelly Mud	4
	7	slightly shelly sandy Mud	2
	1	slightly shelly sandy Mud	16
	2	slightly gravelly Mud	15
Low	4	sandy Silt	14

Decreasing Roughness

It should be noted that in Table 8.3 the 'Finest Mode' data refers to the finest modal grain size values obtained from the frequency weight percentage plots in Chapter 7. In order to delimit the presence of a mode which will be significant in terms of the bed

roughness, these modes must exceed 10% of the frequency weight percentage to be included in this analysis.

In the absence of any clearly conformable pattern, the implications of the above trends between varying ground-truthed sediment statistics and the surface roughness perceived by the remote acoustic analysis, requires an in-depth discussion and evaluation.

CHAPTER 9:

DISCUSSION

The acoustic-sediment relationship results will be discussed with respect to each survey area prior to the evaluation of acoustic-sediment discrimination between the survey areas. The discussion will focus upon the 'TS-AS v RI' plots, summarised by the trend lines in Figure 8.47 and Tables 8.2, 8.3, 8.4, 8.5 and 8.6, from Chapter 8.

9.1. Acoustic and sediment roughness within the Calibration survey area

The Calibration survey area provides the highest values of TS-AS for any given RI, of all the areas surveyed. The actual data distribution in Figure 8.9 shows that although the scattering of data is centred around the TS-AS=0 (or TS=AS) condition, the majority of the elements are actually found above this condition where TS>AS. This essentially means that for any given roughness index value, the actual scattering strength recorded over the Calibration site is less than that predicted by Lambert to be scattered from a flat, planar surface. This therefore suggests that the surface sediment in this area must be inducing a decrease in the expected backscattering portion, beyond that which is thought to be minimal. This situation can occur as a result of conditions that lend themselves to the promotion of the alternative acoustic surface interactions of absorption or reflection. In light of the sediment grain size analysis results (especially Figure 7.5) which show that this area has a high percentage of silts and clays, it is thought that the reduction in scattering strength can be attributed to an increase in the absorption fraction.

The high percentage of muddy sediments is also thought to contribute to the reduction in scattering strength by 'smoothing' the particulate roughness of the seabed. This

'smoothing' is the result of the smaller particles filling the interstitial gaps between the larger particles, and thereby smoothing the overall topography.

The cross-correlation between sample sites 1, 2, and 4, illustrated by Figure 8.9, shows an increase in acoustic roughness from sample 4, through sample 2, to sample 1. This trend does not appear to be consistent with any of the sediment statistic trends listed in Tables 8.2, 8.3, 8.4, 8.5 or 8.6, as all of the statistics suggest that sample 4 should be the coarsest, followed by sample 1, and then sample 2.

It is therefore hypothesised that this smoothing of the bed roughness may also be accountable for the differences in actual scattering strength between each individual sample site. This theory is supported by the trend illustrated by the 'Finest Modal' values listed in Table 8.3, which shows that although sample 4 has the coarsest sediment grains of the Calibration samples, it also possesses the highest finest modal value (6.55 phi), or in other words, the finest matrix material. The presence of this very fine matrix material may result in a smoothing of the bed roughness and also in an increase in the degree of acoustic transmission into the sediment, thereby significantly reducing the acoustic scattering strength of this shelly mud. In comparison, the 'slightly shelly sandy mud' of sample 2 may be regarded as being slightly rougher, due to a combination of its lower 'finest modal' value of 6.44 phi, and a 23.66% sand content which will further increase the roughness of the matrix between the shelly fractions.

The fact that Figure 8.9 then suggests that the bed roughness of sample 1 is only marginally rougher than that found at sample 2, can be directly related to the fact that samples 1 and 2 are virtually identical according to the textural classification results (Section 7.5.1).

In general, the low level of acoustic scattering strength detected over this area is consistent with the sediment-acoustic findings outlined in Chapter 3, which stated that muddy sediments are characterised by very low scattering strengths.

9.2. Acoustic and sediment roughness within the Shingle survey area

The Shingle survey site is found to have a TS-AS v RI trend which centres around the TS-AS=0 line at low RI values, and decreases to between –12 and -20 as the RI values increase towards 0.1. The fact that the trend lines lie below the TS-AS=0 line shows that the surface sediment in this area generates a marginally higher scattering strength than predicted by Lambert's Law. This means that the sonar scattering states that the surface roughness is expected to be slightly rougher than a planar surface. This expectation is satisfied by the sediment analysis, which reveals the presence of a bi-modal sediment characterised by a high gravel and silt content. Despite the high gravel/shell content within this survey area, the actual scattering strength is not significantly higher than the theoretical scattering strength, and therefore it is again hypothesised that the very fine particulate content of the matrix is effectively smoothing the surface.

This theory can be supported through the comparison of the TS-AS values recorded over the Calibration and Shingle survey areas, which show that the higher content of coarse material in the Shingle area correlates closely with the decrease in TS-AS (an increase in acoustic scattering).

In comparing sample site 5 with sample site 7, the scatter of the element data in Figure 8.18 appears to suggest that sample 5 has marginally lower TS-AS values than sample 7, and is therefore expected to have a slightly rougher surface. This can be related to the grain size analysis which highlights a difference in the coarse material content composition between sample 5, having 23.79% gravel and 34.27% sand, and sample 7 with 37.35% gravel and 17.78% sand. This again suggests that it is the coarseness of the

sediment matrix, enhanced by the higher sand content in sample 5, that ultimately determines the scattering strength of the surface.

9.3. Acoustic and sediment roughness within the Invincible survey area

The Invincible survey area is relatively uniform throughout, with respect to both the acoustic and sediment analysis.

The acoustic roughness analysis of 'TS-AS v RI' values in Figures 8.29 and 8.30 reveal a much larger actual scattering strength than predicted by Lambert, with TS-AS values ranging from an average of –18 at an RI of 0.001, to an average of –30 at an RI of 0.1. In addition, these figures illustrate a significant conformity between the trend lines of samples 8, 9, 10, and 11, with the maximum TS-AS range being only 5 points. In-spite of this narrow range, the inter-relationship between the trend lines in Figure 8.29 suggests a small increase in acoustic roughness from sample 8, through sample 9, to sample 10. This increased roughness trend is also evident in the Mz values with values of 1.78 phi (sample 8), 1.73 phi (sample 9), and 1.63 phi (sample 10). The data from sample 11 do not fit this trend however, for although an almost identical sediment type to sample 8, it appears to be characterised by an acoustic scattering strength closer to that of sample 10.

Overall, the Invincible survey area exhibits a very strong correlation between high acoustic scattering strengths (low TS-AS values) and a high degree of sediment roughness. In this area the sediment roughness can be evaluated using the mean grain size values (Mz) due to the very narrow grain size range, and the absence of an interstitial matrix material.

It should also be noted that the high levels of acoustic scattering strength detected throughout this area are consistent with the sediment-acoustic findings outlined in

Chapter 3, which indicate that sandy sediments are characterised by very high scattering strengths.

9.4. Acoustic and sediment roughness within the A1 Submarine survey area

The A1 Submarine survey area is observed to have a narrow range of 'TS-AS v RI' data scatter in Figure 8.46, despite a large number of sample sites and many different swaths. This relative uniformity is also evident in the sediment analysis results which, with the exception of sample 12, reveals the presence of a silt-mud surface sediment.

The presence of this silt-mud sediment type at sample sites 13, 14, 15 and 16, suggests that the surface will be relatively smooth, and thus a low acoustic scattering strength centred around TS-AS=0 would be predicted. In contrast, the actual data scatter in Figure 8.46 generates a narrow range of trend lines which run from between –10 and –15 for an RI of 0.001, to between –20 and –25 where the RI increases to 0.1. This unexpectedly high scattering strength remains unaccounted for in-spite of the detailed statistical grain size analysis of the A1 Submarine sediments within Tables 8.2 - 8.6. The implication of this lack of roughness accountability through the grain size analysis is that the surface sediments at sample sites 13, 14, 15, and 16, must somehow be enhancing the scattered proportion of the acoustic signal at the expense of either the absorbed or reflected portion.

This suggestion is supported by a visual observation made at the time of ground-truthing (See section 7.5.4.). At sample sites 13, 14, 15, and 16, the seabed surface was found to have a very rigid 'rough surface crust' comprising of a silty material. It is clear that the presence of such a "rough crust" would enhance the impedance contrast at the water-sediment interface, thus reducing the portion of the acoustic wave that would normally be absorbed into such silty-muddy sediments. The fact that the crust is rough

and not smooth would also favour scattering over reflection, thereby boosting the acoustic scattering strength of the muds beyond the levels stated in Chapter 3.

Sample 12 must be evaluated independently from the other A1 Submarine samples, as the "crust" was not evident at this site. The TS-AS v RI trend exhibited by the data from sample site 12 shows an average decrease in TS-AS from –12 to –21 as the Roughness Index increases from 0.001 to 0.1. This trend is indicative of a relatively high degree of bed roughness, and indeed the sediment grain size analysis reveals the presence of a silty sand.

The high scattering strength associated with this predominantly sandy sediment are regarded as conforming with the findings in Chapter 3, although due to the presence of a silty matrix the scattering strength is likely to be marginally lower than that of a pure sand.

9.5. Acoustic and sediment roughness variations between survey sites

The fact that the Calibration and Shingle survey sites are both located within the estuarine zone of Portsmouth harbour may be regarded as contributing significantly to the similarity in the actual scattering strengths recorded by the sonar. Both of these survey areas are found to contain bi-modal sediments comprising a coarse gravel/shell/sand and silt-clay content, although the Shingle sediments possess a slightly more significant coarse fraction. This reflects the findings of the acoustic roughness data which show that the Shingle survey area produces a marginally higher actual scattering strength than the Calibration survey area. This suggests that the correlation of 'acoustic' and 'actual' roughness between the Calibration and Shingle areas enables detection of the subtle increase in bed roughness over the Shingle area caused by the higher percentage of coarse particles.

In comparison, the silts and muds within the A1 Submarine survey area produce a higher actual scattering strength (lower TS-AS) than both the Calibration and Shingle areas in spite of having a significantly lower content of coarse material. This anomalous result is attributed to the enhanced acoustic impedance at the water-sediment interface caused by the presence of a rigid, cohesive, silt-clay "crust". Thus it may be hypothesised that the actual scattering strength of silts-muds is not solely dependent upon the roughness of the surface, but that it is also influenced by the degree of acoustic absorption at the water-sediment interface. This is a important observation, and one that is indicative of the fact that the degree of sediment "packing" can be a significant factor in determining the strength of the acoustic scattering.

Although this factor is empirically implied by the increase in actual scattering strength between the Calibration and Shingle sites, and the A1 Submarine site, an increase in the acoustic impedance relative to the "packing" of the sediments cannot be accurately evaluated using the sediment analysis techniques employed here. Indeed, a comprehensive evaluation would require an *in-situ* analysis of both the acoustic impedance at the water-sediment interface and the *in-situ* "packing" of the sediment particles.

The acoustic-sediment analysis also exhibits a strong trend in the areas covered by sandy sediments. The acoustic roughness analysis ordering in Table 8.2 shows that sample 11 has the highest perceived roughness, followed by sample 10, sample 9, sample 8, and then sample 12. This general trend, with the exception of sample 11, is also depicted by practically every statistical and compositional analysis of the sediments as listed in Tables 8.3, 8.4, 8.5, and 8.6. The clarity of this acoustic-sediment relationship within the sandy sediments can be directly attributed to the strong modality (greater than 70% on the Frequency weight percentage plots in Chapter 7) of each of the samples.

Overall, the roughness variations between each survey area produce this very clear scattering strength progression:

- low roughness, low scattering from the muddy sediments of the Calibration and Shingle sites
- low roughness, medium scattering from the silt-mud crust of the A1 Submarine site, medium roughness, medium scattering of the silty sand at sample site 12 (A1 Submarine site)
- high roughness, high scattering from the sandy sediments of the Invincible area.

It is worthy of note that as the Invincible area is covered by fine sands (Mz <0.2mm), the entire range of this acoustic-sediment roughness analysis covers only clays (Mz<0.002mm) through to fine sands (Mz<0.2mm). This factor therefore demonstrates the ability of this remote acoustic scattering technique to discriminate between subtle changes in sediment composition.

9.6. Summary of the relationships between 'acoustic roughness' and actual sediment characteristics

This section focuses upon identifying the sediment characteristic which best accounts for the ordering of acoustic roughness values (defined by the TS-AS v RI trend lines), with a view to deriving a reliable, universal methodology for relating the actual scattering detected by a sonar system to the material properties of the surface sediment. Figure 8.47 shows that for any given value of RI, the associated value of TS-AS can be easily related to a broad sediment classification of either mud or sand. However, the correlations between actual scattering strength and sediment statistics presented in

Tables 8.3, 8.4, 8.5, and 8.6, suggest that much more can be inferred about the sediment characteristics.

The correlation between Mz and the actual scattering strength appears to be very strong for well-sorted (low SD values) or strongly uni-modal (frequency wt % >70) sediments, such as samples 8, 9, 10, 11, and 12, with Mz increasing with increasing scattering strength. Where this relationship is evident, the other major statistical parameters, Md and Mode, are also found to conform with this trend. The occurrence of strongly uni-modal sediments is also found to be associated with a relatively narrow scatter range of TS-AS v RI data, as illustrated by Figures8.29 and 8.30.

In addition to a detailed description of the sediment properties, this also enables an approximation of density and porosity values through the application of the 'Mz against Density' and 'Mz against Porosity' regression equations proposed by Hamilton and Bachman (1982).

The fact that the correlation between Mz and the acoustic scattering strength for a known roughness index value is restricted to strongly uni-modal sediments means that its actual application must be confined to TS-AS values which lie within the middle range zones of the broad sediment classification groups. This restriction is applied on the assumption that the sediments with the lowest standard deviation of grain size are found within the middle range zones of each broad class.

The areas outwith the central zones in each broad class are thus implied to relate to a decrease in the level of sorting of the uni-modal sediment type, down to a bi-modal or tri-modal sediment. This poorly-sorted material will therefore be characterised by the presence of a matrix material which, as demonstrated by the Calibration and Shingle datasets, can determine the overall bed roughness of the surface. This means that the

actual scattering strength will reflect a combination of the coarse material roughness and the degree to which it is smoothed by the sediment matrix.

The most accurate acoustic-sediment relationship in such circumstances is found to be between the actual scattering strength and the grain size value of the finest mode (Table 8.3), which reflects the roughness of the matrix. It should again be noted that the finest mode statistic is based upon the lowest significant grain size mode, which must exceed a frequency weight percentage of 10% in order to be incorporated within the analysis. The ordering of the finest mode values in Table 8.3 shows a strong correlation with the acoustic roughness ordering, and it also demonstrates a clustering of the broad sediment classes. The clustering of the finest mode values suggests sediments that provide low scattering strengths in the mud range will possess a finest modal value of >6.0 phi (samples 1, 2, 4, 5, and 7), whilst those which are associated with medium scattering strengths between mud and sand will have a finest modal value closer to 3.0 phi (sample 12), and finally sediments with high scattering strengths will have a finest modal value of <2.0 phi (samples 8, 9, 10, and 11). In order to focus on the acoustic-sediment relationships that are entirely dependent upon bed roughness, samples 13, 14, 15, and 16, have been excluded from this section of the evaluation due to the presence and anomalous affects of the silt-mud "crust."

It is worthy of note that this correlation between the finest mode value and the acoustic roughness can also be applied to sediments with single modes, whereby the grain size of the finest mode is assumed to be the same as the grain size of the only mode.

In essence, the mean grain size of the sediments can be inferred where the scattering trend of the TS-AS v RI data lies in the middle ranges of a broad sediment class, but in cases where the scattering trend lies towards the upper or lower margins of the broad classification, the Mz measurement becomes less dependable and should be replaced by

the finest modal grain size characteristic which is found to be more universally consistent.

This reverse correlation is illustrated by Figure 9.1 which uses shading on the TS-AS v RI plot to predict the M_Z or finest modal value of the sediments, based upon the nature of the acoustic data distribution.

Figure 9.1 Reverse correlation for the prediction of sediment characteristics using the TS-AS v RI plot

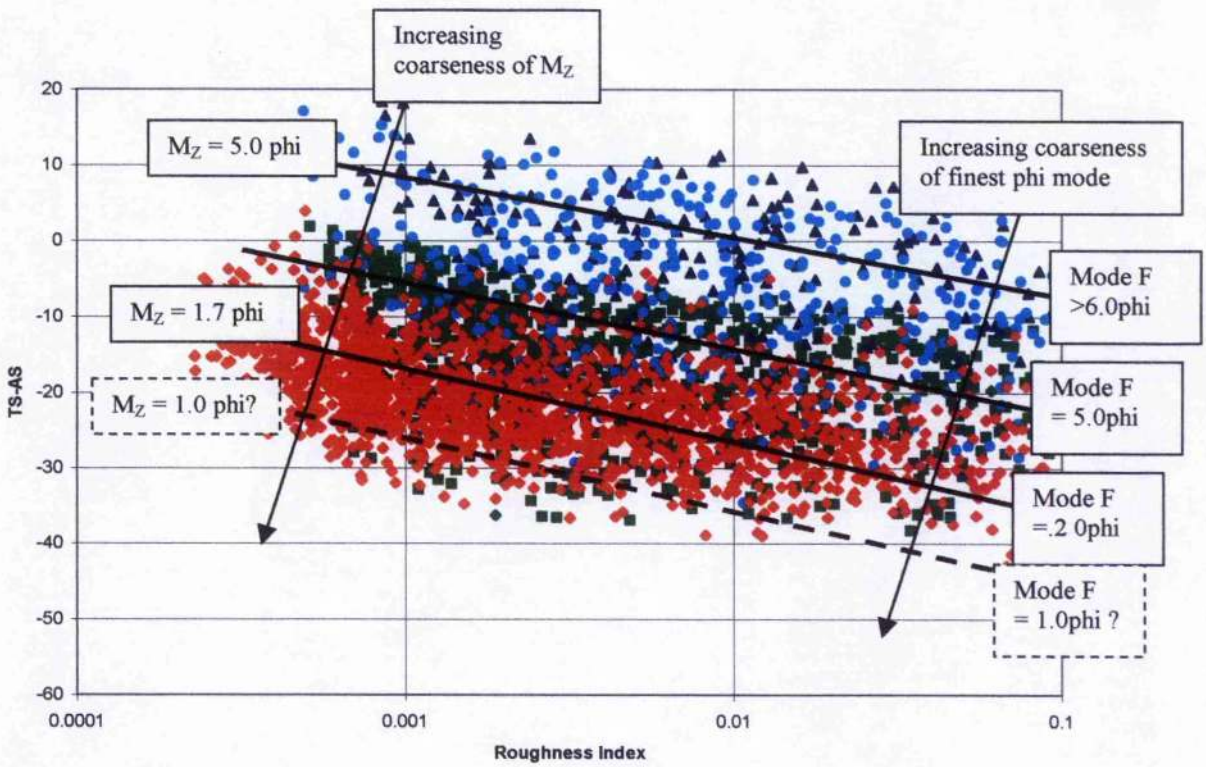

Although this correlation has only been tested for a small range of M_Z and finest modal values, it appears to suggest that there is a strong possibility that this technique could provide a mechanism to perform an 'unsupervised' remote classification scheme – a scheme which is not dependent upon ground-truthed sample proofing.

Figure 9.2 shows a proposed characterisation of sediment type based upon the TS-AS v RI distribution. This general classification scheme can be used in conjunction with the

statistical characterisation proposed in Figure 9.1, with the more reliable M_Z values being found in the uni-modal centre of each broad sediment class.

Figure 9.2 Graph showing zonal classes for an 'unsupervised' sediment classification scheme

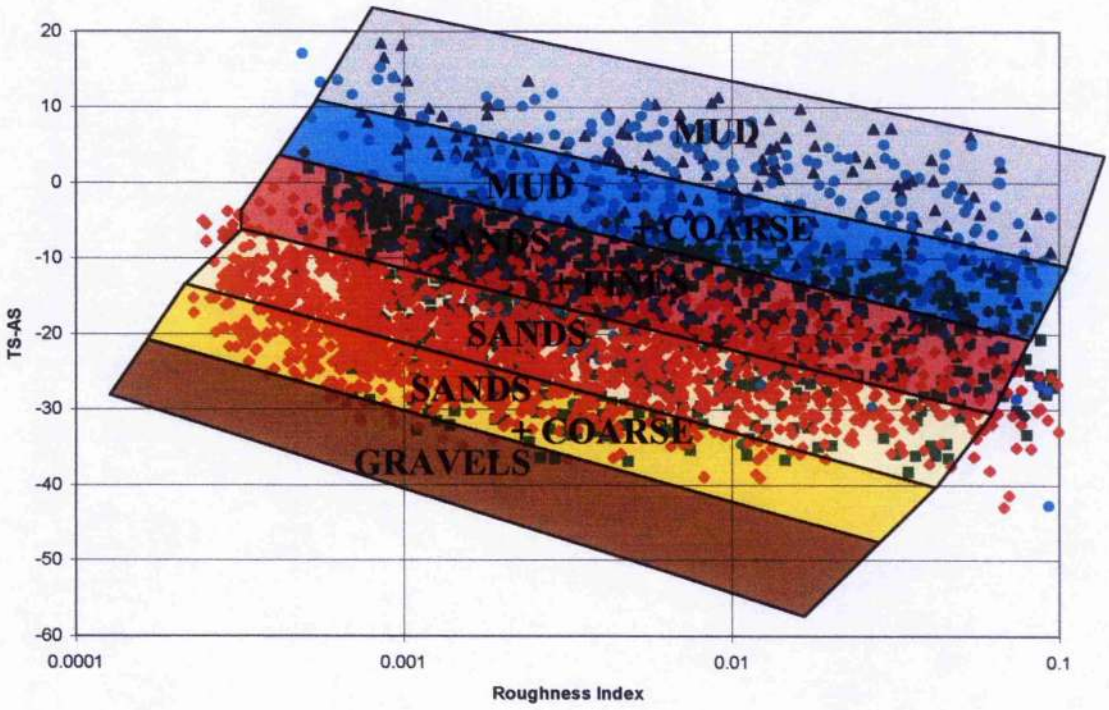

CHAPTER 10:

CONCLUSIONS AND RECOMMENDATIONS FOR FURTHER WORK

The main aim of this research was to investigate the potential of a high precision, high resolution sonar system to remotely classify seabed sediment types based upon empirical relationships between the acoustic scattering strength of the water-sediment interface and the grain size characteristics of the sediment.

Chapter 2 discussed the ability of the universally accepted "sonar equation" to precisely account for the majority of the variables acting upon the acoustic signal as it propagates through the water column, and which are inherent in such a remote sonar surveying technique. The application of this sonar equation provides an accurate accountability for all forms of acoustic propagation processes, and thus leaves the processes active upon the acoustic wave at the water-sediment interface as the only unknowns. Chapter 2 then proceeded to define and evaluate the theoretical and empirical physical relationships that govern the nature of the acoustic processes active at the seabed. This evaluation led to the conclusion that the relative magnitude of the acoustic reflection, scattering and absorption processes could ultimately be determined by the frequency of the sonar signal. The overall acoustic-sediment analysis was focused upon the backscattering process as this is the most practical, economical and universally accepted method of remotely surveying the seabed surface.

A very high frequency, high-resolution interferometric sonar, called the ISIS 100 234kHz system, was selected for use following the findings of Chapters 2 and 3. The combination of a high acoustic frequency and small areas of insonification focused the

acoustic analysis predominantly upon the interface backscattering caused by the roughness of the sediment. In addition, the very high data density achievable using the interferometric technique enables a fuller accountability of the small-scale surface topography of the seabed, thus helping to further focus the surface roughness factor upon the granular roughness element.

Chapter 3 also discussed the findings of previously published research on the relationships between the bottom backscattering strength, plotted against the grazing angle, and the broad seabed sediment types. These empirical relationships suggested a general increase in backscatter strength as the sediment types change from clays, to silts, to sands, to gravels, and therefore provided an approximation to the results which could be expected.

The field methodology centred around the collection of very comprehensive and very accurate acoustic and ground-truthed datasets. This was achieved using the most accurate survey equipment available for a sonar survey; an ISIS 100 234kHz, a RACAL Landstar DGPS, a TSS MRU, and CTD probe; as described in Chapter 4. The ground-truthing programme was also designed to utilise the high precision DGPS system to pin-point the location of each grab sample.

In order to maximise and preserve the resolution and precision of the sonar survey system the sonar systems characteristics were critical in the selection of the survey sites. This ultimately led to the identification in Chapter 5 of four primary survey areas; (1) Calibration area, (2) Shingle area, (3) Invincible area, (4) A1 Submarine area; within the Portsmouth coastal waters. Each of these areas was selected because, according to admiralty charts, they offered flat bottoms of differing seabed sediment types within

shallow (<20m) waters, and therefore offered optimum sonar survey conditions for maximising precision and resolution.

The post-processing of the digital sonar data in Chapter 6 is the most important stage of the overall analysis, due to the intricacies of enhancing data quality and preserving the data quantity, without performing any form of interpolation or extrapolation. This was achieved through the generation of trigonometric parameters based upon the interrelationships between adjacent element on the seabed. These trigonometric parameters also formed the basis of very highly sensitive data filtering algorithms which enabled the careful extraction of non-conforming elements. This was achieved by performing an element by element assessment of the data classes in relation to the values associated with adjacent elements. This level of analysis also enhanced the evaluation of localised seabed slope angles, thereby significantly improving the resolution and precise of the total grazing angle calculations.

Following examining a variety of possible alternatives the final product of the digital data post-processing was the generation of TS-AS maps of each survey area, which defined the areas where the actual scattering strength (AS) either exceeded Lamberts' theoretical scattering strength of a flat surface (TS<AS) or fell short of the Lamberts' theoretical expectations (TS>AS). These values of TS-AS are used as a general indication of the scattering strength of the seabed, with TS-AS>0 indicating a sediment which provides a lower level of scattering than expected from a smooth surface, TS-AS=0 indicating a flat planar scattering surface, and TS-AS<0 indicating a sediment which causes a larger degree of scattering than could be expected from a flat surface. It is this precise scattering strength factor that is required in order to relate the remote acoustic amplitude data to the actual roughness of the seabed.

Chapter 7 detailed the comprehensive analyses of the ground-truthed sediment sample properties which were performed within a laboratory using universally accepted particle size and material composition techniques. The results provided an extensive assessment of all aspects of the particulate and compositional statistical characteristics of the sediments that can be compared and contrasted with other samples, and ultimately correlated with the results of the digital data analysis.

Prior to correlating the acoustic and sediment analyses, Chapter 8 defines the method by which the acoustic scattering strength must be directly related to both the perceived angular aspect of roughness (Resolvable Roughness), and the spatial extent of the insonified area (Roughness Index) in order to account for the varying degrees of acoustic sensitivity to the roughness of the seabed.

The empirical relationships between TS-AS and the Roughness Index over each sample site are then presented in graphical form, in order to compare and contrast the findings associated with each sample site, and also between each survey area. The results of this acoustic roughness analysis are summarised in Table 8.2 which places the samples in order of their degree of acoustic roughness. This ordering reveals a trend of acoustic roughness that falls from a high at the Invincible area, decreasing through the A1 Submarine area and the Shingle area, to a low at the Calibration area.

In Section 8.3 the overall trend in acoustic roughness between each sample site is then cross-correlated with the trends exhibited by all of the statistical properties relating to each sediment sample.

Chapter 9 provides a comprehensive discussion of the implications of these results both within each survey area, and then between each survey area. As presented in Table 8.3 the acoustic roughness trends from within each survey area appear to exhibit very close

correlations with the primary sedimentary statistics of either/both the **mean** and **finest modal** grain size. The only exceptions to this correlation relate to the anomalous results caused by the presence of a firm, cohesive, silt-clay crust at sample sites 13, 14, 15, and 16.

Although a correlation between the acoustic roughness and the **mean** grain size can provide a very detailed description of the sediment characteristics, it is restricted in its application to situations where the sediments are predicted to be strongly uni-modal, i.e. where the data scatter in the TS-AS v RI plots falls within the mid-ranges of a broad sediment class. This is because the mean grain size statistic alone is a poor indicator of the nature of the sediment matrix.

However, the relationship between the **finest modal** grain size (>10% frequency weight percentage) and the acoustic roughness is found to be universally consistent for all of the sediment samples, including uni-modal (samples 2, 8, 9, 10, 11, 12, 13, 14, 15, and 16) bi-modal (samples 1 and 4) and tri-modal (samples 5 and 7) sediments. This means that irrespective of the data scatter trend on the TS-AS v RI plots, it is possible to predict a finest modal value relating to the unknown sediment type.

In conclusion, the results and discussion presented in Chapters 8 and 9 strongly suggest that it is possible to predict the mean or finest modal grain size value of the seabed sediment based solely upon the spatial distribution of the acoustic data within a TS-AS v RI plot. However, the findings also indicate that the accuracy of the prediction may be dependent upon the impact of additional factors such as carbonate content, organic content and the degree of "packing" of the sediment.

RECOMMENDATIONS FOR FURTHER WORK

It is recommended that future research within this field addresses the following aspects in order to increase the precision of the acoustic-sediment data, and also to assess the full range of the acoustic-sediment roughness analysis:-

1. ***Additional datasets covering areas of medium sands, coarse sands, fine gravels, medium gravels, and coarse gravels***

   The addition of such datasets would enable the completion of the acoustic-sediment roughness analysis over the full range of sediment grain sizes. It is also anticipated that a larger grain size range would help to enhance the confidence levels in terms of the universal application of this remote sediment classification system, and to ensure that the empirical trends are consistent in larger grain size classes. This would also help to further constrain the areas within the TS-AS v RI plots where either the **mean** or **finest modal** grain sizes could be predicted.

2. ***3-Dimensional slope analysis***

   Within this report, the angle of incidence of the acoustic wave with the water-sediment interface has been calculated using a 2 dimensional model. This 2-D angle of incidence value is used to determine a compensatory value for surface scattering, which itself is a 3-D phenomenon. It is therefore recommended that further analysis is carried out on the merits of incorporating an along-track dimension, using data from adjacent pings, to create a 3-dimensional surface topography from which 3D grazing angles can be derived.

3. *3D wave tracing*

This research has focused upon the tracing of the acoustic wave in only two dimensions, as the variations in temperature and salinity within the water column at these shallow water sites were assumed to be of insufficient magnitude to warrant a 3-dimensional modelling of the acoustic wave propagation. However, in order to apply these acoustic-sediment analysis techniques to deeper waters, it is imperative that 3-dimensional wave tracing is performed to account for the effects of any thermoclines or more significant variations in salinity and conductivity.

4. *Micro-topographic Roughness, and Scales of Measurement*

The scale of micro-topographic measurements are essentially determined by the resolution and precision of the survey instruments. The main factors in this determination, outwith the overall survey precision, are sonar frequency, beam shape, and water depth. In essence, by altering the sonar frequency it may be possible to focus in upon differing sediment characteristics, via altering the degree of acoustic penetration or resolution. The factors of beam shape and water depth delimit the resolution of the survey data, and therefore research into optimal values for these factors in given conditions may enhance the resolution.

5. *Inclusion of in-situ Density and Porosity Measurements*

The ability to measure density and porosity values of the sediments *in-situ* would provide an additional aspect to the acoustic-sediment analysis, which is strongly sought after by marine engineers.

BIBLIOGRAPHY

Aherns, E. (1957). Use of horizontal sounding for wreck detection. *International Hydrographic Review, Vol. 34, 73-81.*

Al-Ansari, N.A. (1976). Sediments and sediment discharge in the River Earn, Scotland. *PhD thesis, University of Dundee.*

Archaeological Diving Unit (2000). Historic Wreck Sites (in UK coastal waters). *http://www.adu.org.uk*

Bachmann, W. (1973). A theoretical model for the backscattering strength of a composite roughness sea. *Journal of the Acoustical Society of America, Vol.54, 712-716.*

Baker, B.B. and Copson, E.T. (1950). The mathematical theory of Huygen's principle. *Oxford.*

Barrick, D.E. and Peake, W.H. (1968). A review of scattering from surfaces with different roughness scales. *Radio Science, Vol.3, 865-868.*

Beck, R.A. (1991). Automatic sea bed classification using sidescan sonar. *Institute of Acoustics.*

Beldenson, R.H. (1972). Sonographs of the sea floor. *Elsevier Publishing Company, Amsterdam.*

Bennell, J.D., Butcher, J., Davis, A.M., Richardson, I.R. and Simpkin, P.G. (1993). Some developments in high resolution seismic reflection profiling relevant to investigations of very shallow water areas. *Acoustic Classification and Mapping of the Seabed; Proceedings of the Institute of Acoustics, Vol. 15, Part 2, 253-261.*

Boehme, H. (1985). Acoustic backscattering at low grazing angles from the ocean bottom. Part I. Bottom backscattering strength. *Journal of the Acoustical Society of America, Vol.77, No.3, 962-974.*

Boehme, H., and Chotiros, N.P. (1988). Acoustic backscattering at low grazing angles from the ocean bottom. *Journal of the Acoustical Society of America, Vol. 84, No.3, 1018-1029.*

Born, M. and Wolf, E. (1965). Principles of Optics. *Pergamon Press; Oxford.*

Brekhovskikh, L. and Lysanov, Y. (1982). Fundamentals of ocean acoustics. *Springer-Verlag, Berlin.*

Buchan, S., McCann, D.M., and Taylor Smith, D. (1972). Relations between the acoustic and geotechnical properties of marine sediments. *Quarterly Journal of Engineering Geology, Vol.5, 265-284.*

Buller, A.T. and McManus, J. (1979). Sediment sampling and analysis. *In, Dyer, K.R. (1979)* Estuarine hydrography and sedimentation. *Cambridge University Press.*

Caruthers, J.W. and Novarini, J.C. (1993). Modeling swath bathymetry/sidescan sonar image returns. *Proceedings of the Institute of Acoustics, Vol. 15, Part 2.*

Chesterman, W.D., Clynick, P.R. and Stride, A.H. (1958). An acoustic aid to sea bed survey. *Acustica, Vol. 8, 285-290.*

Chesterman, W.D., St Quinton, J.M.P., Chan, Y. and Matthews, H.R. (1967). Acoustic surveys of the sea floor near Hong Kong. *International Hydrological Review, Vol. 44, 35-54.*

Chotiros, N.P. (1985). Acoustic backscattering at low grazing angles from the ocean bottom. Part II. Statistical characteristic of bottom backscatter at a shallow water site. *Journal of the Acoustical Society of America, Vol. 77, No.3, 975-982.*

Clay, C.S., Ess, J. and Weisman, I. (1964). Lateral echo sounding of the ocean bottom on the continental rise. *Journal of Geophysical Research, Vol. 69, 3823-3835.*

Clay, C.S. and Medwin, H. (1977). Acoustical Oceanography Principles and Application. *Wiley, New York.*

Collins, M.B. and Voulgaris, G. (1993). Empirical field and laboratory evaluation of a real-time acoustic seabed surveying system. *Proceedings of the Institute of Acoustics, Vol.15, Part 2, 343-351.*

Collins, W., Gregory, R. and Anderson, J. (1996). A digital approach to seabed classification. *Sea Technology (August 1996).*

Collins, W. and Galloway, J.L. (1998). Seabed classification with multibeam bathymetry. *Sea Technology (September, 1998).*

Crowther, P.A. (1983). Some statistics of the seabed and scattering therefrom. *In,* Acoustics and the Seabed, *edited by N.G. Pace, Bath University Press, 147-155.*

Czarnecki, M.F. (1979). An application of pattern recognition techniques to sidescan sonar data. *Institute of Electrical and Electronic Engineers.*

Davis, A.M., Huws, D.G., and Haynes, R. (1996). Geophysical ground-truthing experiments in Eckernforde Bay. *Geo-Marine Letters, Vol.16, No.3, 160-166.*

de Moustier, C. and Alexandrou, D. (1991). Angular dependence of 12 kHz seafloor acoustic backscatter. *Journal of the Acoustical Society of America, Vol. 90, 522-531.*

de Moustier, C. and Matsumoto, H. (1993). Seafloor acoustic remote sensing with multibeam echo-sounders and bathymetric sidescan sonar systems. *Marine Geophysical Researches, Vol. 15, 27-42.*

de Moustier, C., Michalopoulou, Z. and Alexandrou, D. (1994). Application of maximum likelihood processor to acoustic backscatter for the estimation of seafloor roughness parameters. *Journal of the Acoustical Society of America, Vol. 95, No.5.*

Denbigh, P.N. (1977). Phase only side-scan sonar for underwater mapping. *Acoustic Letters 1, 84-87.*

Denbigh, P.N. (1979). A bathymetric side-scan sonar. *Proceedings of the Ultrasonics International Conference, 321-326.*

Denbigh, P.N. (1980). Glint and its effects on the accuracy of a seabed profiling sonar. *Proceedings of the Institute of Acoustics, 7.1-7.8.*

Denbigh, P.N. (1981). Stereoscopic visualisation and contour mapping of the seabed using BASS. *Proceedings of IERE Conference, No. 51, 291-311.*

Denbigh, P.N. (1983). Stereoscopic visualisation and contour mapping of the seabed using a bathymetric side-scan sonar (BASS). *Radio Electrical Engineering, Vol. 53, 301-307.*

Donovan, D.T. and Stride, A.H. (1961). An acoustic survey of the seafloor south of Dorset and its geological interpretation. *Philos. Trans. R. Soc., B244, 299-330.*

Dyer, K.R. (1979). Estuarine hydrography and sedimentation. *Cambridge University Press.*

Eckart, C. (1946). Principles and applications of underwater sound. *U.S. Department of the Navy, NAVMAT, P9674 (re-issued in 1968).*

Ewing, M., Vine, A.C. and Worzel, J.L. (1946). Recent results in submarine geophysics. *Geological Society of America Bulletin, Vol. 57, 909-934.*

Fish, J.P. and Carr, H.A. (1991). Sound Underwater Images: A guide to the generation and interpretation of side scan sonar data. *Taken from http://www.marine-group.com*

Fisher, F.H. and Simmons, V.P. (1977). Sound absorption in seawater. *Journal of the Acoustical Society of America, Vol.62, 558-564.*

Folk, R.L. (1954). The distinction between grain size and mineral composition in sedimentary rock nomenclature. *Journal of Geology, Vol.62, 344-359.*

Folk, R.L. (1968). Petrology of sedimentary rocks. *University of Texas Publication.*

Folk, R.L. and Ward, W.C. (1957). Brazos river bar: a study of the significance of grain size parameters. *Journal of Sedimentary Petrology, Vol.27, 3-26.*

Fox, C.G. and Hayes, D.E. (1985). Quantitative methods for analysing the roughness of the seafloor. *Review of Geophysics, Vol.23, 1-48.*

Friedman, G.M. (1962). On sorting, sorting coefficients, and the lognormality of the grain size distribution of sandstones. *Journal of Geology, Vol.70, 737-756.*

Gapper, G.R. and Hollis, T. (1985). The accuracy of an interferometric side-scan sonar. *Proceedings of the Institute of Acoustics, Vol. 7, Part 3, 126-134.*

Geen, M.F., Hewitt, P.D. and Adams, A.R. (1993). The ISIS Interferometric Seabed Inspection Sonar. *Proceedings of the Institute of Acoustics, Vol. 15, Part 2, 187-194.*

Geen, M.F. (1997). ISIS technical overview. *Submetrix Internal Report.*

Glenn, M.F. (1970). Introducing an operational multi-beam array sonar. *International Hydrographic Review, Vol.47, No.1, 35-39.*

Goodfellow, I.T. (1996). Analysis of co-registered bathymetry and sidescan data. *University of Bath, PhD thesis.*

Green, C.D. (1974). Sedimentary and morphological dynamics between St. Andrews Bay and Tayport, Tay Estuary, Scotland. *PhD thesis, University of Dundee.*

Greishar, L.L. and Clay, C.S. (1972). Use of side-scanning sonar for contouring bottom features. *Journal of the Acoustical Society of America, Vol.51, No.3, 1073-1075.*

Haines, R.G. (1963). Developments in ultrasonic instruments. *International Hydrological Review, Vol. 40, 49-57.*

Haines, R.G. (1970). Searoom for the supertanker. *Navy, Vol.75, No.6, 189-190.*

Hamilton, E.L. (1959). Thickness and consolidation of deep-sea sediments. *Bulletin of the Geological Society of America, Vol. 70, 1399-1424.*

Hamilton, E.L. (1980). Geoacoustic modelling of the seafloor. *Journal of the Acoustical Society of America, Volume 68, 1313-1340.*

Hamilton, E.L. and Bachman, R.T. (1982). Sound velocity and related properties of marine sediments. *Journal of the Acoustical Society of America, Vol. 72, No.6, 1891-1904.*

Haynes, R., Davis, A.M., Reynolds, J.M. and Taylor, D.I. (1993). The extraction of geotechnical information from high-resolution seismic reflection data. *Society of Underwater Technology, Vol. 28, 215-228.*

Haynes, R., Huws, D.G., Davis, A.M. and Bennell, J.D. (1997). Geophysical sea-floor sensing in a carbonate sediment regime. *Geo-Marine Letters, Vol.17, Issue 4, 253-259.*

Heaton, M.J.P. and Haslett, W.G. (1971). Interpretation of Lloyd mirror in sidescan sonar. *Proceedings of the Society of Underwater Technology, Vol. 1, 24-38.*

Hersey, J.B. (1960). Sonar uses in oceanography. *Instrument Society of America conference pre-print, Instrument Automation Conference, 21-Ny-60, NY.*

Hickley, T.J. (1966). Narrow-beam transducer sounding system. *International Hydrographic Review, Vol.43, No.1, 37-42.*

Hooper, D.J. (1979). Hydrographic surveying. *In, Dyer, K.R. (1979)* Estuarine hydrography and sedimentation. *Cambridge University Press.*

Horn, D.R., Horn, B.M. and Delach, M.N. (1968). Correlation between acoustic and other physical properties of deep-sea cores. *Journal of Geophysical Research, Vol. 73, 1939-1957.*

Howson, E.A. and Dunn, J.R. (1961). Directional echo-sounding. *Journal of the Institute of Navy, Vol. 14, No. 3, 348-359.*

Hughes-Clarke, J.E. (1993). The potential for seabed classification using backscatter from shallow water multibeam sonars. *Proceedings of the Institute of Acoustics, Vol. 15, Part 2, 381-388.*

Hughes-Clarke, J. (1994). Toward remote sea-floor classification using the angular response of acoustic backscattering – A case-study from multiple overlapping Gloria data. *Institute of Electrical and Electronic Engineers, Journal of Oceanic Engineering, Vol.19, No.1, 112-127.*

Hughes-Clarke, J.E., Miller, J.E., and Patterson, J. (1997). Are you really getting 'full bottom coverage'? *Hydrographic Journal, No.83, 3-10.*

Inman, D.L. (1952). Measures for describing the size distribution of sediments. *Journal of Sedimentary Petrology, Vol.22, 125-145.*

Isaaks, E.H. and Srivastava, R.M. (1989). An introduction to applied geostatistics. *Oxford University Press, New York, Oxford.*

Jackson, D.R. and Briggs, K.B. (1992). High-frequency bottom scattering: Roughness versus interface scattering. *Journal of the Acoustical Society of America, Volume 92, 962-977.*

Jackson, D.R. (1994). Models for scattering from the seabed. *Proceedings from the Institute of Acoustics, Vol.16, Part 6, 161-172.*

Jackson, D.R., Winebrenner, D.P., and Ishimaru, A. (1986). Application of the composite roughness model to high-frequency bottom scattering. *Journal of the Acoustical Society of America, Volume 79, 1410-1422.*

Johnson, H.P. and Helferty, M. (1990). The geological interpretation of side-scan sonar. *Reviews of Geophysics, Volume 28, No.4, 357-380.*

Krumbein, W.C. (1934). Size frequency distributions of sediments. *Journal of Sedimentary Petrology, Vol.4, 65-77.*

Kunze, W. (1957). General aspects of application of horizontal echo sounding method in shipping. *International Hydrographic Review, Vol. 34, 63-72.*

Kuryanov, B.F. (1963). The scattering of sound at a rough surface with two types of irregularity. *Soviet Physics Acoustics, Vol. 8, 252-257.*

Lambert, D.N., Cranford, J.C. and Walter, D.J. (1993). Development of a high resolution acoustic seafloor classification survey system. *Proceedings of the Institute of Acoustics, Vol. 15, Part 2, 149-157.*

Lees, A., Buller, A.T. and Scott, J. (1969). Marine carbonate sedimentation processes, Connemara. *Reading University Geological Reports 1.*

Liebermann, L.N. (1948). Origin of sound absorption in water and in sea water. *Journal of the Acoustical Society of America, Vol. 20, 868.*

Liebermann, L.N. (1949). Sound propagation in chemically active media. *Physics Review, Vol. 76, 1520.*

Ligdas, N. and Davies, J. (1998). ELIFONTS: Mapping the distribution of sediment types. *Interim Report, Seamap Research Group, University of Newcastle.*

Linnett, L.M., Clarke, S.J., Bell, J.M. and Carmichael, D.R. (1996). Tools for sonar processing and seabed mapping. *Sea Technology (June, 1996).*

Lyons, A.P., Anderson, A.L. and Dwan, F.S. (1994). Acoustic scattering from the seafloor: Modelling and data comparisons. *Journal of the Acoustical Society of America, Vol. 95, No.5, Part 1.*

Mackenzie, K.V. (1961). Bottom reverberation for 530 and 1030Hz sound in deep water. *Journal of the Acoustical Society of America, Vol. 33, 1498-1504.*

Marshall, H.O. and Rhoads, D.C. (1982). Acoustic imaging of structures in the upper 10cm of sediments using a megahertz backscattering system: preliminary results. *Marine Geology, Vol.46, 117-129.*

Matsumoto, H., Dziak, R.P. and Fox, C.G. (1993). Estimation of seafloor microtopographic roughness through modeling of acoustic backscatter data recorded by multibeam sonar systems. *Journal of the Acoustical Society of America, Vol. 94, No.5, 2776-2787.*

Matthews, D.J. (1939). Tables of the velocity of sound in pure water and seawater for use in echo sounding and sound ranging. *Admiralty Hydrographic Department Publication No.282.*

McCave, I.N. and Jarvis, J. (1973). Use of the model T Coulter Counter in size analysis of fine to coarse sand. *Sedimentology, Vol.20, 305-315.*

McDaniel, S.T. and Gorman, A.D. (1982). Acoustic and radar sea-surface backscatter. *Journal of Geophysical Research, Vol.87, 4127-4136.*

McDaniel, S.T. and Gorman, A.D. (1983). Examination of the composite roughness scattering model. *Journal of the Acoustical Society of America, Vol.73, 1476-1486.*

McKinney, C.M. and Anderson, C.D. (1964). Measurements of backscattering of sound from the ocean bottom. *Journal of the Acoustical Society of America, Vol.36, No.1.*

Medwin, H. (1975). Speed of sound in water: a simple equation for realistic parameters. *Journal of the Acoustical Society of America, Vol.58, 1318-19.*

Medwin, H. and Clay, C.S. (1998). Fundamentals of Acoustical Oceanography. *Academic Press.*

Mitchell, N.C. (1992). The acoustics of multi-beam sonar. *Seminar Paper, Wimpol Ltd.*

Mitchell, N.C. (1993). A model for attenuation of backscatter due to sediment accumulations and its application to determine sediment thicknesses with Gloria Sidescan sonar. *Journal of Geophysical Research – Solid Earth, Vol.98, No.B12, 22477-22493.*

Mitchell, N.C. and Hughes-Clarke, J. (1994). Classification of seafloor geology using multibeam sonar data from the Scotian Shelf. *Marine Geology, Vol.121, No.3-4, 143-160.*

Murray, J. and Pullar, L. (1910). Bathymetrical survey of the Scottish fresh water lochs. *Challenger Office, Edinburgh.*

Nishimura, C.E. (1997). Fundamentals of Acoustic Backscatter Imagery. *Naval Research Laboratory, Washington DC, NRL/FR/7420-97-9848.*

Nolle, A.W., Hoyer, W.A., Misfud, J.F., Runyan, W.R., and Ward, M.B. (1963). Acoustical properties of water-filled sands. *Journal of the Acoustical Society of America, Volume 35, 1394-1408.*

Ogilvy, J.A. (1987). Wave scattering from rough surfaces. *Rep. Prog. Physics, Vol.50, 1553-1608.*

Ogilvy, J.A. (1991). Theory of wave scattering from a random rough surface. *Adam Hilger.*

Pace, N.G. and Gao, H. (1988). Swath seabed classification. *Institute of Electrical and Electronic Engineers, Journal of Ocean Engineering, Vol. 13, 83-90.*

Pierce, W. and Graus, R.R. (1981). Use and misuses of the phi-scale: Discussion. *Journal of Sedimentary Petrology, Vol.51, 1348-1350.*

Rayleigh, Lord (1945). The theory of sound Vol. 2. *Dover Publications Inc., New York.*

Reut, Z., Pace, N.G. and Heaton, H.J.P. (1985). Computer classification of seabeds by sonars. *Nature, Vol. 314, 426-428.*

Richardson, M.D. and Briggs, K.B. (1993). On the use of acoustic impedance values to determine sediment properties. *From the Proceedings of the Institute of Acoustics, Vol. 15, Part 2.*

Richie, G.S. (1970). British hydrography since Cook. *The Naval Review, Vol.58, No.1, 126-134.*

Roe, G.M. (1943). Propagation of sound in shallow water. *U.S. Navy Bur. Ships Minesweeping Branch Report No.65.*

Schreiber, B.C. (1968). Sound velocity in deep sea sediments. *Journal of Geophysical Research, Vol. 73, 1259-1269.*

Schulkin, M. and Marsh, H.W. (1962). Sound absorption in seawater. *Journal of the Acoustical Society of America, Vol. 34, 864.*

Sheldon, R.W. and Parsons, T.R. (1967). A practical manual on the use of the Coulter Counter in marine science. *Coulter Electronics Sales Co., Toronto.*

Shepard, F.P. (1954). Nomenclature based on Sand-Silt-Clay ratios. *Journal of Sedimentary Petrology, Vol.24, 151-158.*

Sheriff, R.E. (1973). Encyclopaedic dictionary of exploration geophysics. *Published by The Society of Exploration Geophysicists.*

Shishido, M. and Naito, K. (1979). A study on picture improvement for side looking sonar. *NEC Research and Development, No.53, 62-74.*

Smailes, I.C. (1978). Bottom reverberation measurements at low grazing angles in the NE Atlantic and Mediterranean Sea. *Journal of the Acoustical Society of America, Vol. 64, No.5, 1482-1486.*

Smith, K.R. and McConnaughey, R.A. (1999). Surficial sediments of the eastern Bering Sea continental shelf. *EBSSED database documentation. U.S. Dep. Commer., NOAA Technical Memorandum NMFS-AFSC-104.*

Somers, M.L. and Stubbs, A.R. (1984). Sidescan sonar. *Institute of Electrical and Electronic Engineers Proceedings, Vol. 131 Part F, No.3, 243-256.*

Stanic, S. and Briggs, K.B. (1988). Shallow-water high-frequency bottom scattering off Panama City, Florida. *Journal of the Acoustical Society of America, Vol. 83, No.6, 2134-2144.*

Stanic, S. and Briggs, K.B. (1989). High-frequency acoustic backscattering from a coarse shell ocean bottom. *Journal of the Acoustical Society of America, Vol. 85, No.1, 125-136.*

Stanic, S., Kennedy, E. and Ray, R.I. (1991). Variability of shallow-water bistatic bottom scattering. *Journal of the Acoustical Society of America, Vol. 90, No.1, 547-553.*

Stephenson, E.B. (1935). Transmission of sound in seawater: absorption and reflection coefficients and temperature gradients. *US Naval Research Laboratory Report, S-1204.*

Stewart, W.K., Chu, D.Z., Malik, S., Lerner, S., and Singh, H. (1994). Quantitative seafloor characterisation using a bathymetric side-scan sonar. *Institute of Electrical and Electronic Engineers, Journal of Oceanic Engineering, Vol. 19, No.4, 599-610.*

Stockhausen, J.H. (1963). Scattering from the volume of an inhomogeneous half-space. *Naval Research Establishment, Canada, Report No.63/9.*

Stride, A.H. (1959). A linear pattern on the sea floor and its interpretation. *Journal of Marine Biological Association UK, Vol. 38, 313-318.*

Stride, A.H. (1982). Offshore tidal sands: Processes and deposits. *Chapman and Hall.*

Stubbs, A.R., McCartney, B.S. and Legg, J.G. (1974). Telesounding, A method of wide swathe depth measurement. *International Hydrographic Review, Vol.51, 23-59.*

Sutton, G.H., Berckhemer, H. and Nafe, J.E. (1957). Physical analysis of deep-sea sediments. *Geophysics, Vol. 22, 779-812.*

Talukdar, K.K., Tyce, R.C. and Clay, C.S. (1995). Interpretation of SeaBeam backscatter data collected at the Laurentian Fan off Nova-Scotia using acoustic backscatter theory. *Journal of the Acoustical Society of America, Vol.97, No.3, 1545-1558.*

Tamsett, D. (1993). Seabed characterisation and classification from the power spectra of side-scan sonar data. *Marine Geophysical Researches, Vol. 15, 43-64.*

Thorne, P.D., Hardcastle, P.J., Flatt, D. and Humphery, J.D. (1994). On the use of acoustics for measuring shallow water suspended sediment processes. *Institute of Electrical and Electronic Engineers, Journal of Oceanic Engineering, Vol. 19, No.1.*

Thorne, P.D., Holdaway, G.P. and Hardcastle, P.J. (1995). Constraining acoustic backscatter estimates of suspended sediment concentration profiles using the bed echo. *Journal of the Acoustical Society of America, Vol.98, No.4, 2280-2288.*

Trefethen, J.M. (1950). Classification of sediments. *American Journal of Science, No. 248(I), 55-62.*

Tucker, D.G. (1960). Directional echo-sounding. *International Hydrological Review, Vol. 37, No.2, 43-53.*

Tucker, M.J. (1961). Beam identification in multiple echo-sounders. *International Hydrological Review, Vol. 38, No.2, 25-32.*

Tucker, M.J. and Stubbs, A.R. (1961). A narrow-beam echo-ranger for fishery and geological investigations. *British Journal of Applied Physics, Vol. 12, 103-110.*

Urick, R.J. and Pieper, A.G. (1952). Determination of the target strength of a submarine by a new method. *US Office of Naval Research Informal Report.*

Urick, R.J. (1956). The processes of sound scattering at the ocean bottom and surface. *Journal of Marine Resources, Vol. 15, No.134.*

Urick, R.J. and Saling, D.S. (1962). Backscattering of explosive sound from the deep-sea bed. *Journal of the Acoustical Society of America, Vol. 34, 1721-1724.*

Urick, R.J. (1983). Principles of underwater sound. *3rd Edition; Peninsula Publishing, Los Altos, California.*

Visher, G.S. (1969). Grain size distributions and depositional processes. *Journal of Sedimentary Petrology, Vol.39, 1074-1106.*

Volgin, A.V. and Woodside, J.M. (1996). Sidescan sonar images of mud volcanoes from the Mediterranean Ridge – possible causes of variations in backscatter intensity. *Marine Geology, Vol.132, No.1-4, 39-53.*

Walker, F. (1963). The geology and scenery of Strathearn. *Dundee Museum and Art gallery publication.*

Wentworth, C.K. (1922). A scale of grade and class for clastic sediments. *Journal of Geology, Vol.30, 377-392.*

Winn, K., Becker, G. and Theilen, F. (1983). The relationship between sediment parameters and the acoustic reflectivity of the sea-bed. *From,* Acoustics and the seabed, *edited by Pace, N.G., Proceedings of the Institute of Acoustics: Conference Papers; Bath University Press.*

Wong, How-Kin and Chesterman, W.D. (1968). Bottom backscattering near grazing incidence in shallow water. *Journal of the Acoustical Society of America; Vol. 44, No.6, 1713-1718.*

The relationships between TS-AS and the Roughness Index (RI) can be summarised at each site using the Log-Linear equations derived from the trend lines in Figures 8.9, 8.18, 8.29, 8.30, 8.43, 8.44 and 8.45. These equations, along with a general description of the sediment type are tabulated below.

Sample No.	Log-linear equation for TS-AS v RI where, TS-AS (y) and RI (x)	General Sediment Class
1	y = -2.6988 Ln(x) - 16.913	Mud
2	y = -2.3025 Ln(x) - 13.506	Mud
4	y = -3.0381 Ln(x) - 14.4	Mud
4	y = -2.8868 Ln(x) - 9.371	Mud
5	y = -3.7549 Ln(x) - 32.044	Mud + Coarse
5	y = -1.3221 Ln(x) - 14.884	Mud + Coarse
7	y = -4.039 Ln(x) - 26.852	Mud + Coarse
7	y = -2.1853 Ln(x) - 17.664	Mud + Coarse
8	y = -2.3369 Ln(x) - 30.696	Sand
9	y = -3.0402 Ln(x) - 39.243	Sand
10	y = -2.8224 Ln(x) - 40.489	Sand
11	y = -2.3406 Ln(x) - 34.864	Sand
11	y = -2.6568 Ln(x) - 39.361	Sand
11	y = -3.0623 Ln(x) - 41.421	Sand
12	y = -1.8085 Ln(x) - 24.451	Sand
13	y = -2.717 Ln(x) - 38.49	Sands + Fines
13	y = -1.6884 Ln(x) - 28.208	Sands + Fines
13	y = -2.822 Ln(x) - 30.649	Sands + Fines
14	y = -2.3534 Ln(x) - 29.014	Sands + Fines
14	y = -2.1599 Ln(x) - 26.042	Sands + Fines
14	y = -2.5089 Ln(x) - 26.184	Sands + Fines
14	y = -1.445 Ln(x) - 25.526	Sands + Fines
15	y = -2.9195 Ln(x) - 32.748	Sands + Fines
15	y = -3.1515 Ln(x) - 34.448	Sands + Fines
16	y = -4.0318 Ln(x) - 41.396	Sands + Fines